Complex Materials : Frustrated Self-Assembly and Nonlinear Elasticity

Félix Benoist

université
PARIS-SACLAY

Complex Materials : Frustrated Self-Assembly and Nonlinear Elasticity

Matériaux complexes : auto-assemblages frustrés et élasticité non-linéaire

Thèse de doctorat de l'université Paris-Saclay

École doctorale n° 564, Physique en Île-de-France
Spécialité de doctorat : Physique
Graduate School : Physique, Référent : Faculté des sciences d'Orsay

Thèse préparée dans l'unité de recherche LPTMS (Université Paris-Saclay, CNRS), sous la direction de Martin Lenz

Thèse soutenue à Paris-Saclay, le 28 septembre 2022, par

Félix Benoist

Composition du jury

Benoit Roman Directeur de recherche, Sorbonne Université	Président
Anđela Šarić Associate Professor, IST Austria	Rapporteure & Examinatrice
Haim Diamant Professor, Tel Aviv University	Rapporteur & Examinateur
Yair Shokef Associate Professor, Tel Aviv University	Examinateur
Martin Lenz Directeur de recherche CNRS, Université Paris-Saclay	Directeur de thèse

THESE DE DOCTORAT
NNT : 2022UPASP075

Matériaux complexes: auto-assemblages frustrés et élasticité non-linéaire

Félix Benoist

septembre 2022

Cette thèse est divisée en deux parties avec peu de recoupement. La première partie traite de l'auto-assemblage pathologique de protéines normalement solubles. Dans un certain nombre de cas, elles ont tendance à former des agrégats "frustrés" qui ne grandissent que dans une seule direction. Nous étudions ici la forme et la taille des agrégats à l'équilibre formés par des particules avec des interactions directionnelles. Cette étude devrait permettre de mieux comprendre le mécanisme sous-jacent à la formation de fibres. La deuxième partie se concentre sur la transmission des contraintes internes dans les matériaux complexes tels que les réseaux de fibres biologiques et la matière granulaire. Nous développons un modèle continu de ces matériaux, qui tient compte de l'asymétrie mesurée dans leur réponse à la tension par rapport à la compression. Nous montrons analytiquement et numériquement que cela peut conduire les réseaux fibreux à rectifier les contraintes internes vers la contraction, et les milieux granulaires vers l'expansion.

1 Formation de fibres par auto-assemblage frustré de particules irrégulières

Dans de nombreux cas d'agrégation de protéines, les grappes formées ont tendance à avoir une nature fibreuse, c'est-à-dire se développent dans une seule direction tout en conservant une certaine largeur finie. Certaines de ces fibres telles que celles formées par l'actine dans le cytosquelette cellulaire (Oosawa and Kasai, 1962) ou certains amyloïdes exécutent des fonctions biologiques (Mankar et al., 2011). Mais les fibres sont souvent le résultat d'un auto-assemblage pathologique (Knowles et al., 2014), comme dans la drépanocytose. Dans ce cas, les fibres d'hémoglobine déforment les globules rouges en les faisant prendre cette forme de faucille qui se traduit par des problèmes de flux sanguin (Eaton and Hofrichter, 1990; Turner et al., 2003), voir Fig. 1, *gauche*. En fait, l'agrégation des protéines dans les cellules humaines est associée à de nombreuses maladies neurodégénératives (Brundin et al., 2010), le diabète de type II (Pytowski et al., 2020), etc. La nature pathologique de ces agrégats indiquent que les protéines constitutives ne sont *a priori* pas optimisées par la sélection naturelle pour former des fibres (Jia et al., 2020). Les protéines sont des objets très complexes, elles contiennent en effet de nombreux résidus différents qui interagissent potentiellement avec les autres résidus à l'intérieur des mêmes protéines, avec le solvant ou avec les résidus des protéines voisines. Les biologistes expliquent généralement la formation de fibres pathologiques sur la base d'interactions moléculaires détaillées (Eaton and Hofrichter, 1990; Ross and Poirier, 2004), où le mécanisme d'auto-assemblage typique est celui des amyloïdes (Knowles et al., 2014). Mais il a été montré par Bousset et al. (2002) que, par exemple, certains fibres de prions de levure, bien que présentant de nombreuses caractéristiques des amyloïdes, n'ont pas la structure typique en feuillets-β des amyloïdes. En fait, un nombre croissant de fibrilles de protéine diffèrent des amyloïdes (Knowles et al., 2007; Pohl et al., 2021), indiquant ainsi que l'auto-assemblage pathologique des protéines peut conduire à la formation de fibres de manière générique. Nous adoptons ici une approche subsidiaire, en ce sens qu'au lieu d'analyser chaque type de fibre en particulier, nous examinons si de telles fibres pourraient être attendues de principes physiques généraux. Par exemple, nous aimerions déterminer les mécanismes qui fixent la largeur des fibres à une valeur finie.

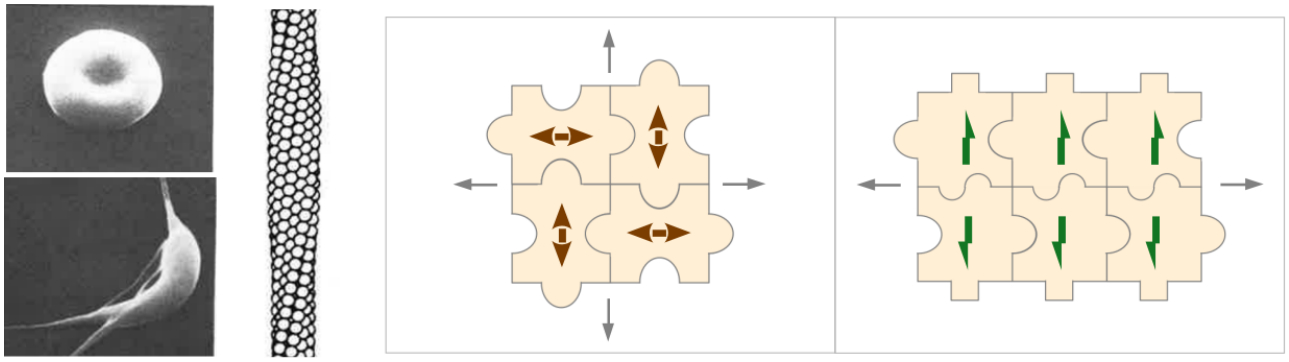

Figure 1: **Auto-assemblage fibreux de protéines et de pièces de puzzle.** *Gauche*, dans les globules rouges désoxygénés, les protéines d'hémoglobine se regroupent en fibres qui déforment la forme cellulaire habituelle (en haut) en formes de faucille (en bas). Croquis de fibres d'hémoglobine. Figures adaptées de (Eaton and Hofrichter, 1990). *Droite*, l'attribution d'une orientation permet de représenter les interactions directionnelles de copies d'une pièces de puzzle avec une matrice de couplage. Sur la gauche, la pièce de puzzle formant une feuille est π-périodique, comme indiqué par la double flèche. Celle plus asymétrique sur la droite forme une fibre de largeur 2.

Dans notre modèle grand-canonique, des copies d'une particule unique sont placées sur un réseau régulier infini et n'interagissent qu'avec leurs plus proches voisins dans les directions du réseau, comme dans le modèle d'Ising avec des variables de gaz sur réseau. Par exemple, on peut penser à des pièces de puzzle carrées sur un réseau carré, voir Fig. 1, *droite*. Nous considérons la distribution de probabilité de Boltzmann, telle qu'une configuration avec énergie E a une probabilité $\propto e^{-E/(k_B\theta)}$, k_B étant la constante de Boltzmann et θ la température. Disons qu'un couplage entre des côtés assortis est énergétiquement plus favorable que si les côtés ne matchent pas. Pour les particules isotropes qui interagissent de manière similaire dans toutes les directions de réseau, nous ne nous attendons pas à une formation extensive de fibres. En effet, dans les modèles à patches, alors que les interactions isotropes sont bien adaptées pour modéliser des liquides, les agrégats fibreux nécessitent une forte spécificité dans les interactions (Karner et al., 2020; Malhotra and Babu, 2020; Whitelam et al., 2009; Zhang and Glotzer, 2004). Cela peut être introduit via des partenaires d'interaction préférés (McManus et al., 2016; Whitelam et al., 2009). Nous considérons une approche similaire où les particules interagissent en fonction de leurs orientations discrètes, qui sont par exemple au nombre de 4 pour une particule carrée. Ces interactions sont caractérisées par une matrice de couplage avec en indices les orientations des deux particules par rapport à la direction de leur lien. Ces particules, possédant des côtés attractifs et répulsifs, ne seront donc pas automatiquement liés à leurs plus proches voisins pour former des cristaux. Cela peut induire une frustration géométrique, qui peut conduire à des morphologies d'agrégats non triviales, y compris des fibres. Dans des simulations numériques, M. Lenz et P. Ronceray ont étudié l'agrégation irréversible de copies d'une particule irrégulière sur un réseau 3D, avec des interactions directionnelles simples. Selon la forme spécifique des particules, les agrégats associés peuvent être des agrégats finis, des fibres, des feuilles ou des cristaux. Mais le lien entre la forme des particules et l'agrégat formé reste flou. Dans ce projet, nous cherchons à comprendre ce lien en étudiant les structures à l'équilibre qui découlent de l'auto-assemblage de ces particules avec des orientations discrètes. Nous étudions spécifiquement si certains types de particules frustrées pourraient favoriser la formation d'agrégats fibreux, qui ont une dimension réduite par rapport aux agrégats 2D ou 3D.

Dans un réseau 1D, les agrégats ne peuvent être que des amas finis ou des fibres potentiellement infinies. Seulement à deux dimensions ou plus y-a-t'il une différence entre une fibre et un cristal. Nous commençons par développer le formalisme de matrice de couplage en 1D pour n'importe quel nombre d'orientations discrètes n. Nous appliquons ensuite les méthodes du groupe de renormalisation dans l'espace réel pour étudier les caractéristiques pertinentes des systèmes décrits par leur matrice de couplage (Niemeijer and van Leeuwen, 1976). Par renormalisation, on entend un processus itératif de décimation d'une fraction des spins et de calcul des paramètres effectifs à chaque pas. Dans le cas d'une agrégation efficace où de longs agrégats se forment à faible densité, nous obtenons en particulier la

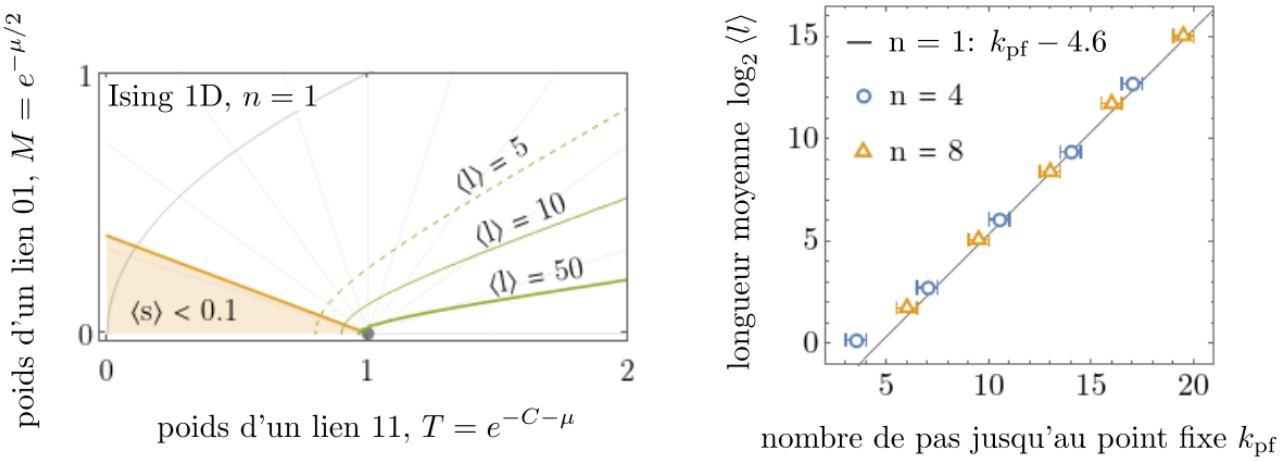

Figure 2: **Pour une agrégation efficace à 1D, la longueur moyenne des fibres décroît exponentiellement en la distance au point fixe stable non-interactif $k_{\rm pf}$.** *Gauche*, contours de la longueur moyenne d'un agrégat $\langle l \rangle$ et région à faible densité $\langle s \rangle$ pour $n = 1$. L'agrégation efficace se produit dans une région triangulaire à droite du point fixe répulsif ($M = 0, T = 1$). A cet endroit, la distance au point fixe attractif et non-interactif (courbe grise $T = M^2$) notée $k_{\rm pf}$ est grande et la densité faible. *Droite*, longueur moyenne théorique $\langle l \rangle$ versus $k_{\rm pf}$ obtenu par analyse numérique de l'itération de renormalisation. Les points pour $n = 4$ et 8 correspondent assez bien à l'ajustement calculé pour $n = 1$. $k_{\rm pf}$ peut ensuite être relié aux paramètres initiaux du systèmes (M, T pour $n = 1$).

longueur moyenne des agrégats d'équilibre quelque soit le nombre d'orientations discrètes des particules, voir Fig. 2. Nous montrons également que la plus grande valeur propre des matrices de couplages permet distinguer les types de particules qui ne peuvent former que des agrégats de taille finie, et ceux qui peuvent former des agrégats couvrant toute la chaîne. Dans l'ensemble, nous trouvons de nombreuses similitudes dans l'étude de la chaîne Ising ($n = 1$) et du modèle pour les orientations $n > 1$. En raison de la difficulté des calculs et puisque l'étude 1D importe moins en soi que comme préparation pour le cas 2D, nous ne nous attelons pas à prouver tous les résultats 1D, mais ouvrons plutôt la voie à la compréhension de la réduction dimensionnelle à 2D. Nous espérons identifier les classes d'universalité à travers une analyse de la dynamique des paramètres de couplage sous renormalisation (Efrati et al., 2014), qui contient en quelque sorte des informations sur la dimensionnalité des agrégats.

Suite à l'étude 1D présentée dans le dernier chapitre, nous discutons ici de l'agrégation en fonction du nombre d'orientations discrètes n sur les réseaux carrés et triangulaires. Ici, la zoologie des agrégats est assez variée et comprend plusieurs types d'agrégats de taille finie (triangle, hexagone, carré, etc.), plusieurs types de fibres (largeur 1 ou 2, zigzag) et plusieurs types d'agrégats 2D (amorphes, cristaux à trous, etc.) Nous adaptons avec succès le formalisme de matrice de couplage unidimensionnel aux réseaux bidimensionnels. Nous présentons plusieurs procédures de renormalisation simples qui devraient aider à trier les matrices de couplage selon la dimension de leur agrégat associé. Pour le modèle Ising ($n = 1$), nous obtenons la densité moyenne $\langle s \rangle$ par une approximation de champ moyen. Puis, nous relions la taille moyenne des agrégats $\langle R \rangle$ au nombre d'étapes de renormalisation pour arriver au point fixe attractif, voir Fig. 3. En effet, cette taille moyenne décroît du fait de la décimation d'une fraction des spins sous renormalisation jusqu'au point fixe non-interactif où elle vaut juste une taille de particule. Pour des orientations multiples $n > 1$, nous obtenons $\langle s \rangle$ dans des cas particulièrement pertinents, mais nous avons du mal à trouver un régime d'agrégation efficace où pouvoir calculer $\langle R \rangle$. En effet, la formulation $n > 1$ s'avère trop difficile à comprendre de façon purement analytique, c'est pourquoi une autre doctorante du groupe L. Koehler s'est attelée à des simulations numériques du processus de renormalisation. En outre, nous constatons que les procédures analytiques simples de renormalisation que nous proposons ne décrivent pas correctement certaines caractéristiques dynamiques des fibres sous renormalisation observées par L. Koehler. Dans le cas d'une procédure de renormalisation relativement correcte qui a des fibres comme points fixes, on pourrait à l'avenir considérer certaines statistiques pour la matrice de couplage, et regarder combien de matrices initiales tombent dans ces points fixes.

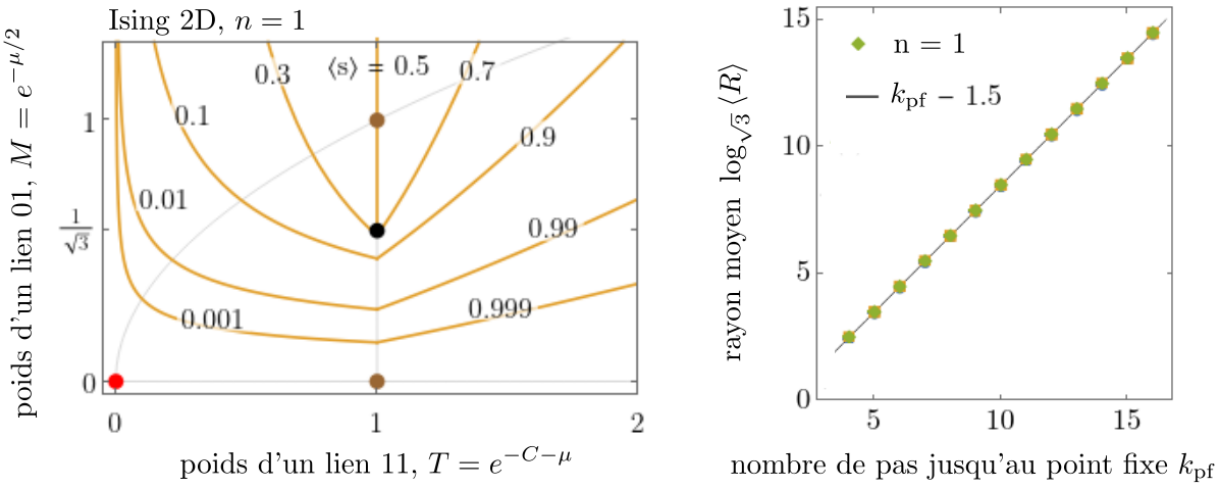

Figure 3: **Comme à 1D, pour une agrégation efficace à 2D, le rayon moyen croît exponentiellement avec la distance au point fixe k_{pf}.** *Gauche*, contours approximatif de la densité moyenne $\langle s\rangle$ en champ moyen. Sur la ligne $T = 1$ en dessous de $M_c = \frac{1}{\sqrt{3}}$, $\langle s\rangle$ est bivalué. *Droite*, rayon moyen théorique $\langle R\rangle$ versus k_{pf} obtenu par analyse numérique de l'itération de renormalisation 2D.

2 Rectification générique des stresses dans les milieux élastiques non-linéaires

Notre intuition de la mécanique des matériaux non-linéaires est largement basée sur l'étude de leur comportement lors de déformations aux bords. Nous nous attendons à ce qu'un matériau uniformément comprimé réagisse avec une contrainte expansive, tandis que l'application d'un cisaillement provoquera une contrainte de cisaillement opposée. Nous montrons ici que si les forces sont exercées de l'intérieur du matériau, ces attentes peuvent être bouleversées. Par exemple, le cytosquelette cellulaire consiste en des réseaux de biopolymères avec des unités actives intégrées telles que les moteurs moléculaires. Ronceray et al. (2016) ont simulés des réseaux de fibres flambables discrètes qui propagent davantage la tension que la compression. Soumis à de larges dipôles de forces localisés, le champ lointain des contraintes transmises par le réseau est rectifié vers la contraction, même dans les cas où les forces locales sont plutôt expansives. Ceci peut expliquer pourquoi l'acto-myosine désordonnée dans les cellules non-musculaires est majoritairement contractile malgré la présence de dipôles de force mixtes (Hatano, 1994; Lenz et al., 2012a). Les milieux granulaires peuvent également être soumis à des contraintes internes sous forme d'événements plastiques dus à de grandes déformations par cisaillement aux bords. Nous étudions la propagation de ces contraintes internes et leur impact sur l'écoulement des empilements de disques.

Pour cela, nous généralisons les résultats de Ronceray et al. (2016) au-delà des réseaux de fibres, et démontrons analytiquement que la rectification du stress est un corollaire générique de la propagation du stress dans un milieu élastique non-linéaire. Notre approche est basée sur un formalisme continu qui permet une discussion générale des non-linéarités arbitraires. Dans une géométrie circulaire, nous considérons un matériau élastique, isotrope et achiral soumis à une unité active annulaire, qui produit des contraintes moyennées au milieu du matériau. Nous définissons ces contraintes en termes d'une pression et d'un cisaillement locaux $\mathcal{P}_l$ et $\mathcal{S}_l$, voir Fig. 4(a). Ces contraintes sont ensuite propagées vers le bord fixe du matériau, produisant une pression et d'un cisaillement actifs $\mathcal{P}_a$ et $\mathcal{S}_a$, au sens du gel actif de Prost et al. (2015). Nous étudions ensuite les conditions d'émergence de phénomènes de rectification tels que lorsqu'une unité active localement expansive conduit à une contraction au bord. Nous montrons ici que cette correction de contrainte peut provenir de non-linéarités géométriques et/ou constitutives dans la réponse élastique du matériau, par rapport à la tendance du matériau au flambage ou à l'anti-flambement.

Notre modèle est basé sur sur un développement tensoriel de la loi d'élasticité linéaire de Hooke, où le tenseur des contraintes est proportionnel au tenseur des déformations, dans le régime faiblement non-linéaire. Ceci afin de pouvoir effectuer des calculs analytiques relativement simples. Lors d'une

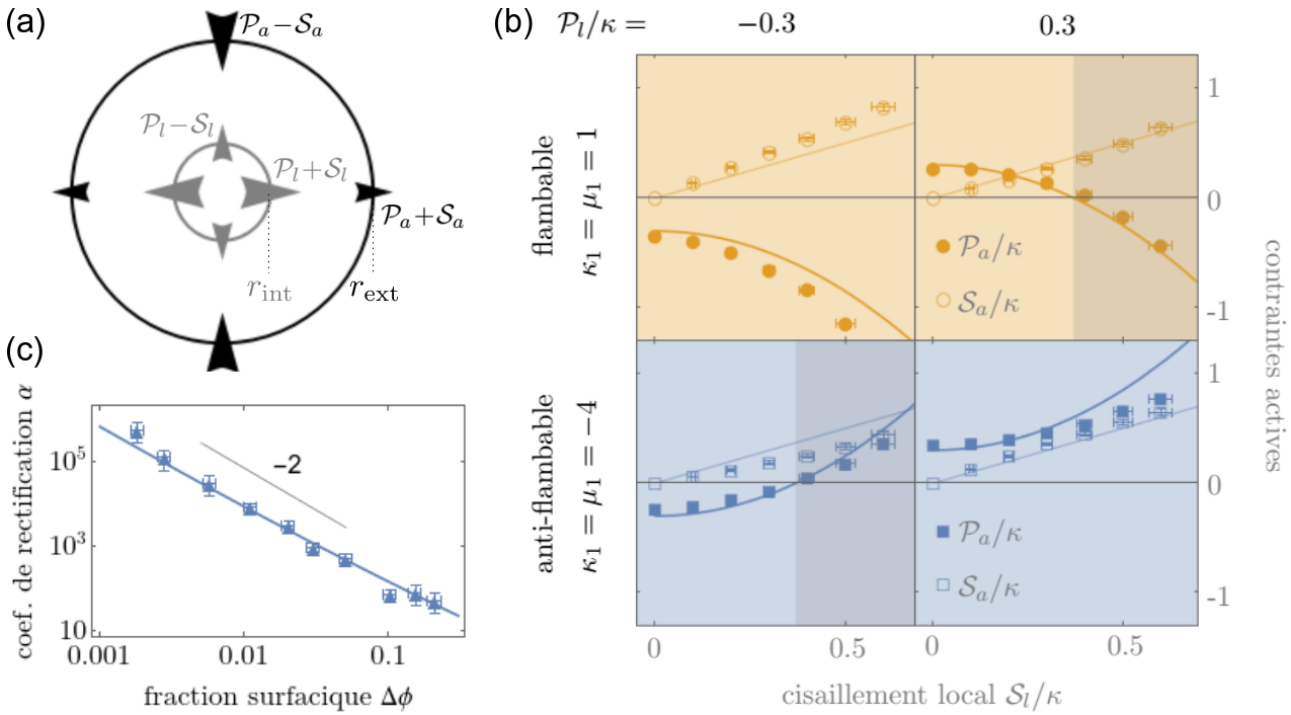

Figure 4: **Plusieurs simulations retrouvent les prédictions de rectification.** (a) Schéma des contraintes moyennées induites par les déformations internes. Composantes du tenseur des contraintes dans une situation particulière où la pression locale $\mathcal{P}_l$ est positive et la pression active $\mathcal{P}_a$ au bord est négative. (b) Les prédictions faiblement non-linéaires de l'Eq. (2) (lignes) capturent avec précision les résultats de simulation aux éléments finis (symboles), même pour les valeurs de contrainte intermédiaires. Ici le coefficient de Poisson $\nu = (\kappa - \mu)/(\kappa + \mu) = 0.1$ et $r_{\text{ext}}/r_{\text{int}} = 2$. *Haut*, un modèle flambable comme un réseau de fibres. *Bas*, un modèle très anti-flambable imitant un milieu granulaire. L'ombrage de fond correspond à un biais vers la contraction (jaune) ou l'expansion (bleu). La pression active va jusqu'à changer de signe dans les zones grisées. (c) Le coefficient de rectification α diminue comme une loi de puissance avec la distance à la transition de rigidité $\Delta\phi$. Coefficients obtenus en ajustant plusieurs séries de données sur des empilements d'environ 6700 disques (symboles). L'accord avec le coefficient de rectification théorique (ligne) est quantitatif.

combinaison de déformation volumique $\eta_{ii} = \eta_{xx} + \eta_{yy}$ et de cisaillement simple η_{xy}, la réponse d'un matériau peut être caractérisée par ses modules élastiques volumique et de cisaillement différentiels. Dans notre cas, ils s'écrivent respectivement

$$K \sim \kappa\,(1 + \kappa_1 \eta_{ii}) \quad \text{et} \quad G \sim \mu\,(1 + \mu_1 \eta_{ii})\,, \tag{1}$$

où les corrections non-linéaires de premier ordre aux modules κ_1, μ_1 comprennent des contributions de non-linéarités géométriques ainsi que constitutives. Les non-linéarités par lesquelles le matériau se raidit sous tension ($\eta_{ii} > 0$) et s'assouplit sous compression sont caractéristiques des réseaux de fibres flambables (Storm et al., 2005) et correspondent à des corrections $\kappa_1, \mu_1 > 0$. À l'inverse, les matériaux avec $\kappa_1, \mu_1 < 0$ s'assouplissent sous tension et se raidissent sous compression. Ce comportement "anti-flambant" peut offrir une description des milieux granulaires, où les contacts entre les grains sont perturbés à mesure que la pression de confinement diminue (Ellenbroek et al., 2009b). Nous montrons que la rectification des contraintes au bord est un phénomène générique, et que les corrections aux modules élastiques κ_1, μ_1 décrivant la réponse faiblement non-linéaire d'un matériau sont un prédicteur fiable du signe et de l'ampleur de la rectification. En effet, par un calcul analytique des déformations dans le matériau, nous arrivons à une équation simple entre les contraintes moyennées locales et au bord :

$$\mathcal{P}_a \sim \mathcal{P}_l + \alpha \mathcal{S}_l^2, \quad \mathcal{S}_a \sim \mathcal{S}_l. \tag{2}$$

Le seul paramètre α est le coefficient de rectification qui est toujours négatif pour $\kappa_1, \mu_1 > -3/2$, ce

qui biaise les réseaux de fibres vers la contraction. De même, α est toujours positif pour $\kappa_1, \mu_1 < -3/2$, induisant un biais expansif dans les empilements de grains. Dans les cas les plus extrêmes, une unité active intégrée qui se dilate (se contracte) dans toutes les directions peut provoquer des contraintes contractiles (expansives) dans toutes les directions. Le système "oublie" ainsi la forme des unités actives, et son comportement à grande échelle est contrôlé par les caractéristiques du matériau élastique.

Nous mettons ensuite cette conclusion analytique à l'épreuve avec deux séries de simulations et une série d'expériences. Nous utilisons d'abord des simulations d'éléments finis de modèles grandement non-linéaires pour montrer que nos conclusions restent qualitativement valides aux ordres supérieurs, voir Fig. 4(b). Deuxièmement, nous étudions la réponse élastique des milieux granulaires à une transformation de cisaillement grâce à des simulations de dynamique granulaire. Nos résultat concordent avec les observations expérimentales antérieures de Desmond and Weeks (2015) selon lesquelles les contraintes de champ lointain deviennent biaisées vers l'expansion au voisinage de la transition de rigidité, où les effets non-linéaires jouent un rôle important, voir Fig. 4(c). De tels effets dus à la rectification pourraient alors affecter de manière significative les caractéristiques de l'écoulement dans les systèmes juste rigides (Merabia and Detcheverry, 2016; Nicolas et al., 2018). Enfin, nous présentons des expériences préliminaires de F. Box montrant le biais de contraction de minces feuilles élastiques, qui peuvent flamber librement hors du plan. Ces comportements sont donc génériques dans les médias élastiques au-delà des réseaux de fibres discrètes étudiés précédemment.

Cette description faiblement non linéaire avec les corrections aux modules élastiques κ_1, μ_1 élabore un parallèle intéressant entre les réseaux de fibres et la matière granulaire. Ainsi, leurs biais similaires mais opposés vers la contraction et l'expansion peuvent être compris comme faisant partie du même phénomène de rectification, voir Fig. 5. Des similitudes entre ces classes de matériaux ont déjà été soulignées par, notamment, Broedersz et al. (2011) et Wyart et al. (2008) aux environs de la transition de rigidité. Une ressemblance plus profonde est trouvée en considérant les empilements granulaires comme des réseaux de ressorts aléatoires. De même que le flambement des fibres individuelles est

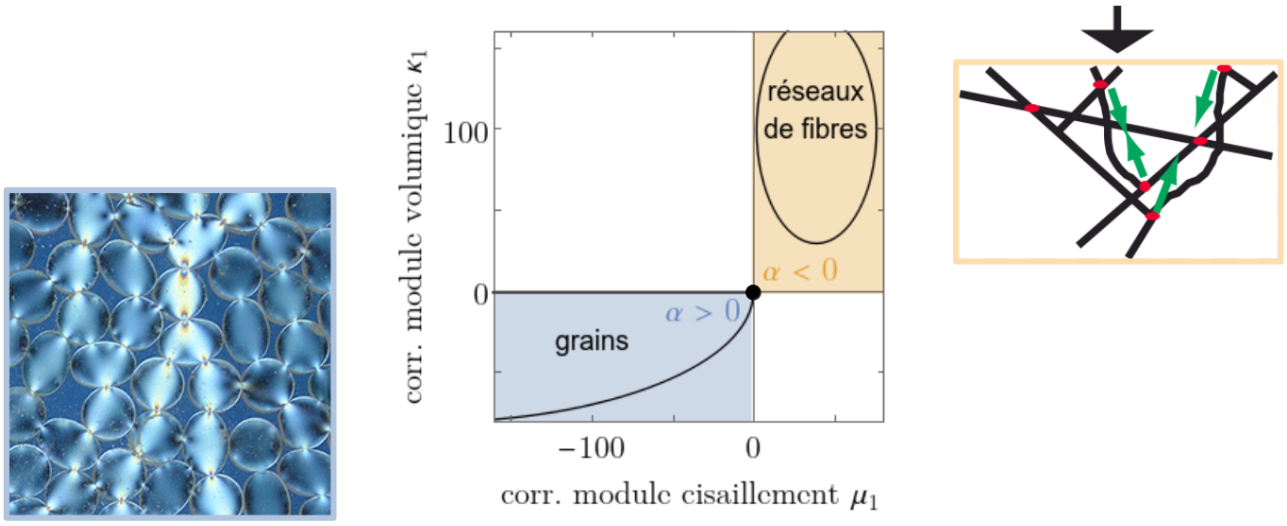

Figure 5: **Diagramme de rectification schématisé en fonction des corrections aux modules élastiques κ_1 et μ_1.** D'une part, les milieux granulaires (dans le quadrant inférieur gauche) propagent la compression mieux que la tension, ce qui biaise vers l'expansion $\alpha > 0$. Cela correspond à l'image de gauche dans laquelle les disques photo-élastiques illustrent les chaînes de force de compression. Extrait de (Daniels, 2014). D'autre part, les réseaux de fibres (dans le quadrant supérieur droit) ont tendance à se déformer et à propager ainsi la tension plus que la compression, comme le montre la figure de droite de (Chaudhuri et al., 2007). Cela induit un biais de contraction $\alpha < 0$. D'autres matériaux avec des propriétés moins proéminentes de flambement ou d'anti-flambement se trouvent généralement à l'intérieur du disque noir au centre. Pour les matériaux hypothétiques dans les autres quadrants blancs, le coefficient de rectification α est en général plus petit et son signe dépend du coefficient de Poisson ν et de la taille du système $r_{\text{ext}}/r_{\text{int}}$.

fondamental pour le biais de contraction des réseaux fibreux (Ronceray et al., 2016), le comportement élastique anti-flambant des matériaux granulaires semble être le principal facteur du biais d'expansion observé (Ronceray, 2016). Dans une certaine mesure, on peut ainsi modéliser symétriquement des gels de biopolymères comme réseaux d'éléments flambables, et des empilements de disques comme réseaux d'éléments anti-flambables. De plus, dans les valeurs de κ_1, μ_1 que nous avons collectées à partir de modèles expérimentaux ou réalistes, nous n'avons vu jusqu'à présent que de grandes valeurs de $|\kappa_1|, |\mu_1|$ avec le même signe. Cela suggère que les comportements flambables ($\kappa_1, \mu_1 > 0$) et anti-flambables ($\kappa_1, \mu_1 < 0$) sont mutuellement exclusifs à l'échelle mésoscopique. En ajoutant des grains à un réseau de fibres, le comportement du milieu passera probablement continuellement d'un comportement flambable avec un biais contractile, à un comportement anti-flambable avec un biais expansile.

Foreword

This thesis is divided into two parts with little overlap. The first part deals with the pathological self-assembly of normally soluble proteins. In a number of cases, they tend to form "frustrated" aggregates which grow only in one direction. We hereby study the shape and size of the equilibrium clusters formed by particles with directional interactions. This investigation hopefully leads to a better understanding of the underlying mechanism of fiber-formation. The second part focuses on the transmission of internal stresses in complex materials such as biological fiber networks and granular matter. We develop a continuum model of such materials, which accounts for the measured asymmetry in their response to tension versus compression. We show analytically and numerically that this may lead fibrous networks to rectify internal stresses towards contraction, and granular media to rectify towards expansion.

This work would not have been possible without the help of my supervisor Martin Lenz who was there at every step of the way. He is one of the best researchers I know, and his pedagogical and communication skills command admiration. He pushed me into doing this PhD when I was unsure and accepted to fund me himself when I messed up all other funding opportunities. He has since then been very patient when I was being stubborn, and very encouraging of my pursuit in the academic world. This has certainly been a significant factor in my continuation in a postdoc. He helped me portray the physicist that I aspire to become.

I would also like to thank my many collaborators both in and outside the lab. Many thanks to everybody in the biophysics group who helped develop the ideas in this thesis through many fruitful discussions. Lara Koehler and Mehdi Bouzid who directly participated in the first and second parts of this project. Hugo Le Roy, Mayarani M., Valerio Sorichetti, M. Mert Terzi, Samuel Cazayus-Claverie, Natascha Hey, Martin Garic and Lukas Kalvoda for their help in the bibliography during many journal clubs.

Likewise, cheers to Finn Box who collaborated on the experimental part from his lab in Manchester. Pierre Ronceray who is responsible, together with Martin, for the idea of using renormalization to find fibers among protein aggregates. Guglielmo Saggiorato who helped pave the way for the theorizing of the rectification effect in elastic materials. Jay Amrit and Sylvain Pralong for their help in my teaching of thermodynamics at the IUT. And my thesis advisors Frédéric van Wijland and Raoul Santachiara.

Furthermore, thanks to everyone at the lab. Primarily to Claudine Le Vaou and Karolina Kolodziej who were of great help for planning trips abroad and understanding administrative rulings. Emmanuel Trizac and Alberto Rosso for their thoughtful management of the lab. And my comrades from LPTMS among which Louis Bremaud and Matteo Butano for many relaxing chess games.

Finally, I am grateful for many passionate teachers who gave me the taste for math and physics during all those years of high school, preparatory classes and at the ENS. Especially Mr. Fortin-Ripoche for his wonderful courses and for encouraging me to get into the ENS. This work is dedicated to him.

Contents

General introduction

Although the following two parts are greatly disconnected, there is a common thread, namely protein fibers. Even though one often views cells as amorphous bodies, some cells such as fibroblasts actually contain very ordered structures (Alberts et al., 2015). Fibroblasts, which are the main cells of connective tissues, play a critical role in, *e.g.*, wound healing. As sketched in Fig. 6, *top*, their cytoskeleton consists of a vast array of filaments including microtubules and actin fibers. Microtubules are stiff polar filaments on which kinesin molecular motors (Vale and Milligan, 2000) can walk to transport components inside the cell, as shown in the movie from XVIVO and Harvard University (2006). Actin fibers are semiflexible polar filaments, which can be subjected to dipolar forces via myosin motors. Provided that the actin fibers are crosslinked into a network, these forces can be transmitted throughout the cell. The cytoskeleton as a whole helps the cell maintain its shape, divide and move around in its environment (Plotnikov et al., 2012). But not all fibers inside cells execute functions; some fibers are indeed very deleterious to the cell health. This is the case in sickle cell disease, where normally soluble hemoglobin proteins inside red blood cells tend to aggregate into long fibers, see Fig. 6, *bottom*. These fibers subsequently deform red blood cells into sickle-like shapes which causes blood flow issues. In the following, we study both functional and deleterious types of fibers. The first part deals with the self-assembly of proteins into deleterious fibers. The second part then focuses on the propagation of internal stresses in fiber networks, in comparison with that in granular matter. In both parts, we aim at understanding some macroscopic behaviors using simplified microscopic descriptions.

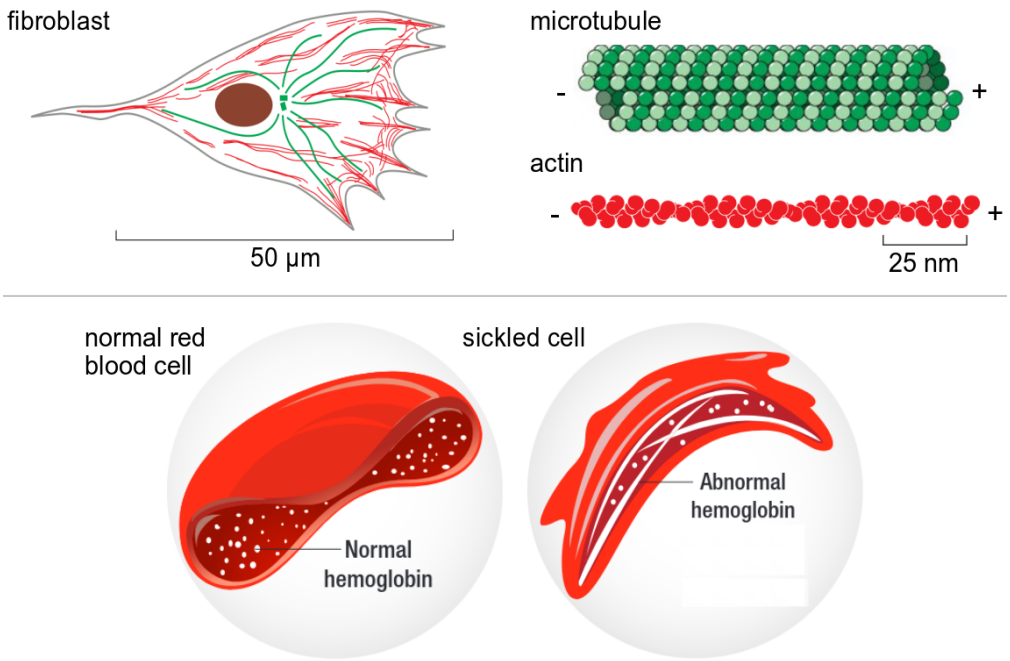

Figure 6: **Functional and deleterious protein fibers.** *Top*, sketched fibroblast comprising its membrane (in black), its nucleus (in brown), microtubules (in green, sketch from (Lodish et al., 2021)) and actin fibers (in red), reproduced from (Alberts et al., 2015). *Bottom*, sketched red blood cell with soluble hemoglobin protein and sickled cell due to hemoglobin fibers, adapted from (National Heart, Lung and Blood Institute, 2022).

Part I

Frustrated self-assembly of irregular particles

Chapter 1

Introduction to protein aggregation

Proteins are complex three-dimensional (3D) objects which tend to self-assemble under certain conditions into different types of aggregates. As discussed in Sec. 1.1, in many cases, multiple copies of an anisotropic protein type form fiber-like aggregates which grow only in one direction, instead of forming three-dimensional crystals or amorphous clumps. To understand this generic dimensionality reduction, several classes of models have been proposed which consider different types of interactions between protein-like particles. We review these models in Sec. 1.2. In Sec. 1.3, we then focus on self-assembly models where copies of a lattice particle interact directionally with their nearest neighbors. In particular, we present previous numerical simulations from M. Lenz and P. Ronceray where particles self-assemble irreversibly. Although they find aggregates of different dimensions depending on the particle type, the link between the interaction properties and the aggregate formed remains unclear. We thus discuss finding this link by renormalizing the interactions to probe the large-scale physics of the system in Sec. 1.4.

1.1 Fibrous self-assembly of anisotropic proteins

Proteins are large biomolecules (roughly 5 nm in diameter) made of long chains of amino acid residues called polypeptides, which usually results in protein folding into a specific anisotropic 3D structure that determines its activity. They are found either in "globular" forms, *i.e.* in solution inside or outside the cell, in aggregated forms or at the membrane. They form the cell's building blocks and execute most of the cell's functions (Alberts et al., 2015). Globular proteins in solution generally keep a rather stable 3D structure. Their collective behavior can however vary substantially depending on parameters such as temperature or protein concentration. At equilibrium, these behaviors correspond to different regions in the so-called phase diagram of these proteins. The experimental phase diagram in the temperature-concentration plan of the protein γ_{IIIb}-crystallin found inside calf cataract cells is plotted with open symbols in Fig. 1.1, *left* (Lomakin et al., 1999). The top left curve at relatively high temperature corresponds to the liquid-solid transition line. Whereas the bottom curve with circles corresponds to the liquid-liquid phase transition, such that below this curve, there is coexistence of two liquid phases with different concentrations (Alberti et al., 2019). This phase transition has been shown to help trigger protein aggregation into larger structures (Kurita and Tanaka, 2019; Pytowski et al., 2020; Zbinden et al., 2020). This can lead to many types of protein clusters including crystals, amorphous melts, fibrils which can stack to form sheet-like structures, and finite-size clusters such as viral capsids or bacterial microcompartments (McManus et al., 2016). This self-assembly process can be even more complex when it includes several protein species, but for simplicity purposes, we will further restrict to the case of a single type of protein in a uniform solvent.

Upon trying to analytically recover the phase diagram of the protein γ_{IIIb}-crystallin, it turns out that the anisotropy of the proteins plays a huge role, which reflects in their collective behavior. Indeed, when considering a typical colloidal model with isotropic interactions (Asherie et al., 1996), one obtains the green curves [Fig. 1.1, *left*], which fail to match the experimental data points. The real question now becomes: what is the best way to take this anisotropy into account? A first idea consists in specifying a certain number of patches which mediate inter-particle interactions. The

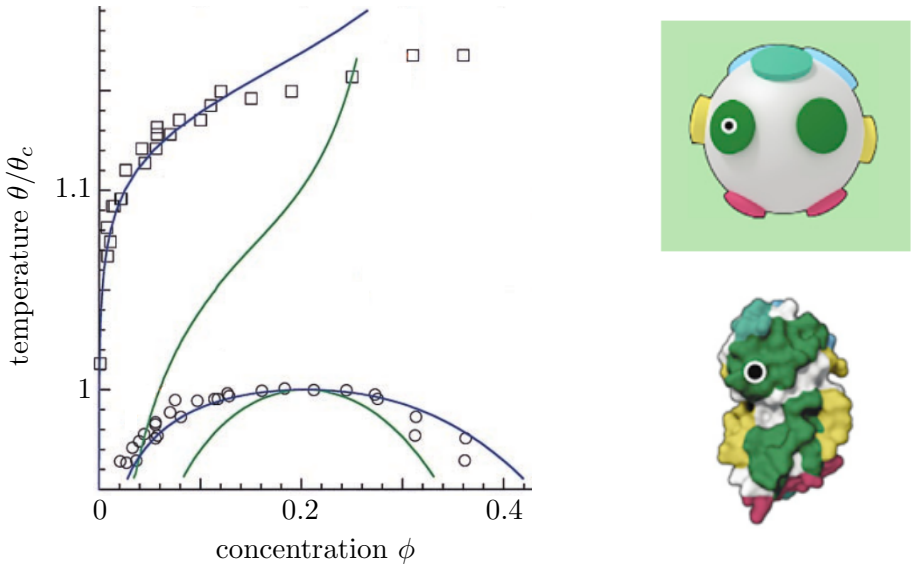

Figure 1.1: **Protein phase diagrams depend on their anisotropy.** *Left*, phase diagram of a calf crystallin protein, reproduced from (Lomakin et al., 1999). Data points indicate experimental transition lines, while the green and blue curves are the best fit from two distinct analytical models. The green ones come from a colloidal model with isotropic interactions. While for the blue ones, the authors consider a random map of attractive regions covering 1% of the surface area. *Right*, patchy model for a certain mutant of the human protein γD-crystallin, adapted from (Khan et al., 2019). The colors of the patches on the top refer to the experimentally investigated interaction sites, as seen on the detailed protein sketches on the bottom. The black dot denotes the same point on the two representations.

patches can represent a mixture of weak non-covalent bonds, such as hydrogen bonds and hydrophobic interactions (Fusco and Charbonneau, 2013). One implementation of this idea is shown in Fig. 1.1, *right*, where interactions between particles require two patches to come into contact. These patchy models can lead to quantitative agreement with experimental data, as shown by the blue curves in Fig. 1.1, *left*. In certain conditions, the normally soluble crystallin proteins tend to crystallize. This causes a change in the refraction index of the milieu that becomes opaque, which can lead to blindness in what is known as cataract disease (Khan et al., 2019).

But in many other cases of protein aggregation, the clusters formed tend to have a fibrous nature, *i.e.* grow in only one direction while conserving a certain finite width. Some of these fibers such as those made by actin in the cell cytoskeleton (Oosawa and Kasai, 1962) or certain amyloids provide biological functions (Mankar et al., 2011). But fibers are often the result of pathological self-assembly (Knowles et al., 2014), as in sickle cell disease, see Fig. 1.2, *left*. In this case, hemoglobin fibers deform the red blood cells causing them to take this sickle-like shape which results in blood flow issues (Eaton and Hofrichter, 1990; Turner et al., 2003). In fact, protein aggregation in human cells is associated to many diseases including Alzheimer's (Ghosh et al., 2019), Parkinson's (Zbinden et al., 2020), Huntington's (Peskett et al., 2018) and other neurodegenerative diseases (Brundin et al., 2010), type II diabetes (Pytowski et al., 2020), etc. Yet, the pathological nature of these clusters indicate that the aggregating proteins were *a priori* not optimized through natural selection to form fibers (Jia et al., 2020). We thus lack an explanation for why fibers are so prevalent in protein aggregates.

1.2 A physicist's frustrated approach

Proteins are very complicated objects, they indeed contain many different amino acid residues which potentially interact with the other residues inside the same proteins, with the solvent or with residues of neighboring proteins. Biologists typically explain pathological fiber formation on the grounds of detailed molecular interactions between specific parts of the proteins (Eaton and Hofrichter, 1990; Ross and Poirier, 2004). In this approach, the classic self-assembly mechanism is the one of

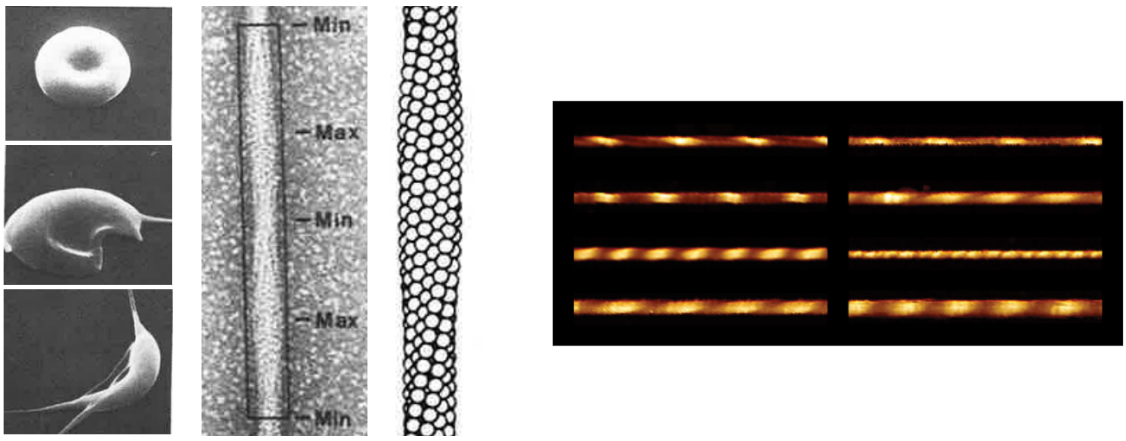

Figure 1.2: **Fibers are ubiquitous in protein self-assembly.** *Left*, in deoxygeneated red blood cells (roughly 7 μm in diameter), hemoglobin proteins aggregate into fibers which distort the usual cell shape (top) into sickle-like shapes (middle and bottom). Electron micrographs of hemoglobin fibers and sketch from image reconstruction. Figures adapted from (Eaton and Hofrichter, 1990). *Right*, amyloid fibril polymorphism reconstructed from atomic force microscopy data sets, taken from (Aubrey et al., 2020). Protofilaments made from the same peptide show different widths and helical pitches.

amyloids. Individual globular proteins subjected to mild conformational fluctuations first aggregate into disordered oligomers, which then change conformation to adopt β-rich structures (Chen et al., 2020; Jia et al., 2020; Knowles et al., 2014; Šarić et al., 2014). The stacking of β-sheets and the resulting electrostatic zippers of hydrogen bonds enable these oligomers to grow into long rigid fibers (Boyer et al., 2020; Knowles et al., 2007). As seen in Fig. 1.2, *right*, amyloid protofilaments made from the same small peptide present large shape variations (Alam et al., 2019; Aubrey et al., 2020; Meinhardt et al., 2009). This indicates the robustness of their characteristic β-sheet stacking mechanism, which explains the widespread use of the amyloid framework. But it was shown by Bousset et al. (2002) that *e.g.* certain yeast prions retain their native α-helical conformation upon assembly into fibrils. The authors thus concluded that while these fibers exhibited many characteristics of amyloids (such as shape and some binding affinity), they were not built on the β-sheet framework of amyloids. In fact, an increasing number of protein fibrils have been shown to differ from amyloids (Knowles et al., 2007; Pohl et al., 2021), thus indicating that pathological self-assembly of proteins may generically lead to fibers, even beyond the amyloid framework.

In this project, instead of looking at each fiber type specifically, we take a step back and investigate whether such fibers could be expected from general physical principles. For instance, we would like to determine the mechanisms that fix the width of the fibers to a finite constant value, as is observed in many living systems (Hagan and Grason, 2021). For instance, amyloids have a one-protein width, while actin fibers have a width of two, and hemoglobin fibers typically stack and attain higher widths. In this sense, fibers are different from *e.g.* needle crystals which grow with different speeds in different directions so as to reach aspect ratios of 1:1:1000 (Lovette and Doherty, 2013). The better understanding of how proteins self-assemble into fibers can lead to many applications (Mankar et al., 2011). For instance, the reliable pH-dependent assembly and disassembly of amyloids encourages their use as stable depots that would guarantee a controlled release of an active drug (Langer, 1990; Maji et al., 2008; Pohl et al., 2021). Conducting nanowires can also be built by controlled self-assembly of protein fibers and selective metal deposition (Scheibel et al., 2003). Additionally, harnessing this fiber formation could help design scaffolds for cell culture in 3D (Gelain et al., 2006). And if it turns out that certain particular conformations of proteins lead preferentially to fibers, we could develop new ways of inhibiting fibrous self-assembly when toxic by targeting these conformations specifically, either at the level of monomers or oligomers (Michaels et al., 2020; Šarić et al., 2014). Besides the broad applications to understanding the self-assembly of natural proteins, this research could help design "de novo" proteins which would not aggregate, or on the contrary whose fiber formation would execute a particular relevant function (Shen et al., 2018).

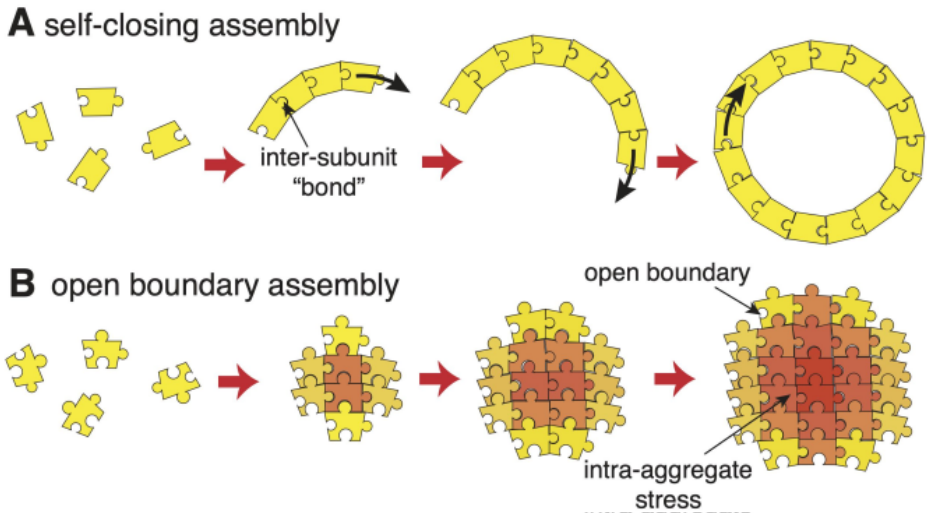

Figure 1.3: **Two types of self-assembly of copies of an irregular particle show self-limitation.** In the first case, the linear aggregation process falls back on itself, which forces its finiteness. In the open-boundary case, finiteness can also arise from elastic frustration, *i.e.* stress build-up due to mismatching. Taken from (Hagan and Grason, 2021).

We now attempt to sketch out possible mechanisms bringing about finite sizes in protein assemblies. As shown in Fig. 1.3, Hagan and Grason (2021) classify self-assembly into two categories: self-closing as in the case of a circular loop, and open-boundary when aggregation can potentially go on indefinitely. In the first case, the principle leading to finite sizes in aggregates is pretty obvious. But in the second case, self-limitation in size can have multiple origins. They for instance consider a toy model where misfitting jigsaw puzzle pieces preferentially aggregate with an angle [Fig. 1.3, *bottom*]. This forces the elastic pieces to deform, such that stress builds up as particles are added to the cluster. These effectively long-range interactions can favor finite sizes in one or several directions. In a 2D space, this can lead to fibers with only one dimension of growth, or finite-size aggregates with bounded growth in both dimensions, making them effectively zero-dimensional. We qualify the aggregation process leading to aggregates with a reduced dimension as "frustrated" compared to the case of well-fitting particles potentially forming infinite bulk structures.

Other studies on colloids with a competition of short-range attraction and long-range repulsion have yielded similar results (Mossa et al., 2004; Sciortino et al., 2004; 2005). But fibers can also be formed with exclusively short-range interactions. Indeed, in patchy models, while isotropic interactions are well-suited to model liquids, fiber-like aggregates can be obtained using high interaction specificity (Karner et al., 2020; Malhotra and Babu, 2020; Zhang and Glotzer, 2004). This can be introduced via preferred interaction partners (McManus et al., 2016), which has brought about accurate models of *e.g.* amyloid fibrils or virus capsids. This has also led to the numerical reproduction of the observed frustrated aggregation of archaeal chaperonin proteins which form both fibrillar and planar structures (Whitelam et al., 2009). Frustration also arises upon self-assembly of colloids on the positively curved surface of a sphere. They first tend to form an isotropic crystalline structure since the compact hexagonal conformation is easily accessible. This continues until a critical size function of the curvature radius is reached. At this lengthscale, the curvature of the surface can no longer tolerate the compact hexagonal conformation. The growth then becomes anisotropic, which leads to branched structures with a constant width (Meng et al., 2014). In numerical simulations, Lenz and Witten (2017) studied the irreversible aggregation of copies of an elastic polygonal particle in 2D. In their algorithm, the particles are added sequentially by minimizing the energy of the aggregate. This energy is the sum of an elastic term penalizing deformation of the particles and an adhesion term favoring contact between particle sides. For particle types not easily tiling the plane like pentagons and as elastic frustration decreases, they observe a generic transition from tree-like structures to fibers to 2D crystals. However, they find that the fibers are never more energetically favorable than the bulks, which makes them metastable. Finally, the formation of certain types of glasses has been modeled using geometrical frustration. In

this interpretation, locally favored structures displaying icosahedral order cannot fill up the space, hence preventing them from crystallizing (Shintani and Tanaka, 2006). Overall, the aforementioned studies usually consider either elastic or geometrical frustration. This is of course a simplification since protein self-assembly is probably frustrated both mechanically and geometrically.

1.3 Lattice particles with directional interactions

Contrarily to the freely placed particles in the models above, a different approach consists in placing undeformable copies of a unique particle on an infinite regular lattice, which mediates interactions with the nearest neighboring particles. This formalism with lattice particles is especially relevant in the study of the structures formed by functional organic molecules adsorbed on a crystal surface (Yokoyama et al., 2001; 2004). Depending on the placing of the interaction sites and on the possible chirality of the molecules, this may lead to the formation of "cluster" or "wire" structures on the flat surface of the adsorbent. To understand the formation of these structures, Akimenko et al. (2015; 2016) introduced a lattice-gas model with generic directional interactions.They then focus on simple examples where *e.g.* square (or cross-shaped) particles have one or two preferred interaction sites, see Fig. 1.4, *left*. Their minimal model admits only a few parameters, namely temperature θ, the chemical potential μ corresponding to the molecule-surface interaction, and two or three types of inter-molecular interactions. For square particles with two functional groups on the square lattice, the aggregates formed through the interactions of functional groups can only result in finite-size square-like or fiber-like structures. This depends especially on the positions of the groups on the particle: either on neighboring sides in the *cis* conformation, or on opposite sides in the *trans* conformation (Akimenko et al., 2016). They manage to find the ground-state phase diagram of a given conformation by energy minimization, see Fig. 1.4, *right*. They additionally solve the model on an infinite strip using a transfer-matrix method, that is however inapplicable on the full two dimensional infinite lattice that we further consider (Kramers and Wannier, 1941). At finite temperature, ordered structures appear as the chemical potential in units of temperature increases. From an initially empty system at constant values of the favored and unfavored strength $w_1 < 0$ and $w_2 > 0$, they observe the formation of fibers, before the system transitions to a fully occupied state consisting in a stacking of these fibers, as shown in the ground-state phase diagram. Their results compare well with Monte-Carlo simulations. Similar studies focusing on the adsorption of trimesic acid on the triangular lattice also show several types of bulk structures with varying surface coverages (Gorbunov et al., 2013; Ye et al., 2007).

Although the formation of fibers in the aforementioned model with simple interactions is not due to

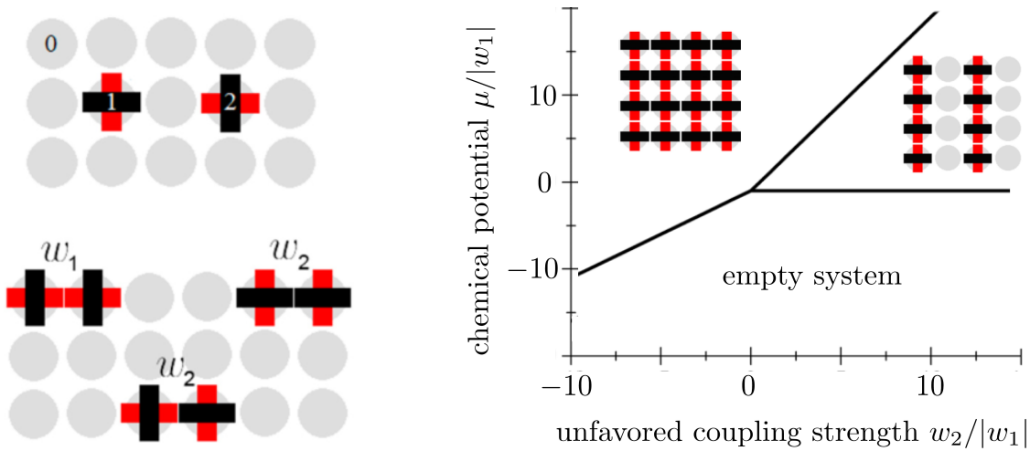

Figure 1.4: **Lattice-gas model for the adsorption of particles with directional interactions on the square lattice.** *Left*, each site can be empty or filled with a square particle in either orientation. In this case, the particles possess two functional groups (in red) in the *trans* position. *Right*, ground-state phase diagram of the adsorption layer of these particles, adapted from (Akimenko et al., 2016).

Figure 1.5: **Geometrical frustration on lattice spin systems.** Considering the Ising model with anti-ferromagnetic interactions favoring links between ↑ and ↓ spins, the square lattice favors all bonds in the ground state, while the triangular lattice does not. Indeed, as shown on the right sketch, for all the links with green ticks to be satisfied, there has to be an unsatisfied one, marked with a red cross.

frustration, we believe that in the presence of more complex interactions, geometrical frustration could explain the substantial formation of fibrous aggregates. Depending on the particular type of interactions, geometrical frustration can exist on a number of regular lattices. For instance, the triangular lattice exhibits frustration in the anti-ferromagnetic Ising case (Wannier, 1950), see Fig. 1.5. Likewise, a mix of nearest-neighbor ferromagnetic and next-nearest neighbor anti-ferromagnetic interactions can also trigger frustration on the square lattice (Hu and Charbonneau, 2021; Oitmaa et al., 1987). Ronceray and Le Floch (2019) recently came up with a quantitative definition of geometrical frustration for a bulk configuration with N lattice particles. Considering a symmetrical cluster of z particles, the frustration f_z is defined as the difference between the ground state energy per particle and the minimum cluster energy per particle. This quantity is always non-negative and decreases with the scale, *i.e.* with z. For instance, in the anti-ferromagnetic Ising model on the triangular lattice [Fig. 1.5], the energy of a favored bond (corresponding to a cluster of $z = 2$ particles) is lower than the ground-state energy per particle yielding $f_2 > 0$. But at the level of the three bonds in a triangle ($z = 3$), already the frustration vanishes: $f_3 = 0$. Indeed, there exist ground-state configurations where all triangles have two favored bonds and an unfavored one. This kind of situation, where f_z vanishes at finite z corresponds to what the authors call "finite-range" frustration. Here, the finiteness could potentially be linked to the typical width of potential fibers. On the contrary, an example of "long-range" frustration, where f_z only tends to 0 as z increases, is yet to be found. Considering a case where f_z displays *e.g.* an exponential relaxation with a characteristic length l: $f_z \sim e^{-z/l}$, this length could again be a good candidate for the potential fiber width. In another recent study, Meiri and Efrati (2022) introduce a frustrated Potts-like model, where the spin orientation at each site of a triangular lattice can take n possible values (*e.g* $n = 2$ in the Ising model). They show that for low n values, a compromise local triangular structure can be made uniform on the lattice, which is not possible at large n. Above a certain finite number of discrete orientations, the system resembles its continuous-orientation counterpart: the (frustrated) XY-model (Meiri and Efrati, 2021). This shows that the effect of frustration can depend drastically on the number of orientations.

We now discuss the problem at hand in this project. Recently, M. Lenz and P. Ronceray numerically studied the irreversible self-assembly of copies of an irregular lattice particle, with a similar algorithm as in (Lenz and Witten, 2017). In the 3D model on a FCC lattice from which Fig. 1.6 is drawn, depending on the specific shape of the particles, the associated aggregates can be finite clusters, fibers, sheets or crystals. Once again, the bulks are more energetically favorable than the fibers. But this could be due to the specific interaction types that they consider, where the particle faces must match the colors of their sites. Moreover, the link between the shape of the particles and the aggregate formed is unclear. It is indeed difficult to rationalize the dimension of the aggregate formed by such similar-looking particles as displayed in Fig. 1.6. In this project, we seek to understand this link by studying the equilibrium structures which arise from the self-assembly of these particles with discrete orientations. As a simplified view, one can think of square or octagonal particles on a square lattice, see Fig. 1.7, which interact depending on their discrete orientations, which are numbered *e.g.* 4 in the case of the square particle, or 8 for the octagonal one. These particles possess attractive and repulsive sides

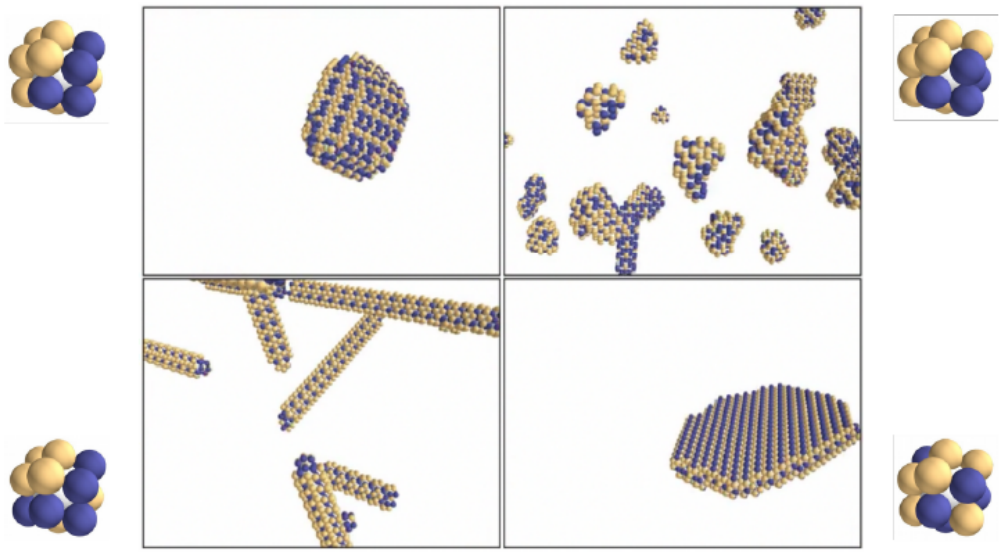

Figure 1.6: **Simulations of geometrically frustrated aggregation in 3D.** Complex lattice particles with geometrically incompatible orientational preferences (in the corners: sites with identical colors attract) give rise to aggregates of different dimensions (respectively a bulk, finite clusters, fibers and a sheet). Courtesy of P. Ronceray and M. Lenz.

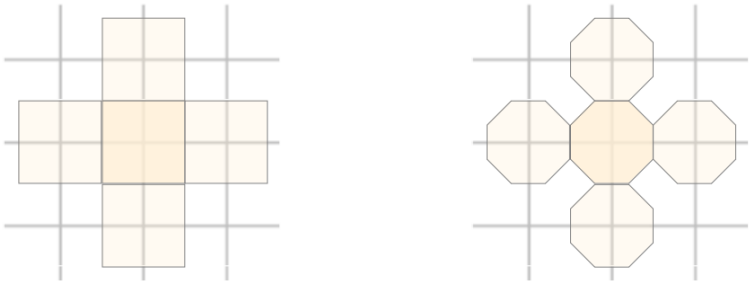

Figure 1.7: **Lattice particles with different numbers of interacting sides on the square lattice.** Square or octagonal particles interact only with their 4 nearest neighbors, at the places shown in lighter color. Each side of a particle can potentially interact specifically with another side of a particle, as in the lock-and-key framework of Fig. 1.3.

hence will not automatically link with their nearest neighbors to form crystals. We further consider more generic interaction types than the ones in Fig. 1.6, *e.g.* with more than two colors or that are perhaps not even representable with colors. This potentially induces geometrical frustration, which could lead to non-trivial aggregate morphologies, including fibers.

In the case of lattice particles, a simple way to visualize orientation-dependent couplings in 2D is through puzzle pieces, as in Fig. 1.8. In this view, a coupling between matching sides is favorable, hence decreases the energy by a factor $-c < 0$. Whereas a coupling between mismatching ones is defavorable, increasing the energy by c. We consider Boltzmann's probability distribution, such that a configuration with energy E is attributed a probability $\propto e^{-E/(k_B\theta)}$, k_B being Boltzmann's constant and θ the temperature. In the zero-temperature limit, where $c/(k_B\theta) \to \infty$, the left puzzle piece can form clusters that grow in every direction, *i.e.* sheets, while the right one can only form fibers. Indeed, it has one square side that does not match with any of the others. This fiber of width 2 then corresponds to the most stable state of this particle type, due to the square key with no match. This comes as a proof of concept that we can come up with simple lattice particles with directional interactions that do not tile the plane. In the presence of more complex interactions, geometrical frustration could play a role in the self-assembly process. To get an idea of the kind of situations where it could play a role, consider the simplistic view in Fig. 1.9. In this particular example, although each side of a particle potentially matches with a side of another particle, the bulk aggregate is unfavorable

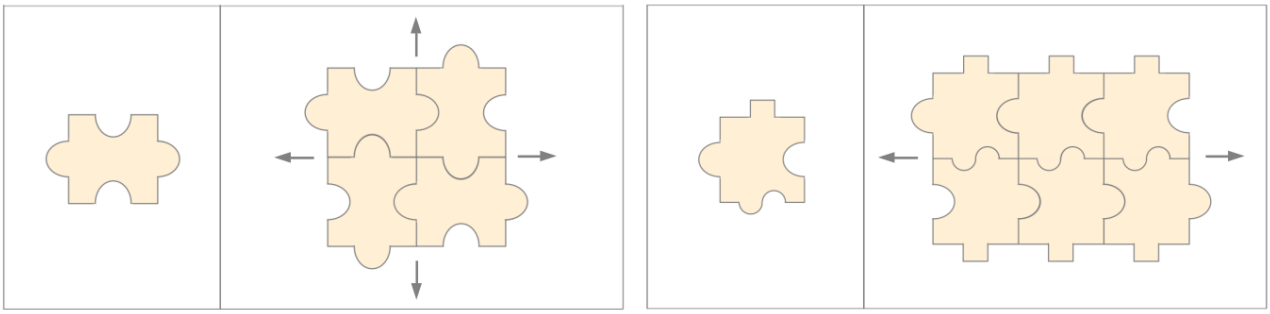

Figure 1.8: **Different irregular puzzle pieces form aggregates of different dimensions.** On the left, the aggregate can tile the plane, while the right one can grow into only one dimension. Here, the dimensional reduction does not come from frustration, but on the absence of a match for the side with a square-like key.

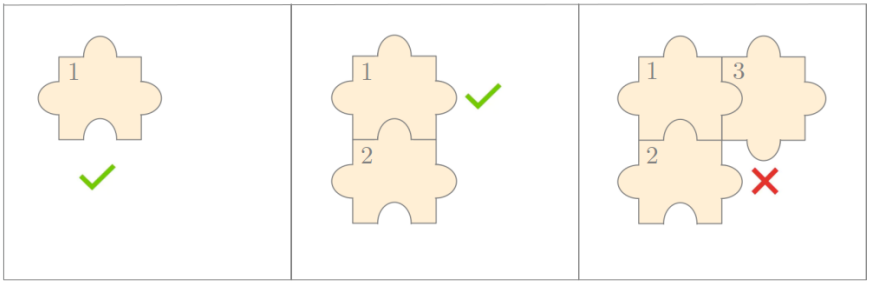

Figure 1.9: **A simplistic situation of geometrical frustration in the self-assembly of copies of an irregular puzzle piece.** After the third particle is linked to the previous two, a fourth one cannot be added to finish the square. Yet, a particle could perfectly link to the right of particle 2 alone and another to the bottom of particle 3 alone. This prevents this particle type to tile the plane although all of their sides match with at least one other side.

at low temperatures, which forces the self-assembly into holed or tree-like structures. In the following study, our main goal is to investigate whether certain frustrated particle types could energetically favor the formation of fiber-like clusters, or even have them as ground states. We further focus on energetic considerations and we do not examine the dynamic pathways leading to these equilibrium states. We thus do not consider the possibly long-lived metastable states that may form a large subset of the observed fibers (Schmit et al., 2011; Whitelam and Jack, 2015).

1.4 Distinguishing aggregate types via renormalization

While it is straightforward to determine the aggregate formed by the simple particle types of Fig. 1.8, the reverse question of determining the broad class of particles which form, *e.g.*, fibers (in their ground state) is fairly non-trivial. To tackle this issue, we develop a formalism which allows us to represent any particle type by a $n \times n$ coupling matrix $\mathbf{C}$ of nearest-neighbor interactions. This is such that the coupling between particles with discrete orientations ϕ and ψ from 1 to n is written $C_{\phi\psi}$. In principle, globular proteins can display very attractive sites close to very repulsive sites. We therefore consider the coupling matrix $\mathbf{C}$ as a random object, which can feature both isotropic attraction or repulsion, and very rugged anisotropic interaction landscapes. Then, we use the methods of the renormalization group in real space (Niemeijer and van Leeuwen, 1976) to study their large-scale behaviors and their associated ground-state clusters (Efrati et al., 2014). Indeed, renormalization is a transformation that describes the results of changes in the length scale. The idea of the renormalization group is thus to map a system onto another coarse-grained one with equivalent properties at a larger lengthscale.

In practice, the forms of the initial and renormalized Hamiltonians can differ due to correlations

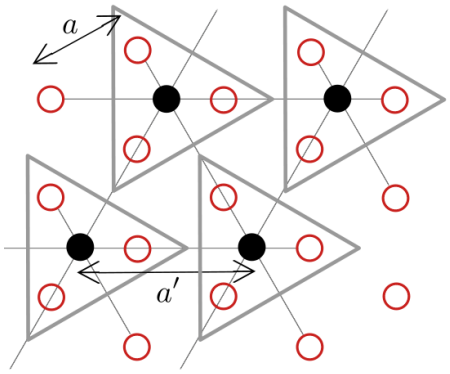

Figure 1.10: **Plaquette renormalization scheme of** Niemeijer and van Leeuwen (1973)**.** At the center of each triangular plaquette, the new spins in black have the same sign as the majority of the old red spins. The new triangular network thus has a lattice spacing $a' = \sqrt{3}a$.

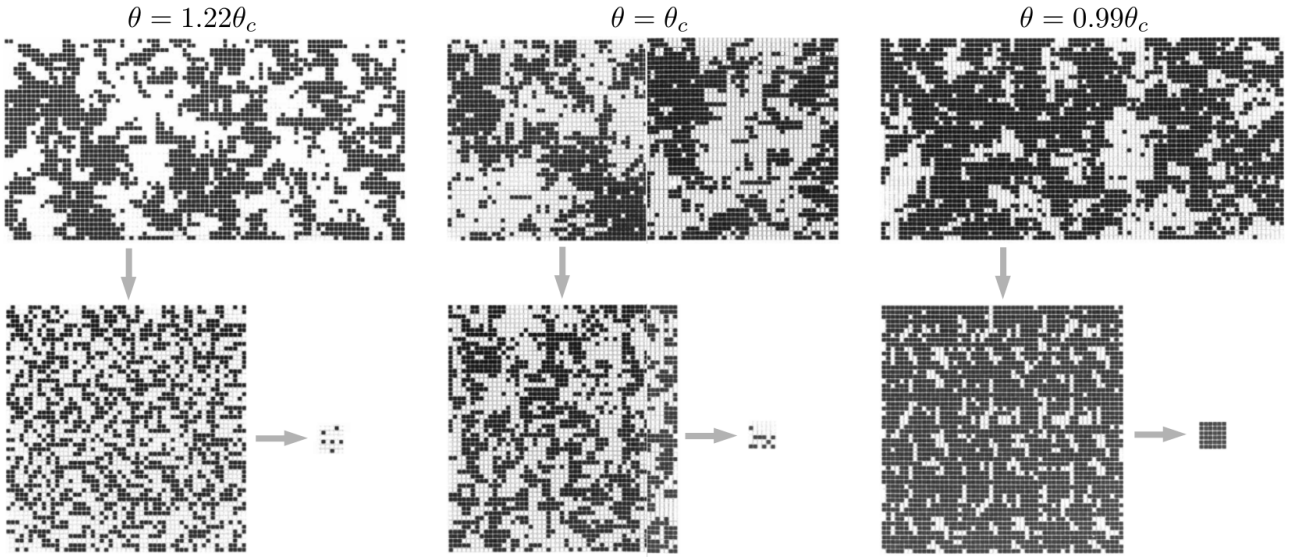

Figure 1.11: **Visualization of a renormalization process on the square-lattice.** Here, the ferromagnetic Ising model at zero magnetic field and coupling $J = 1/(k_B\theta) > 0$ is renormalized using the majority rule on 9-spin plaquettes. Above the critical temperature θ_c, the system renormalizes to the non-interacting gas (coupling $J = 0$), such that the spins become more and more random with each iteration. Whereas below θ_c, the spins become more and more uniform as the coupling strength diverges $J \to \infty$. At θ_c however, the system conserves its large-scale fluctuations upon renormalization. Adapted from (Wilson, 1979).

arising in the renormalization process. In the following, we systematically neglect these form differences and focus on the renormalization of the initial couplings. For instance, Niemeijer and van Leeuwen (1973) proposed a renormalization scheme for the triangular Ising model involving spin plaquettes, see Fig. 1.10. After one renormalization step, the new spins, determined by the majority rule, are further away. By zooming out, we can face several situations, where couplings vanish, diverge or converge to some constant (Wilson, 1979), see Fig. 1.11. The latter case can in principle be mapped to a phase transition, where the scale-invariant couplings are indicative of a critical behavior.

Alongside this analytical study, L. Koehler is currently performing numerical simulations of the renormalization process in 2D (Swendsen, 1979). She focuses on hexagonal particles (with $n = 6$ sides) on the triangular lattice with the same coupling matrix formalism as developed here, but in the canonical ensemble, and she proceeds as follows. She chooses a particular formulation of the coupling matrix $\mathbf{C}$, and she performs Monte-Carlo simulations (Metropolis and Ulam, 1949) to analyze the resulting collective behavior of the particles. This allows her to numerically compute the mean fractions of first- and third-neighbor bonds between particles in all possible discrete orientations ϕ and ψ from 1

to 6, and between particles and empty sites. She then put these fractions into two composition vectors for the first- and third-neighbor bonds written respectively $\langle \mathbf{c}_1 \rangle_{\mathbf{C}}$ and $\langle \mathbf{c}_3 \rangle_{\mathbf{C}}$. Then, she numerically computes the renormalized coupling matrix $\mathbf{C}'$ from the original one $\mathbf{C}$, by enforcing that the new composition vector of first-neighbor bonds be equal to the old composition vector of third-neighbor bonds: $\langle \mathbf{c}_1 \rangle_{\mathbf{C}'} = \langle \mathbf{c}_3 \rangle_{\mathbf{C}}$. This is sketched in Fig. 1.12. She then goes on recursively to obtain the renormalization dynamics of the coupling matrix. Despite minor differences in the renormalization processes, we will see that her numerical study of the renormalization dynamics recovers many of the analytical results presented hereafter.

We detail the self-assembly model and its analytical renormalization study in the two next chapters. We first develop the formalism on a one-dimensional chain of sites in Ch. 2. We show that several relevant results can be obtained concerning the preferred size and shape of aggregates depending on the particle type and its associated coupling matrix. Second, in Ch. 3, we present attempts to derive similar results on two-dimensional lattices, where aggregates can be either bulks, fibers or finite-sized. Difficulties arise which lead us to envision different renormalization procedures. It could be interesting that this analytical study be coupled to the renormalization simulations of L. Koehler, as to provide a guide for further calculations.

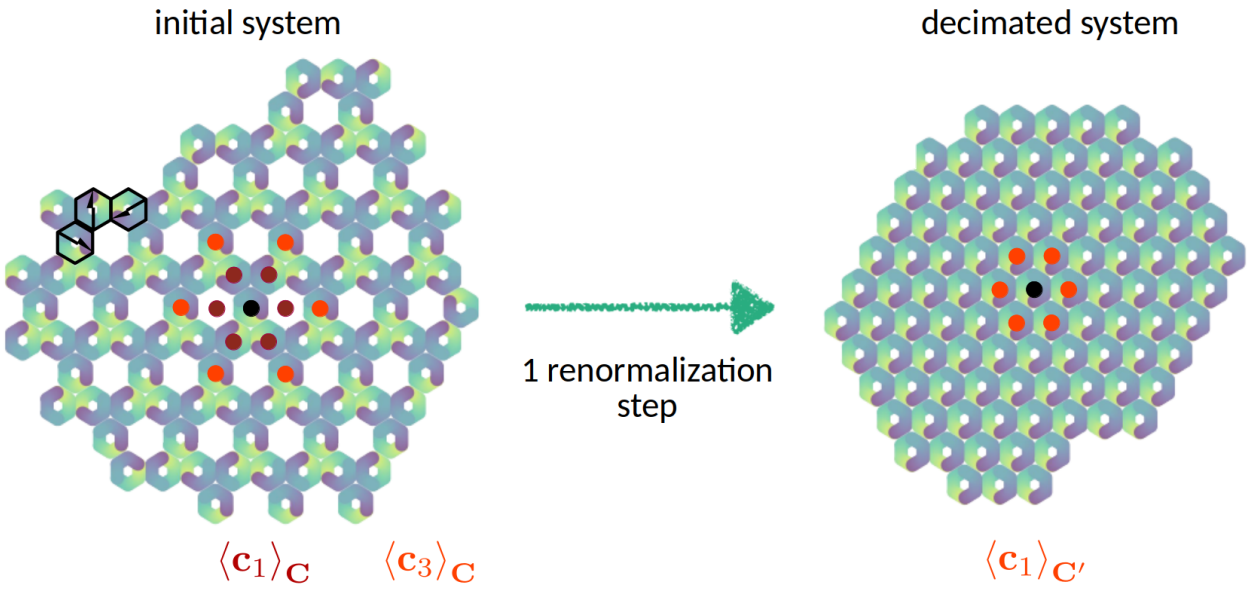

Figure 1.12: **Sketch of the numerical renormalization scheme implemented by L. Koehler.** The self-assembling hexagons with $n = 6$ orientations interact with their nearest neighbors on the triangular lattice depending on the coupling matrix $\mathbf{C}$. Here, the coupling matrix $\mathbf{C}$ which preferentially forms the aggregate on the left is renormalized after one step to $\mathbf{C}'$, which forms the aggregate on the right. This is done by equating the new composition vector of first-neighbor bonds $\langle \mathbf{c}_1 \rangle_{\mathbf{C}'}$ with the old one of third-neighbor bonds $\langle \mathbf{c}_3 \rangle_{\mathbf{C}}$. Courtesy of L. Koehler.

Chapter 2

Warm-up study in one dimension

In a 1D lattice, aggregates can only be finite clusters, when the length is bounded, or fibers, when the length is unbounded. Only in two and higher dimensions is there a difference between a fiber and a bulk. Therefore, the 1D study is meant as a basis for the 2D case. In this chapter, we start by developing the coupling matrix formalism in 1D for any number of discrete orientations of the particles n. We then obtain relevant characteristics of the system via transfer matrix calculations. But since these calculations are not applicable in 2D lattices, we discuss using methods of the real-space renormalization group theory to characterize the system. We particularly obtain the typical length of the equilibrium aggregates for any number of discrete orientations of the particles. We also find a distinction between the particle types, *i.e.* coupling matrices, which can only form finite-size aggregates, and those who can form aggregates spanning the whole chain. All in all, we find many similarities in the study of the Ising chain ($n = 1$) and of the model for $n > 1$ orientations. Due to the difficulty of the calculations and since the 1D study matters less in itself than as a preparation for the 2D case, we do not proceed to prove every result in 1D, but rather pave the way for understanding dimensional reduction in 2D. We proceed as follows: we first recall the Ising chain model on which our model with orientation-dependent interactions is based in Sec. 2.1. In Sec. 2.2, we present the real-space renormalization procedure in 1D and we study the dynamics of the coupling parameters in the flow diagrams for $n = 1$ and $n > 1$. We additionally investigate the link between the fixed points of the dynamics and the particle density $\langle s \rangle$. Finally, in Sec. 2.3 we explain how to access the aggregate length $\langle l \rangle$ from the distance to a stable non-interacting fixed point.

2.1 Self-assembly model on a 1D lattice

As discussed in Ch. 1, in order to obtain fibers, anisotropic interactions between particles seem to be required. Indeed, isotropic or patchy particles will tend to aggregates in all directions forming crystals or amorphous clusters. That is why we develop a formalism where interactions between irregular particles depend on the orientations of the particles. Additionally, for the sake of simplicity, we focus on the aggregation of copies of a unique particle. These particles are further placed on the nodes of a lattice and interact with the particles on their nearest neighboring nodes in the directions of the lattice. We consider a finite number of discrete orientations n and we represent the orientation-dependent interactions with a $n \times n$ coupling matrix. Sec. 2.1.1 details this approach and provides examples of coupling matrices where the dimensions of the aggregates is readily obtained from the matrix formulation. More specifically, we consider a chain of sites in equilibrium with a reservoir of particles. In Sec. 2.1.2, we recall the Ising chain model, where the characteristics of the chain occupation, namely the average density $\langle s \rangle$ and the average aggregate length $\langle l \rangle$ can be obtained via transfer matrix calculations. We then present our model for orientation-dependent particle interactions in Sec. 2.1.3, and we successfully extend the transfer matrix formalism.

2.1.1 Irregular particles to form sheets or fibers

We model proteins as copies of a polygonal particle with n possible orientations $\phi = 1, \dots, n$ with respect to a right-oriented link between *e.g.* sites i and $i+1$. Here, we especially focus on self-assembly on the square and triangular lattices, and thus consider even values for n. The orientations are defined modulo n, such that $n+1 \equiv 1$. Then, interactions between two particles present on neighboring vertices of the lattice depend on both of their orientations. For instance, considering a square particle with $n = 4$ orientations as in Fig. 2.1, its 4 sides can interact specifically with any of the 4 sides of another square particle. In particular, except in the case of π-periodic particles (*i.e.* invariant by rotation of π), a particle generally interacts differently with its right-wing neighbor than with its left-wing one. In the lattice-gas Ising model, the particles have only one orientation: $n = 1$. Whereas in the general case $n \geq 1$, each type of particle to be studied is characterized by its $n \times n$ coupling matrix $\mathbf{C} = (C_{\phi\psi})_{\phi,\psi=1,\dots,n}$, and its n-vector of *right* chemical potentials $\boldsymbol{\mu} = (\mu_\phi)_{\phi=1,\dots,n}$, both with real entries. Indeed, by invariance of the full chain under rotation of π, a link with an empty right site and a particle on the left with orientation ϕ has an energetic price $\mu_{\phi+n/2}/2$ which can in principle differ from $\mu_\phi/2$. In this sense, the n-vector of *left* chemical potentials reads $(\mu_{\phi+n/2})_{\phi=1,\dots,n}$. This is such that the energy of the following bond configurations are

- 0 if both particles are absent, a configuration which we further represent as 00.
- $\mu_\phi/2$ if the left particle with orientation ϕ is present and the right particle absent, further represented as $\phi 0$.
- $\mu_{\psi+n/2}/2$ if the left particle is absent and the right particle with orientation ψ is present, further represented as 0ψ.
- $C_{\phi\psi}$ if both the left particle with orientation ϕ and the right particle with orientation ψ are present, further represented as $\phi\psi$.

We will later see that even if the chemical potentials are all equal prior to renormalization, their variations upon renormalization are orientation-dependent. Therefore, we absolutely need to consider $\boldsymbol{\mu}$ as a vector.

To make sense of the coupling matrix formalism, we come back to the self-assembling jigsaw puzzle pieces of Ch. 1. The particles of Fig. 2.1 have $n = 4$ sides and can take as many orientations on a 2D square lattice. After attributing an orientation, on the left, the favored interactions as sketched on a right-oriented link are $\leftrightarrow\updownarrow$ and $\updownarrow\leftrightarrow$. On the right, the favored ones are $\uparrow\uparrow$, $\downarrow\downarrow$ and $\leftarrow\rightarrow$. Therefore, they can be represented in the basis $(\rightarrow, \downarrow, \leftarrow, \uparrow)$, referring to orientations $\phi = 1, 2, 3, 4$, with the

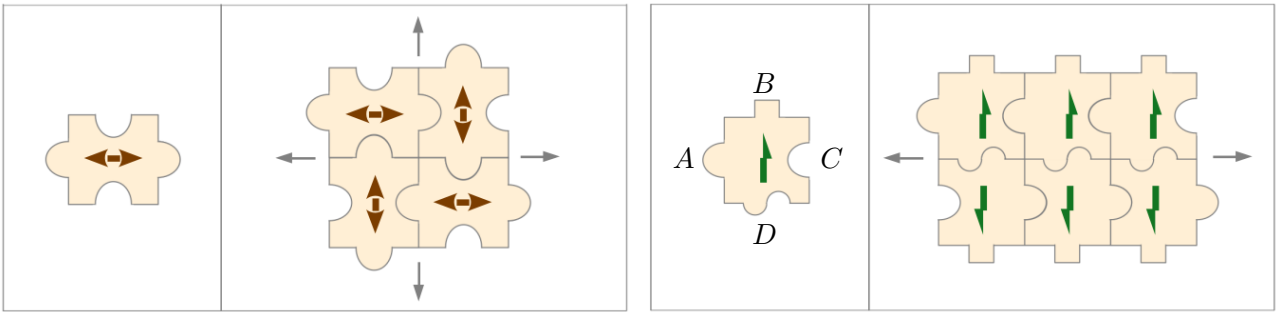

Figure 2.1: **The attribution of an orientation enables the representation of these puzzle pieces as coupling matrices, see** Eq. (2.1)**.** On the left, the sheet-forming puzzle piece is π-periodic, as indicated by the double arrow. On the right, the sides of the puzzle piece are attributed letters, in order to study the interactions between sides rather than orientations.

following coupling matrices:

$$\mathbf{C}^S = \begin{pmatrix} \widetilde{\mathbf{C}}^S & \widetilde{\mathbf{C}}^S \\ \widetilde{\mathbf{C}}^S & \widetilde{\mathbf{C}}^S \end{pmatrix} \quad \text{where} \quad \widetilde{\mathbf{C}}^S = \begin{pmatrix} c & -c \\ -c & c \end{pmatrix}, \quad \text{and} \quad \mathbf{C}^F = \begin{pmatrix} c & c & c & c \\ c & -c & c & c \\ -c & c & c & c \\ c & c & c & -c \end{pmatrix}, \tag{2.1}$$

corresponding respectively to the sheet-forming particle and the fiber-forming one. In this simple example, c is some positive constant, but we would definitely consider different versions of these matrices with more than two distinct coefficients. Thus, the coupling matrix formalism allows to represent both fiber-forming particles and sheet-forming ones. Obviously, on a linear chain of sites, both of these particles have the infinite fiber as their ground state.

We further introduce the matrix $\mathbf{\Pi} = \begin{pmatrix} \mathbf{0} & \mathbb{1}_{n/2} \\ \mathbb{1}_{n/2} & \mathbf{0} \end{pmatrix}$, where $\mathbb{1}_k$ is the identity matrix of size k, such that $(\mathbf{\Pi}\boldsymbol{\mu})_\phi = \mu_{\phi+n/2}$. With this notation, the interactions between the A, B, C, D sides of the puzzle piece on the left of Fig. 2.1 can be represented by the symmetric matrix $\mathbf{C}^F\mathbf{\Pi} = (C^F_{\phi,\psi+n/2})_{\phi,\psi=1,\dots,4}$. The favored interactions are then AC, CA and DD, such that in the basis of the sides (*i.e.* not orientations) written (A, B, C, D), the fiber-forming coupling matrix reads

$$\mathbf{C}^F\mathbf{\Pi} = \begin{pmatrix} c & c & c & c \\ c & c & c & -c \\ c & c & -c & c \\ c & -c & c & c \end{pmatrix}. \tag{2.2}$$

The matrix $\mathbf{C\Pi}$ is generically symmetric due to the fact that the side-interactions are symmetric. Therefore, $\mathbf{C\Pi}$ represents couplings between sides, while $\mathbf{C}$ denotes couplings between orientations.

2.1.2 The Ising chain

Let us start with a quick recall of the 1D lattice-gas Ising model and some of its important results (Lee and Yang, 1952; Yang and Lee, 1952). This model was first introduced to study the adsorption of gas particles on a crystal surface (Akimenko et al., 2016). At each site $i = 1, \dots, N$ of the chain, we define the occupation number as a spin-like variable s_i which is 1 (0) if a particle is present (absent). In the translationally invariant case, the Hamiltonian for a given spin configuration $\mathbf{s} = (s_1, \dots, s_N)$ is generically written (Ising, 1925; Maris and Kadanoff, 1978)

$$\frac{\mathcal{H}(\mathbf{s})}{k_B\theta} = \sum_i C s_i s_{i+1} + \frac{\mu}{2}(s_i + s_{i+1}), \tag{2.3}$$

where $C \in \mathbb{R}$ is the coupling constant, $\mu \in \mathbb{R}$ is the chemical potential, θ is the temperature and k_B is Boltzmann's constant. Here the sum is performed over the network bonds. While $C = 0$ corresponds to the gas of hard spheres, $C < 0$ ($C > 0$) corresponds to attractive (repulsive) interactions. When $\mu > 0$ ($\mu < 0$), it is a price to pay (reward) for placing a particle on the chain. In the study of aggregation, we are rather interested in the regime of high positive chemical potential and high attractive coupling, such that there are only a few particles on the chain that clump up together. A mapping from the lattice-gas variables $s_i = 0, 1$ to the usual spin-$\frac{1}{2}$ variables $\sigma_i = \pm 1$ is shown in Appendix 2.4.1. Considering a chain of N sites, the probability of a given spin configuration is written $e^{-\mathcal{H}(\mathbf{s})/(k_B\theta)}/Z$, where the partition function is obtained by summing over the configurations: $Z = \sum_{\mathbf{s}} e^{-\mathcal{H}(\mathbf{s})/(k_B\theta)}$. To calculate the partition function, it is useful to rewrite it using the transfer matrix (Kramers and Wannier, 1941)

$$\mathscr{T} = \begin{pmatrix} 1 & M \\ M & T \end{pmatrix}, \quad \text{where} \quad M = e^{-\mu/2} \geq 0 \quad \text{and} \quad T = e^{-C-\mu} = e^{-C}M^2 \geq 0 \tag{2.4}$$

parameterize the system (Kramers and Wannier, 1941). In this sense, $M^2 = e^{-\mu}$ corresponds to the usual fugacity of a lattice gas (Yang and Lee, 1952), such that for a non-interacting gas $C = 0$, the probability of a configuration with N_p particles is $\propto (M^2)^{N_p}$. Each entry $\mathscr{T}_{ss'}$ thus represents a

bond-configuration with neighboring spins (s, s'): $\mathscr{T}_{00} = 1$, $\mathscr{T}_{10} = \mathscr{T}_{01} = M$ and $\mathscr{T}_{11} = T$. The partition function hence takes the simple form $Z = \operatorname{Tr} \mathscr{T}^N$, see Appendix 2.4.2. One can also obtain *e.g.* the mean density of particles on the chain $\langle s \rangle = \sum_{\mathbf{s}} s_0 \, e^{-\mathcal{H}(\mathbf{s})/(k_B\theta)}/Z$ with a similar calculation.

This 1D model was solved completely by Ising himself, who found no phase transition in the infinite system limit, meaning that the partition function remains analytic everywhere in the phase space. Indeed, setting $\mu = C$, the critical temperature at which the transition would take place is zero (the critical coupling $C \to \infty$) in both the attractive and repulsive cases. The behavior of the system with temperature is as follows, at low θ (high $|C|$ and $|\mu|$), most sites are either occupied or empty depending on the sign of the chemical potential, while at high θ (low $|C|$ and $|\mu|$), the system is completely disordered. Besides, spin correlations between sites distant of $i \gg 1$ lattice spacings decay exponentially with the distance:

$$\langle s_0 s_i \rangle - \langle s_0^2 \rangle \propto e^{-i/\xi}, \tag{2.5}$$

where the correlation length ξ diverges at vanishing temperature (and $T = 1$, such that $-C = \mu \to \infty$) [Appendix 2.4.2]. Contrarily, for infinite systems in two and higher dimensions, the correlation length diverges at finite temperature, which indicates the occurrence of a phase transition. We further discuss the spin statistics and correlations respectively in the end of Sec. 2.2.1 and in Sec. 2.3.2. We focus on the 2D model in Sec. 3.1.

2.1.3 The chain of irregular particles

We now consider the case of multiple orientations. Given the coupling matrix formalism developed in Sec. 2.1.1, we thus define the Hamiltonian for a given configuration of the spins and orientations $\mathscr{C} = (\mathbf{s}, \boldsymbol{\phi})$ as

$$\frac{\mathcal{H}(\mathscr{C})}{k_B\theta} = \sum_i C_{\phi_i\phi_{i+1}} s_i s_{i+1} + \frac{\mu_{\phi_i}}{2} s_i + \frac{(\boldsymbol{\Pi}\boldsymbol{\mu})_{\phi_{i+1}}}{2} s_{i+1}, \tag{2.6}$$

where $(\boldsymbol{\Pi}\boldsymbol{\mu})_\phi = \mu_{\phi+n/2}$. Note that the symmetric $n \times n$ block matrix $\boldsymbol{\Pi}$ verifies $\boldsymbol{\Pi}^2 = \mathbb{1}$. We further introduce the n-vector $\mathbf{M}$, and the $n \times n$-matrix $\mathbf{T}$ with non-negative entries defined by

$$M_\phi = e^{-\mu_\phi/2} \quad \text{and} \quad T_{\phi\psi} = e^{-C_{\phi\psi}} M_\phi (\boldsymbol{\Pi}\mathbf{M})_\psi. \tag{2.7}$$

The quantity $M_\phi(\boldsymbol{\Pi}\mathbf{M})_\phi$ corresponds to the full chemical potential of a particle with orientation ϕ. It is indeed the Boltzmann weight of the configuration $0\phi0$. This allows us to define the entries of the transfer matrix $\mathscr{T}_{s\phi,s'\psi}$ and the bond-configurations with neighboring spin times orientations $(s\phi, s'\psi)$ are attributed the following terms:

$$\mathscr{T}_{00} = 1, \quad \mathscr{T}_{\phi 0} = \mathscr{T}_{0,\phi+n/2} = M_\phi, \quad \mathscr{T}_{\phi\psi} = \mathscr{T}_{\psi+n/2,\phi+n/2} = T_{\phi\psi}, \tag{2.8}$$

through enforcement of the physical invariance by rotation of π. With this formalism, we obtain the partition function by summing over the spin configurations, and the orientations when a particle is present:

$$Z = \sum_{\mathscr{C}} e^{-\mathcal{H}(\mathscr{C})/(k_B\theta)} = \operatorname{Tr} \mathscr{T}^N, \quad \text{where} \quad \mathscr{T} = \begin{pmatrix} 1 & \mathbf{M}^\mathsf{T}\boldsymbol{\Pi} \\ \mathbf{M} & \mathbf{T} \end{pmatrix} \tag{2.9}$$

is a block matrix of size $n + 1$, similar to the one of Eq. (2.4). For a given particle type with parameters $(\mathbf{M}, \mathbf{T})$, the site occupancy is also summed over the orientations of the particles, such that $\langle s \rangle = \sum_{\mathscr{C}} s_0 \, e^{-\mathcal{H}(\mathscr{C})/(k_B\theta)}/Z$.

Furthermore, Eq. (2.8) implies that the matrix $\mathbf{T}$ verifies $\boldsymbol{\Pi}\mathbf{T}\boldsymbol{\Pi} = \mathbf{T}^\mathsf{T}$, such that $\mathbf{T}\boldsymbol{\Pi}$ is symmetric (see Sec. 2.1.1). We can introduce a symmetric matrix $\mathbf{S}$ to write generically $\mathbf{T} = \mathbf{S}\boldsymbol{\Pi}$. We make use of this trick in Sec. 2.2.2. Additionally, if the particles are π-periodic, we can write

$$\mathbf{M} = \begin{pmatrix} \widetilde{\mathbf{M}} \\ \widetilde{\mathbf{M}} \end{pmatrix} \quad \text{and} \quad \mathbf{T} = \begin{pmatrix} \widetilde{\mathbf{T}} & \widetilde{\mathbf{T}} \\ \widetilde{\mathbf{T}} & \widetilde{\mathbf{T}} \end{pmatrix}, \tag{2.10}$$

where $\widetilde{\mathbf{M}}$ is a $n/2$-vector and $\widetilde{\mathbf{T}}$ a $n/2 \times n/2$-matrix. Here, $\widetilde{\mathbf{T}}$ is symmetric, hence $\mathbf{T}$ also is, leading to many simplifications. Besides, when $\mathbf{T}$ is a positive matrix (*i.e.* with positive entries), which we write $\mathbf{T} > 0$, it has powerful properties.

Perron-Frobenius theorem Considering a matrix $\mathbf{T} > 0$, its largest eigenvalue is real and positive, and the single corresponding eigenvector is the only one to have strictly positive components (Meyer, 2000).

This model for generic interactions can be mapped in particular cases to already existing models. If the coupling matrix $\mathbf{C} = C\mathbb{1}$ and the chemical potential are all zero, then the Hamiltonian of Eq. (2.6) corresponds to the standard Potts model (Wu, 1982) with spins $s_i\phi_i = 0, \ldots, n$. Indeed, we can rewrite it as $\mathcal{H}(\mathscr{C})/(k_B\theta) = C\sum_i \delta_{s_i\phi_i, s_{i+1}\phi_{i+1}}$, where δ_{ij} is the Kronecker delta. This corresponds to a special kind of sheets on 2D lattices, see Sec. 3.1.2. The clock model constitutes another particular case where $C_{\phi\psi} = C\cos(\phi - \psi)$, while $\mu_\phi = 0$, $\phi, \psi = 1, \ldots, n$ (Chen et al., 2017). In this case, nearly collinear orientations interact more strongly than nearly orthogonal ones. In our understanding of protein conformations where attractive sites can be placed closed to non-interacting or repulsive ones [Fig.1.1, *right*], this does not constitute a particularly relevant model for their self-assembly. Additionally, the Ising model of Sec. 2.1.2 is recovered when taking the limit $n = 1$, where $\mathbf{M}, \mathbf{T}$ and $\mathbf{\Pi}$ become M, T and 1.

2.2 Exact 1D renormalization procedures

Now that the model of oriented particles is defined, we use the methods of the Renormalization Group in real space in order to study the large-scale behavior of systems defined through the parameters $(\mathbf{M}, \mathbf{T})$. Renormalization is based on a recursive process which consists in decimating a fraction of the spins at each step and analyzing the evolution of the parameters of the system along the way. From step k to $k+1$, the relation between $(\mathbf{M}, \mathbf{T})^{(k)} = (\mathbf{M}, \mathbf{T})$ and $(\mathbf{M}, \mathbf{T})^{(k+1)} = (\mathbf{M}, \mathbf{T})'$ is called the Renormalization Group transformation: $(\mathbf{M}, \mathbf{T})' = \mathcal{R}(\mathbf{M}, \mathbf{T})$ (Efrati et al., 2014). The particular expression of $\mathcal{R}$ comes from the invariance upon renormalization of the partition function (up to a multiplicative constant). In 1D, the renormalization transformation is exact, as it conserves the properties of the system upon renormalization. As we will see in Sec. 3.1, this is not true in 2D.

The dynamics of systems under renormalization defines a flow in the $(\mathbf{M}, \mathbf{T})$-space. Of particular interest are the fixed points $(\mathbf{M}, \mathbf{T})_*$ of $\mathcal{R}$, such that $(\mathbf{M}, \mathbf{T})_* = \mathcal{R}(\mathbf{M}, \mathbf{T})_*$. These fixed points can contain infinite entries as will be discussed later. We associate each fixed point with the set of initial conditions that fall into its basin of attraction, and we analyze their dynamical stability. We then gather fixed points with the same stability into fixed subspaces. As discussed in the beginning of Ch. 2, rather than studying the renormalization dynamics extensively, we aim at a general understanding of the flow diagram in 1D, so that we can be best prepared for the 2D study of Ch. 3. In Sec. 2.2.1, we study the dynamics under renormalization of the Ising model. We turn to the case of multiple orientations in Sec. 2.2.2, where we discuss useful formulations for the matrix $\mathbf{T}$. In our investigation of the renormalization for $n > 1$ orientations in Sec. 2.2.3, we find many similarities between the dynamics and the fixed points of the two models. Particularly, in both flow diagrams, the only stable fixed points are all non-interacting. We finally discuss in Sec. 2.2.4 some cases where systems upon renormalization display some recurring patterns in their favored configurations. This leads us to consider limit cycles as another class of limit behavior.

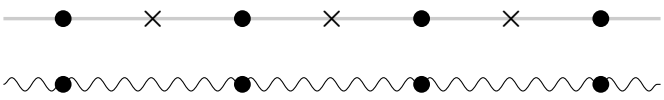

Figure 2.2: **Decimation of one spin every two on the Ising chain.** The new links between sites distant of two lattice spacings are shown as wavy.

2.2.1 Renormalizing the Ising chain model

The renormalization procedure consists in decimating half of the spins at each step, as displayed in Fig. 2.2 where $\times$-spins are decimated. Considering the Ising model on a chain of N sites, after one renormalization step, $N' = N/2$ and by invariance of the partition function, $A\mathscr{T}' = \mathscr{T}^2$, with A a nonphysical scalar constant and $\mathscr{T}' = \begin{pmatrix} 1' & M' \\ M' & T' \end{pmatrix}$. This leads us to the following renormalization formulae for the system parameters:

$$M' = \frac{1+T}{1+M^2}M, \quad T' = \frac{M^2+T^2}{1+M^2}. \tag{2.11}$$

We can make sense of this transformation in the following way. Consider a new link between two non-decimated sites i and j separated by a decimated site a. The Boltzmann weights of the renormalized (s_i, s_j)-bonds are obtained by summing over the values of s_a. For instance, the weight of a new 00-bond is the sum of the weights of the configurations 000 and 010, such that $A1' = 1 + M^2$. We then ensure $1' = 1$ by defining $A = 1 + M^2$. This amounts to a nonphysical shift in all configuration energies. In 2D where the partition function is not invariant under renormalization, we will see that this way of conceptualizing the renormalization is of great use, see Sec. 3.2.

Although the iteration in Eq. (2.11) appears laborious to study, we find that the (M, T) dynamics is effectively one-dimensional. Indeed, the system of equations can be reduced with an integral of motion α (constant of motion independent of the step k), such that

$$\text{at each step } k, \quad T^{(k)} = 1 + \alpha M^{(k)}, \quad \text{for} \quad M^{(k)} > 0. \tag{2.12}$$

This integral of motion can thus be expressed with the initial conditions as $\alpha = (T^{(0)} - 1)/M^{(0)}$. Therefore, our renormalization formulae read

$$\begin{cases} M' = \dfrac{2+\alpha M}{1+M^2}M, & T' = 1 + \alpha M', & \text{if } M > 0, \\ M' = 0, & T' = T^2, & \text{if } M = 0, \end{cases} \tag{2.13}$$

where for $M = e^{-\mu/2}$ to be zero, the chemical potential has to be positive and infinite, such that it corresponds to a limit case. Other limit cases include $T = e^{-C-\mu} = 0$, and obviously $M = \infty$ and $T = \infty$. This iteration possesses different kinds of fixed points depending on the initial conditions $(M, T)^{(0)}$. We perform a linear stability analysis for each fixed point, where we distinguish between M-stability and T-stability, related to an infinitesimal variation of M or T. If a fixed point is dynamically attractive (regardless of the attractiveness of the interaction) in some direction, meaning that the perturbation decreases, we call it stable in this direction. Conversely, it is dynamically repulsive if the perturbation increases, and we thus call it unstable in this direction. If the perturbation leads to another nearby fixed point, then we call the fixed point neutrally stable. We find that the following initial conditions fall into the following fixed points:

- $(M = 0, T = 1)$ is the M- and T-unstable fixed point.
- $(M^{(0)} = 0, T^{(0)} > 1)$, *i.e.* $\alpha \to \infty$ fall into the M-unstable fixed point $(0, \infty)$.
- $(M^{(0)} = 0, T^{(0)} < 1)$, *i.e.* $\alpha \to -\infty$ and $\forall \alpha \in \mathbb{R}$, $(M^{(0)} > 0, T^{(0)} = 1 + \alpha M^{(0)})$, both fall on a curve of neutrally stable fixed points, *i.e.* a neutrally stable fixed curve. It corresponds to the hard sphere gas (*i.e.* $C_* = 0$), which can be rewritten as

$$(M_*, T_*) = \left(M_\alpha = \frac{\alpha + \sqrt{\alpha^2+4}}{2}, \quad T_\alpha = M_\alpha^2 \right), \quad \forall \alpha \in \mathbb{R} \cup \{-\infty\}. \tag{2.14}$$

Indeed for $M > 0$, $M'_\alpha = M_\alpha$ leads to the quadratic equation $1 + \alpha M_\alpha = M_\alpha^2$, which has only one positive root given by Eq. (2.14). The linear stability calculations are performed in Appendix 2.4.3. In

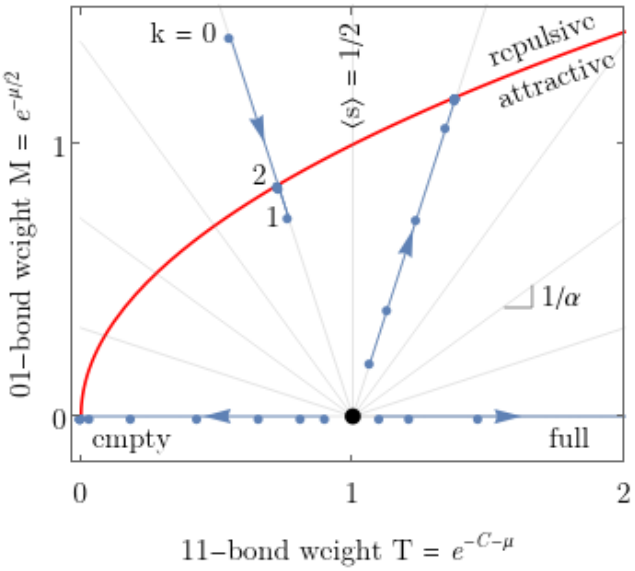

Figure 2.3: **Flow diagram for the Ising chain, where the trajectories follow the iteration of** Eq. (2.13)**.** The black point denotes the unstable fixed point, and the red curve $M_\alpha = \sqrt{T}_\alpha$ denotes the hard sphere gas ($C = 0$). Above the red curve, interactions are repulsive ($C > 0$), while they are attractive below ($C < 0$). Each trajectory in blue, obtained by numerical analysis, lies on a line with slope $1/\alpha$. The trajectory with the steps indexed from $k = 0$ to 2 beginning in the repulsive region becomes attractive and stays so at later times.

the end, except on the line $M = 0$, from an initial condition $\left(M^{(0)}, 1 + \alpha M^{(0)}\right)$ with a given $\alpha \in \mathbb{R}$, the parameters converge to the unique fixed point. Given Eq. (2.14), we can thus write

$$\text{as} \quad k \to \infty, \quad \left(M,\ 1 + \alpha M\right)^{(k)} \to \left(M_\alpha,\ M_\alpha^2 = 1 + \alpha M_\alpha\right), \tag{2.15}$$

where the proof of convergence is given in Appendix 2.4.3.

The flow diagram is shown in Fig. 2.3 with several trajectories obtained by numerical analysis of Eq. (2.13). As we see, the trajectories in the (M, T)-space are all linear due to the integral of motion, which justifies the change of variables from (C, μ) to (M, T). Interestingly, a repulsive initial condition (*i.e.* with a repulsive interaction $C^{(0)} > 0$) is directly mapped to an attractive point (*i.e.* $\{C^{(k)},\, k > 0\} = C^{(>0)} \leq 0$). Indeed, upon decimation of a repulsive-like configuration with spins 101010, we obtain attractive-like configurations: 111 or 000, which stay attractive-like when decimated. Moreover, as expected, the segment $M \leq 1, T = 1$, *i.e.* $C = -\mu < 0$ (corresponding to zero magnetic field) contains the zero-temperature unstable fixed point $M_* = 0$ ($C_* \to \infty$) and the infinite-temperature stable fixed point $M_* = 1$ ($C_* = 0$). In Appendix 2.4.2, we show that for $M > 0$, the density of particles can be expressed solely with M_α:

$$\langle s \rangle = \frac{M_\alpha^2}{1 + M_\alpha^2} = \frac{1}{1 + e^{\mu_*}}. \tag{2.16}$$

Therefore, $\langle s \rangle$ remains constant under renormalization, just as the integral of motion α. This hints that the conservation of these two quantities might be connected, although the physical link is unclear. On the red curve, from left to right, $\langle s \rangle = 0$ (empty chain) at $(M = 0, T = 0)$; $\frac{1}{2}$ at $(1, 1)$; and 1 (full chain) at (∞, ∞). On the line $M = 0$, for $T < 1$, $\langle s \rangle = 0$; for $T > 1$, $\langle s \rangle = 1$; and at the unstable fixed point, $\langle s \rangle$ is not defined. It is worth noticing that in the repulsive region with positive chemical potential $\mu > 0$ and $C \in [-\mu, 0]$, the renormalization increases $M = e^{-\mu/2} < 1$ and decreases $T = e^{-C-\mu} < 1$. This means that μ decreases while $C + \mu$ and thus C increases. Therefore, except on the $T = 1$ line, renormalization does not always decrease the temperature. Let us see if we can recover some of these results for irregular particles.

2.2.2 Useful formulation for the matrix T

Before jumping into the renormalization for multiple orientations, we discuss general formulations for the $n \times n$-matrix $\mathbf{T}^{(0)}$. Although its entries are non-negative, it is not necessarily symmetric, hence not always diagonalizable. We thus cannot always write $\mathbf{T}$ as a matrix product such as $\mathbf{PDP}^{-1}$, with $\mathbf{D}$ a diagonal matrix and $\mathbf{P}$ an invertible matrix (Horn and Johnson, 2012). For instance, $\left(\begin{smallmatrix} 1 & 1 \\ 0 & 1 \end{smallmatrix}\right)$ has a double eigenvalue $t = 1$ but a single eigenvector, hence is not diagonalizable. And even if we can diagonalize it, the left eigenvectors are not always the same as the right eigenvectors, *i.e.* $\mathbf{P}^{-1} \neq \mathbf{P}^{\mathsf{T}}$. Indeed, in order for the non-null vector $\mathbf{u}$ to be a left eigenvector of the matrix $\mathbf{T}$ for the eigenvalue t, it has to satisfy $\mathbf{u}^{\mathsf{T}}\mathbf{T} = t\mathbf{u}^{\mathsf{T}}$. Then taking the transpose, we obtain $\mathbf{T}^{\mathsf{T}}\mathbf{u} = t\mathbf{u}$. Thus $\mathbf{u}$ is a right eigenvector of $\mathbf{T}$ only if $\mathbf{T}$ is symmetric. For example, the diagonalizable matrix

$$\mathbf{T} = \mathbf{t}\,\mathbf{u}\mathbf{u}^{\mathsf{T}}\mathbf{\Pi} \quad \text{with} \quad \mathbf{u}^{\mathsf{T}}\mathbf{\Pi}\mathbf{u} = \mathbf{1} \tag{2.17}$$

has a left eigenvector $\mathbf{\Pi v}$ and a right eigenvector $\mathbf{v}$ for the eigenvalue t. This makes calculating *e.g.* powers of $\mathbf{T}$ uneasy. We thus look for other decompositions.

Using the *Jordan normal form* (Horn and Johnson, 2012), any matrix, diagonalizable or not, can be written as

$$\mathbf{T} = \mathbf{PJP}^{-1}, \tag{2.18}$$

where $\mathbf{J}$ is a block diagonal matrix and $\mathbf{P}$ an invertible matrix. The diagonal blocks of $\mathbf{J}$ are of the form

$$\mathbf{J}_i = \begin{pmatrix} t_i & 1 & & \\ & t_i & \ddots & \\ & & \ddots & 1 \\ & & & t_i \end{pmatrix}, \tag{2.19}$$

where the t_i in different blocks can be equal. These t_i, $i = 1, \dots, n$ are the eigenvalues of $\mathbf{T}$. The Jordan normal form appears to be very convenient for the calculation of matrix functions. In particular, for any integer l, $\mathbf{T}^l = \mathbf{PJ}^l\mathbf{P}^{-1}$, such that the eigenvalues of $\mathbf{T}^l$ are the t_i^l. Another decomposition of the matrix $\mathbf{T}$ involves the symmetric matrix $\mathbf{S} = \mathbf{T\Pi}$, and is known as the *singular value decomposition* (Horn and Johnson, 2012). We can indeed write $\mathbf{T}$ with the real eigenvalues $s_1, \dots, s_n$ and orthonormal eigenvectors $\mathbf{v}_1, \dots, \mathbf{v}_n$ of $\mathbf{S}$:

$$\mathbf{S} = \sum_i s_i\,\mathbf{v}_i\mathbf{v}_i^{\mathsf{T}} \quad \Rightarrow \quad \mathbf{T} = \sum_i s_i\,\mathbf{v}_i(\mathbf{\Pi v}_i)^{\mathsf{T}}. \tag{2.20}$$

With this writing, the s_i^2 are eigenvalues of $\mathbf{TT}^{\mathsf{T}}$, such that the s_i are the so-called singular values of $\mathbf{T}$. We note that in general the eigenvalues and singular values of $\mathbf{T}$ are not the same, and that the $\mathbf{v}_i$ are not eigenvectors of $\mathbf{T}$. However, computing powers of $\mathbf{T}$ with Eq. (2.20) is not easy since in general $\mathbf{v}_i^{\mathsf{T}}\mathbf{\Pi v}_j \neq \delta_{ij}$.

2.2.3 Renormalization for multiple orientations

Now that we dispose of generic formulations for the matrix $\mathbf{T}$, we discuss the renormalization dynamics for multiple orientations. According to the definition of the transfer matrix $\mathscr{T}$ for $n > 1$ orientations given in Eq. (2.9), $\mathscr{T}' = A\mathscr{T}^2$ yields the following renormalization formulae:

$$\mathbf{M}' = \frac{\mathbb{1} + \mathbf{T}}{1+q}\mathbf{M}, \quad \mathbf{T}' = \frac{\mathbf{M}\mathbf{M}^{\mathsf{T}}\mathbf{\Pi} + \mathbf{T}^2}{1+q}, \quad \text{where} \quad q = \mathbf{M}^{\mathsf{T}}\mathbf{\Pi}\mathbf{M} \tag{2.21}$$

is the fugacity for $n > 1$, such that $\sqrt{q}$ is defined as the $\mathbf{\Pi}$-norm of $\mathbf{M}$. Indeed, the Boltzmann weight of a renormalized 00-bond is the sum over the weights of the configurations 000 and $0\phi0$, $\phi = 1, \dots, n$, such that $1' = 1 + \sum M_{\phi+n/2}M_\phi = 1 + q$ and we define $A = (1+q)^{-1}$. Likewise, a new $\phi0$-bond comes from $\phi00$ and $\phi\psi0$, $\psi = 1, \dots, n$, such that M'_ϕ depends on all M_ψ Eq. (2.21) has a similar form than Eq. (2.11), except that now $\mathbf{M}$ is a vector and $\mathbf{T}$ a matrix, which makes it challenging to plot the

flow diagram. Once again, the fixed points depend on the initial conditions $(\mathbf{M},\mathbf{T})^{(0)}$. Assuming that the dynamics converge (which seems difficult to show in the general case), we find the following fixed points and their associated basins of attraction.

- If $\mathbf{M}^{(0)}=\mathbf{0}$, then $\mathbf{M}^{(>0)}=\mathbf{0}$ and thus the fixed point value $\mathbf{M}_*=\mathbf{0}$. Using the Jordan normal form [Eq. (2.18)], Eq. (2.21) hence gives

$$\mathbf{T}'=\mathbf{T}^2,\quad \text{i.e.}\quad \mathbf{J}'=\mathbf{J}^2. \tag{2.22}$$

  In particular, the *a priori* complex eigenvalues verify $t_i'=t_i^2$, $i=1,\dots,n$, such that at the fixed points, $|t_{i*}|\in\{0,\,1,\,\infty\}$. This defines a fixed subspace in $(\mathbf{M},\mathbf{T})$. However, the cases with infinite eigenvalues are problematic and should only be viewed as limits, as discussed in Appendix 2.5.1. This fixed subspace is unstable, except for the point $\mathbf{T}_*=\mathbf{0}$ which is neutrally stable. If some eigenvalues have a non-zero imaginary part, the iteration can become cyclic, and we discuss the consequences in Sec. 2.2.4.

- If $\mathbf{M}^{(0)}>0$ (*i.e.* with positive entries), then the components of $\mathbf{M}^{(>0)}$ and $\mathbf{T}^{(>0)}$ are all strictly positive, *i.e.* $\mathbf{M}_*,\mathbf{T}_*>0$. And writing $q_*=\mathbf{M}_*^\mathsf{T}\mathbf{\Pi}\mathbf{M}_*$, the fixed subspace verifies

$$\forall\,\mathbf{M}_*=\sqrt{q}_*\mathbf{u}_*>0,\quad \mathbf{T}_*=\mathbf{M}_*\mathbf{M}_*^\mathsf{T}\mathbf{\Pi}=q_*\mathbf{u}_*\mathbf{u}_*^\mathsf{T}\mathbf{\Pi}, \tag{2.23}$$

  recalling Eq. (2.14). Here $q_*\in\mathbb{R}_*^+$ is the only non-zero eigenvalue of $\mathbf{T}_*$, with eigenvector $\mathbf{u}_*\in\mathbb{R}^n$ such that $\mathbf{u}_*^\mathsf{T}\mathbf{\Pi}\mathbf{u}_*=1$. Each point of the fixed subspace is defined by $\mathbf{M}_*$ which is an unknown function of the initial conditions. Since by definition $T_{\phi\psi}=e^{-C_{\phi\psi}}M_\phi(\mathbf{\Pi}\mathbf{M}_\psi)$, this fixed subspace together with the point $(\mathbf{0},\mathbf{0})$ correspond to the neutrally stable hard sphere gas $\mathbf{C}_*=\mathbf{0}$.

The proofs of these assertions are given in Appendix 2.5.2 and 2.5.3. Especially, in Appendix 2.5.2, we demonstrate Eq. (2.23), and we perform the linear stability analysis of both cases in Appendix 2.5.3. Then, Appendix 2.5.4 contains the study in the other cases, where some $M_\phi^{(0)}$ are zero and some are not. We find that these cases generally fall into one of the two categories above.

Contrary to the Ising chain, here it is still unsure whether there is a conserved quantity in the general case. Upon attempting to perform the calculation leading to $\alpha=(T^{(k)}-1)/M^{(k)}$ for $n=1$, we only arrive at this relation in the vectorial $n>1$ case:

$$\forall k,\ \big(\mathbf{T}^{(k+1)}-\mathbb{1}\big)\mathbf{M}^{(k)}=\big(\mathbf{T}^{(k)}-\mathbb{1}\big)\mathbf{M}^{(k+1)}. \tag{2.24}$$

Nevertheless, we will see in Sec. 2.3.4 that in some relevant cases, there is a quantity similar to the α of Eq. (2.12), which can be approximated as an integral of motion. We believe that it would indicate that $\langle s\rangle$ is again constant under renormalization. In these cases, we would have $\langle s\rangle^{(0)}=\langle s\rangle_*$, where $\langle s_*\rangle$ is easily expressed since the fixed point for $M^{(0)}>0$ is non-interacting:

$$\forall n\geq 1,\ \forall\mathbf{M}_*>0,\quad \langle s\rangle_*=\frac{q_*}{1+q_*},\quad q_*=\mathbf{M}_*^\mathsf{T}\mathbf{\Pi}\mathbf{M}_*, \tag{2.25}$$

where for $n=1$, the quantity q_* reduces to M_*^2. We have therefore come across many similarities between the cases of one and multiple orientations.

2.2.4 Cyclic iteration

But some features are specific to the case $n>1$, such as the appearance of recurring patterns in the renormalization dynamics of the system parameters. In the case $\mathbf{M}=\mathbf{0}$, from an initial matrix $\mathbf{T}^{(0)}$ with some non-real eigenvalues, the iteration $\mathbf{T}'=\mathbf{T}^2$, *i.e.* $\forall i,\ t_i'=t_i^2$, can be cyclic. For instance, in $n=4$ and given $a,b,c>0$, the matrix

$$\mathbf{T}=\begin{pmatrix}0&0&0&a\\b&0&a&0\\0&0&0&b\\0&c&0&0\end{pmatrix}\quad\text{has}\quad \mathbf{T}'=\begin{pmatrix}0&ac&0&0\\0&0&0&2ab\\0&bc&0&0\\bc&0&ac&0\end{pmatrix}\quad\text{and}\quad \mathbf{T}''=2abc\mathbf{T} \tag{2.26}$$

in the basis with orientations $\phi = 1, 2, 3, 4$. In this case, the only accepted configurations are made of two repeating patterns of 3 elements: 421 and 423 which we further call 3-loops. By decimation of a full line made of pattern 421 (the decimated orientations are crossed out), one obtains the following cyclic sequences of patterns with period 2:

$$421421421 \;\to\; \begin{matrix} 42\cancel{1}4\cancel{2}1\cancel{4}2\cancel{1} \\ \cancel{4}2\cancel{1}4\cancel{2}1\cancel{4}\cancel{2}1 \end{matrix} \;\to\; 412412412 \;\to\; \begin{matrix} 4\cancel{1}2\cancel{4}1\cancel{2}4\cancel{1}2 \\ \cancel{4}1\cancel{2}4\cancel{1}2\cancel{4}\cancel{1}2 \end{matrix} \;\to\; 421421421 \tag{2.27}$$

likewise for 423. Therefore, if $2abc = 1$, then we have $\mathbf{T}'' = \mathbf{T} \neq \mathbf{T}'$, *i.e.* the iteration is in a limit cycle of order 2, or 2-cycle. Moreover, the eigenvalues of $\mathbf{T}$ are written

$$\left(r, re^{i2\pi/3}, re^{-i2\pi/3}, 0\right), \quad \text{where} \quad r = (2abc)^{1/3}. \tag{2.28}$$

Since $r' = r^2$, if $r < 1$ (> 1), the eigenvalues decrease (increase) upon renormalization, but the iteration remains cyclic, and the accepted patterns also vary cyclically. In the general case of Eq. (2.21) where $\mathbf{M} > \mathbf{0}$, it is still unsure whether iteration can be cyclic.

We have seen the case of a 3-loop forming a 2-cycle in $n = 4$, but cycles and loops are not restricted to $n = 4$, as for instance the 5-loop system that only accepts patterns 12345 and 18765 in $n = 8$ forms a 4-cycle under renormalization. We can even generalize this behavior to λ-loops and c-cycles. Consider a system with a single λ-loop (apart from symmetries). The eigenvalues of $\mathbf{T}$ must either be 0 or the λ-th roots of unity, as in Eq. (2.28) for $\lambda = 3$. In order for this system to form a c-cycle in the iteration $\mathbf{T}' = \mathbf{T}^2$, we need $\mathbf{T}^{2^c} = \mathbf{T} \neq \mathbf{T}^{2^k}$, $k = 1, ..., c-1$. The condition for a c-cycle with a λ-loop is therefore written

$$(2^c - 1)/\lambda \in \mathbb{N}, \quad \text{while} \quad \forall k \in [\![1, c-1]\!],\ (2^k - 1)/\lambda \notin \mathbb{N} \tag{2.29}$$

The table below relates c to the smallest λ verifying Eq. (2.29), for the first values of λ:

loop length, λ	1	3	5	7	9	11
cycle length, c	1	2	4	3	6	10

Noticeably, a repeating pattern of length λ even cannot form cycles. Repeating the decimation as in Eq. (2.27) with, *e.g.*, the repeating pattern 4132 indeed yields

$$413241324 \;\to\; \begin{matrix} 434343 \\ 121212 \end{matrix} \;\to\; \begin{matrix} 444 \\ 333 \\ 111 \\ 222 \end{matrix}, \tag{2.30}$$

which is not cyclic. This cyclicity is an artifact of the decimation rather than a physical phenomenon, such that a decimation of two spins out of three would produce different cycles.

2.3 Absence of frustration and efficient aggregation in 1D

We now focus on aggregates of particles, *i.e.* successions of occupied sites whatever the orientations of the particles, which we call fibers. The first question is whether the lengths l of fibers are bounded or if the chain can be filled completely, *i.e.* whether $l = \infty$ is possible. It is answered in Sec. 2.3.1. We then look for a measure of the mean length of fibers $\langle l \rangle$ in units of the lattice spacing. As for $\langle s \rangle$, $\langle l \rangle$ is easily calculated for the Ising model ($n = 1$), but hard to obtain for multiple orientations ($n > 1$). However, for systems with an "efficient aggregation", such that forming aggregates is more favorable than putting particles alone on the chain, the study of the dynamics under renormalization should lead to $\langle l \rangle$.

Indeed, systems with an efficient aggregation form a small amount of large fibers at low density. In the limit of absolutely efficient aggregation, only one aggregate is formed. Therefore, just as the

correlation length ξ of Eq. (2.5) is divided by two at each step due to decimation $\xi' = \xi/2$, in this limit we have

$$\langle l \rangle' \sim \langle l \rangle / 2 \quad i.e. \quad \langle l \rangle^{(k)} \sim \langle l \rangle^{(0)} / 2^k. \tag{2.31}$$

We can even prove that efficient aggregation requires $\langle l \rangle \sim \xi$ for $n = 1$, see Appendix 2.4.2. Besides, since the dynamically attractive fixed curve is non-interacting, particles are generally alone on the chain so that $\langle l \rangle_* \sim 1$. Assuming that Eq. (2.31) is still valid for a small number of large aggregates, we could obtain an indirect measure of the typical aggregate size in the initial system by counting the number of steps k_{fp} to reach the vicinity of the dynamically attractive fixed point. This is summarized in the following relation:

$$\langle l \rangle^{(k_{\text{fp}})} \sim \langle l \rangle_* \sim 1 \quad \Rightarrow \quad \langle l \rangle^{(0)} \sim 2^{k_{\text{fp}}} \tag{2.32}$$

In Sec. 2.3.2, we look for systems with efficient aggregation in the Ising model and we prove that Eq.(2.31) is recovered for these systems. We then demonstrate a close version of Eq. (2.32) by comparing $2^{k_{\text{fp}}}$ to the transfer matrix result for $\langle l \rangle$. In Sec. 2.3.3, since we cannot directly calculate $\langle l \rangle$ for irregular particles, we assume Eq. (2.31) to be correct and we use Eq. (2.32) to obtain a theoretical value for $\langle l \rangle$. We are finally able to recover this expression in a simplified case whatever n in Sec. 2.3.4. This allows us to generically link the mean length of fibers to the renormalization dynamics.

2.3.1 Upper bounds in the length of fibers

Some systems have an intrinsic limit for the size of their fibers, which cannot fill the chain completely. This amounts to the only dimensional reduction in 1D. We find that this effect requires a certain condition on the coupling term T for $n = 1$, or on $\mathbf{T}$ for $n > 1$. For $n = 1$, the Boltzmann weight of a full self-closing chain of size N is T^N, which is zero only if $T = 0$. In this case, necessarily $l_{\max} = 1$ since particles cannot have neighbors. The transition between finite-size aggregates (of size $l = 1$ particle) and the chain-filling fiber is thus at $T = 0$.

Likewise, for $n > 1$, the Boltzmann weight of a full self-closing chain is $\operatorname{Tr} \mathbf{T}^N = \sum_i t_i^N$, where the sum is taken over the eigenvalues $t_1, \dots, t_n$ of $\mathbf{T}$. Thus, for a large enough chain $N \gg 1$, this term is zero only if $\mathbf{T}$ is nilpotent, meaning that all its eigenvalues $t_i = 0$. This means that there does not exist any repeating pattern of particles with orientations ϕ_1, ϕ_2, ... , ϕ_m, $m \geq 1$ such that the interactions $T_{\phi_1\phi_2}$, $T_{\phi_2\phi_3}$, ... , $T_{\phi_m\phi_1}$ are all non-zero. For instance in $n = 4$, let us consider the simple sparse matrix

$$\mathbf{T} = \begin{pmatrix} 0 & 0 & a & 0 \\ 0 & 0 & 0 & 0 \\ 0 & b & 0 & 0 \\ b & 0 & 0 & 0 \end{pmatrix} \quad \text{in the basis} \quad (\rightarrow, \downarrow, \leftarrow, \uparrow), \quad \text{where} \quad a, b > 0. \tag{2.33}$$

This represents the case where only the pattern $\uparrow\rightarrow\leftarrow\downarrow$ is favored, while $\downarrow$ does not accept anyone at its right. The maximum length of clusters is then 4. Additionally, when $\mathbf{T}$ is nilpotent, it always verifies $\mathbf{T}^n = \mathbf{0}$, *i.e.* whatever the values of the non-zero coefficients of $\mathbf{T}$ and whatever M, necessarily the aggregate size is at most n. This amounts to a dimensional reduction of the aggregates from one to zero. Similarly than in the example on the right of Fig. 2.1, the forced finiteness of the fiber width does not come from frustration, but on the absence of matches for the left of orientation ϕ_1, and for the right of orientation ϕ_m. Indeed, in 1D there cannot be any frustration of the kind displayed in Fig. 1.9.

If $\mathbf{T}$ is diagonalizable, then $\operatorname{Tr} \mathbf{T}^N = 0$ directly means $\mathbf{T} = \mathbf{0}$, *i.e.* $l_{\max} = 1$. This is the case for, *e.g.* π-periodic particles, see Sec. 2.1.3. Indeed, if a π-periodic particle favors some interaction at its right, it necessarily favors it also at its left, and if $l = 2$ was possible, then l would not be bounded. Thus the maximal length of finite-size aggregates with π-periodic particles is 1. Now let us study systems were the length of fibers is unbounded, *i.e.* we hereafter choose $T > 0$ or $\mathbf{T}$ not nilpotent, hence with at least one non-zero eigenvalues.

2.3.2 Efficient aggregation in the Ising chain

To understand the potential of the renormalization study, we hereafter compare the analytical expression of the average aggregate length with the number of steps for a system to renormalize to its

fixed point. For $n = 1$, the exact average length of fibers $\langle l \rangle$ is calculated in the general case using transfer matrices. Details of the calculation are given in Appendix 2.4.4. Considering a chain with N sites, for $N \to \infty$, we find via transfer matrix calculations

$$\langle l \rangle = \begin{cases} 0 & \text{for} \quad M = 0,\, T < 1, \\ M_\alpha^2 + M_\alpha / M & \text{for} \quad M > 0, \\ N \to \infty & \text{for} \quad M = 0,\, T \geq 1. \end{cases} \tag{2.34}$$

Thus, from both Eq. (2.16) and (2.34), we deduce that efficient aggregation, with $\langle l \rangle$ large and $\langle s \rangle$ small, requires α negative and large, M small and thus T just below 1. This can be rewritten as

$$M \ll 1, \quad T = 1 + \alpha M, \quad \text{where} \quad \alpha < 0 \quad \text{and} \quad -\alpha M \ll 1 \tag{2.35}$$

and $M \ll M_\alpha \ll 1$, such that the mean aggregate length in these cases reads

$$\langle l \rangle \sim \frac{M_\alpha}{M} \sim \frac{\sqrt{\langle s \rangle}}{M}. \tag{2.36}$$

To understand this result, we compare the Boltzmann weight of a chain with l particles, each without nearest neighbors lM^2, with the one corresponding to the particles all next to one another $M^2 T^{l-1}$. At constant density $\langle s \rangle$ and when T is just below one, as M decreases, particles prefer to cluster, which increases the typical size of fibers $\langle l \rangle$. In Fig. 2.4, *left*, some curves at constant $\langle l \rangle$ have been plotted in the (M, T)-space. The low density region is shown in light green, for which $\alpha \sim -1/M_\alpha$ is negative and rather large. Then, the closer to $T = 1$, the longer the fibers.

We now turn to the relationship between the aggregate length $\langle l \rangle^{(0)}$ of an initial condition ($M^{(0)} > 0, T^{(0)} = 1 + \alpha M^{(0)}$) and the number of steps to reach the fixed point k_{fp}. We already defined k_{fp} rather loosely in Eq. (2.32). More precisely, given $\epsilon \ll 1$, we introduce $k_{\text{fp}}(\epsilon)$ as the number of steps to reach the fixed point by ϵ, *i.e.*

$$M_* - M^{(k_{\text{fp}}(\epsilon))} \sim \epsilon. \tag{2.37}$$

We hereafter set the average density at a low value, *e.g.* $\langle s \rangle \lesssim 0.1$ and we vary $M^{(0)}$ to see how the theoretical expression of $\langle l \rangle^{(0)}$ varies with k_{fp} obtained through numerical analyses of the renormalization

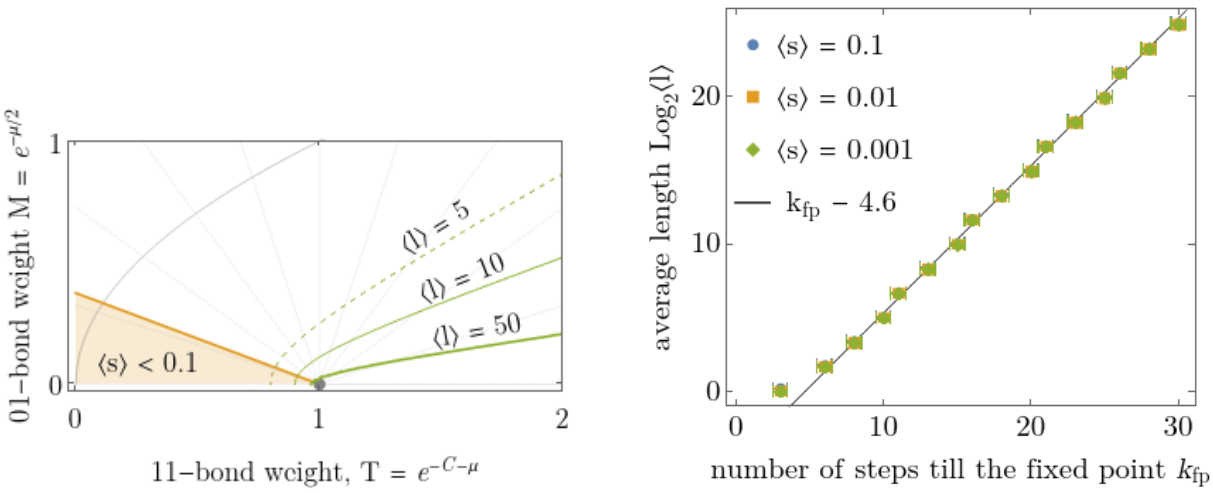

Figure 2.4: **For efficient aggregation in 1D, the average fiber length is exponential in k_{fp}.** *Left*, contour plot of $\langle l \rangle$ obtained from Eq. (2.34) and low $\langle s \rangle$ region from Eq. (2.16) for $n = 1$. Efficient aggregation happens in a triangular-like region at the right of the point $(M = 0, T = 1)$. *Right*, theoretical mean aggregate length $\langle l \rangle$ versus k_{fp} obtained via numerical analyses of the iteration in Eq. (2.13). The linear fit from Eq. (2.38) is calculated for $\langle s \rangle \lesssim 0.1$, $\epsilon = 10^{-10}$ and $k_{\text{fp}} \gtrsim 10$. The oscillating pattern comes from the fact that we round the values of k_{fp} to the nearest integer. Hence the ± 0.5 error bars.

iteration of Eq. (2.13). Results are shown in Fig. 2.4, *right*. Whatever $\epsilon \ll 1$, we find that

$$\text{for } k_{\rm fp} \gtrsim 10, \quad \langle l \rangle^{(0)} \approx 2^{\,k_{\rm fp}-\beta}, \tag{2.38}$$

where β depends only on ϵ. For instance, at $\epsilon = 10^{-10}$, $\beta \approx 5$. Therefore, we have recovered Eq. (2.32) in the case of efficient aggregation.

Furthermore, the formula for $\langle l \rangle$ in Eq. (2.36) obtained with transfer matrices can be recovered analytically in approximating the dynamics for efficient aggregation. Since $M^{(0)} \ll -\alpha M^{(0)} \ll 1$ from Eq. (2.35), then at the beginning,

$$M' = \frac{2+\alpha M}{1+M^2} M \sim 2M, \tag{2.39}$$

i.e. the dynamics is approximately exponential in the number of steps and $M_\alpha \sim M^{(k_{\rm fp})} \sim M^{(0)} 2^{k_{\rm fp}}$. But, this approximation converges more rapidly than the real function which yields $M_\alpha \approx \langle l \rangle^{(0)} M^{(0)} \approx 2^{k_{\rm fp}-\beta} M^{(0)}$. This means that the real dynamics takes $\approx \beta$ more steps to converge that its exponential approximation. From the definition of efficient aggregation give in Eq. (2.35), $M' \sim 2M$ leads to $T' \sim T^2$, which is identical to the iteration of T from $M^{(0)} = 0$ displayed in Eq. (2.13). A similar correspondence between the cases $(M = 0, \forall T)$ and $(M \ll 1, 1 - T \ll 1)$ can be recovered for irregular particles in some relevant cases, see Sec. 2.3.4. To conclude, we considered efficient aggregation, quantitatively characterized by $\langle s \rangle \lesssim 0.1$ and $k_{\rm fp} \gtrsim 10$. And in this case, we have linked the mean length of fibers $\langle l \rangle$ to the number of steps to reach the fixed point $k_{\rm fp}$ in one hand, and to the initial conditions $(M, T = 1 + \alpha M)^{(0)}$ in the other hand. Now let us do the same study for multiple orientations.

2.3.3 Efficient aggregation for multiple orientations

We hereby attempt to transpose the results of the $n = 1$ case for $n > 1$ orientations, by performing numerical analyses of the renormalization iteration in Eq. (2.21) for $n = 4$ and 8. Each point with error bars in Figs. 2.5 and 2.6 correspond to the mean and standard deviation of a dozen data points. Based on the study of Sec. 2.3.2, we consider the case, $(\mathbf{M}, \mathbf{T})^{(0)} > 0$, we set $q^{(0)} = \mathbf{M}^{(0)\mathsf{T}} \mathbf{\Pi} \mathbf{M}^{(0)}$ small and we look for efficient aggregation by varying the entries of the n-vector $\mathbf{M}^{(0)}$ and the $n \times n$-matrix $\mathbf{T}^{(0)}$. We start by defining $k_{\rm fp}$ properly for $n \geq 1$ orientations. Introducing $x^{(k)} = \left(\mathbf{M}^{(k)}, \mathbf{T}^{(k)}\right)$ as the coordinates of the system at step k, the number of steps to reach the fixed point with the error $\epsilon \ll 1$ written $k_{\rm fp}(\epsilon)$ is such that the distance

$$d\Big(x_*,\, x^{(k_{\rm fp}(\epsilon))}\Big) \sim \epsilon. \tag{2.40}$$

We can consider several distances $d(x_*,\, x^{(k)})$ such as

$$\max_{\phi,\psi} \left| T^{(k)}_{\phi\psi} - M^{(k)}_{\phi} M^{(k)}_{\psi+n/2} \right| \quad \text{or} \quad \left| \mathbf{T}^{(k)} - \mathbf{M}^{(k)} \mathbf{M}^{(k)\,\mathsf{T}} \mathbf{\Pi} \right|, \tag{2.41}$$

which are both 0 at the fixed point where $\mathbf{T}_* = \mathbf{M}_* \mathbf{M}_*^{\mathsf{T}} \mathbf{\Pi}$. Hopefully, for ϵ small enough (*e.g.* $\epsilon = 10^{-10}$ as for $n = 1$), we find that they give similar values of $k_{\rm fp}$. The entries of $\mathbf{M}^{(0)}$ are chosen uniformly in $[0, 1]$. As for $\mathbf{T}^{(0)}$, its entries can be generated in different ways. We write its eigenvalues as $t_1^{(0)}, \ldots, t_n^{(0)}$ ranked in descending absolute values. From the Perron-Frobenius theorem of Sec. 2.1.3, the first eigenvalue $t_1^{(0)}$ of the positive matrix $\mathbf{T}^{(0)}$ is single and positive, while its other eigenvalues are complex in general. As will be discussed later, we want its first eigenvalue $t_1^{(0)}$ to be relatively close to 1. This can be achieved by *e.g.* choosing the entries of the symmetric and positive $n \times n$-matrix $\mathbf{T}^{(0)} \mathbf{\Pi}$ to be either $2/n$ or a small quantity in $[0, 0.1]$, or else choose them uniformly in $[0, 2/n]$. In these case, we find multiple instances where $t_1^{(0)} \approx 1$ and some of the other eigenvalues are non-zero. We also consider diagonalizable matrices $\mathbf{T}$ where all $t_i^{(0)}$, $i > 1$ are zero, and where the entries of the first eigenvector are again chosen uniformly in $[0, 1]$.

We now focus on the low density systems and we find that we can once again define a quantity α function of the initial conditions, that depends only on the average density at the fixed point $\langle s \rangle_*$,

obtained by Eq. (2.25). Specifically, for all systems with the same small value of $\langle s\rangle_*$ (which can differ from $\langle s\rangle^{(0)}$), the first eigenvalue $t_1^{(0)} > 0$ and the quantity $q^{(0)} = \mathbf{M}^{(0)\mathsf{T}}\mathbf{\Pi}\mathbf{M}^{(0)} > 0$, verify a close relationship written

$$t_1^{(0)} \approx 1 - \sqrt{q}^{(0)} f\big(\langle s\rangle_*\big), \quad \text{for} \quad \langle s\rangle_* \lesssim 0.1. \tag{2.42}$$

This is shown in Fig. 2.5, *left* for $\langle s\rangle_* = 0.1$, where $f(0.1) \approx \frac{8}{3}$. This relationship remains approximately valid whatever the other complex eigenvalues $t_i^{(0)}$, $i > 1$, the eigenvectors of $\mathbf{T}^{(0)}$ and the direction of the vector $\mathbf{M}^{(0)}$. This $f\big(\langle s\rangle_*\big)$ is reminiscent of the definition of the integral of motion $-\alpha = (1-T^{(k)})/M^{(k)}$ for $n = 1$, given in Eq. (2.12). Moreover, as displayed in Fig. 2.5, *right*, the function f is in quantitative agreement with the function linking $-\alpha$ and $\langle s\rangle$ for $n = 1$. By combining the Eqs. (2.14) and (2.16) of the $n = 1$ study, we obtain $f(x) = (1-2x)/\sqrt{x(1-x)}$. However, defining $y^{(0)}$ as $f\big(\langle s\rangle_*\big)$, the renormalized quantities

$$y^{(k)} = (1 - t_1^{(k)})/\sqrt{q}^{(k)} \tag{2.43}$$

are not always equal, such that we cannot easily define an integral of motion for $n > 1$. Yet, we show in Sec. 2.3.4 that in some interesting cases of efficient aggregation, the $y^{(k)}$ vary very little, such that we recover $\alpha = y^{(0)} = f\big(\langle s\rangle_*\big)$ as a *quasi* integral of motion.

In Fig. 2.6, we show that for low density systems verifying Eq. (2.42), the number of steps to the fixed point depends only on the values of q at step 0 and at the fixed point. This is such that

$$\text{for } k_{\text{fp}} \gtrsim 10, \quad \sqrt{q_*/q^{(0)}} \approx 2^{k_{\text{fp}}-\beta}, \tag{2.44}$$

where $q_* = \mathbf{M}_*^{\mathsf{T}}\mathbf{\Pi}\mathbf{M}_*$ and β is consistent with its expression for $n = 1$ displayed in Eq. (2.38). From the conjecture of Eq. (2.31) and Eq. (2.32), as for $n = 1$, we infer that the mean aggregate length, when large, verifies

$$\langle l\rangle \sim \sqrt{q_*/q}\,. \tag{2.45}$$

However, the fixed point value q_* is still an unknown function of $M^{(0)}$ and $\mathbf{T}^{(0)}$. In Sec. 2.3.4, we present a simple case where we obtain this function between the fixed point and the initial conditions. In the end, systems with long fibers take a *long* time to renormalize, such that $2^{k_{\text{fp}}} \sim \sqrt{q_*/q^{(0)}} \gg 1$. If we add the condition of low average density, we obtain that efficient aggregation requires

$$q = 0^+ \quad \text{and} \quad t_1 = 1^-. \tag{2.46}$$

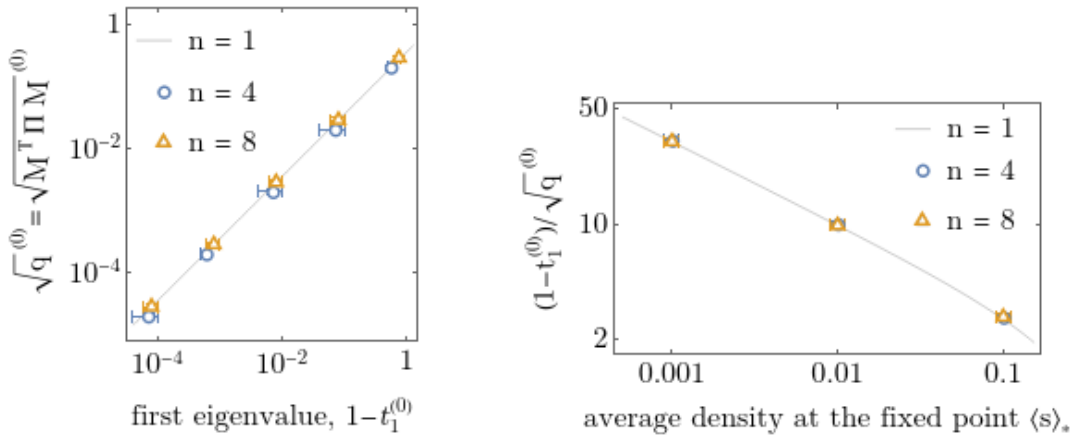

Figure 2.5: **Numerical analyses of the iteration in** Eq. (2.21) **for** $n = 4$ **and** 8 **allow to extend the** $n = 1$ **results to the case of irregular particles.** *Left*, for $\langle s\rangle_* = 0.1$ obtained with Eq. (2.25), the initial conditions verify: $\sqrt{q}^{0)} \approx \frac{3}{8}(1 - t_1^{(0)})$ whatever n and the other initial parameters. *Right*, plot of Eq. (2.42). The values of $(1 - t_1^{(0)})/\sqrt{q}^{(0)}$ at $\langle s\rangle_* = 0.1, 0.01$ and 0.001 for $n = 4, 8$ fall right on the curve $\alpha = f(\langle s\rangle)$ computed for $n = 1$. Error bars are all at most 10%.

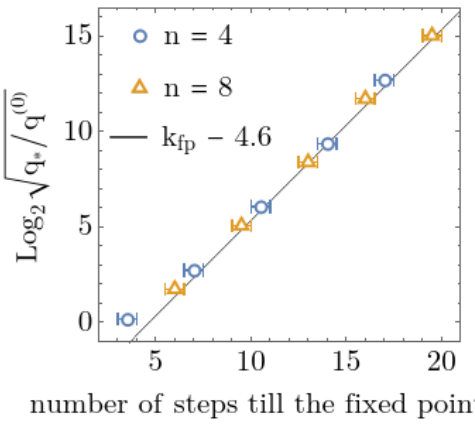

Figure 2.6: **Plot of the theoretical aggregate length $\sqrt{q_*/q^{(0)}}$ vs $k_{\rm fp}$ obtained via numerical analyses of the renormalization iteration of** Eq. (2.21)**.** As in Eq. (2.44), the points for $n = 4$ and 8 align quite well with the fit calculated for $n = 1$, see Fig. 2.4, *right*. In this plot, $\epsilon = 10^{-10}$, $q* = \frac{1}{9}$, the only non-zero eigenvalue of $\mathbf{T}^{(0)}$ is $1 - \frac{8}{3}\sqrt{q}^{(0)}$, $\mathbf{M}^{(0)} = \sqrt{q}^{(0)}\mathbf{m}$. Error bars are ± 0.5 for the abscissae, and less than 1% for the ordinates.

Indeed, the (possibly many) patterns of favored interactions required for long fibers (see Sec. 2.3.1) impose that t_1 is large, while the low density constraint forces $t_1 < 1$. This means that the chemical potentials need to be positive and large, but the condition on the couplings is a bit obscure.

Intuitively, the first eigenvalues is related to the couplings $T_{\phi\psi}$ that correspond to the longest possible fibers. We hereby study what it means concretely in simple examples of matrices $\mathbf{T}$, for which we numerically compute the eigenvalues. Indeed, analytically computing eigenvalues of matrices of any size n would be very time-consuming. For instance, let the entries of $\mathbf{T}$ be either a or $a\epsilon \ll a$, corresponding to favored and unfavored interactions respectively. If only one diagonal entry of $\mathbf{T}$ is equal to a, *e.g.* $T_{\phi\phi} = T_{\phi+n/2,\phi+n/2} = a$, while all other entries are ϵa, then the chain is going to be populated mostly by fibers of particles in the orientation ϕ. In this case, it seems that the largest eigenvalue $t_1 = a + \mathcal{O}(\epsilon)$, and efficient aggregation requires $a \sim 1^-$. Likewise, in the case of a repeatable pattern of favored interactions, such that only $T_{\phi_1\phi_2}, T_{\phi_2\phi_3}, \ldots, T_{\phi_m\phi_1} = a\mathcal{O}(1)$, $m \geq 1$, then it seems that $t_1 = a\mathcal{O}(1)$, and again a must be close and below 1. Interestingly, if only $T_{\phi\psi}$ and $T_{\psi\phi}$ are favored, the low density condition actually reads

$$T_{\phi\psi}T_{\psi\phi} < 1, \tag{2.47}$$

which can be satisfied even if *e.g.* $T_{\phi\psi} > 1$. However, if only $T_{\phi\psi} = a$, it seems that $t_1 \sim a\sqrt{2\epsilon}$, and we may need $a > 1$ to have large fibers. Besides, it seems that if two repeating patterns such as 12 and 13 are favored, then $t_1 \sim \sqrt{2}a$. And

$$\text{if all } T_{\phi\psi} = a,\ \phi, \psi = 1, \ldots, n, \quad \text{then} \quad t_1 = na. \tag{2.48}$$

In these cases, the low density constraint $t_1 < 1$ is stronger on a, because the fibers can be made of particles in any orientation. Unfortunately, for reasons still unclear, this condition that t_1 be large to have large aggregates does not hold in higher dimensions, and we discuss other possible conditions on two-dimensional lattices in Sec. 3.3.

2.3.4 Simplified renormalization dynamics for irregular particles

Although analyzing the dynamics $(\mathbf{M}^{(k)}, \mathbf{T}^{(k)})$ for all k in the general case looks intractable, we recover both the equivalence of Eq. (2.42) and Eq. (2.44) in a simple case of efficient aggregation. To do so, we investigate the dynamics from a non-generic initial condition, where $\mathbf{M}^{(0)} > 0$ and $\mathbf{T}^{(0)} > 0$ is diagonalizable. We specifically consider the form

$$\left(\mathbf{M}^{(0)} = \sqrt{q}^{(0)}\mathbf{m}, \quad \mathbf{T}^{(0)} = \sum_i t_i^{(0)} \mathbf{u}_i \mathbf{u}_i^\mathsf{T} \mathbf{\Pi}\right), \quad \text{where} \quad \mathbf{m}^\mathsf{T}\mathbf{\Pi}\mathbf{m} = 1, \quad \mathbf{u}_i^\mathsf{T}\mathbf{\Pi}\mathbf{u}_j = \delta_{ij}, \tag{2.49}$$

$t_1^{(0)} > 0$ and $\forall i > 1,\ t_i^{(0)} \in \mathbb{C}$. Its unique fixed point

$$\Big(\mathbf{M}_* = \sqrt{q}_*\mathbf{u}_*, \quad \mathbf{T}_* = q_*\mathbf{u}_*\mathbf{u}_*^\mathsf{T}\mathbf{\Pi}\Big), \quad \text{where} \quad \mathbf{u}_*^\mathsf{T}\mathbf{\Pi}\mathbf{u}_* = 1, \tag{2.50}$$

is reached through the iteration that we recall to be

$$\mathbf{M}' = \frac{\mathbb{1} + \mathbf{T}}{1+q}\mathbf{M}, \quad \mathbf{T}' = \frac{\mathbf{M}\mathbf{M}^\mathsf{T}\mathbf{\Pi} + \mathbf{T}^2}{1+q}, \quad \text{where} \quad q = \mathbf{M}^\mathsf{T}\mathbf{\Pi}\mathbf{M}. \tag{2.51}$$

Given $\epsilon \ll 1$ and $b \geq 0$, we introduce the statement $\mathbf{a} = \mathcal{O}(\epsilon^b)$, as to mean that the entries of the vector/matrix $\mathbf{a}$ are at most of order b. Considering the eigenvalues $t_1^{(0)}, \dots, t_n^{(0)}$ ranked in descending absolute values, we then simplify the iteration by enforcing two conditions:

$$\begin{aligned}
&(i) \quad \sqrt{q}^{(0)} = \epsilon \ll 1, \quad t_1^{(0)} = 1 + \alpha\epsilon + \mathcal{O}(\epsilon^2) < 1 \quad \text{and} \quad \mathbf{u}_1 = \mathbf{m} + \epsilon\mathbf{n} + \mathcal{O}(\epsilon^2), \\
&(ii) \quad \forall i > 1, \quad \left|t_i^{(0)}\right| = \mathcal{O}(\epsilon^a) < 1 \quad \text{and} \quad t_i^{(0)}\mathbf{u}_i = \mathcal{O}(1).
\end{aligned}$$

where α is an unknown constant at this stage, $\mathbf{n} = \mathcal{O}(1)$ and $a > 0$. Condition (i) is basically a proper rewriting of the efficient aggregation criterion sketched in Eq. (2.46), with the additional requirement that the first eigenvector of $\mathbf{T}^{(0)}$ be in a similar direction than $\mathbf{M}^{(0)}$. Condition (ii) is motivated by the fact that the eigenvalues at the fixed point $t_{>1\,*}$ (all except $t_{1\,*}$) are always 0, so we begin with small values and expect that they decrease to 0 under renormalization. With the numerical analyses of Sec.2.3.3, we also find that usually when $t_{>1}^{(0)} = 0$, then $\left|t_{>1}^{(>0)}\right| \ll 1$. After 1 renormalization step, the iteration in Eq. (2.51) leads to

$$\begin{aligned}
\mathbf{M}^{(1)} &= \frac{\sqrt{q}^{(0)}}{1+q^{(0)}}\Big[\mathbf{m} + t_1^{(0)}\mathbf{u}_1(\mathbf{u}_1^\mathsf{T}\mathbf{\Pi}\mathbf{m}) + t_2^{(0)}\mathbf{u}_2(\mathbf{u}_2^\mathsf{T}\mathbf{\Pi}\mathbf{m}) + \dots\Big] \\
&= \sqrt{q}^{(0)}\Big[\mathbf{m} + \mathbf{u}_1\big(\mathbf{u}_1^\mathsf{T}\mathbf{\Pi}\mathbf{u}_1 + \mathcal{O}(\epsilon)\big) + t_2^{(0)}\mathbf{u}_2\big(\mathbf{u}_2^\mathsf{T}\mathbf{\Pi}\mathbf{u}_1 + \mathcal{O}(\epsilon)\big) + \dots\Big] + \mathcal{O}(\epsilon^2) \\
&= \sqrt{q}^{(0)}\Big[\mathbf{m} + \mathbf{m}\big(1 + \mathcal{O}(\epsilon)\big) + t_2^{(0)}\mathbf{u}_2\,\mathcal{O}(\epsilon) + \dots\Big] + \mathcal{O}(\epsilon^2) \\
&= 2\mathbf{M}^{(0)} + \mathcal{O}(\epsilon^2),
\end{aligned} \tag{2.52}$$

and

$$\begin{aligned}
\mathbf{T}^{(1)}\mathbf{\Pi} &= \frac{1}{1+q^{(0)}}\left[q^{(0)}\mathbf{m}\mathbf{m}^\mathsf{T} + (t_1^{(0)})^2\mathbf{u}_1\mathbf{u}_1^\mathsf{T} + (t_2^{(0)})^2\mathbf{u}_2\mathbf{u}_2^\mathsf{T} + \dots\right] \\
&= \Big[1 + 2\alpha\epsilon + \mathcal{O}(\epsilon^2)\Big]\mathbf{u}_1\mathbf{u}_1^\mathsf{T} + \Big[(t_2^{(0)})^2 + \mathcal{O}(\epsilon^2)\Big]\,\mathbf{u}_2\mathbf{u}_2^\mathsf{T} + \dots + \epsilon^3\big(\mathbf{u}_1\mathbf{n}^\mathsf{T} + \mathbf{n}\,\mathbf{u}_1^\mathsf{T}\big) + \mathcal{O}(\epsilon^4)
\end{aligned} \tag{2.53}$$

This means that, from step 1 on, the dynamics of $\mathbf{M}$ and $\mathbf{T}$ are independent and at lowest order in ϵ, we have $\mathbf{M}' \sim 2\mathbf{M}$ and $\mathbf{T}' \sim \mathbf{T}^2$. Moreover, Eq. (2.52) can be rewritten as a scalar iteration: $\sqrt{q}' \sim 2\sqrt{q}$, since $\mathbf{m}' \sim \mathbf{m}$. Concerning $\mathbf{T}$ however, the study of Eq. (2.53) turns out to be trickier. As detailed in Appendix 2.5.5, determining the order of the corrections to the eigenvalues and eigenvectors due to the term $\propto \mathbf{u}_1\mathbf{n}^\mathsf{T} + \mathbf{n}\,\mathbf{u}_1^\mathsf{T}$ is far from trivial. It seems to depend on the multiplicity, such that single eigenvalues have lowest-order corrections of order 3, while the corrections of multiple eigenvalues are only greater than 0. From the Perron-Frobenius theorem of Sec. 2.1.3, the largest eigenvalue $t_1^{(0)}$ of the positive matrix $\mathbf{T}^{(0)}$ is single. It follows that the eigenvalue in front of $\mathbf{u}_1\mathbf{u}_1^\mathsf{T}$ in Eq. (2.53) can be rewritten with a correction of order 3 as

$$t_1^{(1)} = 1 + 2\alpha\epsilon + \mathcal{O}(\epsilon^3) = 1 + \big[\alpha + \mathcal{O}(\epsilon^2)\big]\sqrt{q}^{(1)}, \tag{2.54}$$

which is just below $t_1^{(0)}$ (since $\alpha < 0$) and has the same form. But the other eigenvalues can have a multiplicity higher than 1. Therefore, introducing $b > 0$ as the order of the lowest-order corrections of t_i', we can only write

$$t_i' = t_i^2 + \mathcal{O}\Big(\epsilon^b\Big), \quad i > 1. \tag{2.55}$$

From this writing together with condition (ii), it follows that $t_i^{(1)} = \mathcal{O}\big(\epsilon^{\min(a,b)}\big)$. In any case, from step 1 on, the $(t_i)_{i>1}$ go "quickly" to zero, such that $t_i^{(k)} = (t_i^{(1)})^{2^{k-1}}$ and $t_{i,*} = 0$.

Therefore, the interesting "slow" dynamics is effectively one-dimensional, and can be rewritten at any step k as

$$\sqrt{q}^{(k+1)} \sim 2\sqrt{q}^{(k)}, \quad \text{where} \quad t_1^{(k)} \sim 1 + \alpha\sqrt{q}^{(k)}. \tag{2.56}$$

This means that conditions (i) and (ii) lead to the same exponential approximation as we had for the Ising model, see Eq. (2.39). Moreover, in this simple case of efficient aggregation, we have recovered α as a quasi integral of motion, such that the renormalized value $\alpha' = \alpha + \mathcal{O}\big(\epsilon^2\big)$. It follows that, at the fixed point given by Eq. (2.50), $\mathbf{u}_* \sim \mathbf{m} \sim \mathbf{u}_1$, $\sqrt{q_*/q^{(0)}} \sim 2^{k_{\text{fp}}}$ and $q_* \sim 1 + \alpha\sqrt{q}_*$, such that we can write

$$\sqrt{q}_* = \sqrt{q}_\alpha = \frac{\alpha + \sqrt{\alpha^2+4}}{2}, \quad \text{where} \quad -\alpha \sim \frac{1 - t_1^{(0)}}{\sqrt{q}^{(0)}} > 0 \tag{2.57}$$

in agreement with the expression for $n = 1$ given in Eq. (2.14). In particular, at the fixed point, $\sqrt{q_*} \sim -1/\alpha \ll 1$. Besides, the parameter β is once again explained as the difference between the exponential approximation and the real function. As for $n = 1$ where α and $\langle s\rangle$ are simultaneously conserved, we believe that the quasi conservation of α in the case discussed here indicates that the mean density is also roughly constant under renormalization. This would mean that

$$\langle s\rangle^{(0)} \sim \langle s\rangle_* \sim q_* \tag{2.58}$$

from the definition of Eq. (2.25). In the end, the mean length of fibers $\langle l\rangle \sim \sqrt{q_*/q}$ depends, at lowest order, only on one scalar parameter in $\mathbf{T}^{(0)}$, namely its largest eigenvalue. We can understand this as follows. As the system renormalizes, weak couplings that lead to short fibers go quickly to zero, while repeatable patterns with strong couplings that make long fibers take many decimations to effectively vanish. As shown in Sec. 2.3.3, the first eigenvalue t_1 corresponds to these strong couplings and is thus the one to renormalize slowly. This makes t_1 the foremost relevant parameter.

Moreover, combining the study of these simple cases of efficient aggregation with the $n = 1$ study, we attempt to write a general expression for the average length of fibers as a function of the number of orientations n. To do so, we introduce the $\mathbf{\Pi}$-averaged Boltzmann weight of a 01-bond for particles with $n > 1$ orientations as

$$M = \sqrt{\sum_{\phi=1}^{n} M_\phi M_{\phi+n/2}/n} = \sqrt{q/n}, \tag{2.59}$$

which reduces to the previously defined $M = e^{-\mu/2}$ for $n = 1$. In our understanding, M^2 corresponds to the generalized Boltzmann weight of putting one particle on the line whatever n. Assuming this is correct, in the case of efficient aggregation, we can eventually write that

$$(i) \text{ and } (ii) \quad \Rightarrow \quad \forall n \geq 1, \quad \langle l\rangle \sim \frac{\sqrt{\langle s\rangle}}{\sqrt{n}M} \sim \frac{\langle l\rangle_{n=1}}{\sqrt{n}}, \tag{2.60}$$

where $\langle l\rangle_{n=1} \sim -1/(M\alpha)$. The physical reasoning could go like this. As n increases, more fibers can be formed since the particles have potentially more attractive sides. Therefore, at constant average particle density $\langle s\rangle$, the typical size of fibers $\langle l\rangle$ would decrease with n. This assertion however requires further study.

Conclusion

Let us now recapitulate our findings in 1D. We first developed a formalism to study the self-assembly of copies of a lattice particle with orientation-dependent interactions. We then focused on the relevant case of efficient aggregation, where large aggregates form at low density, i.e. $\langle l\rangle \gg 1$ and $\langle s\rangle \ll 1$. Via a study of the renormalization dynamics, we linked $\langle s\rangle$ to the fixed point properties, and $\langle l\rangle$ to the time needed to reach the fixed point. We thus showed that in 1D, $\langle l\rangle$ and $\langle s\rangle$ depend mostly on two scalars,

namely the largest eigenvalue t_1 of matrix $\mathbf{T}$ and the $\mathbf{\Pi}$-norm of vector $\mathbf{M}$, related to the coupling matrix $\mathbf{C}$ and the vector of chemical potential $\boldsymbol{\mu}$. We additionally linked dimensional reduction (from potentially infinite fibers to finite aggregates) to a condition on t_1 in 1D. Indeed, finite-size aggregates require $t_1 = 0$ and are at most of size n. Finally, we have hinted that the typical length of fibers could decrease with the number of orientations. This would mean that particles with *e.g.* 100 orientations sides, perhaps because they have on average more sides which are potentially repulsive to any other, would form smaller aggregates than particles with 10 orientations. Besides, in 1D, there is a priori no benefit to having a smooth or rugged interaction landscape. What only matters for fibers is that particles have at least one couple of opposite sides that are both very attractive.

The question now is whether this renormalization method can be used for the study of aggregates in a 2D environment, and whether it can distinguish fibrous (1D) aggregates from bulk-like (2D) aggregates. What looks promising is that the numerical simulations of L. Koehler [Fig. 1.12] recover instances of the cyclicity in the coupling matrix $\mathbf{C}$ analyzed in Sec. 2.2.4. To go further, one could consider a certain statistics for the $n \times n$-matrix $\mathbf{C}$ and the n-vector $\boldsymbol{\mu}$, taking into account the symmetries of $\mathbf{C}$ discussed in Sec. 2.1.1. One could thus investigate *e.g.* whether the aforementioned conditions on the first eigenvalue t_1 of $\mathbf{T}$ are restrictive. Similarly for the conditions on the other eigenvalues necessary for the approximations of Sec. 2.3.4. If these are restrictive, this would make efficient aggregation from random interaction landscapes rather unlikely, at least in the equilibrium framework of this model.

2.4 Appendix: calculations on the Ising chain model

We hereby perform calculations in the Ising model. In Sec. 2.4.1, we sketch the mapping from lattice-gas to spin variables. In Sec. 2.4.2, we recall some basic results obtained by transfer matrix calculations. We particularly compute the average density $\langle s \rangle$ and the correlation length ξ. We then study the renormalization dynamics in Sec. 2.4.3. We finally compute the mean length of fibers $\langle l \rangle$ in Sec. 2.4.4.

2.4.1 Lattice-gas to spin-$\frac{1}{2}$ variables mapping

The Hamiltonian of Eq. (2.3) with lattice-gas variables $s_i = 0, 1$ can be mapped bijectively with the following Hamiltonian (Fisher, 1967):

$$\frac{\mathcal{H}(\boldsymbol{\sigma})}{k_B\theta} = \sum_i -J\sigma_i\sigma_{i+1} - h\sigma_i, \tag{2.61}$$

where the spin-$\frac{1}{2}$ variables $\sigma_i = \pm 1$. Here $J > 0$ (< 0) denotes a ferromagnetic (anti-ferromagnetic) coupling, and h is the magnetic field. The mapping comes from the change of variables $\sigma_i = 2s_i - 1$, which implies the following relationships:

$$J = -C/4 \quad \text{and} \quad h = -(C + \mu)/2, \tag{2.62}$$

up to an irrelevant constant energy shift. Therefore, the line $T = e^{2h} = 1$ in Fig. 2.3 corresponds to $h = 0$.

2.4.2 Textbook calculations with the transfer matrix

For the Ising model, the transfer matrix reads $\mathscr{T} = \left(\begin{smallmatrix} 1 & M \\ M & T \end{smallmatrix}\right)$, where the indices i, j of $\mathscr{T}_{ij}$ are between 0 and 1. In the non-trivial case $M > 0$ and $T = 1 + \alpha M$, we can express its eigenvalues $\lambda_\pm$ and unit eigenvectors $\mathbf{w}_\pm$ using the fixed point $M_\alpha = \left(\alpha + \sqrt{\alpha^2 + 4}\right)/2 > 0$ of the renormalization iteration of Eq. (2.13). We find

$$\begin{aligned} \lambda_+ &= 1 + MM_\alpha, & \lambda_- &= 1 - M/M_\alpha, \\ \mathbf{w}_+ &= \begin{pmatrix} w_1 \\ w_2 \end{pmatrix} = \frac{1}{\sqrt{1 + M_\alpha^2}} \begin{pmatrix} 1 \\ M_\alpha \end{pmatrix}, & \mathbf{w}_- &= \begin{pmatrix} -w_2 \\ w_1 \end{pmatrix}, \end{aligned} \tag{2.63}$$

where we can easily show that $\lambda_+ > 1 > \lambda_-$ and $\lambda_+ > T > \lambda_-$ Indeed, $\lambda_+ - T = M\left(\sqrt{\alpha^2 + 4} - \alpha\right)/2 > 0$ and $T - \lambda_- = MM_\alpha > 0$. Therefore, we can rewrite the transfer matrix at any power k as

$$\mathscr{T}^k = \begin{pmatrix} w_1 & -w_2 \\ w_2 & w_1 \end{pmatrix} \begin{pmatrix} \lambda_+^k & 0 \\ 0 & \lambda_-^k \end{pmatrix} \begin{pmatrix} w_1 & w_2 \\ -w_2 & w_1 \end{pmatrix}, \tag{2.64}$$

and we can easily compute several meaningful quantities. On a chain of N sites with periodic boundary conditions, the partition function reads (Kramers and Wannier, 1941)

$$Z = \sum_{\mathbf{s}} e^{-\mathcal{H}(\mathbf{s})/(k_B\theta)} = \sum_{\mathbf{s}} \prod_i \mathscr{T}_{s_i,\, s_{i+1}} = \operatorname{Tr} \mathscr{T}^N = \lambda_+^N + \lambda_-^N. \tag{2.65}$$

Likewise, the site occupancy reads

$$Z \langle s \rangle = \sum_{\mathbf{s}} s_0\, e^{-\mathcal{H}(\mathbf{s})/(k_B\theta)} = \sum_{\mathbf{s}} \mathscr{T}_{1,s_1} \ldots \mathscr{T}_{s_k,s_{k+1}} \ldots \mathscr{T}_{s_{N-1},1} = \left(\mathscr{T}^N\right)_{11} = w_2^2\lambda_+^N + w_1^2\lambda_-^N, \tag{2.66}$$

and higher order moments are expressed as

$$Z \langle s_0 s_i \rangle = \left(\mathscr{T}^i\right)_{11} \left(\mathscr{T}^{N-i}\right)_{11} = \left(w_2^2\lambda_+^i + w_1^2\lambda_-^i\right)\left(w_2^2\lambda_+^{N-i} + w_1^2\lambda_-^{N-i}\right) \tag{2.67}$$

and

$$Z\,\langle s_1 \cdots s_N\rangle = T^N. \tag{2.68}$$

From Eq. (2.63), since $\lambda_+ > \lambda_-$, in the limit $N \to \infty$, we can rewrite all previous quantities as

$$Z \sim \lambda_+^N, \quad \langle s\rangle \sim w_2^2, \quad \langle s_0 s_i\rangle \sim \langle s\rangle^2 + w_2^2 w_1^2 \left(\frac{\lambda_-}{\lambda_+}\right)^i \quad \text{and} \quad \langle s_1 \cdots s_N\rangle \sim \left(\frac{T}{\lambda_+}\right)^N. \tag{2.69}$$

This gives the expression of $\langle s\rangle$ in Eq. (2.16). We can finally rewrite the two-point correlation as $\langle s_0 s_i\rangle - \langle s\rangle^2 \propto e^{-i/\xi}$ as in Eq. (2.5), where the correlation length reads $\xi = 1/\ln\frac{\lambda_+}{\lambda_-}$ in units of the lattice spacing. Therefore, when $T = 1$, *i.e.* $M_\alpha = 1$,

$$\text{as } M \to 0, \quad \xi = \left(\ln\frac{1+M}{1-M}\right)^{-1} \sim \frac{1}{2M} \to \infty. \tag{2.70}$$

Besides, in the case $M = 0$, situations with non-zero Boltzmann weights amount only to the empty and full line. Therefore, the aforementioned quantities are written

$$Z = 1 + T^N \text{ and } \langle s\rangle = \langle s_0 s_i\rangle = \langle s_1 \cdots s_N\rangle = \frac{T^N}{1+T^N} \xrightarrow[N\to\infty]{} \Theta(T), \tag{2.71}$$

where Θ is the Heaviside step function.

2.4.3 Convergence to the hard sphere gas and stability analysis

Given the iteration

$$\begin{cases} M' = \dfrac{2+\alpha M}{1+M^2} M, & T' = 1 + \alpha M', & \text{if } M > 0, \\ M' = 0, & T' = T^2, & \text{if } M = 0, \end{cases} \tag{2.72}$$

let us first prove the convergence to the hard sphere gas fixed curve in the case ($M > 0$, $T = 1 + \alpha M$). We define $e_k = M_\alpha - M^{(k)}$ and we hereby show that $(e_k)_{k\geq 1}$ is a positive and decreasing sequence, hence converges to its null limit. Since $\alpha = (M_\alpha^2 - 1)/M_\alpha$, we can rewrite Eq. (2.72) as

$$e_{k+1} = M_\alpha - \frac{2M^{(k)} + \alpha (M^{(k)})^2}{1 + (M^{(k)})^2} = \frac{1}{M_\alpha}\frac{e_k^2}{1 + (M^{(k)})^2}, \tag{2.73}$$

where $M_\alpha > 0$, hence proving the positivity of the e_k for $k > 1$. Moreover,

$$e_{k+1} - e_k = -\frac{e_k}{M_\alpha}\frac{X(e_k)}{1 + (M^{(k)})^2}, \quad \text{where} \quad X(e_k) = M_\alpha(1 + M_\alpha^2) - (1 + 2M_\alpha^2)e_k + M_\alpha e_k^2. \tag{2.74}$$

The discriminant of the quadratic function $X(e_k)$ equals 1, hence its square-roots are written

$$-\frac{1 + 2M_\alpha^2 \pm 1}{2M_\alpha(1 + M_\alpha^2)} \tag{2.75}$$

and are both negative. Therefore, $X(e_k)$ is positive for $e_k > 0$ which proves the decreasing of the sequence and thus its convergence. This demonstrates the validity of Eq. (2.15).

Second, we consider small perturbations around a fixed point of a fixed subspace and we analyze whether the perturbation linearly increases under renormalization, decreases, or leads to another nearby fixed point belonging to the same fixed subspace. This defines fixed subspaces that are (respectively) unstable, stable or neutrally stable. Given $\epsilon \ll 1$, we consider $M = M_* + \epsilon M_1$ and $T = T_* + \epsilon T_1$.

- If $M_* = 0$, then at first order in ϵ, Eq. (2.72) gives

$$M_1' = (1 + T_*)M_1 \quad \text{and} \quad T_1' = 2T_* T_1. \tag{2.76}$$

  Thus, $(M_* = 0, T_* = 0)$ is neutrally stable, $(0, 1)$ is fully unstable and $(0, \infty)$ is M-unstable.

- If $M_* > 0$, then $T_* = M_*^2$ and we obtain

$$(1 + M_*^2)M_1' = M_1(1 - M_*^2) + M_* T_1 \quad \text{and} \quad T_1' = 2M_* M_1'. \tag{2.77}$$

  Thus, $T' = (M')^2 + \mathcal{O}(\epsilon^2)$ which proves the neutral stability of the hard sphere gas fixed curve.

2.4.4 Average length of fibers

To compute $\langle l \rangle$, we begin by introducing the probability $p(l,i)$ that a fiber made of l consecutive occupied sites begins at site i in a chain of N sites. It reads

$$p(l,i) = \begin{cases} \langle (1-s_{i-1}) s_i \cdots s_{i+l-1} (1-s_{i+l}) \rangle, & \text{for} \quad l = 1, \dots, N-1 \\ \langle s_1 \cdots s_N \rangle, & \text{for} \quad l = N \end{cases}, \tag{2.78}$$

and is independent of i since the Hamiltonian of Eq. (2.3) is translation invariant. Thus, we will further consider $p(l,1)$ written simply $p(l)$. In summing over the lengths l, we obtain

$$\sum_{l=1}^{N} p(l) = \langle (1-s_0) s_1 \rangle + \langle s_1 \cdots s_N \rangle \,, \tag{2.79}$$

since terms cancel each other out two by two. Then, the average length of fibers (conditioned on having a fiber) written $\langle l \rangle$ is given by the first moment of this probability distribution:

$$\langle l \rangle = \frac{\sum_l l p(l)}{\sum_l p(l)} \tag{2.80}$$

We now compute the probabilities $p(l)$ for $l < N$. With the transfer matrix of Sec. 2.4.2, we obtain

$$Z p(l) = \mathscr{T}_{01} (\mathscr{T}_{11})^{l-1} \mathscr{T}_{10} \big(\mathscr{T}^{N-l-1}\big)_{00} = M^2 T^{l-1} \Big(w_1^2 \lambda_+^{N-l-1} + w_2^2 \lambda_-^{N-l-1} \Big), \tag{2.81}$$

where $\lambda_\pm$ and $w_{1,2}$ are given by Eq. (2.63). When $N \to \infty$, since $Z \sim \lambda_+^N$, we see that

$$p(l) \sim \frac{M^2}{\lambda_+^2} \left[w_1^2 \left(\frac{T}{\lambda_+} \right)^{l-1} + \left(\frac{\lambda_-}{\lambda_+} \right)^{N-2} w_2^2 \left(\frac{T}{\lambda_-} \right)^{l-1} \right]. \tag{2.82}$$

Therefore

$$\sum_{l=1}^{N-1} l p(l) \sim \frac{M^2}{\lambda_+^2} \left[w_1^2 \sum_{l=1}^{N-1} l \left(\frac{T}{\lambda_+} \right)^{l-1} + \left(\frac{\lambda_-}{\lambda_+} \right)^{N-2} w_2^2 \sum_{l=1}^{N-1} l \left(\frac{T}{\lambda_-} \right)^{l-1} \right], \tag{2.83}$$

where for $M > 0$, $\lambda_+ > T > \lambda_-$. Finally, the second sum and the last term $N p(N) = N T^N / Z$ are negligible in front of the first sum, and we can use the identity $\sum_1^N l x^{l-1} \to_{N\to\infty} 1/(1-x)^2$, for $|x| < 1$, to obtain

$$\sum_{l=1}^{N} l p(l) \to \left(\frac{M w_1}{\lambda_+ - T} \right)^2 = w_2^2. \tag{2.84}$$

Thus for $M > 0$, when $N \to \infty$, the average length of fibers reads

$$\langle l \rangle = \frac{w_2^2}{\langle s \rangle - \langle s_0 s_1 \rangle} = \frac{1}{w_1^2 (1 - \lambda_-/\lambda_+)} = M_\alpha^2 + \frac{M_\alpha}{M}, \tag{2.85}$$

and for $M = 0$, $\langle l \rangle = N p(N) = N \Theta(T)$, where Θ is the Heaviside step function. This ends up proving Eq. (2.34). In the case of efficient aggregation, this expression for $\langle l \rangle$ turns out to be similar to the one of the correlation length ξ defined in Appendix 2.4.2. Indeed,

$$\text{for } M \ll M_\alpha \ll 1, \quad \xi = 1 / \ln \frac{1 + M M_\alpha}{1 - M/M_\alpha} \sim 1 / \ln (1 + M/M_\alpha) \sim \frac{M_\alpha}{M} \sim \langle l \rangle \,. \tag{2.86}$$

Therefore, the formation of a few large clusters requires correlations over a lengthscale similar to their typical size: $\xi \sim \langle l \rangle$.

2.5 Appendix: detailed analysis of the renormalization for multiple orientations

We hereby focus on the model for oriented particles and we study the fixed spaces of the renormalization transformation. We further use either the Jordan decomposition or the singular value decomposition depending on convenience. Sec. 2.5.1 deals with the issues of the fixed points for $\mathbf{M} = \mathbf{0}$. In Sec. 2.5.2, we show Eq. (2.23) which describes the structure of the hard sphere gas fixed subspace. Then Sec. 2.5.3 contains the analysis of the linear stabilities of the fixed subspaces. The fixed points of the renormalization dynamics for the untreated initial condition cases are analyzed in Sec. 2.5.4. Finally, Sec. 2.5.5 shows how to expand the eigenvalues and eigenvectors of the matrix $\mathbf{T}^{(1)}\mathbf{\Pi}$ in the simplified renormalization dynamics of Sec. 2.3.4.

2.5.1 Fixed points for $\mathbf{M} = \mathbf{0}$

When $\mathbf{T}^{(0)}$ is not diagonalizable and has some eigenvalues greater or equal to 1, the fixed point of the iteration $\mathbf{T}' = \mathbf{T}^2$ for $\mathbf{M} = \mathbf{0}$ can be tricky to compute. In particular, we seem to find some inconsistencies between the Jordan normal form and the singular value decomposition. For instance, consider a diagonal block of $\mathbf{J}^{(0)} = \mathbf{P}^{-1}\mathbf{T}^{(0)}\mathbf{P}$ written

$$\mathbf{J}_i^{(0)} = \begin{pmatrix} t & 1 \\ 0 & t \end{pmatrix}, \quad \text{such that} \quad \mathbf{J}_i^{(k)} = \begin{pmatrix} t^l & lt^{l-1} \\ 0 & t^l \end{pmatrix}, \quad \text{where} \quad l = 2^k. \tag{2.87}$$

In the limit $k \to \infty$, the fixed point depends on the value of t. For $t < 1$, it reads $\left(\begin{smallmatrix} 0 & 0 \\ 0 & 0 \end{smallmatrix}\right)$ which poses no issues. But for $t = 1$, defining $x \to \infty$, it is written $\left(\begin{smallmatrix} 1 & x \\ 0 & 1 \end{smallmatrix}\right)$, and for $t > 1$, $\left(\begin{smallmatrix} x & x \\ 0 & x \end{smallmatrix}\right)$. Therefore, upon iteration, none of the blocks $\mathbf{J}_i^{(k)}$, k finite, are diagonalizable. The matter however becomes delicate for $k \to \infty$, since "$0 \times \infty$" is ill-defined.

With the singular value decomposition, where $\mathbf{T\Pi} = \mathbf{S}$ is symmetric, the dynamics is harder to study, since $\mathbf{T}' = \mathbf{T}^2$ leads to $\mathbf{S}' = \mathbf{S\Pi S}$. However, the fixed point verifies

$$\mathbf{S}_* = \mathbf{S}_*\mathbf{\Pi}\mathbf{S}_*, \tag{2.88}$$

which leads to many simplifications. Indeed, writing $\mathbf{S}_* = \sum_{i=1}^n s_i\, \mathbf{v}_i\mathbf{v}_i^\mathsf{T}$, where the s_i are real and $\mathbf{v}_i^\mathsf{T}\mathbf{v}_j = \delta_{ij}$, Eq. (2.88) yields

$$\sum_i s_i\, \mathbf{v}_i\mathbf{v}_i^\mathsf{T} = \sum_{i,j} s_i s_j (\mathbf{v}_i^\mathsf{T}\mathbf{\Pi}\mathbf{v}_j)\, \mathbf{v}_i\mathbf{v}_j^\mathsf{T}. \tag{2.89}$$

By orthonormality of the eigenvectors, the cross terms in the double sum are all zero:

$$s_i s_j (\mathbf{v}_i^\mathsf{T}\mathbf{\Pi}\mathbf{v}_j) = 0 \quad \text{for} \quad i \neq j, \tag{2.90}$$

and the remaining terms give

$$s_i = s_i^2 (\mathbf{v}_i^\mathsf{T}\mathbf{\Pi}\mathbf{v}_i). \tag{2.91}$$

Therefore, the eigenvalues of $\mathbf{S}_*$ belong to $\left\{0,\ (\mathbf{v}_i^\mathsf{T}\mathbf{\Pi}\mathbf{v}_i)^{-1},\ \infty\right\}$, and we can write

$$\forall j, \quad s_j \mathbf{T}_* \mathbf{v}_j = \sum_i s_i s_j (\mathbf{v}_i^\mathsf{T}\mathbf{\Pi}\mathbf{v}_j)\mathbf{v}_i = s_j^2 (\mathbf{v}_j^\mathsf{T}\mathbf{\Pi}\mathbf{v}_j)\mathbf{v}_j. \tag{2.92}$$

This means that either $s_j = 0$ or $t_j = s_j(\mathbf{v}_j^\mathsf{T}\mathbf{\Pi}\mathbf{v}_j)$ is an eigenvalue of $\mathbf{T}_*$. Eventually, writing $n_0 \leq n$ the number of zero eigenvalues of $\mathbf{S}_*$, we can write

$$\mathbf{T}_* = \sum_{i=1}^{n-n_0} t_i\, \mathbf{u}_i\mathbf{u}_i^\mathsf{T}\mathbf{\Pi}, \quad \text{where} \quad t_i \in \{1, \infty\} \quad \text{and} \quad \mathbf{u}_i^\mathsf{T}\mathbf{\Pi}\mathbf{u}_j = \delta_{ij}. \tag{2.93}$$

Therefore, using the singular value decomposition, we find that all fixed points are diagonalizable, which seems to contradicts the iteration study with the Jordan decomposition above. But again, the eigenvalues of matrices with infinite entries are ill-defined.

2.5.2 Hard sphere gas

Here, we determine the structure of the fixed subspaces, *i.e.* the different ensembles of points $(\mathbf{M},\mathbf{T})_*$ such that $(\mathbf{M},\mathbf{T})' = (\mathbf{M},\mathbf{T})$ from the initial condition $(\mathbf{M},\mathbf{T})^{(0)}$ with $\mathbf{M}^{(0)} > 0$. The dynamics is given by the renormalization formulae:

$$\mathbf{M}' = \frac{\mathbb{1}+\mathbf{T}}{1+q}\mathbf{M}, \quad \mathbf{T}' = \frac{\mathbf{M}\mathbf{M}^\mathsf{T}\mathbf{\Pi}+\mathbf{T}^2}{1+q}, \quad \text{where} \quad q = \mathbf{M}^\mathsf{T}\mathbf{\Pi}\mathbf{M}. \tag{2.94}$$

Since $\mathbf{M}^{(0)} > 0$, then through iteration $\mathbf{M}^{(>0)}, \mathbf{T}^{(>0)} > 0$, and at the fixed point $\mathbf{M}_*, \mathbf{T}_* > 0$. We use the singular value decomposition to write the fixed point matrix $\mathbf{T}_* = \mathbf{S}_*\mathbf{\Pi} = \sum_i s_i\, \mathbf{v}_i\mathbf{v}_i^\mathsf{T}\mathbf{\Pi}$, where the eigenvalues of $\mathbf{S}_*$ are real, and the eigenvectors are orthonormal. Then from $\mathbf{M}'_* = \mathbf{M}_*$ in Eq. (2.94), we obtain that

$$\mathbf{S}_*\mathbf{\Pi}\mathbf{M}_* = q_*\mathbf{M}_* = (\mathbf{M}_*^\mathsf{T}\mathbf{\Pi}\mathbf{M}_*)\mathbf{M}_*. \tag{2.95}$$

This is satisfied by writing the fixed point as

$$\mathbf{M}_* = M_*\mathbf{v}_1 \quad \text{and} \quad \mathbf{S}_* = \mathbf{M}_*\mathbf{M}_*^\mathsf{T} + \sum_{i>1} s_i\, \mathbf{v}_i\mathbf{v}_i^\mathsf{T}, \tag{2.96}$$

such that $(M_*^2, \mathbf{v}_1)$ forms an eigenpair of $\mathbf{S}_*$. We focus next on the equality $\mathbf{T}'_* = \mathbf{T}_*$, which can be rewritten as $(1+q_*)\mathbf{S}_* = \mathbf{M}_*\mathbf{M}_*^\mathsf{T} + \mathbf{S}_*\mathbf{\Pi}\mathbf{S}_*$. Removing the term $\mathbf{M}_*\mathbf{M}_*^\mathsf{T}(1+q_*)$ on both sides and writing $s_1 = M_*^2$, this yields

$$(1+q_*)\sum_{i>1} s_i\, \mathbf{v}_i\mathbf{v}_i^\mathsf{T} = \sum_{i,j/(i,j)\neq(1,1)} s_i s_j(\mathbf{v}_i^\mathsf{T}\mathbf{\Pi}\mathbf{v}_j)\, \mathbf{v}_i\mathbf{v}_j^\mathsf{T}. \tag{2.97}$$

Thus, as in Sec. 2.5.1,

$$0 = s_i s_j(\mathbf{v}_i^\mathsf{T}\mathbf{\Pi}\mathbf{v}_j) \quad \text{for} \quad i \neq j, \tag{2.98a}$$

$$(1+q_*)s_i = s_i^2(\mathbf{v}_i^\mathsf{T}\mathbf{\Pi}\mathbf{v}_i) \quad \text{for} \quad i > 1. \tag{2.98b}$$

Therefore, the eigenvalues of $\mathbf{S}_*$ for $i > 1$ belong to $\{0,\ (1+q_*)/(\mathbf{v}_i^\mathsf{T}\mathbf{\Pi}\mathbf{v}_i),\ \infty\}$, and either $s_j = 0$ or $t_j = s_j(\mathbf{v}_j^\mathsf{T}\mathbf{\Pi}\mathbf{v}_j)$ is an eigenvalue of $\mathbf{T}_*$. The eigenvalues of $\mathbf{T}_*$ thus verify $t_1 = q_* > 0$ since $\mathbf{M}_* > 0$, and

$$\forall i > 1, \quad s_i = 0 \quad \text{or} \quad t_i \in \{1+t_1, \infty\}. \tag{2.99}$$

From the Perron Frobenius theorem of Sec. 2.1.3, since $\mathbf{T}_* > 0$ and $\mathbf{v}_1 > 0$, then t_1 has the largest absolute value, *i.e.*

$$\forall i > 1, \quad |t_i| < t_1. \tag{2.100}$$

Therefore, from the contradictory conditions of Eq. (2.99) and (2.100), the only possibility is that all s_i, $i > 1$ be zero. Finally $\forall \mathbf{M}_* > 0$, $\mathbf{T}_* = \mathbf{M}_*\mathbf{M}_*^\mathsf{T}\mathbf{\Pi}$, and the hard sphere gas is the only fixed point from an initial condition with $M^{(0)} > 0$.

2.5.3 Linear stability of the fixed subspaces

We now consider small perturbations around a fixed point belonging to a fixed subspace. We analyze whether the perturbation linearly increases under renormalization, decreases, or leads to another nearby fixed point belonging to the same fixed subspace. This defines fixed subspaces that are (respectively) unstable, stable or neutrally stable. Given $\epsilon \ll 1$, we consider perturbations around a fixed point, *i.e.* write $\mathbf{M} = \mathbf{M}_* + \epsilon\mathbf{M}_1$ and $\mathbf{T} = \mathbf{T}_* + \epsilon\mathbf{T}_1$. Then at first order, Eq. (2.94) leads to

$$(1+q_*)\mathbf{M}'_1 = \big(\mathbb{1} + \mathbf{T}_* - 2\mathbf{M}_*\mathbf{M}_*^\mathsf{T}\mathbf{\Pi}\big)\mathbf{M}_1 + \mathbf{T}_1\mathbf{M}_*, \tag{2.101a}$$

$$(1+q_*)\ \mathbf{T}'_1 = \mathbf{M}_1\mathbf{M}_*^\mathsf{T}\mathbf{\Pi} + \mathbf{M}_*\mathbf{M}_1^\mathsf{T}\mathbf{\Pi} - 2(\mathbf{M}_*^\mathsf{T}\mathbf{\Pi}\mathbf{M}_1)\mathbf{T}_* + \mathbf{T}_*\mathbf{T}_1 + \mathbf{T}_1\mathbf{T}_*. \tag{2.101b}$$

Once again, we hereafter distinguish cases depending on the considered fixed point:

- If $\mathbf{M}_* = \mathbf{0}$, the dynamics is decoupled:

$$\mathbf{M}_1' = (\mathbb{1} + \mathbf{T}_*)\mathbf{M}_1 \overset{\text{def}}{=} \mathbf{A}\mathbf{M}_1, \quad \mathbf{T}_1' = \mathbf{T}_*\mathbf{T}_1 + \mathbf{T}_1\mathbf{T}_*. \tag{2.102}$$

Following the study of Sec. 2.5.2, introducing $n_0 \leq n$, we can write

$$\mathbf{T}_* = \sum_{i=1}^{n-n_0} t_i\, \mathbf{u}_i\mathbf{u}_i^\mathsf{T}\mathbf{\Pi}, \quad \text{where} \quad t_i \in \{1, \infty\} \quad \text{and} \quad \mathbf{u}_i^\mathsf{T}\mathbf{\Pi}\mathbf{u}_j = \delta_{ij}. \tag{2.103}$$

Unless the point $\mathbf{T}_* = \mathbf{0}$ ($n_0 = n$) which is neutrally stable, all other points $\mathbf{T}_* > 0$ ($n_0 < n$) are unstable as we will now prove. Indeed, summing the real eigenvalues of $\mathbf{A}$ yields

$$\sum_{i=1}^{n} a_i = \operatorname{Tr}\mathbf{A} = n + \operatorname{Tr}\mathbf{T}_* > n, \tag{2.104}$$

since for $i = 1, \ldots, n - n_0$, the eigenvalues $t_i \geq 1$. Thus at least one $a_i > 1$ and the perturbation increases. Likewise defining the n-vectors $\mathbf{w}_i = \mathbf{T}_1\mathbf{u}_i$, $i \leq n - n_0$, Eq. (2.102) leads to

$$\mathbf{w}_i' = \mathbf{T}_*\mathbf{T}_1\mathbf{u}_i + \sum_{j=1}^{n-n_0} s_j\, \mathbf{T}_1\mathbf{u}_j\mathbf{u}_j^\mathsf{T}\mathbf{\Pi}\mathbf{u}_i = \Big[\mathbf{T}_* + s_i\mathbb{1}_n\Big]\mathbf{w}_i \overset{\text{def}}{=} \mathbf{B}^i\mathbf{w}_i, \tag{2.105}$$

where for each i, summing the real eigenvalues of $\mathbf{B}^i$ yields

$$\sum_{j=1}^{n} b_j^i = \operatorname{Tr}\mathbf{T}_* + n s_i > n, \tag{2.106}$$

by definition of the s_i. Thus at least one $b_j^i > 1$. To conclude, this subspace is unstable with respect to variations of both $\mathbf{M}$ and $\mathbf{T}$.

- For the hard sphere gas, $\mathbf{T}_* = \mathbf{M}_*\mathbf{M}_*^\mathsf{T}\mathbf{\Pi}$, and we can rewrite the two equations in (2.101) to obtain

$$\mathbf{T}_1' = \mathbf{M}_1'\mathbf{M}_*^\mathsf{T}\mathbf{\Pi} + \mathbf{M}_*\mathbf{M}_1'^\mathsf{T}\mathbf{\Pi}. \tag{2.107}$$

This means that at first order in ϵ, $\mathbf{T}'$ also belongs to the subspace. Therefore, this subspace is neutrally stable.

2.5.4 Fixed points for the other initial conditions

We hereby consider the dynamics from an initial condition where some $M_\phi^{(0)}$ are zero, while the others are non-zero. From Eq. (2.94), we see that for the M_ϕ' to also be zero, we need $M_\phi = 0$ and $(\mathbf{TM})_\phi = 0$. Or else we return to the case $\mathbf{M} > 0$ of Sec. 2.5.2. Then for $M_\phi'' = 0$, we additionally need $(\mathbf{T}^2\mathbf{M})_\phi = 0$. We see that it generalizes into

$$\forall k,\ M_\phi^{(k)} = 0 \quad \Rightarrow \quad \forall l \geq 0,\ \left[(\mathbf{T}^{(0)})^l\mathbf{M}^{(0)}\right]_\phi = 0. \tag{2.108}$$

This condition means that for the bond-configurations with neighboring spin times orientations $(\phi, 0)$ to be impossible at any step of renormalization, there cannot be any possible configuration such as $(\phi, \psi_1, \ldots, \psi_l, 0)$, $\forall l$ because they would renormalize to $(\phi, 0)$. We find a solution for Eq. (2.108), where the initial conditions have the following form, that remains stable under renormalization. Given $n_1 < n/2$, we introduce the n_1-vectors $\mathbf{M}_1, \mathbf{M}_3 \geq 0$, the $n_1 \times n_1$-matrices $\mathbf{T}_{ij} \geq 0$, $i, j = 1, 3$ and the $(n/2 - n_1) \times (n/2 - n_1)$-matrices $\mathbf{T}_{ij} \geq 0$, $i, j = 2, 4$. The stable form reads

$$\mathbf{M} = \begin{pmatrix} \mathbf{M}_1 \\ \mathbf{0} \\ \hline \mathbf{M}_3 \\ \mathbf{0} \end{pmatrix}, \quad \mathbf{T} = \left(\begin{array}{cc|cc} \mathbf{T}_{11} & \mathbf{0} & \mathbf{T}_{13} & \mathbf{0} \\ \mathbf{0} & \mathbf{T}_{22} & \mathbf{0} & \mathbf{T}_{24} \\ \hline \mathbf{T}_{31} & \mathbf{0} & \mathbf{T}_{33} & \mathbf{0} \\ \mathbf{0} & \mathbf{T}_{42} & \mathbf{0} & \mathbf{T}_{44} \end{array}\right), \tag{2.109}$$

where the lines indicate $n/2$. This means that the orientations in $[n_1+1, n/2]$ can only either fill the chain or not be there at all. They thus cannot interact with the orientations in $[1, n_1]$, which can populate the chain either alone or in fibers. Introducing the block vectors and matrices

$$\mathbf{M}_A = \begin{pmatrix} \mathbf{M}_1 \\ \mathbf{M}_3 \end{pmatrix}, \quad \mathbf{T}_A = \begin{pmatrix} \mathbf{T}_{11} & \mathbf{T}_{13} \\ \mathbf{T}_{31} & \mathbf{T}_{33} \end{pmatrix} \quad \text{and} \quad \mathbf{T}_B = \begin{pmatrix} \mathbf{T}_{22} & \mathbf{T}_{24} \\ \mathbf{T}_{42} & \mathbf{T}_{22} \end{pmatrix}, \tag{2.110}$$

with size $2n_1$, their renormalization formulae read

$$\mathbf{M}'_A = \frac{\mathbb{1} + \mathbf{T}_A}{1+q_A}\mathbf{M}_A, \quad \mathbf{T}'_A = \frac{\mathbf{M}_A\mathbf{M}_A^\mathsf{T}\mathbf{\Pi} + \mathbf{T}_A^2}{1+q_A} \quad \text{and} \quad \mathbf{T}'_B = \frac{\mathbf{T}_B^2}{1+q_A}, \tag{2.111}$$

where $q_A = \mathbf{M}_A^\mathsf{T}\mathbf{\Pi}\mathbf{M}_A$. Therefore the dynamics of $(\mathbf{M}_A, \mathbf{T}_A)$ is independent of $\mathbf{T}_B$ and renormalizes to the hard sphere gas of Sec. 2.5.2. However, the dynamics of $\mathbf{T}_B$ depends on $(\mathbf{M}_A, \mathbf{T}_A)$ and is therefore difficult to study. But, we can assert that, as in Sec. 2.5.1, the eigenvalues of the fixed points of $\mathbf{T}_B$ belong to $\{0, 1+q_{A*}, \infty\}$, where q_{A*} denotes the value of q_A at the fixed point of $(\mathbf{M}_A, \mathbf{T}_A)$. The stability of these fixed points is as in the case $\mathbf{M} = \mathbf{0}$, meaning that it is unstable if any $t_{i*} > 0$, while the point $\mathbf{T}_{B*} = \mathbf{0}$ is neutrally stable.

2.5.5 Lowest-order corrections to eigenvalues and eigenvectors

Given $\epsilon \ll 1$, we introduce the diagonalizable $n\times$n-matrix $\mathbf{T} = \sum_i t_i\, \mathbf{u}_i\mathbf{u}_i^\mathsf{T}\mathbf{\Pi} > 0$, such that $t_i\mathbf{u}_i = \mathcal{O}(1)$ and $\mathbf{u}_i^\mathsf{T}\mathbf{\Pi}\mathbf{u}_j = \delta_{ij}$. We then focus on the matrix

$$\mathbf{T}' = \mathbf{T}^2 + \epsilon^3\mathbf{N}, \quad \text{where} \quad \mathbf{N} = \mathcal{O}(1), \tag{2.112}$$

and $\mathbf{N\Pi}$ is symmetric. This corresponds to a simple rewriting of the issue at hand in Eq. (2.53). We hereby investigate the possible forms of the lowest-order corrections to the eigenvectors and eigenvalues. Let us start by rephrasing the problem of Eq. (2.112) in a much simpler, yet insightful manner for 2×2-matrices. We define the real diagonalizable matrix $\mathbf{A} = \left(\begin{smallmatrix} a & b \\ c & d \end{smallmatrix}\right)$, which has the characteristic polynomial $\chi_A = \lambda^2 - \lambda\,\mathrm{Tr}\,A + \det A$. Its complex eigenvalues, solutions of $\chi_A = 0$, are written

$$2\lambda_\pm^A = \mathrm{Tr}\,\mathbf{A} \pm \sqrt{\Delta_A}, \quad \text{where} \quad \Delta_A = \mathrm{Tr}^2\,\mathbf{A} - 4\det\mathbf{A}. \tag{2.113}$$

The corresponding eigenvectors of $\mathbf{A}$, solutions of $\mathbf{Aa} = \lambda_\pm^A\mathbf{a}$ are written

$$\mathbf{a}_\pm \propto \begin{pmatrix} b \\ \lambda_\pm^A - a \end{pmatrix} \quad \text{for} \quad \Delta_A \neq 0, \tag{2.114}$$

while necessarily $\mathbf{A} = \lambda^A\mathbb{1}$ if $\Delta_A = 0$. We now introduce $\mathbf{A}_1 = \left(\begin{smallmatrix} a_1 & b_1 \\ c_1 & d_1 \end{smallmatrix}\right)$ and we consider the matrix $\mathbf{B} = \mathbf{A} + \epsilon^3\mathbf{A}_1$. The characteristic polynomial of $\mathbf{B}$ and its eigenvalues have the same form as the ones of $\mathbf{A}$. Introducing $X = ad_1 + da_1 - bc_1 + cb_1$, we obtain

$$2\lambda_\pm^B = \mathrm{Tr}\,\mathbf{A} + \epsilon^3\,\mathrm{Tr}\,\mathbf{A}_1 \pm \sqrt{(\mathrm{Tr}\,\mathbf{A} + \epsilon^3\,\mathrm{Tr}\,\mathbf{A}_1)^2 - 4\,(\det\mathbf{A} + \epsilon^3 X)} + \mathcal{O}\big(\epsilon^6\big). \tag{2.115}$$

We then distinguish the cases:

$$\lambda_\pm^B - \lambda_\pm^A = \begin{cases} \pm\dfrac{\epsilon^{3/2}}{2}\sqrt{2\,\mathrm{Tr}\,\mathbf{A}\,\mathrm{Tr}\,\mathbf{A}_1 - 4X} + \mathcal{O}\big(\epsilon^3\big), & \text{if} \quad \Delta_A = 0, \\ \dfrac{\epsilon^3}{2}\left(\mathrm{Tr}\,\mathbf{A}_1 \pm \dfrac{\mathrm{Tr}\,\mathbf{A}\,\mathrm{Tr}\,\mathbf{A}_1 - 2X}{\sqrt{\Delta_A}}\right) + \mathcal{O}\big(\epsilon^4\big), & \text{if} \quad \Delta_A \neq 0. \end{cases} \tag{2.116}$$

Thus, the corrections to the eigenvalues could a priori be of order $\frac{3}{2}$ in the case of eigenvalues with multiplicities higher than 1 (and $\Delta_A = 0$). Similarly, the eigenvectors of $\mathbf{B}$ written

$$\mathbf{b}_\pm \propto \begin{cases} \begin{pmatrix} b + \epsilon^3 b_1 \\ \lambda_\pm^B - a - \epsilon^3 a_1 \end{pmatrix} & \text{for} \quad \Delta_A \neq 0, \\ \begin{pmatrix} \epsilon^3 b_1 \\ \lambda_\pm^B - \lambda^A - \epsilon^3 a_1 \end{pmatrix} & \text{for} \quad \Delta_A = 0, \end{cases} \tag{2.117}$$

contain corrections of the same order as the eigenvalues. Discussing diagonalization for any $n \times n$-matrix, let alone the lowest-order corrections, seems quite intractable. Assuming that the very simplified study of the previous paragraph can be transposed for the larger matrices of Eq. (2.112) (which is a big "if"), the correction of the t_i' and the $\mathbf{u}_i'$, $i = 1, \ldots, n$ could be of order 3 for single eigenvalues, but of order $\frac{3}{2}$ for *e.g.* double eigenvalues.

We additionally generate random positive 4×4-matrices $\mathbf{T}$ and $\mathbf{N}$ such that $\mathbf{T\Pi}$ and $\mathbf{N\Pi}$ are symmetric. Since the positivity condition is difficult to satisfy, we generate $\mathbf{T}$ and $\mathbf{N}$ by their entries. To find eigenvalues with multiplicities higher than one, we choose the entries of a matrix $\mathbf{B}$ in a uniform integer distribution between *e.g.* 1 and 3. We then write $\mathbf{T} = (\mathbf{B} + \mathbf{B}^\mathsf{T})\mathbf{\Pi}/2$. In this case, numerical analyses of 100 instances of matrices $\mathbf{T}$ and $\mathbf{N}$ suggest that the lowest order for the corrections to the single eigenvalues of $\mathbf{T} + \epsilon^3\mathbf{N}$ seem to be 3. However, for the double eigenvalues that we encounter, it seem to be $\frac{3}{2}$. For instance, given

$$\mathbf{T} = \begin{pmatrix} 2 & 2 & 2 & 2 \\ 5/2 & 2 & 2 & 3 \\ 1 & 2 & 2 & 5/2 \\ 2 & 2 & 2 & 2 \end{pmatrix} \quad \text{and} \quad \mathbf{N} = \begin{pmatrix} 1 & 2 & 2 & 2 \\ 5/2 & 3 & 2 & 3 \\ 2 & 2 & 1 & 5/2 \\ 2 & 1 & 2 & 3 \end{pmatrix} \tag{2.118}$$

the eigenvalues of $\mathbf{T} + \epsilon^3\mathbf{N}$ can be expanded for $\epsilon \ll 1$ as

$$0 \pm \frac{\sqrt{5}}{2} e^{3/2} + \mathcal{O}(\epsilon^3) \quad \text{and} \quad (4 \pm 3\sqrt{2}) + \frac{\pm 4759 + 3372\sqrt{2}}{\pm 24 + 17\sqrt{2}} \frac{e^3}{24} + \mathcal{O}(\epsilon^4). \tag{2.119}$$

The double eigenvalue 0 thus has a correction of order $\frac{3}{2}$, while the simple eigenvalues $4 \pm 3\sqrt{2}$ have corrections of order 3.

Since generating positive matrices with triple or quadruple eigenvalues is challenging, we let go of the positivity constraint hoping that it is not cardinal in this study, and we generate 100 matrices by their eigenvalues. For eigenvalues with multiplicity m obtained by numerical analysis, the lowest order for the corrections $o_{\min}$ seem to be

$$o_{\min} = \begin{cases} 3/m, & \text{if } m \text{ odd} \\ 3/2, & \text{if } m \text{ even} \end{cases} \tag{2.120}$$

This indicates that the analytical study above is not completely incorrect and that the lowest order for the corrections seem to depend on their multiplicities.

Chapter 3

Modestly fruitful attempts in two dimensions

Following the 1D study presented in the last chapter, we hereby discuss aggregation depending on the number of discrete orientations n on the square and triangular lattices. Our goal is to characterize the dimensional reduction of aggregates, from crystalline sheet-like structures with two dimensions of growth, to fibers with one dimension of growth and finite-size aggregates, via the same real-space renormalization group approach. We hope to identify several aggregate phases through an analysis of the renormalization flow (Efrati et al., 2014), that in some way contain information on the dimensionality of the aggregates. To this end, we present several renormalization procedures that should help sort coupling matrices according to the dimension of their associated aggregate in 2D lattices. We begin, in Sec. 3.1, by presenting the details of the model and the zoology of aggregates (triangles, zigzag fibers, etc.) which arises from particular formulations of the coupling matrix $\mathbf{C}$, in both the triangular and square lattices. We also discuss which kind of renormalization procedure to implement in order to reach our aforementioned goal.

In Sec. 3.2, we introduce a simple yet insightful renormalization scheme based on a diamond spin plaquette, which allows us to analytically compute relevant characteristics of the system for $n = 1$, as we did in 1D. However, the $n > 1$ formulation turns out to be far too difficult to be understood purely analytically. Moreover, we find that this procedure fails to properly describe the dynamical characteristics of fibers under renormalization. We then consider in Sec. 3.3 the regime of efficient aggregation, where large aggregates form at low densities. For the Ising model ($n = 1$), we obtain the average density $\langle s \rangle$ by a mean-field approximation, and the average aggregate radius $\langle R \rangle$ by numerically computing the number of renormalization steps to arrive to the fixed point. For multiple orientations $n > 1$, we obtain $\langle s \rangle$ in particularly relevant cases, but we struggle to find any efficient aggregation regime with this diamond plaquette. We thus discuss more elaborate renormalization procedures in Sec. 3.4. The first idea is to consider a larger hexagonal spin plaquette, which leads to very cumbersome renormalization formulae. But it turns out to recover many of the renormalization dynamics observed in the numerical simulations of L. Koehler. We last present another possible extension by considering next-nearest-neighbor interactions on top of the nearest-neighbor ones.

3.1 From 1D to 2D

Going from 1D to 2D, several things need to be re-thought. First, we need to choose a lattice to work on. With regards to frustration, we slightly prefer the triangular lattice, since it already displays some frustration in the simple Ising anti-ferromagnetic case, with spin-$\frac{1}{2}$ variables $\sigma_i = \pm 1$ (Wannier, 1950). Indeed, there is no configuration of the spins which satisfies all the links, see Fig. 1.5, where the +1 (-1) state of the spin is represented with the arrow $\uparrow$ ($\downarrow$). However, the square lattice is also a serious candidate, since it can become frustrated *e.g.* in the case of nearest-neighbor ferromagnetic interactions and next-nearest-neighbor anti-ferromagnetic interactions.

For $n > 1$ orientations, we introduce the variables $\phi_i^{jk} \in [\![1, n]\!]$ which denote the discrete orientation of a particle at site i with respect to the direction of the link between the neighboring sites j and

Figure 3.1: **The energy of a given configuration is invariant by global rotation of the lattice, such that these two configurations have the same energy.** On the left configuration, the orientations with respect to given links can be written $\phi_b^{ab} = \leftarrow$, while $\phi_b^{bc} = \uparrow = \phi_a^{ab}$.

k. Think of puzzle pieces as in Fig. 2.1. This is such that the links between the occupied sites on both left and right configurations of Fig. 3.1 have the same energy. We first present the self assembly model in Sec. 3.1.1, which displays qualitatively different behavior in 2D than in 1D. In particular, we examine the phase transition between the ordered and the disordered phases, which appears at different temperatures in different lattices. In Sec. 3.1.2, we investigate the different kinds of aggregate shapes that arise from simple formulations of the coupling matrix $\mathbf{C}$. We last discuss in Sec. 3.1.3 the specific requirements that a physically adequate renormalization transformation must meet. For instance, we require large fibers at small density to renormalize into fibers with a smaller but still large length.

3.1.1 Self-assembly model on 2D lattices

As in 1D, we differentiate the cases where the particle types that have only one orientation $n = 1$ from those that have multiple ones. In the latter case, for simplicity purposes, we focus on particles with $n = 6$ orientations on the triangular lattice, and $n = 4$ on the square lattice. We hope that this study will give some insight on systems composed of *e.g.* regular octagons ($n = 8$) interacting only on 4 of their sides in the square lattice, see Fig. 1.7. For $n = 1$, on a lattice with N sites, given a spin configuration $\mathbf{s} = \{s_i\}_{1\leq i\leq N}$, $s_i \in \{0, 1\}$, we define the Hamiltonian of the 2D lattice-gas Ising model as

$$\frac{\mathcal{H}(\mathbf{s})}{k_B\theta} = \sum_{\langle i,j\rangle} C s_i s_j + \frac{\mu}{\kappa}(s_i + s_j), \tag{3.1}$$

where $\langle i, j\rangle$ refers to pairs of nearest neighbor sites. Here, κ is the lattice coordination, such that $\kappa = 4$ for the square lattice and $\kappa = 6$ for the triangular lattice. The coupling C between nearest neighbors is defined as in 1D, and in this formulation, the chemical potential μ is split between the κ bonds of each site. But contrary to the 1D case where the critical temperature is zero, the critical point in 2D is non-trivial. This critical point is situated on the line $C = -\mu\frac{2}{\kappa}$, which corresponds to zero magnetic field in the ferromagnetic formulation with spins $\sigma_i = \pm 1$, see Appendix 3.5.1. At this point, the ordering C term exactly compensates the disordering effect of temperature, such that the correlation length of Eq. (2.5) diverges: $\xi = \infty$. This phase transition between order and disorder is of second order due to the singularity in ξ. At the transition, changing the scale does not change the physics, such that the system is in a self-similar state. This corresponds to a particular kind of long-distance physics involving macroscopic fluctuations, different from the ordered and disordered phases.

This model was solved analytically by L. Onsager on the infinite square lattice for $C = -\mu\frac{2}{\kappa}$ (Onsager, 1944). He found a phase transition in both attractive ($C < 0$, or ferromagnetic) and repulsive ($C > 0$, or antiferromagnetic) cases at the same finite critical temperature θ_c^{sq}, such that

$$C_c^{\text{sq}} = \pm 2\ln(1 + \sqrt{2}) \quad \text{and} \quad k_B\theta_c^{\text{sq}} = 1/|C_c^{\text{sq}}|, \tag{3.2}$$

where k_B is Boltzmann's constant. Considering the attractive case $C < 0$, the spins are therefore ordered for low temperatures/high couplings ($|C| \gg |C_c^{\text{sq}}|$), such that for a finite but large system, the average density $\langle s\rangle$ is close to 1 (0), for $\frac{2}{\kappa}\mu < -C$ ($> -C$). At the critical point $\frac{2}{\kappa}\mu = -C$, $\langle s\rangle$ is bi-valued. Whereas the spins are disordered for high temperatures/low couplings $|C| \ll |C_c^{\text{sq}}|$,

$\langle s \rangle$ is close to $\frac{1}{2}$. On the triangular lattice, the attractive and repulsive critical points are however not identical (Stephenson, 1970). Repulsive systems have a vanishing critical temperature (infinite positive coupling), such that the system is always disordered at non-zero temperatures. On the contrary, attractive systems have a non-zero critical temperature, corresponding to a finite critical coupling (Eltinge, 2015)

$$C_c^{\text{tri}} = -\ln 3. \tag{3.3}$$

As in 1D, we further parameterize the system with the non-negative variables $M = e^{-\mu/\kappa}$ and $T = e^{-C-\mu\frac{2}{\kappa}}$, corresponding to the Boltzmann weights of a 01-bond and a 11-bond respectively.

For $n > 1$ orientations, the Hamiltonian must assign the same energy to the same configurations, regardless of the direction from which the lattice is looked at. The Hamiltonian for a given configuration of the spins and orientations $\boldsymbol{\phi} = \{\phi_i\}_{1 \le i \le N}$ thus reads

$$\frac{\mathcal{H}(\mathbf{s}, \boldsymbol{\phi})}{k_B \theta} = \sum_{\langle i,j \rangle} C_{\phi_i^{ij} \phi_j^{ij}} \, s_i s_j + \frac{\mu_{\phi_i^{ij}}}{\kappa} s_i + \frac{(\boldsymbol{\Pi}\boldsymbol{\mu})_{\phi_j^{ij}}}{\kappa} s_j. \tag{3.4}$$

With this formulation, the links between the occupied sites on both left and right configurations of Fig. 3.1 have the same energy written

$$C_{\uparrow\leftarrow} + \frac{\mu_\uparrow}{4} + \frac{(\boldsymbol{\Pi}\boldsymbol{\mu})_\leftarrow}{4} \tag{3.5}$$

on a right-oriented *horizontal* link. Indeed, $\kappa = 4$ on the square lattice. As in the 1D study, the orientations $\phi = 1, \dots, n$ are defined modulo n and the matrix $\boldsymbol{\Pi}$ is such that $(\boldsymbol{\Pi}\boldsymbol{\mu})_\phi = \mu_{\phi+n/2}$. The matrix $\boldsymbol{\Pi}$ thus corresponds to a rotation of π, such that the right chemical potentials $\mu_{\phi+n/2}$ can be mapped to the left chemical potentials μ_ϕ, see Sec. 2.1.1.

We formulate the different configurations of a bond via the spin times orientations of the linked sites written $s\phi$ and $s'\psi$, where ϕ and ψ are the orientations relative to the direction of the bond. The Boltzmann weights of a bond with $(s\phi, s'\psi) = (0, 0)$ called a 00-bond is thus 1. We introduce the n-vector $\mathbf{M}$, and the $n \times n$-matrix $\mathbf{T}$ such that $\mathbf{T}\boldsymbol{\Pi}$ is symmetric, see Sec. 2.1.3. They have the non-negative entries

$$M_\phi = e^{-\mu_\phi/\kappa} \quad \text{and} \quad T_{\phi\psi} = T_{\psi+n/2,\phi+n/2} = e^{-C_{\phi\psi}} M_\phi (\boldsymbol{\Pi}\mathbf{M})_\psi, \tag{3.6}$$

corresponding to the Boltzmann weights of a ϕ0-bond and a $\phi\psi$-bond respectively. As for the full chemical potential of a particle (alone on the lattice) with $n = 4$ orientations on the square lattice, or $n = 6$ on the triangular lattice, it reads $\prod_\phi M_\phi$ whatever the orientation. This indeed corresponds to the Boltzmann weight of a particle alone on the lattice, which shows all its orientations to the neighboring empty sites.

3.1.2 Aggregate zoology on the triangular and square lattices

Now that our model for multiple orientations is defined, let us present a non-exhaustive list of different kinds of aggregates that can arise when only a few entries of the matrix $\mathbf{T}$ are non-zero. This corresponds to particles with only a few non-repulsive interactions at low temperature. This allows us to give a concrete representation of what we call finite-size aggregates, fibers and sheets. In the following, we depict finite-size aggregates in shades of blue, fibers in shades of green, and sheets in shades of brown. We first consider particles with $n = 6$ orientations on the triangular lattice. In the base $(\nearrow, \rightarrow, \searrow, \swarrow, \leftarrow, \nwarrow)$ with respect to a horizontal right-oriented link, we rewrite the orientations as $\phi = 1, \dots, 6$ respectively. From the symmetries of the matrix $\mathbf{T}$, it only has $n(n+1)/2 = 21$ independent entries. We see that if $\mathbf{T}$ has only one non-zero independent entry which is on the diagonal (two entries total due to the symmetries of $\mathbf{T}$), written $T_{\phi\phi} = T_{\phi+3,\phi+3}$, then this will tend to generate fibers with the same orientations. However, if only $T_{\phi,\phi+1} \neq 0$, then the aggregates formed are going to have a finite-size and a hexagonal shape. The hexagons which form a circular loop correspond to

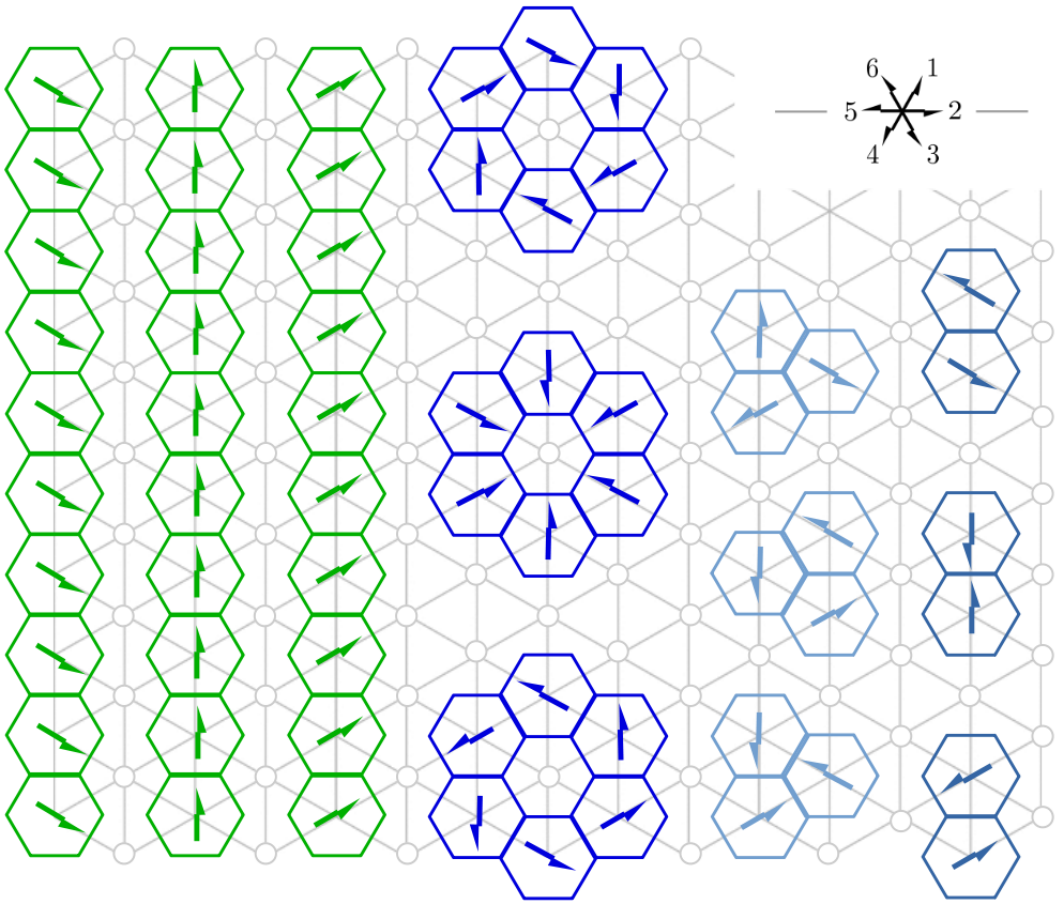

Figure 3.2: **When only one type of interactions is favored on the triangular lattice, the aggregates are only finite-size in shades of blue, or fibers in shades of green.** The orientations with respect to a right-oriented link are given by the clock on the top right. The first green fiber is obtained when only $T_{11}(=T_{44})$ non zero. The top blue hexagon requires $T_{23}=T_{65}>0$, the top teal triangle $T_{62}=T_{53}>0$, and the top dimer $T_{41}>0$. The white dots denote sites that cannot be filled.

what Hagan and Grason (2021) call self-closing [Fig. 1.3]. This is shown in Fig. 3.2, where the fibers are made of green arrows, while the hexagons are made of blue arrows. In the end, the matrix $\mathbf{T}$ (or $\mathbf{C}$) can be represented schematically as

$$\begin{pmatrix} \text{fiber} & \text{hex.} & \text{tri.} & \text{dimer} & \text{tri.} & \text{hex.} \\ \text{hex.} & \text{fiber} & \text{hex.} & \text{tri.} & \text{dimer} & \text{tri.} \\ \text{tri.} & \text{hex.} & \text{fiber} & \text{hex.} & \text{tri.} & \text{dimer} \\ \text{dimer} & \text{tri.} & \text{hex.} & \text{fiber} & \text{hex.} & \text{tri.} \\ \text{tri.} & \text{dimer} & \text{tri.} & \text{hex.} & \text{fiber} & \text{hex.} \\ \text{hex.} & \text{tri.} & \text{dimer} & \text{tri.} & \text{hex.} & \text{fiber} \end{pmatrix}, \tag{3.7}$$

where the color code is the same as in Fig. 3.2. This means that diagonal entries are fiber generators, while non-diagonal entries generate finite-size aggregates: either dimers, triangles (tri.), or hexagons (hex). Indeed, non-diagonal entries of the form $T_{\phi,\phi\pm k}$, $k\geq 1$, when positive, favor changing the orientation by k after each bond. In the case of favorable clustering, the aggregates thus form circular loops of $6/k$ particles, which diverges as it should for $k=0$.

Then, as shown in Fig. 3.3, when two or three of these generators are non-zero, we obtain several aggregate types depending on which orientations are accessible. For instance, two dimer generators of the form $T_{\phi,\phi+3}$ and $T_{\phi+3,\phi}$ generate a (straight) fiber; while $T_{\phi,\phi+3}$ and $T_{\phi+2,\phi-1}$, as well as $T_{\phi,\phi+3}$ and $T_{\phi+4,\phi+1}$ generate snake-like fibers. We also observe fibers of width 2 generated by a fiber generator and two dimer generators, written $T_{\phi\phi}$, $T_{\phi-1,\phi+2}$ and $T_{\phi-2,\phi+1}$. With multiple types of interactions, we often encounter sheets, *i.e.* aggregates that can grow in every direction and can possibly span the

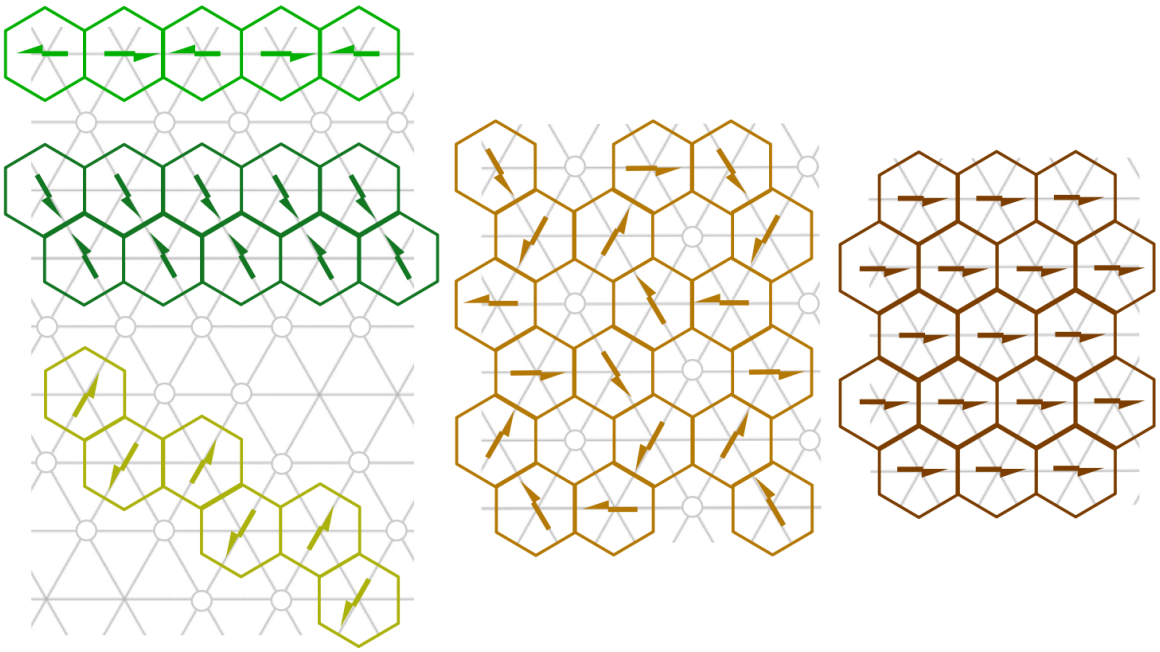

Figure 3.3: **When only a few types of interactions are favored, a great variety of aggregate types emerges, among which sheets shown in shades of brown.** The top green fiber corresponds to $T_{25}, T_{52} > 0$, the middle one with width 2 to $T_{33}, T_{14}, T_{25} > 0$, and the zigzag one on the bottom to $T_{41}, T_{63} > 0$. Then the light brown sheet with holes requires $T_{23}, T_{41} > 0$, while the full sheet on the right needs all diagonal terms positive, i.e. $T_{11}, T_{22}, T_{33} > 0$.

whole lattice. We further make a distinction between full sheets and sheets with holes. Sheets with holes can be formed by association of certain dimer, triangle or hexagon generators. For instance, the holed sheet with light brown orientations of Fig. 3.3 is made from a hexagon and a dimer, which can be written generically as $T_{\phi,\phi+1}$ and $T_{\phi+2,\phi-1}$. Regarding filled sheets, an interesting one is displayed on the right of Fig. 3.3, which requires only the diagonal components. This leads to the formation of what would be Weiss domains of constant orientation in a Potts model (Wu, 1982). Finally, aggregates do not have to display the kind of regularity visible on Fig. 3.2 and 3.3. Some exhibit a single loop (*e.g.* hexagonal) as the base from which branching structures emerge but never reconnect. In this sense, we do not classify them as sheets. They can be formed by association of *e.g.* a hexagon and a fiber written $T_{\phi,\phi+1}$ and $T_{\phi+2,\phi+2}$, or two hexagons written $T_{\phi-1,\phi}$ and $T_{\phi+1,\phi}$.

Second, we consider $n = 4$ orientations on the square lattice, where in the base $(\rightarrow, \downarrow, \leftarrow, \uparrow)$, the matrix $\mathbf{T}$ can be represented schematically as

$$\begin{pmatrix} \text{fiber} & \text{square} & \text{dimer} & \text{square} \\ \text{square} & \text{fiber} & \text{square} & \text{dimer} \\ \text{dimer} & \text{square} & \text{fiber} & \text{square} \\ \text{square} & \text{dimer} & \text{square} & \text{fiber} \end{pmatrix}. \tag{3.8}$$

From the symmetries of the matrix $\mathbf{T}$, it only has 10 independent entries. Compared to the $n = 6$ case, the triangle and hexagon generators have been replaced by square generators for interactions written $T_{\phi,\phi\pm1}$, $\phi = 1, \ldots, 4$. Examples of the zoology in this case are displayed in Fig. 3.4. For multiple favored interactions, we recover fibers of width 2, zigzag fibers, holed sheets and filled sheets, with some differences. For instance, the holed sheet in the middle of Fig. 3.4 has only 1 hole every 5 sites, while the one of Fig. 3.2 on the triangular lattice has $\frac{1}{3}$ of holes. And the simplest filled sheet is made of two squares written $T_{\phi,\phi+1}$ and $T_{\phi+1,\phi}$. As displayed in the right of Fig. 3.4, it has alternating orientations, contrary to the previous Weiss domains. The zoology is thus similar in both lattices. In the next sections, we focus on the triangular lattice, and we come back to the square lattice when we consider next-nearest-neighbor interactions in Sec. 3.4.3.

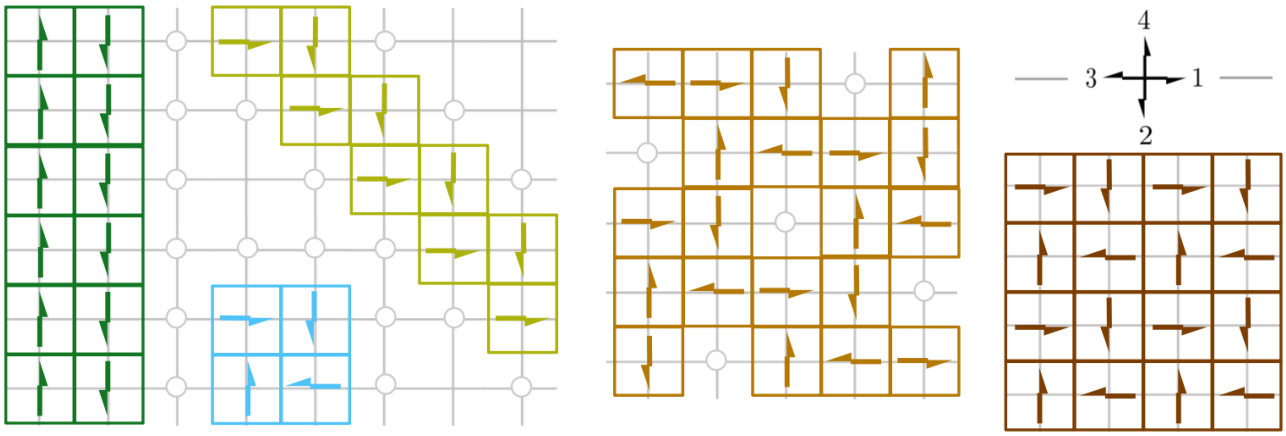

Figure 3.4: **Examples of configurations when only a few types of interactions are favored on the square lattice.** The cyan square corresponds to $T_{12} > 0$, the dark green fiber with width 2 to $T_{11}, T_{24} > 0$, and the zigzag one to $T_{12}, T_{13} > 0$. Then the light brown holed sheet needs $T_{12}, T_{31} > 0$, while the full sheet on the right needs $T_{12}, T_{21} > 0$.

3.1.3 Choosing the right renormalization procedure

Contrary to the 1D study of Ch. 2, there is no easy way to exactly compute the partition function for the 2D Ising model. And we cannot perform transfer matrix calculations to obtain the physical quantities as a function of the parameters (M, T), even for $n = 1$ in the general case (Kramers and Wannier, 1941). We derive the average density $\langle s \rangle$ using a mean-field approximation for $n = 1$ in Sec. 3.3.1, and in simple cases for $n = 4$ or 6 orientations in Sec. 3.3.2. To obtain the average cluster radius $\langle R \rangle$, we then turn to renormalization, and try to recover some of the 1D results. We particularly consider the case of efficient aggregation, *i.e.* $\langle s \rangle$ small and $\langle R \rangle$ large, as characterized in Sec. 2.3. Yet, performing renormalization in 2D requires some creativity since 1D-like procedures fail to account for the properties of 2D systems. Indeed, decimated sites have other decimated sites as nearest neighbors, see Fig. 3.5. Maris and Kadanoff (1978) found that on any 2D lattice with nearest-neighbor interactions, higher order couplings systematically arise in the partition function Z upon renormalization. And it turns out that the approximation which consists in simply neglecting these couplings (which might very well diverge under renormalization) fails to reproduce the experimental and numerical observations close to the critical point. This specifically concerns the critical exponents from the scaling behaviors between relevant quantities such as the correlation length ξ and the temperature difference $|\theta - \theta_c|$ (with the critical temperature θ_c). In the 70s, when Renormalization Group theory was developed, several

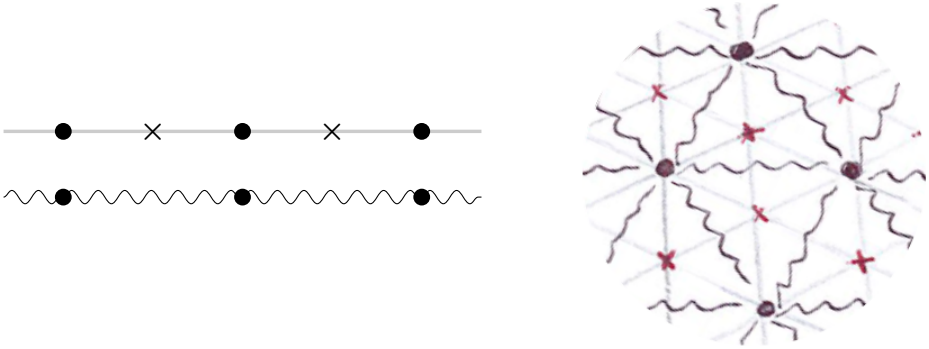

Figure 3.5: **Contrary to the 1D case displayed on the left, in 2D, decimated sites are linked to the rest of the network.** Thus, the plaquette of spins on which the renormalization iteration is computed should be infinite to satisfy the constraint of invariance of the partition function. Here, $\times$-spins are decimated and $\bullet$-spins are kept after one renormalization step. The new links are shown as wavy. The same thing happens on other 2D lattices than the triangular one shown here.

approximate renormalization schemes were introduced such as Kadanoff's well-known bond-moving process (Efrati et al., 2014). Other renormalization schemes, such as those of Niemeijer and van Leeuwen (1973) include majority rules [Fig. 1.10]. Unfortunately, in our case the majority of a collection of orientations is rather tricky to define.

Nevertheless, these approximate schemes were built to study criticality precisely. Namely to give good approximations for the critical temperature and the critical exponents (Sneddon and Barber, 1977). Our objectives here are rather different. Indeed, we are less preoccupied by the exact values of the critical temperature and exponents, than by the fact that there indeed is a phase transition in the system. Moreover, our renormalization scheme must satisfy other physical constraints. For instance, in the case of multiple orientations and when fibers are favorable, we want these fibers to renormalize into the same kind of fibers, yet slightly less favorable. As we will see in the following examples, this condition is generally difficult to satisfy, as some renormalization procedures tend to renormalize fibers into sheets after one step. We further present simple renormalization schemes which attempt to satisfy the aforementioned conditions in Sec. 3.2 and 3.4. In our view, a physically accurate renormalization procedure should display several fixed points in the flow diagram, corresponding to aggregates of different dimensions. Indeed, a fixed point is associated to a certain class of large-scale physics which necessarily depends on the dimension of the typical aggregate formed. Flow trajectories passing close to these fixed points in the parameter space should then correspond to systems displaying similar large-scale characteristics than those at the fixed point.

Concerning sheet-like clusters, they cannot percolate on 2D lattices for average densities $\langle s\rangle < \frac{1}{2}$, contrary to bulk aggregates on 3D lattices (Aizenman et al., 1987). Then when $\langle s\rangle = \frac{1}{2}$, the onset of percolation coincides with the occurrence of long-range order and symmetry breaking at θ_c, corresponding to the point $M = M_c$ on the line $T = 1$ in the Ising model. In the study of clusters, we focus on the low density region, where there is no percolation. It thus makes sense to discuss the behavior of the average cluster radius $\langle R\rangle$. For the Ising model in 1D, we proved that the average cluster length $\langle l\rangle$ behaves as the correlation length ξ of Eq. (2.5). In 2D, we will assume similarly that the average cluster radius $\langle R\rangle$ behaves as ξ, at least in certain relevant cases of efficient aggregation. Assuming that the renormalization iteration is well-defined, after one step $\xi' = \xi/b$ where b is a parameter that depends on the lattice and on the precise type of renormalization. If we keep next-nearest neighbors on the triangular lattice, as in Fig. 3.5, the new lattice spacing is increased of a factor $b = \sqrt{3}$ compared to the old lattice spacing. Similarly, we would obtain $b = \sqrt{2}$ for next-nearest neighbors on the square lattice (since the new links are on the diagonal of a square of old links). Assuming that $\xi^{(k)}$ tends to ~ 1 particle under renormalization, and defining $k_{\rm fp}$ as the number of steps such that $\xi^{(k_{\rm fp})} \sim 1$, this would mean that $\xi^{(0)}$ and thus $\langle R\rangle$ would behave as $b^{k_{\rm fp}}$ for efficient aggregation. Additionally, as $\langle R\rangle$ is related to the two-point correlation function, we believe that quantities such as the aspect ratio of aggregates could be obtained via *e.g.* three-point correlations. However, it is still unsure whether such higher-order correlations can ever be obtained by the kind of renormalization that we perform here.

3.2 A simple renormalization scheme in 2D

Let us start with the simplest renormalization scheme on the triangular lattice that we can think of, represented in Fig. 3.6, *left*. At each step, we keep only the next-nearest neighboring nodes indicated with bullets, and we decimate all their nearest neighbors labeled with red crosses. New links are black and wavy, while old links are gray. In doing so, after one renormalization step, we recover a triangular lattice, yet rotated by $\pi/6$. Therefore, particles are rotated as well, so as to keep the definition of orientation with respect to the direction of the link. In this simple procedure, we split the decimated sites into three independent ghost copies [Fig. 3.6, *middle*], which overestimates their entropies. We simultaneously split their links with non-decimated sites into two. We find that a phase transition requires non-split links to have double strength. These double couplings approximately compensate the entropy excess of the decimated sites, such that the overall free energy is better estimated. Then, the basis element upon which we implement the renormalization is a diamond plaquette (Kadanoff, 1976) containing two decimated sites [Fig. 3.6, *right*], which interact only inside

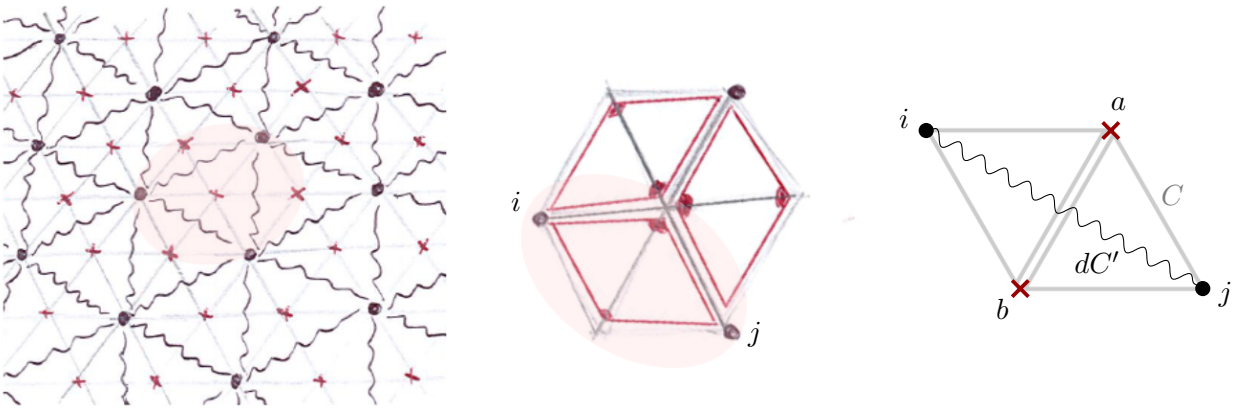

Figure 3.6: **Decimation of $\frac{2}{3}$ of the spins on the triangular lattice.** The spins at the red and/or crossed sites are decimated, while the black ones are kept. *Left*, the next-nearest neighbors kept after decimation are connected two-by-two by diamond plaquettes. *Middle*, three diamond plaquettes are delimited by red edges. The decimated spins are split into three ghost copies interacting only inside one diamond. Concomitantly, the gray edges linking decimated sites with kept ones are split into two red edges. These red edges are attributed half the strength of gray edges. *Right*, a detailed diamond, where the link between sites a and b has double strength. Additionally, the new wavy link between sites i and j has strength d.

the diamond. In all that follows, the lattice coordination is $\kappa = 6$. We begin in Sec. 3.2.1 by presenting the renormalization formula associated to the diamond plaquette in the Ising model. Although this procedure is approximate, we are able to recover many physical features including the exact value of the critical temperature. Then, Sec. 3.2.2 contains the renormalization study of particular relevant cases for $n = 6$ orientations. Unfortunately, we find that this procedure does not recover the expected renormalization dynamics of certain fibers and sheets.

3.2.1 Approximate renormalization for the Ising model

We first consider the Ising model on the triangular lattice. In the renormalization scheme displayed in Fig. 3.6, due to the symmetries of the lattice and the diamond plaquette, there is only one parameter to be tuned. It is defined as the strength increase d attributed to the new wavy link compared to the old gray links, such that the Boltzmann weights for the link between sites i and j are thus $(1')^d$, $(M')^d$ and $(T')^d$. We choose the parameter d in order to recover the exact value of the attractive (*i.e.* $C < 0$) critical coupling: $C_c = -\mu_c/3 = -\ln 3$ from Eq. (3.3). In terms of the variables $M = e^{-\mu/6}$ and $T = e^{-C-\mu/3}$, the attractive critical point reads

$$T_c = 1 \quad \text{and} \quad M_c = 1/\sqrt{3}. \tag{3.9}$$

We now translate the renormalization scheme with diamond plaquettes in terms of the transfer matrix $\mathscr{T}$, as we did in 1D in Sec. 2.2. In order to see the indices better, we introduce the notation

$$\mathscr{T}(s,s') = \mathscr{T}_{s,s'}, \quad \text{such that} \quad \mathscr{T}(0,0) = 1, \quad \mathscr{T}(1,0) = \mathscr{T}(0,1) = M \quad \text{and} \quad \mathscr{T}(1,1) = T. \tag{3.10}$$

In 1D, we had the renormalization formula $A\mathscr{T}' = \mathscr{T}^2$ corresponding to one new link replacing two old ones [Fig. 2.2]. Similarly, for the diamond procedure of Fig. 3.6, *right*, the renormalization formula reads

$$A(\mathscr{T}')^d(s_i,s_j) = \sum_{s_a,s_b} \mathscr{T}(s_i,s_a)\,\mathscr{T}(s_i,s_b)\,\mathscr{T}^2(s_a,s_b)\,\mathscr{T}(s_a,s_j)\,\mathscr{T}(s_b,s_j), \tag{3.11}$$

where we sum over the values of the decimated spins at sites a, b. Here, the link between a and b has double strength, such that $\mathscr{T}(s_a,s_b)$ is squared. This is such that the weight of, *e.g.*, a new 00-bond is the sum of the weights of the configurations $(i,j,a,b) = (0000)$, (0010), (0001), and (0011). This yields

$A(1')^d = 1 + M^4 + M^4 + M^4T^2$. Choosing A such that $1' = 1$, the iteration is written

$$(M')^d = M^2 \frac{1 + 2M^2T + T^4}{1 + M^4(2 + T^2)}, \quad (T')^d = \frac{M^4(1 + 2T^2) + T^6}{1 + M^4(2 + T^2)}. \tag{3.12}$$

We can simplify Eq. (3.12) in at least three special cases:

$$\text{for} \quad M = 0, \qquad M' = 0, \quad T' = T^{6/d}, \tag{3.13a}$$

$$\text{for} \quad T = 1, \qquad (M')^d = M^2 \frac{2 + 2M^2}{1 + 3M^4}, \quad T' = 1, \tag{3.13b}$$

$$\text{for} \quad T = M^2, \qquad (M')^d = M^2, \quad T' = (M')^2. \tag{3.13c}$$

To enforce that $(M = 1/\sqrt{3},\ T = 1)$ be a fixed point, we set $d = \ln \frac{9}{4} / \ln 3$, which is close to 0.74. The curve $T = M^2$ corresponds once again to the hard sphere gas (*i.e.* $C = 0$), although it does not constitute a curve of fixed points. Indeed on this curve, $M' = M^{2/d}$ which is different from M. Yet, this curve together with the lines $M = 0$ and $T = 1$, are stable under renormalization. Analytically studying the fixed points of Eq. (3.12), such that $M' = M$ and $T' = T$, is challenging. We thus turn to numerical analysis, and we seem to find that the fixed points are all on the aforementioned stable curves. The fixed points, along with their basins of attraction and linear stabilities are as follows:

- $(M = 1/\sqrt{3},\ T = 1)$ is the attractive critical fixed point, and is fully unstable.
- $(M > 1/\sqrt{3},\ T = 1)$ fall into the M-stable and T-unstable fixed point $(1, 1)$.
- $(M < 1/\sqrt{3},\ T = 1)$ fall into the M-stable and T-unstable fixed point $(0, 1)$.
- $(M = 0,\ T < 1)$, and more generally $T < 1$ fall into $(0, 0)$, which is stable and non-interacting.
- $(M = 0,\ T > 1)$ fall into the M-unstable fixed point $(0, \infty)$.
- $(M > 0,\ T > 1)$ fall into the stable fixed point (∞, ∞) which is non-interacting.

The fixed points that are M-stable and T-unstable are further called hyperbolic. All of this is shown in the flow diagram of Fig. 3.7, *left*, which greatly resembles the 1D one of Fig. 2.3.

Upon studying the dynamics, we recover additional results. First, writing $T = xM^2$ where $x = e^{-C}$, we find that

$$(x')^d - 1 = M^4(x - 1)^2 \frac{2 + 2M^8x^4 + M^4x^2(1 + x)^2}{(1 + 2M^4x + M^8x^4)^2}, \tag{3.14}$$

which is always positive, leading to $x' \geq 1$. This means that interactions are always attractive from the first step on: $C^{(>0)} \leq 0$. It is still unclear whether repulsive interactions should physically renormalize directly into attractive interactions. This is because even the ground state configurations of the antiferromagnetic Ising model ($C = -\mu/3 > 0$) on the triangular lattice are rather difficult to study. This system indeed possesses a finite entropy at vanishing temperature, such that on an infinite lattice, there are infinitely many types of arrangements with the ground state energy (Wannier, 1950), see Fig. 3.8. When second neighbors are kept upon decimation, it is thus hard to say whether their interactions are rather ferromagnetic or anti-ferromagnetic. Besides, it is worth noticing that the iteration in Eq. (3.12) does not exactly recover the repulsive critical point $(\infty, 1)$ as a fixed point. Yet, for $T = 1$, as $M \to \infty$, $M' \sim (\frac{2}{3})^d \sim 1/\sqrt{3}$, *i.e.* the repulsive critical point is directly mapped to the attractive critical point, which makes it almost a fixed point. Anyway, it may not matter for us, since we are more interested in the dynamics from attractive initial conditions leading to aggregation, which remain attractive when renormalized.

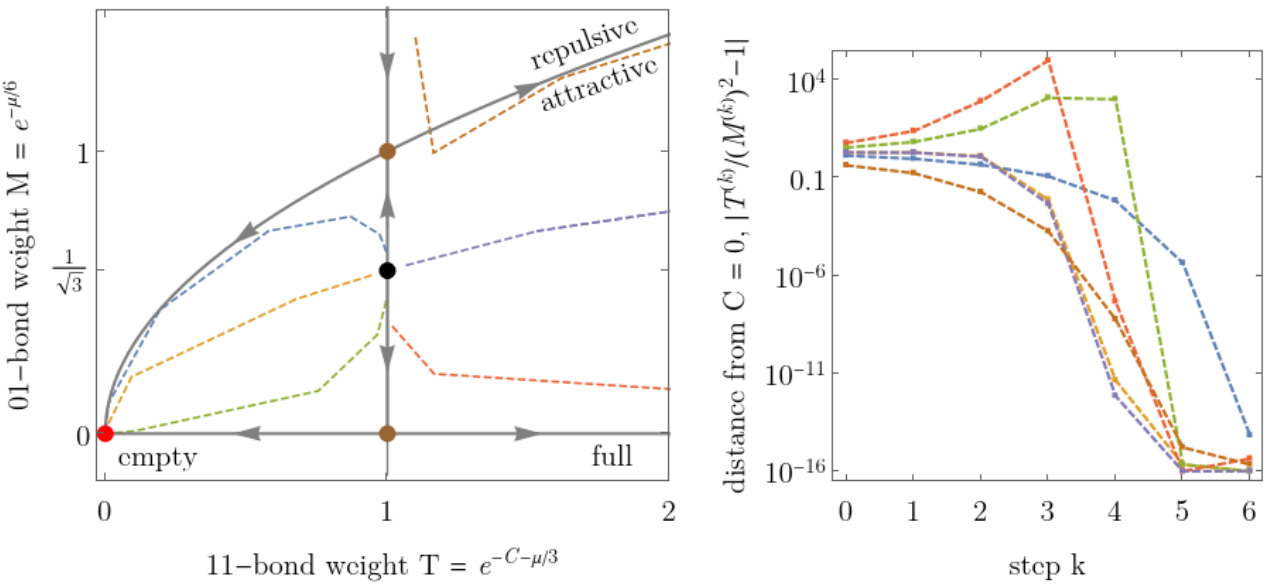

Figure 3.7: **Most trajectories renormalize to one of the two non-interacting fixed points.** *Left*, flow diagram for the 2D Ising model, where the colored dashed trajectories are numerically computed from the iteration of Eq. (3.12). Red, brown and black points correspond to stable, hyperbolic and unstable/critical fixed points respectively. The gray curves are stable under renormalization. We find that the longest trajectories begin close to the critical point ($M_c = \frac{1}{\sqrt{3}} \approx 0.58,\ T = 1$). The blue and green trajectories begin very close but not on the $T = 1$ line. Before looking at the precise values of the average density $\langle s \rangle$, we can surely say that on the $M = 0$ line, $T < 1$ (> 1) corresponds to an empty (full) system. *Right*, all the trajectories shown on the flow diagram seem to renormalize to the gas curve $T = M^2$, *i.e.* $C = 0$. The ordinate axis is in log-scale and extends to the machine precision: 10^{-16}. In the red trajectory, the huge jump from nearly 10^5 to $10^{-}7$ could unfortunately be due to precision mistakes.

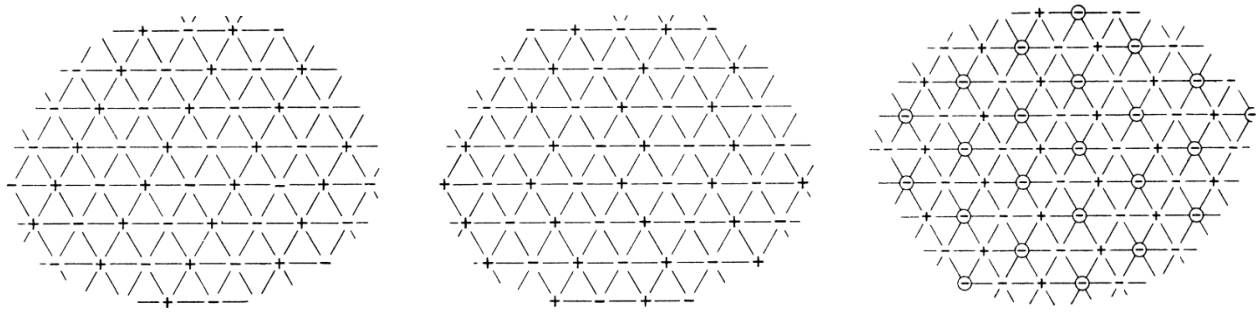

Figure 3.8: **Ground state anti-ferromagnetic configurations ($\sigma_i = \pm 1$) from** Wannier (1950)**.** The antiferromagnetic Ising model on the triangular lattice is peculiar since it can never satisfy all links. This frustration leads to a finite entropy at vanishing temperature, such that on an infinite lattice, there are infinitely many ground states. *Left*, a particular regular arrangement where the second-neighbor interactions seem one-third ferromagnetic-like ($++$ or $--$) and two-third anti-ferromagnetic-like ($+-$), while the third-neighbor interactions look ferromagnetic-like. *Middle*, an irregular arrangement. *Right*, more generally, configurations can look like this one where the circled spins can take any value. The second-neighbor interactions seem one-sixth ferromagnetic-like and five-sixth anti-ferromagnetic-like, while the third-neighbor interactions look one-third ferromagnetic-like and two-third anti-ferromagnetic like.

Second, we find that the regions $T < 1$ and $T > 1$ are dynamically separated, such that there is no renormalization dynamics that can go from one to the other. Indeed,

$$\frac{(T')^d - 1}{T - 1} = (T+1)\frac{1 + M^4 + T^2 + T^4}{1 + M^4(2 + T^2)} > 0, \quad \text{since} \quad M, T > 0, \tag{3.15}$$

i.e. if $T < 1$, then $T' < 1$ and vice versa. Third, by numerically analyzing 100 initial conditions (M, T), we find that outside of the lines $M = 0$ and $T = 1$, the only fixed points are non interacting: $C_* = 0$. Indeed, as shown in Fig. 3.7, *right*, the quantities $T^{(k)}/(M^{(k)})^2 = (e^{-C})^{(k)} \to 1$. This happens even for the red trajectory contrary to what Fig. 3.7, *left* may indicate. However, this could be wrong since the numerical calculations tend to involve products of a very big number and a very small number, such that precision mistakes could be made. On the $T = 1$ line, in the attractive region $M \leq 1$, we recover the three typical fixed points corresponding to the infinite-temperature disordered system $M = 1$, the zero-temperature ordered one $M = 0$ (either completely empty or full), and the order-disorder transition $M = M_c$.

Since this renormalization is approximate, some of the results above could be non-physical. However, in varying the strengths of the links in the diamond of Fig. 3.6, *right*, we find that, *e.g.*, the fact that the line $T = M^2$ is not made of fixed points is tightly linked to the presence of a phase transition. Moreover, the other renormalization procedure that we investigate in Sec. 3.4.1 recovers many of the above dynamical properties in the flow diagram.

3.2.2 Renormalization for $n = 6$ orientations

We now consider particles with $n = 6$ orientations in the coupling matrix formalism of Sec. 2.1.1. We define the Boltzmann weights of a bond with spins times orientations $s\phi, s'\psi$ as $\mathscr{T}[s\phi, s'\psi] = \mathscr{T}_{s\phi,s'\psi}$, where $\mathscr{T}$ is the transfer matrix defined in Sec. 2.1.3. All links are thus still invariant under rotation of π:

$$\mathscr{T}\big[s\phi, s'\psi\big] = \mathscr{T}\big[s'(\psi+3), s(\phi+3)\big], \quad \phi, \psi = 1, \dots, 6 \tag{3.16}$$

where the orientations are defined modulo 6. Since the wavy link is not aligned with any of the gray links in Fig. 3.9, *left*, renormalized orientations are turned by $\pi/6$ in the clockwise direction. Similarly as in Eq. (3.11), the renormalization formula reads

$$\begin{aligned} A(\mathscr{T}')^c\big[s_i\phi_i, s_j\phi_j\big] = \sum_{a,b} \mathscr{T}\big[s_i\phi_i, s_a\phi_a\big]\, \mathscr{T}\big[s_i(\phi_i - 1), s_b(\phi_b - 1)\big]\, \mathscr{T}^2\big[s_a(\phi_a - 2), s_b(\phi_b - 2)\big] \\ \times\, \mathscr{T}\big[s_a(\phi_a - 1), s_j(\phi_j - 1)\big]\, \mathscr{T}\big[s_b\phi_b, s_j\phi_j\big], \end{aligned} \tag{3.17}$$

where the renormalized links keep the symmetries, *i.e.* satisfy Eq. (3.16). This leads to cumbersome iteration formulae for $\mathbf{M}'$ and $\mathbf{T}'$, given in full in Appendix 3.6. They are comparable with their $n = 1$

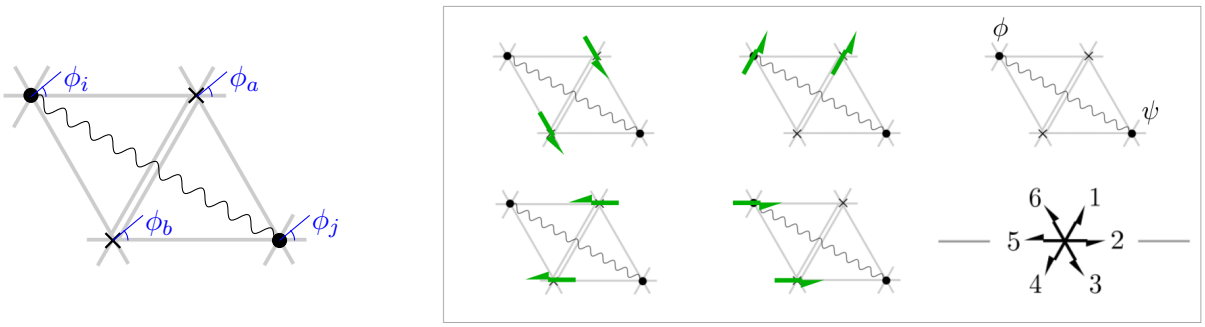

Figure 3.9: **Diamond renormalization procedure for multiple orientations.** *Left*, a diamond plaquette with the scalar orientations predefined with respect to a horizontal right-oriented link. *Right*, sketched renormalization of a fiber with the diamond procedure. The new orientations at the non-decimated sites are rotated, so that they correspond to the same numbers than the old ones.

counterparts, but involve the summation of four tensor entries at a time on multiple occasions. For instance, $A(1')^d$ contains a term that reads

$$\sum_{\chi} M_{\chi-3} M_{\chi-2}^2 M_{\chi-1}, \tag{3.18}$$

coming from the summation of the Boltzmann weights of configurations where the spins times orientations of sites (i,j,a,b) are $(0,0,\chi,0)$. These are not like scalar products such as *e.g.* $\sum_\chi M_{\chi-3}M_{\chi-2}$. This makes the analytical study of these iterations very challenging. In particular, we find that the fixed points are hard to obtain in the general case. If we cannot calculate the fixed points for all matrices $\mathbf{T}$, then renormalization cannot give us a criterion to distinguish between finite-size aggregates, fibers, sheets, based on them having hypothetically different critical fixed points.

We thus take a different approach, where instead of studying the general iteration formula, we consider simple cases where only a few entries of $\mathbf{T}^{(0)} = \mathbf{T}$ are non-zero and all set to a, and $\mathbf{M}^{(0)} = m\mathbf{1}$ for simplicity. We consider the regime of very attractive interactions where $a \gg m^2$. From step zero to one, the iteration thus takes the still complicated form

$$A = 1 + 12m^4 + m^4 \sum_{\chi,\omega} T_{\chi\omega}^2, \tag{3.19a}$$

$$A \left(M_\phi^{(1)}\right)^d = m^2 + m^4 \sum_{\chi} (T_{\phi\chi} + T_{\phi-1,\chi}) + m^2 \sum_{\chi,\,\omega} T_{\phi\chi} T_{\phi-1,\omega-1} T_{\chi-2,\omega-2}^2, \tag{3.19b}$$

$$\begin{aligned} A \left(T_{\phi\psi}^{(1)}\right)^d &= m^4 + m^4 \sum_{\chi} (T_{\phi\chi} T_{\chi-1,\psi-1} + T_{\phi-1,\chi-1} T_{\chi\psi}) \\ &\quad + \sum_{\chi,\,\omega} T_{\phi\chi} T_{\phi-1,\omega-1} T_{\chi-2,\omega-2}^2 T_{\chi-1,\psi-1} T_{\omega\psi}. \end{aligned} \tag{3.19c}$$

This form is not stable under renormalization, but it can help us visualize renormalization on simple examples. For instance, in our idea of renormalization, large fibers with width 1 must renormalize into fibers with the same width and a smaller average length.

- Let $T_{11} = T_{44} = a$ be the only non-zero entries, such that aggregates are only fibers. The most favorable configurations on a diamond plaquette are shown with sketches in Fig. 3.9, *right*. At the first renormalization step, all entries of $\mathbf{T}^{(1)}$ are the same: $A(T_{\phi\psi}^{(1)})^d = m^4$. We thus lose the directionality of the aggregates, such that these fibers are not stable under renormalization: they become a gas. This is because the sites i,a,j or i,b,j are not aligned and prevent a straight fiber to remain fibrous under renormalization. Likewise for the other fibers with $T_{\phi\phi}$ or the ones with $T_{\phi,\phi+3}$ and $T_{\phi+3,\phi}$. We can perform the same study for the other kind of aggregates in Fig. 3.3.

- Let us study another example, namely the zigzag fiber where the non-zero entries are $T_{41}, T_{63} = a$. After one step, we obtain

$$A \left(T_{\phi\psi}^{(1)}\right)^d = \begin{cases} m^4 + a^2 m^4, & \text{for} \quad (\phi,\psi) = (1,1),(4,4) \\ m^4, & \text{for the others} \end{cases} \tag{3.20}$$

  such that the most favorable aggregates are now straight fibers. This is in agreement with our idea of renormalization.

- Likewise, the fiber with width 2 with $T_{33}, T_{66}, T_{14}, T_{25} = a$ renormalizes into a zigzag fiber (of width 1), where

$$A \left(T_{\phi\psi}^{(1)}\right)^d = \begin{cases} m^4 + 2a^2 m^4 + a^6, & \text{for} \quad (\phi,\psi) = (2,5),(3,6) \\ m^4, & \text{for the others} \end{cases} \tag{3.21}$$

- The dimers and the triangles renormalize into a gas: $A(T_{\phi\psi}^{(1)})^d = m^4$.

- The hexagons renormalize into triangles: $T_{43}, T_{16} = a$ leads to $A(T^{(1)}_{53})^d = A(T^{(1)}_{62})^d = m^4 + a^2 m^4$, while the other $A(T^{(1)}_{\phi\psi})^d = m^4$.

- The holed sheet with $T_{41}, T_{56}, T_{32} = a$ renormalizes into three kinds of triangles: $A(T^{(1)}_{13})^d = A(T^{(1)}_{26})^d = A(T^{(1)}_{35})^d = m^4 + a^2 m^4$, while the other $A(T^{(1)}_{\phi\psi})^d = m^4$. This leads to the formation of fibers.

- The full sheet with identical orientations $\forall \phi,\ T_{\phi\phi} = a$ is kept under renormalization, such that $\forall \phi,\ A(T^{(1)}_{\phi\phi})^d = m^4 + 2a^2 m^4 + a^6$, while the other $A(T^{(1)}_{\phi\psi})^d = m^4,\ \phi \neq \psi$.

In the end, after one step, all entries of $\mathbf{T}^{(1)}$ are non-zero. But assuming that m is rather small and a rather large, the directionality/dimension of the aggregate is kept in a number of cases. We will discuss particular regimes of m and a, and focus on efficient aggregation in Sec. 3.3. Still, straight fibers and the holed sheet of Fig. 3.3 do not renormalize as planned. The dimension of their most favorable aggregate decreases after one renormalization step. This is because the diamond plaquette contains only a small number of spins and thus cannot take into account large patterns. This leads us to consider a larger hexagonal plaquette in Sec. 3.4.1, and next-nearest neighbor interactions in Sec. 3.4.3. When a good renormalization procedure that verifies all expected renormalization behaviors is found, the study should proceed as follows. On the previous relevant cases, we should first determine which initial condition go to the trivial fixed points, namely $(\mathbf{M}, \mathbf{T}) = (\mathbf{0}, \mathbf{0})$ and $\{M_\phi \to \infty,\ T_{\phi\psi} \to \infty,\ \phi, \psi = 1, \ldots, 6\}$. It is possible that some fixed points contain both zeros and infinite entries in $\mathbf{M}$ and $\mathbf{T}$. These could be problematic, since precision mistakes (*e.g.* from multiplying a very big number with a very small one) could then skew the numerical analyses. Second, we should look for the regions where the number of steps to renormalize to one of the aforementioned fixed points k_{fp} diverges. These should be in the proximity of nontrivial fixed points, characteristic of phase transitions and hypothetically corresponding to aggregates of different dimensions.

3.3 Efficient aggregation in 2D

We now investigate the cases of bounded aggregation, and we discuss obtaining the average density $\langle s \rangle$ and the average aggregate radius $\langle R \rangle$ in the regime of efficient aggregation. In 1D, we made a distinction between bounded and unbounded aggregation, as to whether an aggregate can fill the chain. We specifically showed that the bounded case corresponds to $T = 0$ for $n = 1$, and all eigenvalues of $\mathbf{T}$ zero for $n > 1$. In 2D, the distinction remains for $n = 1$, where aggregates of $l \geq 2$ particles absolutely require $T > 0$. But there does not seem to be such an easy distinction for multiple orientations in 2D. We further consider particular cases where only a small number of entries of $\mathbf{T}$ have the value a, while all others have the value $\epsilon a \ll a$, corresponding to favored and unfavored interactions respectively. We find that having all eigenvalues that vanish when $\epsilon \to 0$ does not coincide with being able to form only finite-size aggregates. Given a non-negative matrix, an extension of the Perron-Frobenius theorem states that its largest eigenvalue is also non-negative (Meyer, 2000). Looking at the aggregates displayed in Fig. 3.2 and 3.3, the largest eigenvalues t_1 of the associated matrices $\mathbf{T}$ are as follows. As expected, the straight fibers of width one and two, and the filled sheet all have t_1/a of zeroth order in ϵ; whereas the dimers, the triangles and the hexagons have $t_1/a = \mathcal{O}(\sqrt{\epsilon})$, which goes to zero when $\epsilon \to 0$. However, the zigzag fiber and the holed sheet of Fig. 3.3 also have $t_1/a = \mathcal{O}(\sqrt{\epsilon})$. It thus appears difficult to distinguish aggregates of different dimensions by looking only at the eigenvalues of their coupling matrices. In particular as $\epsilon \to 0$, the nilpotent matrices with all eigenvalues zero are rather tricky to characterize. An idea would be to look at the eigenvalues of the symmetric matrix $\mathbf{T\Pi}$ (see Sec. 2.1), which cannot all be zero if some entries of $\mathbf{T}$ are non-zero.

In the end, this difficulty in determining the aggregate from the shape of matrix $\mathbf{T}$ justifies using the Renormalization Group approach that we have been developing. Moreover, in 2D the distinction between *e.g.* fibers and sheets could come from frustration as in the example of Fig. 1.9, instead of just the absence of matches for some sides of the particles, which was the only reason for dimensional reduction in 1D. We hereafter focus on the efficient aggregation regime in the $n = 1$ case in Sec. 3.3.1.

As in 1D, this regime corresponds to the region of attractive interactions with M small and $T < 1$, situated at the near left of the critical point in the (M, T)-space. We then consider approximate expressions for the average density $\langle s \rangle$ in simple cases for $n = 6$ in Sec. 3.3.2. We finally discuss in Sec. 3.3.3 whether the efficient aggregation regime can be stable under renormalization, such that very long fibers would remain long after one step.

3.3.1 Efficient aggregation for $n = 1$

Since the partition function Z is not conserved upon renormalization, the average density $\langle s \rangle$ has no *a priori* reason to be constant under renormalization, and we can no longer use the fixed point parameters (M_*, T_*) to compute $\langle s \rangle^{(0)}$. We hereby consider the mean-field approximation and obtain a self-consistent equation for $\langle s \rangle$, from the Curie-Weiss equation for the magnetization m of spin-$\frac{1}{2}$ variables $\sigma_i = \pm 1$. To render the equation for $\langle s \rangle$ consistent with our flow diagram, we input the real value of the critical temperature instead of the mean-field approximated one. Details are given in Appendix 3.5.2. We thus obtain $\langle s \rangle$ in terms of the parameters (M, T) as

$$M = M_c^{\frac{\operatorname{acrth} m}{m}} \, T^{\frac{1}{2} - \frac{\kappa \ln M_c}{4m}}, \quad \text{where} \quad m = 2\langle s \rangle - 1. \tag{3.22}$$

This yields the curves at constant average density in the flow diagram of Fig. 3.10, *left*. Since we do not consider varying M and T dynamically, we do not take hysteresis effects into account, such that $\operatorname{sgn}(T-1) = \operatorname{sgn}(\langle s \rangle - \frac{1}{2})$. This mean-field equation gives only an indication of the value of $\langle s \rangle$. For instance, it is not valid on the line $T = 0$, where Eq. (3.22) yields $\langle s \rangle = 0$ whatever M, while $\langle s \rangle$ should tend to $\frac{1}{3}$ for $M \to \infty$. As in 1D, the low density region is found at the bottom left of the plot. But close to the line $M = 0$, $\langle s \rangle$ takes more extreme values in 2D than it did in 1D [Fig. 2.4, *left*]. It is indeed closer to 0 for $T < 1$, or 1 for $T > 1$. This is because particles or aggregates need more 01-bonds in 2D, i.e. more M. Besides, by comparing Fig. 3.10, *left* with Fig. 3.7, we see that $\langle s \rangle$ is not constant under renormalization. It either decreases from an initial condition with $\langle s \rangle^{(0)} < \frac{1}{2}$, or increases if $\langle s \rangle^{(0)} > \frac{1}{2}$. It is still unclear whether this is a physically accurate renormalization behavior, or if it is due to the approximation used to derive the renormalization formula. This is such that the non-interacting fixed points $C_* = 0$, $\mu_* = \pm\infty$ correspond to empty and full systems respectively.

We now study the dynamics under renormalization $(M^{(k)}, T^{(k)})$ in the low density region $\langle s \rangle \lesssim 0.1$ and we look for large aggregates, such that the aggregation is efficient. Following the 1D study, these

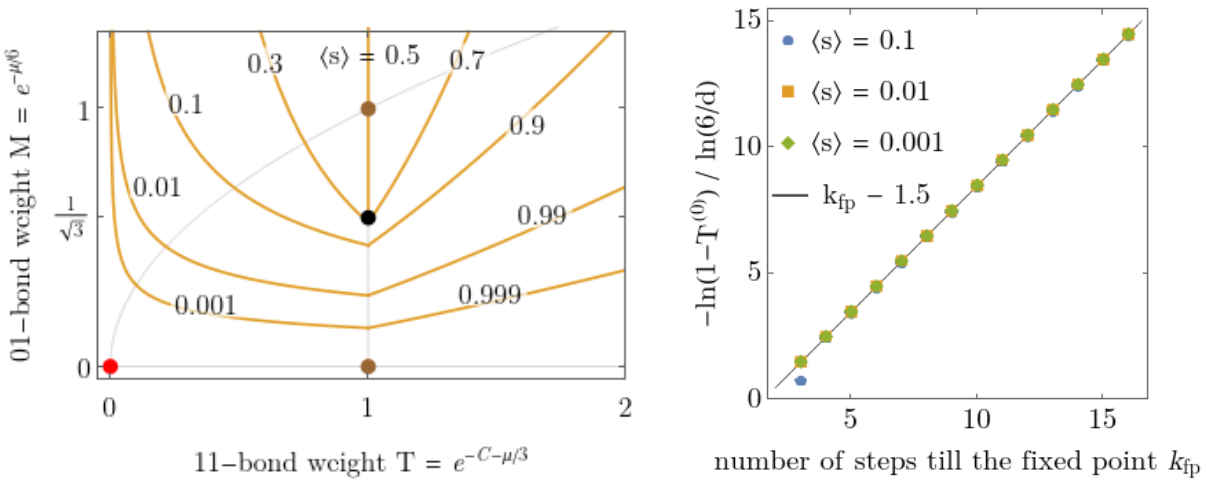

Figure 3.10: **For efficient aggregation in 2D, k_{fp} decreases logarithmically with the distance from the $T = 1$ line.** *Left*, approximate contour plot of the average density $\langle s \rangle$, from the mean-field equation (3.22). On the line $T = 1$ below $M_c = \frac{1}{\sqrt{3}}$, $\langle s \rangle$ is bi-valued. *Right*, $1/(1 - T^{(0)})$ versus k_{fp} obtained by numerical analysis of the iteration in Eq. (3.12) for constant low density. Taking the log in base $6/d$, where $d = \ln \frac{9}{4} / \ln 3$, the fit calculated for $k_{\mathrm{fp}} \gtrsim 4$ has a slope 1. Here the data points are such that $T^{(k_{\mathrm{fp}}(\epsilon))} \approx \epsilon = 10^{-10}$, which gives a 2% error bar for ordinates.

should take a large number of steps to reach the fixed point $(M_* = 0, T_* = 0)$ by ϵ. Naming this number k_{fp}, we define it as

$$T^{(k_{\text{fp}}(\epsilon))} \sim \epsilon, \tag{3.23}$$

since M moves noticeably at the beginning, see the blue trajectory in Fig. 3.7, *left*. We then choose $\epsilon = 10^{-10}$, set $M^{(0)}$ such that $\langle s \rangle$ is constant and small, and numerically compute k_{fp} for $T^{(0)} \in [0, 1)$. As shown in Fig. 3.10, *right*, we find a very reliable relationship written

$$\text{for } k_{\text{fp}} \gtrsim 4, \quad \frac{1}{1 - T^{(0)}} \approx \left(\frac{6}{d}\right)^{k_{\text{fp}} - \beta_2}, \quad \text{where} \quad \frac{6}{d} \approx 8.13 \tag{3.24}$$

where β_2 depends only on the value of ϵ. This means that the dynamics slows down close to the line $T = 1$ below the critical point $(M_c, 1)$, such that large values of k_{fp} coincide with values of $T^{(0)}$ close to 1. We then assume that for efficient aggregation, *i.e.* close to $T = 1^-$ and for $M < M_c$, the typical cluster radius behaves as the correlation length: $\langle R \rangle \sim \xi$, which decays under renormalization as $\xi' = \xi/\sqrt{3}$, see Sec. 3.1.3. Thus, the initial average cluster radius depends exponentially on the number of steps to reach the fixed point $\langle R \rangle^{(0)} \sim \sqrt{3}^{k_{\text{fp}}}$ and

$$\langle R \rangle \sim \frac{1}{(1 - T)^\gamma}, \quad \text{where} \quad \gamma = \frac{\ln \sqrt{3}}{\ln 6/d} \approx 0.26. \tag{3.25}$$

This expression is similar to the 1D expression, except that $\gamma = 1$ in 1D, see Sec. 2.3.2. However, γ appears highly dependent on the precise formulation of the renormalization iteration, such that Eq. (3.25) should be taken with care. Actually, comparing the aforementioned theoretical expression with actual values of $\langle R \rangle$ obtained by *e.g.* Monte Carlo self-assembly simulations could give us an appreciation for the validity of the renormalization procedure. If it turns out that the numerical value of γ is different from the one above, we could perhaps change the value of d such that the theoretical and numerical values of γ match. This is left for future work.

Moreover, we can recover the exponential increase of $1 - T^{(0)}$ with respect to k_{fp}, *i.e.* the exponential decrease of the average aggregate radius under renormalization due to decimation, by approximating the dynamics as we did in 1D. From an initial condition such that $1 - T^{(0)} \ll 1$, then at the beginning and at lowest order, Eq. (3.12) reduces to

$$(M')^d = 2M^2 \frac{1 + M^2}{1 + 3M^4} + \mathcal{O}(1 - T), \quad 1 - T' = \frac{2}{d} \frac{3 + M^4}{1 + 3M^4}(1 - T) + \mathcal{O}\big((1 - T)^2\big) \tag{3.26}$$

where M is at least below $M_c \approx 0.58$, so can be considered small. We see that starting from $M^{(0)} \ll 1$, the $M^{(k)}$ vanish as $M' \sim 2M^{2/d}$, such that at lowest order in h and M, Eq. (3.26) yields $1 - T' \sim (1 - T)6/d$. Finally, since $1 - T_* \approx 1 - \epsilon$, we recover the exponential behavior in Eq. (3.24):

$$1 - T^{(0)} \sim (6/d)^{-k_{\text{fp}}}. \tag{3.27}$$

In the end, we have obtained $\langle s \rangle$ by a self-consistency trick, and $\langle R \rangle$ via numerical analysis of the dynamics under renormalization.

3.3.2 Average density in simple cases of irregular particles

In 1D, we found a unique scalar relationship between the initial condition $(\mathbf{M}^{(0)}, \mathbf{T}^{(0)})$ that corresponds to having a constant low density. As displayed in Eq. (2.42), it involves only the largest eigenvalue t_1 of matrix $\mathbf{T}$ and $q = \mathbf{M}^\mathsf{T} \mathbf{\Pi} \mathbf{M}$. We have had some difficulty to find a similar relationship in 2D. For instance, using only the largest eigenvalue of matrix $\mathbf{T}$ is not possible since it does not take similar values for straight fibers and zigzag fibers. Thus, since computing the average density $\langle s \rangle$ looks pretty difficult in the general case, we hereby attempt to compute $\langle s \rangle$ when only a few types of interactions are favored. We specifically distinguish between the cases where rather finite-size aggregates, fibers or sheets are formed. In all that follows, we set all chemical potentials to the same value, such that $\mathbf{M} = m\mathbf{1}$. We first consider the case where only one kind of dimers is allowed on

the triangular lattice, such that the only non-zero entry is of the form $T_{\phi,\phi+3}$. Then, for a lattice with an infinite number of sites: $N \to \infty$, and considering very attractive interactions: $T_{14} \gg m^2$, *i.e.* $-C_{14} \gg 1$, the system acts as a gas of dimers. For $\langle s \rangle \sim 1$, there are some "excluded volume" interactions, but for low density: $\langle s \rangle \ll 1$, the dimers do not interact, such that

$$\langle s \rangle \sim 6m^{10}\, T_{\phi,\phi+3}, \tag{3.28}$$

see Fig. 3.2. We likewise obtain the average density, in the non-interacting limit, of triangles as $\langle s \rangle \sim 6m^{12}\, T^3_{\phi,\phi+2}$, and of hexagons as $\langle s \rangle \sim 6m^{24}\, T^6_{\phi,\phi+1}$.

Finding $\langle s \rangle$ becomes a bit trickier in the case of fibers. We introduce $\widetilde{M}$ and $\widetilde{T}$, such that the cost of creating a seed is $\widetilde{M}^2$, while the cost of adding a particle next to it is $\widetilde{T}$, as in the Ising chain. Thus, a fiber with length l has the weight $\widetilde{M}^2\widetilde{T}^{l-1}$. For instance, a straight fiber with width one such that only $T_{11} = T_{44} > 0$ has

$$\widetilde{M} = \sqrt{6}\, m^3 \quad \text{and} \quad \widetilde{T} = T_{11} m^4. \tag{3.29}$$

We further consider the regime of low density and very attractive interactions, where $\widetilde{M}^2 \ll \widetilde{T} < 1$. For the fibers not to interact, we need both $\langle s \rangle \ll 1$ and $\langle l \rangle$ not too large. This dilute regime ends when the distance between fibers $\sim 1/\langle s \rangle$ is similar to the typical length of the fibers $\sim \langle l \rangle$, such that it requires the product $\langle s \rangle \langle l \rangle$ to be at most of order 1. In this case, for a lattice of N sites, the number of available sites for starting a fiber is of order N. The partition function can thus be approximated as $Z \sim Z_1^N$, where

$$Z_1 \sim 1 + \widetilde{M}^2 \sum_{l=1}^{\infty} \widetilde{T}^{l-1} \sim 1 + \frac{\widetilde{M}^2}{1-\widetilde{T}}. \tag{3.30}$$

This leads the average density $\langle s \rangle$ to be expressed at lowest order as

$$\langle s \rangle \sim \frac{\widetilde{M}^2 \sum_{l=1}^{\infty} l\widetilde{T}^{l-1}}{Z_1} \sim \left(\frac{\widetilde{M}}{1-\widetilde{T}}\right)^2. \tag{3.31}$$

This means that at constant $\langle s \rangle$, $1-\widetilde{T} \propto \widetilde{M}$ and $\langle s \rangle$ small requires $\widetilde{M} \ll 1-\widetilde{T}$. In this regime, we can additionally compute the typical length of a fiber as

$$\langle l \rangle \sim \frac{\sum_{l=1}^{\infty} l\widetilde{T}^{l-1}}{\sum_{l=1}^{\infty} \widetilde{T}^{l-1}} \sim \frac{1}{1-\widetilde{T}}. \tag{3.32}$$

This means that $\langle l \rangle$ generically increases with $\widetilde{T}$ and decreases with $\widetilde{M}$. Both Eq. (3.31) and (3.32) compare well with the Ising chain study of Sec. 2.2 and 2.3, where $T = 1 + \alpha M$ and $\langle s \rangle$ small leads to $\alpha \sim -1/M_\alpha$.

Likewise, if the only non-zero entries are the diagonal ones, for which $\forall \phi,\ T_{\phi\phi} = a$ then sheet-like aggregates are formed. For very attractive interactions $a \gg m^2$ and low density, only a small number of sheets are formed, which tend to minimize their ratio of surface over volume. Aggregates of $l \gg 1$ particles thus have a surface $\sim \sqrt{l}$, such that their Boltzmann weights scale like $M^{2\sqrt{l}}T^{3l}$, see Fig. 3.3. It is however challenging to compute either $\langle s \rangle$ or $\langle l \rangle$ even in this simple case.

3.3.3 Renormalization for efficient aggregation in $n = 6$

Since it is difficult to locate the low density in the general $(\mathbf{M} = m\mathbf{1}, \mathbf{T})$-space, we come back to the examples of Sec. 3.2.2 where we can visualize renormalization and where the low density condition is easily translated into a relationship between the non-zero entries of $\mathbf{T}$ and m. We particularly focus on the ones where the low density region is locatable and the directionality is kept after one step, *i.e.* the zigzag fiber and the straight fiber of width two. We hereafter study their behavior under renormalization in the regime of efficient aggregation, where large aggregates are formed at low density. We expect large fibers to renormalize into fibers with a smaller average length, such that the efficient aggregation regime is stable under renormalization. We now investigate whether this is true in the diamond procedure, by looking at the entries of the matrix $\mathbf{T}$ at the first renormalization step in two examples of fibers that renormalize into fibers, namely the zigzag one and the one with width two.

- Let $\mathbf{M}^{(0)} = m\mathbf{1}$ and $T^{(0)}_{41} = T^{(0)}_{63} = a$ be the only non-zero entries of $\mathbf{T}^{(0)}$, such that aggregates are only zigzag fibers. The Boltzmann weight of an aggregate of l particles is thus $m^6(am^4)^{l-1}$. We wonder whether there is a regime of efficient aggregation, where at small density, very long fibers renormalize into fibers that are still very favorable. Following the study of Sec. 3.3.2, this regime corresponds to

$$m \ll 1 \quad \text{and} \quad am^4 \sim 1^-, \quad i.e. \quad a \sim 1/m^4 \gg 1, \tag{3.33}$$

such that at constant average density, particles prefer to clump up. At the first renormalization step and at lowest order, the new parameters read

$$M^{(1)}_\phi = \begin{cases} \mathcal{O}\Big(m^{4/d}\Big), & \text{for} \quad \phi = 1,4,5,6 \\ \mathcal{O}\Big(m^{6/d}\Big), & \text{for the others} \end{cases} \tag{3.34a}$$

$$T^{(1)}_{\phi\psi} = \begin{cases} \mathcal{O}(1), & \text{for} \quad (\phi,\psi) = (1,1),(4,4) \\ \mathcal{O}\Big(m^{8/d}\Big), & \text{for the others} \end{cases} \tag{3.34b}$$

Therefore, writing $T^{(1)}_{11} \sim T^{(1)}_{44} \sim a^{(1)}$, after one step, the most favorable aggregates of l particles have the new Boltzmann weight

$$\prod_{\phi=1}^{6} M^{(1)}_\phi \, \Big(a^{(1)} M^{(1)}_2 M^{(1)}_3 M^{(1)}_5 M^{(1)}_6\Big)^{l-1} = \mathcal{O}\Big(m^{(10+20l)/d}\Big). \tag{3.35}$$

Long fibers at small density would require both $m \ll 1$ and $m \sim 1^-$, which is contradictory, hence efficient aggregation is lost after one renormalization step.

- We now turn to the other example, namely the fiber with width 2, such that the non-zero entries of $\mathbf{T}^{(0)}$ are $T^{(0)}_{33}, T^{(0)}_{66}, T^{(0)}_{14}, T^{(0)}_{25} = a$, while $\mathbf{M}^{(0)} = m\mathbf{1}$. In this case, particles alone have the weight m^6, while fibers of $l \geq 2$ particles have the weight $m^9(am)^{2l-3}$, such that efficient aggregation requires

$$m \ll 1 \quad \text{and} \quad am \sim 1^-, \quad i.e. \quad a \sim 1/m \gg 1, \tag{3.36}$$

consistently with Sec. 3.3.2. After one step, we obtain

$$M^{(1)}_\phi = \begin{cases} \mathcal{O}\Big(m^{-2/d}\Big), & \text{for} \quad \phi = 1,2,3 \\ \mathcal{O}\Big(m^{2/d}\Big), & \text{for the others} \end{cases} \tag{3.37a}$$

$$T^{(1)}_{\phi\psi} = \begin{cases} \mathcal{O}\Big(m^{-6/d}\Big), & \text{for} \quad (\phi,\psi) = (1,4),(3,6) \\ \mathcal{O}\Big(m^{4/d}\Big), & \text{for the others} \end{cases} \tag{3.37b}$$

such that, writing $T^{(1)}_{14} \sim T^{(1)}_{36} \sim a^{(1)}$, the most favorable aggregates of l particles have the new weight

$$\prod_{\phi=1}^{6} M^{(1)}_\phi \, \Big(a^{(1)} M^{(1)}_1 M^{(1)}_2 M^{(1)}_3 M^{(1)}_5\Big)^{l-1} = \mathcal{O}\Big(m^{-10(l-1)/d}\Big). \tag{3.38}$$

Long aggregates thus become very favorable under renormalization, but since particles alone on the lattice have a weight of zeroth order in m, the average density becomes large, such that efficient aggregation is again lost after one renormalization step.

In the end, the diamond plaquette does not bring about a physically appropriate renormalization procedure, since it does not keep the dimension of the aggregates under renormalization in the relevant cases, such as for fibers. And in some cases where it does, efficient aggregation is not stable under renormalization: either the density becomes large or the aggregate size become close to one particle.

3.4 Other renormalization procedures in 2D

As renormalization with the diamond plaquette does not recover the entirety of the expected results, we hereby consider more elaborate renormalization procedures. In both procedures that we consider, the renormalization formulae for the Boltzmann weights of bond configurations become very hard to study analytically. We specifically introduce a hexagonal spin plaquette in the triangular lattice in Sec. 3.4.1, which gives similar results to the diamond one for $n = 1$. Yet, we find in Sec. 3.4.2 that the renormalization behaviors of certain relevant aggregate types are qualitatively dissimilar. Unfortunately, this procedure fails once again to recover all expected renormalization behaviors. We last present a second procedure on the square lattice in Sec. 3.4.3. It takes into account the possible emergence of next-nearest-neighbor interactions under renormalization.

3.4.1 Hexagonal plaquette

On the triangular lattice with a coordination $\kappa = 6$, instead of keeping the second neighbors under decimation, we can keep the third neighbors. They are placed on another triangular lattice, with twice lattice spacing. The most straightforward plaquette is then hexagonal, as shown in Fig. 3.11, *left*. The decimated sites are again split into three independent ghost copies, but all links are shared between three plaquettes [Fig. 3.11, *middle*]. We thus hereby give all old links the strength 1, while the new wavy link is attributed a strength g. This choice of strengths hopefully leads to a phase transition. As in Eq. (3.11), by summing over the values of the decimated spins at sites a, b, c, d, e, we obtain the following renormalization formula:

$$A(\mathscr{T}')^g(s_i, s_j) = \sum_{a,b,c,d,e} \mathscr{T}(s_i, s_a)\, \mathscr{T}(s_i, s_c)\, \mathscr{T}(s_i, s_d)\, \mathscr{T}(s_a, s_b)\, \mathscr{T}(s_b, s_c)\, \mathscr{T}(s_c, s_a) \times \mathscr{T}(s_d, s_e)\, \mathscr{T}(s_e, s_c)\, \mathscr{T}(s_c, s_d)\, \mathscr{T}(s_b, s_j)\, \mathscr{T}(s_c, s_j)\, \mathscr{T}(s_e, s_j). \tag{3.39}$$

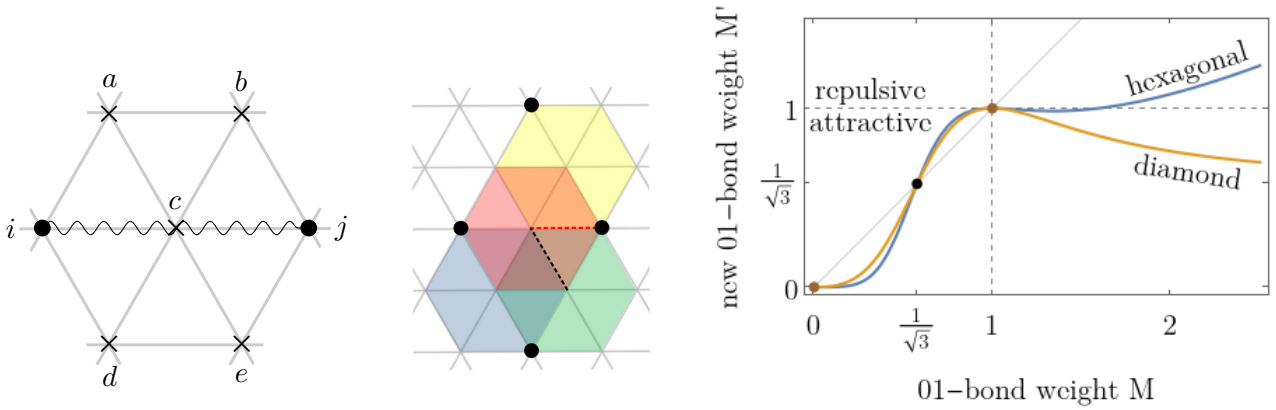

Figure 3.11: **The hexagonal plaquette gives similar results to the diamond one.** *Left*, keeping the third neighbors after decimation on the triangular lattice naturally leads to hexagonal spin plaquettes. *Middle*, the plaquettes overlap, such that both red and black dashed bonds are split into three. The red bond is shared between the yellow, red and green plaquettes, while the black one is shared between the red, blue and green plaquettes. *Right*, on the stable line $T = 1$, the behaviors of M' versus M in the hexagonal and diamond schemes differ particularly in the region $M > 1$. For the diamond plaquette, as $M \to \infty$, $M' \sim (\frac{2}{3})^d \sim 1/\sqrt{3}$, while for the hexagonal plaquette $(M')^g \sim \frac{2}{5}M$. Beginning from a repulsive initial condition $M^{(0)} > 1$, we see that in both cases, the iteration from $M = M^{(k)}$ to $M' = M^{(k+1)}$ eventually leads to the attractive region. Then for M finite, the brown and black fixed points are situated on the $M' = M$ line.

This leads to cumbersome expressions for the new Boltzmann weights M', T':

$$A = 1 + 4M^3 + 5M^6 + (2M^4 + 8M^7)T + 5M^8T^2 + 2M^6T^3 + 4M^7T^4 + M^6T^6, \tag{3.40a}$$

$$A(M')^g = M^3\Big[1 + 2M^3 + M^6 + (2M + 3M^4)T + (3M^2 + 4M^5)T^2 + (4M^3 + M^6)T^3 + 3M^4T^4 + 3M^2T^5 + 2M^3T^6 + 2MT^7 + T^9\Big], \tag{3.40b}$$

$$A(T')^g = M^6 + 4M^7T + 5M^8T^2 + 2M^6T^3 + 8M^7T^4 + 5M^6T^6 + 2M^4T^7 + 4M^3T^9 + T^{12}. \tag{3.40c}$$

To enforce that $(M = 1/\sqrt{3},\ T = 1)$ be a fixed point, we set $g = \ln \frac{7\sqrt{3}-6}{4} / \ln \sqrt{3} \approx 0.76$. As for the diamond renormalization of Sec. 3.2.1, we find three stable curves:

$$\text{for} \quad M = 0, \qquad M' = 0, \quad T' = T^{12/g}, \tag{3.41a}$$

$$\text{for} \quad T = 1, \qquad (M')^g = \frac{2M^3(1+M^2)^2}{1 - 2M + 3M^2 - M^4 + 2M^5 + 5M^6}, \quad T' = 1, \tag{3.41b}$$

$$\text{for} \quad T = M^2, \qquad (M')^g = M^3, \quad T' = (M')^2. \tag{3.41c}$$

Then, the dynamical characteristics and fixed points are very similar to the ones of the diamond scheme, except in two aspects. First, interactions are not always attractive from the first step on, but they seem to always reach the attractive part ($C < 0$) eventually. Second, the iteration in Eq. (3.40) actually recovers the repulsive critical point $(\infty, 1)$ as a fixed point, which the diamond scheme did not. Indeed for $T = 1$, as $M \to \infty$, $(M')^g \sim \frac{2}{5}M$, see Fig. 3.11, *right*. These differences for $n = 1$ are rather minor, but as we will see next, for $n = 6$ orientations this hexagonal plaquette leads to very different renormalization dynamics compared to the diamond plaquette.

3.4.2 Sketched renormalization for $n = 6$ orientations

We now analyze the renormalization dynamics for $n = 6$ orientations. As shown in Fig. 3.11, since the new links are in the same directions as the old links, we keep the directions of the orientations under renormalization. The renormalization formula in terms of the $\mathscr{T}(s\phi, s'\psi)$ is defined similarly than in Eq. (3.17). But in this case, the Boltzmann weights M'_ϕ, and $T'_{\phi\psi}$, $\phi, \psi = 1, \dots, 6$ verify very long renormalization formulae. We thus take once again the sketched renormalization approach and consider simple cases where only a few entries of $\mathbf{T}^{(0)} = \mathbf{T}$ are non-zero and all set to a, while $\mathbf{M}^{(0)} = m\mathbf{1}$. For $a \gg 1$ and $a \gg m^2$, we thus wonder whether there is a regime where for instance the directionality of fibers is kept under renormalization.

- Let only $T_{11} = T_{44} = a$ such that aggregates are only fibers. The most favorable configurations on a diamond plaquette are shown with sketches in Fig. 3.12, *top*. At the first renormalization step, several entries of $\mathbf{T}^{(1)}$ have terms of order a^2, which is the highest possible on a hexagonal plaquette. In particular,

  $$A\left(T^{(1)}_{11}\right)^g = m^6 + a^2m^8 \quad \text{and} \quad A\left(T^{(1)}_{22}\right)^g = A\left(T^{(1)}_{33}\right)^g = m^6 + am^7 + a^2m^8. \tag{3.42}$$

  This means that sheets are formed and the directionality of the fibers is thus lost.

- For the zigzag fiber, where only $T_{14}, T_{52} = a$. After one step, we obtain several things, see Fig. 3.12, *bottom*. But in particular, $T^{(1)}_{23}$ and $T^{(1)}_{41}$ have the highest order term a^2m^8, which leads to the formation of the light brown holed sheet of Fig. 3.3. This means that the directionality is also lost.

- Likewise, the fiber with width 2 with $T_{33}, T_{66}, T_{14}, T_{25} = a$ renormalizes preferentially into itself, since $A\left(T^{(1)}_{33}\right)^g$ has the highest order term a^7m^4 and $A\left(T^{(1)}_{14}\right)^g$ and $A\left(T^{(1)}_{25}\right)^g$ have terms in a^2m^8.

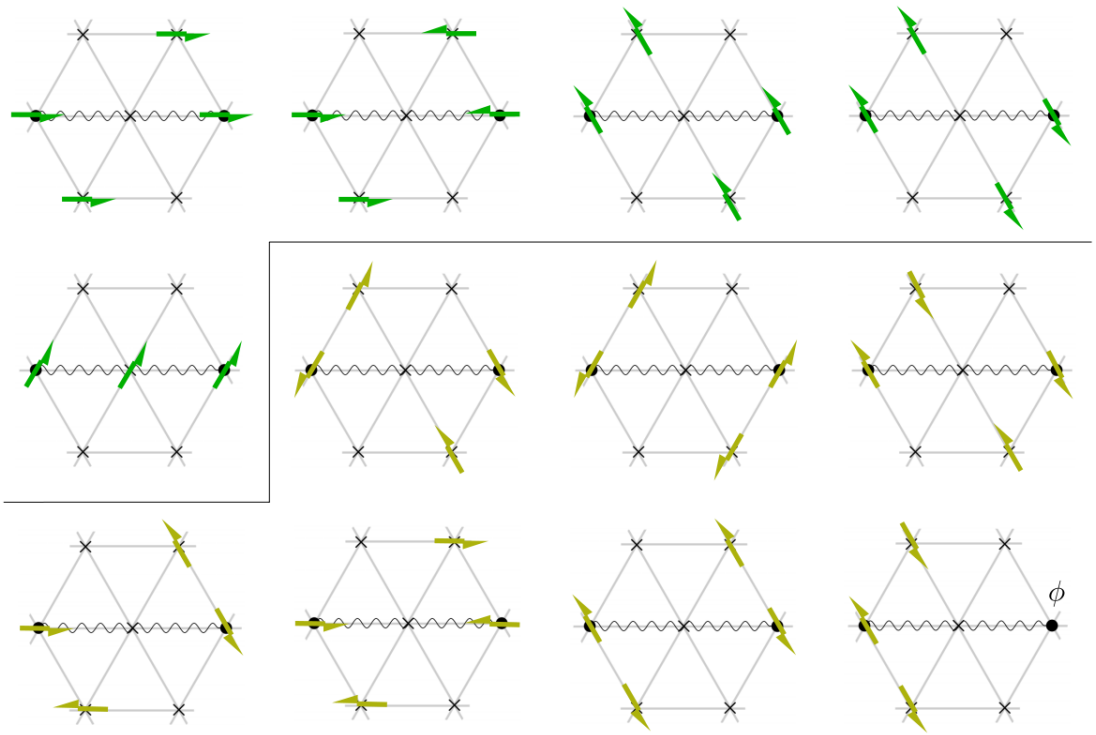

Figure 3.12: **Sketched hexagonal renormalization procedure for a green straight and an olive zigzag fiber.** *Top*, most probable sketches corresponding to the new $\phi\psi$-bonds when only $T_{11} = T_{44} = a$ in the case $a \gg 1$ and $a \gg m^2$. Since $T_{11}^{(1)}, T_{22}^{(1)}$ and $T_{33}^{(1)}$ are favored, the straight fiber turns into sheets after one step. *Bottom*, the zigzag fiber with only $T_{14} = T_{52} = a$ also turns into sheets.

- The dimers renormalize into dimers, the triangles into triangles, and the hexagons into dimers.
- The holed sheet with $T_{23}, T_{65}, T_{41} = a$ renormalizes into another similar holed sheet with $A\left(T_{32}^{(1)}\right)^g, A\left(T_{56}^{(1)}\right)^g, A\left(T_{14}^{(1)}\right)^g$ having the highest order term a^6m^6.
- The full sheet with identical orientations $\forall\phi,\ T_{\phi\phi} = a$ is kept under renormalization, such that $\forall\phi,\ A(T_{\phi\phi}^{(1)})^d$ have the highest terms in a^{12}

As for the diamond procedure, many aggregates renormalize as planned, but some do not. Especially, the straight and zigzag fibers with width one renormalize into sheets, such that the dimension of their most favorable aggregates increases from 1 to 2 after one renormalization step. This is unfortunate, since we are focused primarily on analyzing the formation of fibers via renormalization. Since the aggregate dimension either stagnates or increases on this hexagonal plaquette, while it stagnates or decreases on a diamond plaquette, it is unlikely that considering a larger plaquette will solve the issue. However, another way to deal with this issue, is to favor some links in the hexagonal plaquette, while keeping the symmetries of the lattice and the plaquette. For instance, we could say that the links between sites i and c, and c and j in Fig. 3.11, *left* have a strength superior to 1. Assuming that there still is a phase transition, this could make the straight fiber with width one renormalize rather into itself than into sheets in some regime. Indeed, from only $T_{11} = T_{44} = a$, $T_{11}^{(1)}$ would in general differ from $T_{22}^{(1)}$ and $T_{33}^{(1)}$, see the sketches at the top of Fig. 3.12. But this would not change anything concerning the zigzag fiber. A third possibility consists in setting μ as the chemical potential per site, instead of setting μ/κ per bond, which in a way is a bit peculiar. If implementable, this could make straight fibers with width one renormalize as expected. Last, we could take into account next-nearest neighbor interactions, which forms the focus of Sec. 3.4.3.

3.4.3 Next-nearest neighbor interactions on the square lattice

Since both diamond and hexagonal plaquettes fail to account for all expected renormalization behaviors, we hereby introduce a formalism for next-nearest-neighbor interactions. This includes an additional scalar coupling and chemical potential K and ν for $n = 1$, which means in particular that the full chemical potential of a site now reads $\mu + \nu$. The Hamiltonian under study can be written

$$\frac{\mathcal{H}(\mathbf{s})}{k_B\theta} = \sum_{\langle i,j\rangle} C s_i s_j + \frac{\mu}{\kappa}(s_i + s_j) + \sum_{\langle\langle k,l\rangle\rangle} K s_k s_l + \frac{\nu}{\kappa}(s_k + s_l) \tag{3.43}$$

where $\langle\langle k, m\rangle\rangle$ refers to pairs of next-nearest-neighbor sites. A simple way to implement this idea is to consider the renormalization scheme on the square lattice described in Fig. 3.13. The new nearest-neighbor link between sites i and j results from a square plaquette, while the new next-nearest-neighbor link between sites i and k results from a linear, 1D-like plaquette. In the square plaquette the decimated spins are split into four independent copies, while in the linear one, they are split into two.

Here, the lattice coordination $\kappa = 4$, such that nearest-neighbor bonds are either 1, $M = e^{-\mu/4}$ or $T = e^{-C-\mu/2}$. To deal with next-nearest-neighbor bonds, we introduce new scalar variables written $N = e^{-\nu/4}$ or $U = e^{-K-\nu/2}$, corresponding to the Boltzmann weights of a 01-bond and a 11-bond respectively, between *e.g.* sites i and j in Fig. 3.13. On the square lattice, bonds between next-nearest neighbors are on the diagonal and we define

$$\mathscr{T}_d(s, s') \quad \text{such that} \quad \mathscr{T}_d(0,0) = 1, \quad \mathscr{T}_d(1,0) = \mathscr{T}_d(0,1) = N \quad \text{and} \quad \mathscr{T}_d(1,1) = U. \tag{3.44}$$

Then our renormalization formulae read

$$A\mathscr{T}'(s_i, s_j) = \sum_{s_a, s_b} \mathscr{T}(s_i, s_a)\, \mathscr{T}(s_i, s_b)\, z_d(s_i, s_j)\, \mathscr{T}_d(s_a, s_b)\, \mathscr{T}(s_a, s_j)\, \mathscr{T}(s_b, s_j), \tag{3.45a}$$

$$B\mathscr{T}'_d(s_i, s_k) = \sum_{s_a} \mathscr{T}(s_i, s_a)\, \mathscr{T}(s_a, s_k). \tag{3.45b}$$

This leads the nearest-neighbor and next-nearest-neighbor parameters to be dynamically coupled under renormalization, such that

$$M' = \frac{1 + 2TN + T^2U}{1 + 2M^2N + M^4U} M^2 N, \quad T' = U \frac{M^4 + 2T^2M^2N + T^4U}{1 + 2M^2N + M^4U}, \tag{3.46}$$

and as in 1d,

$$N' = \frac{1+T}{1+M^2} M, \quad U' = \frac{M^2 + T^2}{1 + M^2}. \tag{3.47}$$

We see here that even from an initial condition without next-nearest-neighbor couplings $U^{(0)} = N^{(0)} = 1$, these second-order couplings naturally arise upon renormalization. In this procedure, we still neglect *e.g.*

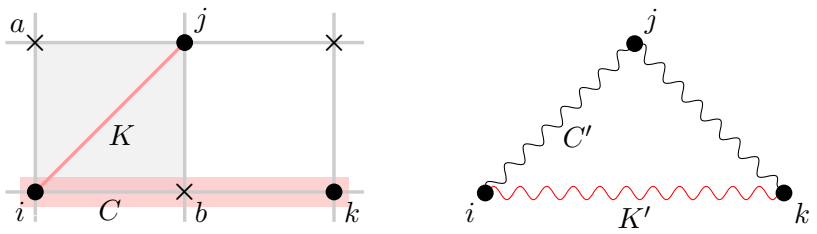

Figure 3.13: **Decimation on the square lattice with next-nearest-neighbor interactions.** The old links are shown on the left, whereas the new wavy ones are shown on the right. The new nearest-neighbor coupling C' between sites i and j is calculated with the light gray square plaquette upon decimation of sites a and b. The new nest-nearest-neighbor coupling K' comes from the red linear plaquette comprising sites i, b, k.

four-body interactions between the spins at sites i, a, j, b. However, the meaning of these second-order couplings is far from trivial, especially in the case $n = 6$. Fortunately, we can rewrite Eqs. (3.46) and (3.47) as an iteration of the form $(M'', T'') = f(M, T, M', T')$, where f is an unwieldy function of the initial weights and the ones after one step. Then, we could consider the initial condition $(M^{(0)}, T^{(0)}, N^{(0)} = 1, U^{(0)} = 1)$. Yet, this greatly complicates the analytical study of *e.g.* fixed points, and is not guaranteed to help make fibers renormalize into fibers.

Conclusion

We have successfully adapted the one-dimensional coupling matrix formalism to two-dimensional lattices. But we found the constraints on the renormalization procedure hard to satisfy. Indeed, the intuitive diamond renormalization scheme leads to erroneous dynamics in the case of *e.g.* straight fibers of width one, which become sheets after one step. Likewise, the hexagonal-plaquette scheme does not include these fibers as a fixed point. A plan for further calculations could be to select a renormalization procedure that actually has fibers as fixed points. Then one could consider a certain probability distribution for the coupling matrix, and look at how many initial matrices fall into these fixed points.

We now compare the hexagonal plaquette scheme of Sec. 3.4.2 with the simulated renormalization study of L. Koehler [Fig. 1.12] performed on the triangular lattice with hexagonal particles ($n = 6$). The hexagonal plaquette indeed corresponds to the calculations of the new first-neighbor bonds from the third-neighbor ones. Her numerical renormalization scheme differs from our analytical one in that she does not use the plaquette approximation as we do. In her case, the values of the new spins depend on the value of all decimated spins (not just the ones in our hexagonal plaquette). Yet, she still approximates (like us) that no new kind of coupling (*e.g.* between next-nearest neighbors) arises upon renormalization. She moreover works at fixed density while we saw that the density may not always be conserved under renormalization. Despite these differences, she for instance recovers the expected behavior that in some efficient aggregation regime, fibers with width w and length l renormalize into fibers with smaller width $w' \sim w/2$ and length $l' \sim l/2$. Until $w = 1$, where in this case $w' = w = 1$, while still $l' \sim l/2$. This is true in our case except for the straight fibers of width 1. Intriguingly, when thinking of the zoology of fibers from square or hexagonal particles on the square and triangular lattices, we find it difficult to come up with a fiber of width higher than 2. It seems that if the width can be 3, it can then be infinite. This statement is in agreement with the observations of L. Koehler, who sees needle crystals with a high aspect ratio but no fibers with a bounded width higher than 2. The mechanism at play however remains elusive at this point. Moreover, hoping that there are not too many precision mistakes from her numerical computations of the renormalization dynamics, she finds a certain number of fixed forms for the matrix $\mathbf{C}$. These fixed forms correspond to aggregates of different dimensions. Preliminary comparisons indicate that our hexagonal renormalization procedure conserves the dimension of the aggregates of most of these fixed forms. This gives hope that the analytical study above can help sort coupling matrices according to their aggregate types.

3.5 Appendix: textbook calculations on the Ising model

3.5.1 Lattice-gas to spin-$\frac{1}{2}$ variables mapping in any dimension

The Hamiltonian of Eq. (3.1) with lattice-gas variables $s_i = 0, 1$ can be mapped bijectively with the following Hamiltonian (Fisher, 1967):

$$\frac{\mathcal{H}(\boldsymbol{\sigma})}{k_B\theta} = \sum_{\langle i,j\rangle} -J\sigma_i\sigma_j + \sum_i -h\sigma_i, \tag{3.48}$$

where the spin-$\frac{1}{2}$ variables $\sigma_i = \pm 1$. Here $J > 0$ (< 0) denotes a ferromagnetic (anti-ferromagnetic) coupling, and h is the magnetic field. The mapping comes from the change of variables $\sigma_i = 2s_i - 1$, which implies the following relationships:

$$J = -C/4 \quad \text{and} \quad h = -\frac{\kappa}{4}\left(C + \frac{2}{\kappa}\mu\right), \tag{3.49}$$

up to an irrelevant constant energy shift.

3.5.2 Mean-field magnetization

We hereby consider the the mean-field approximation and obtain a self-consistent equation for the magnetization m, known as the Curie-Weiss equation (Salinas, 2001). Let the spins mildly fluctuate around their average value m independent of the site due to translational invariance, such that $\delta\sigma_i = \sigma_i - m \ll 1$. Then, at first order in $\delta\sigma_i$, the Hamiltonian in Eq. (3.48) takes the form

$$\frac{\mathcal{H}(\boldsymbol{\sigma})}{k_B\theta} = \sum_i \big(h + \kappa J m\big)\sigma_i + \mathcal{O}\big((\delta\sigma_i)^2\big), \tag{3.50}$$

where the sum over the pairs of nearest neighbors has been transformed as $\sum_{\langle i,j\rangle} = \frac{\kappa}{2}\sum_i$. This leads us to define an efficient magnetic field $h_{\text{eff}} = h + \kappa J m$. Then, the partition function $Z = \sum_{\boldsymbol{\sigma}} e^{-\mathcal{H}(\boldsymbol{\sigma})/(k_B\theta)}$ for a chain of N sites can be approximated at first order as $Z \sim Z_1^N$, where the function partition of one site reads $Z_1 \sim e^{h_{\text{eff}}} + e^{-h_{\text{eff}}}$. This leads the magnetization $m = \sum_{\boldsymbol{\sigma}} \sigma_0\, e^{-\mathcal{H}(\boldsymbol{\sigma})/(k_B\theta)}/Z$ to take the self-consistent form

$$m = \operatorname{th} h_{\text{eff}} = \operatorname{th}\big(h + \kappa J m\big). \tag{3.51}$$

When $h = 0$, this transcendental equation admits two stable solutions for $\kappa J > 1$: $m = \pm m_s$, while it admits only $m = 0$ for $\kappa J \leq 1$. Thus, $1/\kappa$ denotes the critical coupling at which the order-disorder phase transition takes place. However, the mean-field approximation tends to overestimate the system tendency to order and thus underestimates the value of the critical coupling J_c. Indeed, for the triangular lattice, $1/\kappa = \frac{1}{6} \approx 0.17$ is less than $J_c^{\text{tri}} = \frac{\ln 3}{4} \approx 0.27$. To render the equation for m consistent with our flow diagram, we thus replace $1/\kappa$ by the real value of J_c, such that the magnetization satisfies the equation

$$m = \operatorname{th}\left(h + m\frac{J}{J_c}\right). \tag{3.52}$$

It is valid a priori rather in the ferromagnetic region, but since there is no phase transition in the anti-ferromagnetic region, we extend it to the whole parameter regime. Varying h dynamically between positive and negative values can lead to some hysteresis effects, such that $\operatorname{sgn} h$ can be different from $\operatorname{sgn} m$. But here, we do not consider this effect. Writing $J/J_c = C/C_c$, Eq. (3.52) can be rewritten with the variables $M = e^{-\mu/\kappa}$ and $T = e^{-C}M^2 = e^{4h/\kappa}$ as

$$\ln M = \left(\frac{1}{2} - \frac{\kappa \ln M_c}{4m}\right)\ln T + \ln M_c \frac{\operatorname{acrth} m}{m}. \tag{3.53}$$

Since $m = 2\langle s\rangle - 1$, this eventually yields Eq. (3.22).

3.6 Appendix: full formulae for the diamond renormalization and $n = 6$

For particles with $n = 6$ orientations on a triangular lattice, the renormalization formula reads

$$\begin{aligned} A(z')^c\big[s_i\phi_i, s_j\phi_j\big] = \sum_{a,b} z\big[s_i\phi_i, s_a\phi_a\big]\, z\big[s_i(\phi_i-1), s_b(\phi_b-1)\big]\, z^2\big[s_a(\phi_a-2), s_b(\phi_b-2)\big] \\ \times z\big[s_a(\phi_a-1), s_j(\phi_j-1)\big]\, z\big[s_b\phi_b, s_j\phi_j\big]. \end{aligned} \tag{3.54}$$

Therefore, rewriting $\phi_{i,j,a,b}$ as ϕ, ψ, χ, ω to avoid double indices, we obtain

$$A = 1 + 2\sum_{\chi} M_{\chi-3}M^2_{\chi-2}M_{\chi-1} + \sum_{\chi,\omega} M_{\chi-3}M_{\omega+2}T^2_{\chi-2,\omega-2}M_{\chi-1}M_{\omega}, \tag{3.55a}$$

$$\begin{aligned} A(M'_\phi)^c = M_\phi M_{\phi-1} + \sum_{\chi} T_{\phi\chi}M_{\phi-1}M^2_{\chi-2}M_{\chi-1} \\ + \sum_{\omega} M_\phi T_{\phi-1,\omega-1}M^2_{\omega+1}M_\omega + \sum_{\chi,\omega} T_{\phi\chi}T_{\phi-1,\omega-1}T^2_{\chi-2,\omega-2}M_{\chi-1}M_\omega, \end{aligned} \tag{3.55b}$$

$$\begin{aligned} A(T'_{\phi\psi})^c = M_\phi M_{\phi-1}M_{\psi+2}M_{\psi+3} + \sum_{\chi} T_{\phi\chi}M_{\phi-1}M^2_{\chi-2}T_{\chi-1,\psi-1}M_{\psi+3} \\ + \sum_{\omega} M_\phi T_{\phi-1,\omega-1}M^2_{\omega+1}M_{\psi+2}T_{\omega\psi} + \sum_{\chi,\omega} T_{\phi\chi}T_{\phi-1,\omega-1}T^2_{\chi-2,\omega-2}T_{\chi-1,\psi-1}T_{\omega\psi}, \end{aligned} \tag{3.55c}$$

where the orientations are defined modulo 6, such that $\forall\phi,\ \phi + 6 \equiv \phi$.

Chapter 4

Discussion

The self-assembly of proteins has been extensively studied through many types of models. Hagan and Grason (2021) recently proposed a classification of self-assembly mechanisms into either the self-closing of the open-boundary types [Fig. 1.3]. They found self-limiting behaviors in both cases, either in the number of particles inside an aggregate, or in the number of dimensions of growth of an aggregate. While the self-closing case obviously tends to yield self-limited aggregates, understanding self-limitation in the open-boundary case is more challenging. While the authors considered deformable ill-fitting puzzle pieces, we focused on undeformable polygonal lattice particles with preferred binding sites. This is such that two copies of a particle on neighboring lattice sites aggregate depending on both of their discrete orientations, numbered from 1 to n. We thus characterized these pair interactions with a $n \times n$-matrix $\mathbf{T}$. We considered a system in equilibrium with a reservoir of particles and analytically studied the size and shape of the aggregates formed, first on a chain, and then on the square and triangular lattices. It is worth noticing that our results may not be easily transferable to, *e.g.*, the honeycomb lattice, that is not invariant by rotation of π.

We examined self-limitation in two relevant cases. In 1D and in the case of a large number of forbidden interactions, *i.e.* when many entries of matrix $\mathbf{T}$ are zero, we found that particles with a nilpotent interaction matrix such that $t_1 = 0$ can only form aggregates of maximal size n. For instance, square particles with $n = 4$ interactions can form linear aggregates with at most 4 particles. In the case where $t_1 > 0$, we focused on the regime of efficient aggregation corresponding to the formation of large aggregates at low density of particles on the lattice. There, although aggregates can be infinitely long, we found that the mean length of fibers increased with t_1 as $\langle l \rangle \sim 1/(1 - t_1)$ for $t_1 < 1$. We then turned to the 2D case, which appeared difficult to study in the general case. We thus focused on simple relevant examples. In the case of only one authorized interaction, where aggregates can either have a finite-size or grow in one direction, we found that nilpotent interaction matrices corresponded again to finite-sized aggregation. However, in the case of even just a few authorized interactions, we found this distinction not to be valid anymore.

In brief, in the equilibrium self-assembly of polygonal particles with anisotropic interactions, the largest eigenvalue t_1 of the pair-interaction matrix is tightly linked to self-limitation in 1D. Yet it contains only partial information concerning the more complicated case of aggregation in the square or triangular lattices. It would be interesting to see whether we can assimilate the hereby studied cases of polygonal aggregation to the self-closing or the open-boundary assembly mechanisms proposed by Hagan and Grason (2021).

Part II

Generic stress rectification in nonlinear elastic media

Chapter 5

Propagation of internal stresses in complex materials

Our intuition of the mechanics of nonlinear materials is largely based on deforming their outer boundary. We thus expect a uniformly compressed material to respond with an expansile stress, while applying shear will elicit an opposing shear stress. In this chapter, we show that if the forces are exerted from the *inside* of the material, these expectations can be upset. In Sec. 5.1, we present the standard equations of elasticity in the linear regime where stress is proportional to strain, and in the presence of different types of nonlinearities. Then in Sec. 5.2, we investigate the response of biopolymer networks to embedded active units, such as molecular motors in the cell cytoskeleton. Granular media can also be subjected to internal stresses in the form of plastic events due to large shear deformations at the boundaries. We study the propagation of these internal stresses and their impact on the yielding of bead packings in Sec. 5.3.

5.1 Continuum stress-strain relation

Here, we define stresses and strains properly, and we give an overview of the different stress-strain relations which arise in different strain regimes and for different types of materials. For infinitesimal strains, Hooke's law gives a linear relationship between stress and strain that we develop in Sec. 5.1.1. Then in Sec. 5.1.2, we present a first kind of nonlinearity which stems from geometrical effects at larger strains. Finally, Sec. 5.1.3 focuses on a standard finite strain model of rubber which displays constitutive nonlinearities.

5.1.1 Hooke's linear law for infinitesimal strains

We first consider an infinitesimal piece of homogeneous elastic medium of dimension d subjected to infinitesimal deformations due to stresses exerted at its boundaries. The deformations can be of different sorts depending on whether a certain surface is moved alongside its normal, or perpendicular to it. We relate to the first kind as extension or contraction, while the second kind corresponds to shear, see Fig. 5.1. Writing $\mathbf{u}$ the displacement vector, we denote as $\mathbf{X} = \mathbf{x} + \mathbf{u}$ the final location (in the "target space") of a material point initially located in $\mathbf{x}$ (in the "initial space"). We describe the elastic deformation of our medium using the displacement gradient $\eta_{ij} = \partial u_i / \partial x_j$. Likewise, the stress tensor is related to the force $\mathrm{d}\mathbf{F}$ exerted on the surface with outward-directed area element $\mathrm{d}\mathbf{A}$ as $\sigma_{ij} = \mathrm{d}F_i / \mathrm{d}A_j$ (Landau et al., 1986).

We further define the symmetric part of the displacement gradient $U_{ij} = (\eta_{ij} + \eta_{ji})/2$ which corresponds to the linearized strain. Under infinitesimal deformation, Hooke's law states that the stress tensor is proportional to the linearized strain tensor as

$$\sigma_{ij} = \mathcal{K}_{ijkl}\, U_{kl}, \tag{5.1}$$

where the summation over repeated indices is implied. Under the approximation that the material be isotropic and achiral, which we will always make in the following discussion, the four-index tensor

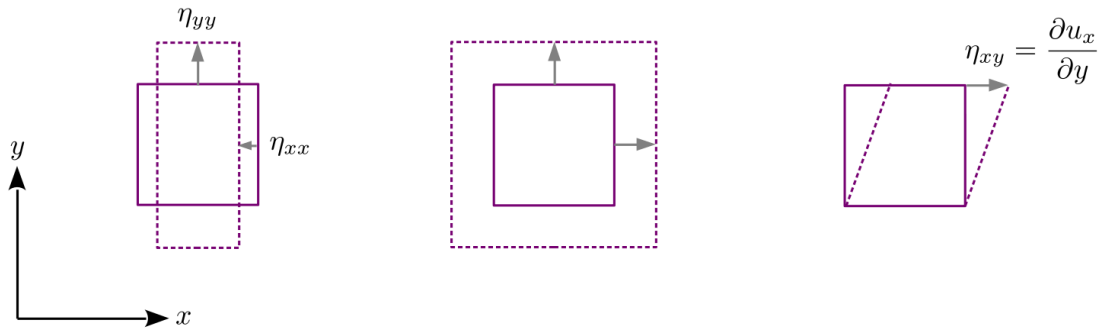

Figure 5.1: **Elementary deformations on an infinitesimal square piece of material.** From left to right, uniaxial extension, isotropic expansion and simple shear. Gray arrows represent the deformations of the materials along the x and y directions.

$\mathcal{K}$ fortunately contains only a small number of independent components. In two or three dimensions, these components can be expressed with the bulk modulus κ and the shear modulus μ, such that Eq. (5.1) translates into

$$\sigma_{ij} = (\kappa - 2\mu/d)\delta_{ij}U_{kk} + 2\mu U_{ij}, \tag{5.2}$$

where U_{kk} denotes the trace of the linearized strain tensor (Wriggers, 2008). The stress tensor $\boldsymbol{\sigma}$ is thus symmetric, *i.e.* $\sigma_{ij} = \sigma_{ji}$, while the deformation gradient $\boldsymbol{\eta}$ can perfectly be asymmetric. We thus write σ_{yx} as a dot since it always equals σ_{xy}. Going back to the 2D examples of Fig. 5.1, **unilateral extension** thus corresponds to

$$\boldsymbol{\sigma} = \begin{pmatrix} 0 & 0 \\ . & \sigma_{yy} \end{pmatrix} \quad \text{and} \quad \boldsymbol{\eta} = \begin{pmatrix} \eta_{xx} & 0 \\ 0 & \eta_{yy} \end{pmatrix}, \quad \text{where} \quad \sigma_{yy} = \frac{4\kappa\mu}{\kappa+\mu}\eta_{yy} \quad \text{and} \quad \eta_{xx} = -\frac{\kappa-\mu}{\kappa+\mu}\eta_{yy}. \tag{5.3}$$

Here, Young's modulus $4\kappa\mu/(\kappa+\mu)$ amounts to the stiffness of the material, whereas Poisson's ratio $\nu = (\kappa-\mu)/(\kappa+\mu)$ quantifies the direction and amount of transverse strain due to the uniaxial stress. For 2D materials, it belongs to $[-1, 1]$, where the upper bound refers to incompressibility. In the following analyses, we exclude the negative values of ν corresponding to rather exotic materials that prefer to deform more uniformly such that η_{xx} and η_{yy} have the same sign. This auxetic behavior typically requires re-entrant geometries (Lakes, 1993; Reid et al., 2018). In the case of **isotropic deformation**, the pressure is defined as

$$P = -\sigma_{ii}/d = \kappa\eta_{ii}, \quad \text{such that} \quad \boldsymbol{\sigma} = \begin{pmatrix} -P & 0 \\ . & -P \end{pmatrix} \quad \text{and} \quad \boldsymbol{\eta} = \begin{pmatrix} \eta_{ii}/2 & 0 \\ 0 & \eta_{ii}/2 \end{pmatrix}, \tag{5.4}$$

where $\eta_{ii} = \delta V/V$ is the change of volume. A positive pressure denotes uniform compression, while a negative pressure refers to expansion. And for **simple shear stress**,

$$\boldsymbol{\sigma} = \begin{pmatrix} 0 & \sigma_{xy} \\ . & 0 \end{pmatrix} \quad \text{and} \quad \boldsymbol{\eta} = \begin{pmatrix} 0 & \eta_{xy} \\ 0 & 0 \end{pmatrix}, \quad \text{where} \quad \sigma_{xy} = \mu\eta_{xy}. \tag{5.5}$$

One can moreover construct an elastic energy density from which Eq. (5.2) derives. It is quadratic in the strain tensor $\mathbf{U}$ and reads

$$E = \frac{\kappa}{2}U_{ii}^2 + \frac{\mu}{d}(dU_{ij}^2 - U_{ii}^2), \tag{5.6}$$

where the bulk and shear moduli κ and μ are both positive for dynamical stability. Here, U_{ij}^2 denotes the trace of $\mathbf{U}^2$, while U_{ii}^2 equals the square of the trace of $\mathbf{U}$. The stress tensor is thus expressed as $\boldsymbol{\sigma} = \partial E/\partial \mathbf{U}$.

Apart from the imposition of stress at the boundaries, the presence of "active units" embedded in an elastic medium can be modeled as a force density $\mathbf{f}$. This results in a stress tensor $\boldsymbol{\sigma}$ given by the force balance equation $f_i = -\partial\sigma_{ij}/\partial x_j$. Away from the active units, mechanical equilibrium is thus given by $\boldsymbol{\nabla}\cdot\boldsymbol{\sigma} = \mathbf{0}$. In the case of purely isotropic deformations in a spherical geometry in dimension d

resulting from a point-like active unit in $r = 0$, the radial displacement field at radius r can generically be expressed as $u_r(r) = Ar + B/r^{d-1}$. It follows that the slowest decrease of the stress away from the active unit scales as $\sigma_{rr} \sim 1/r^d$. The stress is thus diluted in the volume of the material. Apart from this dilution, stress symmetries are unaltered upon propagation in a linearly elastic medium. This will be further discussed in Sec. 6.1.

5.1.2 Geometrical nonlinearities for finite strains

Outside of the infinitesimal strain regime where stress is proportional to strain, we need to be careful in defining the stress and strains to consider. Indeed, the deformed space $\mathbf{X} = \mathbf{x} + \mathbf{u}$ can no longer be conflated with the initial space $\mathbf{x}$. We thus further describe the elastic deformation of our medium using the Green-Lagrange strain tensor

$$\boldsymbol{\varepsilon} = \frac{\boldsymbol{\eta} + \boldsymbol{\eta}^\mathsf{T} + \boldsymbol{\eta}^\mathsf{T}\boldsymbol{\eta}}{2} = \mathbf{U} + \frac{\boldsymbol{\eta}^\mathsf{T}\boldsymbol{\eta}}{2}. \tag{5.7}$$

The last, nonlinear term of $\boldsymbol{\varepsilon}$ is purely geometrical and accounts for *e.g.* material rotations. This measures the changes in distance between points in the deformed target space relative to those in the undeformed reference space: $\mathrm{d}X_i^2 = (1 - 2\varepsilon_{ij})\mathrm{d}x_i\mathrm{d}x_j$. In the spirit of Eq. (5.6), the easiest model to consider has an energy density

$$E = \frac{\kappa}{2}\varepsilon_{ii}^2 + \frac{\mu}{d}\big(d\varepsilon_{ij}^2 - \epsilon_{ii}^2\big), \tag{5.8}$$

which is quadratic in the strain but quartic in the displacement gradient $\boldsymbol{\eta}$. This corresponds to constitutively linear materials and is best suited to model thin structural members like beams or shells, which undergo large displacements and finite rotations but small strains (Wriggers, 2008).

The stress tensor which naturally derives from E describes the surface force measured in the initial space with respect to the initial area: $\mathrm{d}\mathbf{F}^0/\mathrm{d}\mathbf{a} = \partial E/\partial\boldsymbol{\varepsilon}$, it is known as the second Piola-Kirchhoff stress. Then in order to find the Cauchy stress measured fully in the target space: $\boldsymbol{\sigma} = \mathrm{d}\mathbf{F}/\mathrm{d}\mathbf{A}$, we need to transform the surface force and the area as

$$\mathrm{d}\mathbf{F} = (\mathbf{1} + \boldsymbol{\eta})\,\mathrm{d}\mathbf{F}^0 \quad \text{and} \quad \mathrm{d}\mathbf{a} = \frac{\mathbf{1} + \boldsymbol{\eta}^\mathsf{T}}{\det(\mathbf{1} + \boldsymbol{\eta})}\mathrm{d}\mathbf{A}, \tag{5.9}$$

where $\mathbf{1}$ denotes the unit tensor, see Fig. 5.2. The tensor $\mathbf{1} + \boldsymbol{\eta}$ which comes up pretty often instead of $\boldsymbol{\eta}$ denotes the change of coordinates from the initial space to the target space: $\mathrm{d}X_i = (\delta_{ij} + \eta_{ij})\,\mathrm{d}x_j$. Therefore, its determinant is the Jacobean of the transformation and refers to changes in volumes: $\mathrm{d}V = \det(\mathbf{1} + \boldsymbol{\eta})\,\mathrm{d}v$. This ultimately gives the formula for the Cauchy stress as (Wriggers, 2008)

$$\boldsymbol{\sigma} = (\mathbf{1} + \boldsymbol{\eta})\frac{\partial E}{\partial\boldsymbol{\varepsilon}}\frac{\mathbf{1} + \boldsymbol{\eta}^\mathsf{T}}{\det(\mathbf{1} + \boldsymbol{\eta})}. \tag{5.10}$$

Then, given the non-harmonic energy density of Eq. (5.8), the stress-strain relation displays a linear stress term $\boldsymbol{\sigma}^L$ proportional to $\mathbf{U}$ as given by Eq. (5.2), and a term which includes the geometrical nonlinearities $\boldsymbol{\sigma}^G$:

$$\boldsymbol{\sigma}^L = \big(\kappa - 2\mu/d\big)U_{ii}\,\mathbf{1} + 2\mu\,\mathbf{U}, \tag{5.11a}$$

$$\boldsymbol{\sigma}^G = \big(\kappa - 2\mu/d\big)\big(\eta_{ij}^2/2 - U_{ii}^2\big)\mathbf{1} + \mu\big(4\mathbf{U}^2 + \boldsymbol{\eta}\boldsymbol{\eta}^\mathsf{T}\big) + 2\big(\kappa - 2\mu/d - \mu\big)U_{ii}\mathbf{U} + \mathcal{O}\big(\eta^3\big). \tag{5.11b}$$

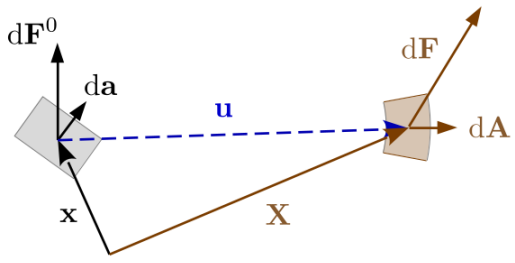

Figure 5.2: Sketch of the are elements and the surface forces in the initial and target spaces.

The Cauchy stress is thus again symmetric. One of the effect of the nonlinearities is that a 2D shear deformation $\boldsymbol{\eta} = \begin{pmatrix} 0 & \eta_{xy} \\ 0 & 0 \end{pmatrix}$ induces both a shear stress response and axial stress responses, such that all components of the Cauchy stress tensor $\boldsymbol{\sigma}$ are non-zero.

In this framework, the force balance equation associating the force density in the target space to the Cauchy stress reads $f_i = -\partial\sigma_{ij}/\partial X_j$. But it may be easier to consider the force density in the initial space $\boldsymbol{\phi} = \mathbf{f}/\det(\mathbf{1}+\boldsymbol{\eta})$. It is related to the first Piola-Kirchhoff stress tensor which relates the surface force in the target space to the initial area: $\boldsymbol{\tau} = \mathrm{d}\mathbf{F}/\mathrm{d}\mathbf{a}$. It can therefore be expressed as $\boldsymbol{\tau} = (\mathbf{1}+\boldsymbol{\eta})\frac{\partial E}{\partial \boldsymbol{\varepsilon}}$. In this case, the force balance equation thus reads $\phi_i = -\partial_j \tau_{ij}$. Since the initial and target spaces are conflated at the linear order, the linear term in the first Piola-Kirchhoff stress is the same in the Cauchy stress $\boldsymbol{\tau}^L = \boldsymbol{\sigma}^L$. But the term due to the geometrical nonlinearities differs from $\boldsymbol{\sigma}^G$ and reads

$$\boldsymbol{\tau}^G = \big(\kappa - 2\mu/d\big)\eta_{ij}^2\,\mathbf{1}/2 + \mu\,\boldsymbol{\eta}^{\mathsf{T}}\boldsymbol{\eta} + \big(\kappa - 2\mu/d\big)U_{ii}\,\boldsymbol{\eta} + 2\mu\,\boldsymbol{\eta}\mathbf{U} + \mathcal{O}\big(\eta^3\big). \tag{5.12}$$

This expression is not symmetric because of the queer nature of the tensor $\boldsymbol{\tau}$, whose first index refers to the target space whereas the second one refers to the initial space.

5.1.3 A neo-Hookean model for constitutive nonlinearities

In two dimensions, a simple example of constitutive nonlinearity is given by a standard "neo-Hookean" model for rubber elasticity:

$$E = \frac{\kappa}{2}\big(J-1\big)^2 + \frac{\mu}{2}\big(I/J - 2\big), \tag{5.13}$$

where

$$I = \mathrm{Tr}(\mathbf{1}+2\boldsymbol{\varepsilon}) = 2(1+\varepsilon_{ii}), \tag{5.14a}$$

$$J = \det(\mathbf{1}+\boldsymbol{\eta}) = \sqrt{\det(\mathbf{1}+2\boldsymbol{\varepsilon})} = \sqrt{1+2(\varepsilon_{ii}+\varepsilon_{ii}^2-\varepsilon_{ij}^2)} \tag{5.14b}$$

are constructed with invariants of the Green-Lagrange strain tensor $\boldsymbol{\varepsilon}$. This model is an attempt to satisfy the physical conditions that stresses be infinite for a volume going to zero and infinity (Wriggers, 2008). For small strains of order $\varepsilon \sim \eta \ll 1$, we recover the Saint Venant-Kirchhoff model of Eq. (5.8):

$$E = \frac{\kappa}{2}\varepsilon_{ii}^2 + \frac{\mu}{2}\big(2\varepsilon_{ij}^2 - \varepsilon_{ii}^2\big) + \mathcal{O}\big(\varepsilon^3\big). \tag{5.15}$$

This means that the constitutive nonlinearities of neo-Hookean materials add up to the purely geometrical ones. For instance, under simple shear plus bulk deformation in the finite strain regime, the shear stress reads

$$\sigma_{xy} = \frac{\mu\,\eta_{xy}}{(1+\eta_{ii}/2)^3}. \tag{5.16}$$

This closed-form expression contains strain terms at all orders in η. It is worth mentioning that experimental stress-strain curves of rubber under *e.g.* uniaxial extension actually show departures from the neo-Hookean law. This has lead to more elaborate models such as Mooney and Rivlin's (Treloar, 1973; Wriggers, 2008) or the one of Arruda and Boyce (1993), in which the network response is decomposed on the principal strain directions.

5.2 Active units in biopolymer networks

The active, stress-generating role of many biological materials stems from their ability to transmit internally generated forces. In cells, the action of molecular motors and the growth of protein fibers over a few nanometers generates anisotropic forces that are further transmitted by a fibrous network, the cytoskeleton, to the scale of the whole cell (Blanchoin et al., 2014; Howard, 2001). At larger length scales, polarized cells in connective tissues exert anisotropic stresses on another fibrous network, the extracellular matrix, which again propagates these stresses far from their application point (Maskarinec et al., 2009; Schwarz and Safran, 2013). The well-characterized nonlinear stress response of these

networks plays a crucial role in force transmission, allowing for quantitative and qualitative changes in the propagated stresses. In the following, we first focus on the force-extension relation of single filaments to understand the shear-stiffening law of biopolymer networks in Sec. 5.2.1. Then in Sec. 5.2.2, we discuss the observed contractility of actomyosin, and we link it to the bucklable behavior of the cell cytoskeleton. We last present a continuum model which accurately reproduces the shear-stiffening tendency of biopolymer gels in Sec. 5.2.3.

5.2.1 Semiflexible polymer networks

In crosslinked polymer networks, the force-extension relation depends principally on $c = l_p/l_c$: the ratio of the persistence length to the distance between two crosslinks. Here, the persistence length quantifies the effect of thermal fluctuations, such that $l_p = \kappa_b/(k_B T)$, where κ_b is the bending modulus, k_B Boltzmann's constant and T the temperature. Contrary to flexible ($c \ll 1$) polymer networks such as rubber or polyacrylamide; semiflexible ($c \gtrsim 1$) and stiff ($c \gg 1$) polymer networks such as actin, fibrin or collagen tend to buckle under compression due to the strain-stiffening behavior of single chains. The bending and buckling tendencies are encapsulated in the term "fiber", which are more than just linear springs (Broedersz and MacKintosh, 2014). In this case, individual semiflexible filaments can be characterized as a worm-like chains with an elastic energy made of a bending and a stretching term. Under compression, an initially straight filament start to buckle as the force exceeds the buckling threshold $f_b = \kappa_b \pi^2/l_c^2$. Applying equipartition on the bending modes leads to the following force-extension relation between the normalized quantities l/l_c and $\varphi = f/f_b$:

$$l/l_c = 1 - \frac{1}{c}\frac{1}{2\pi^2\varphi}\begin{cases}\pi\sqrt{-\varphi}\cot\left(\pi\sqrt{-\varphi}\right) - 1, & \text{for} \quad \varphi < 0,\\ \pi\sqrt{\varphi}\coth(\pi\sqrt{\varphi}) - 1, & \text{for} \quad \varphi > 0,\end{cases} \tag{5.17}$$

while at zero force the average polymer end-to-end distance reads $l_0/l_c = 1 - \frac{1}{6c}$ (Wang and Xu, 2020). As displayed in Fig. 5.3, Eq. (5.17) leads to both stretch-stiffening and compression-softening, the strength of which increases with c. To accurately describe the mechanical properties of biopolymer gels, MacKintosh et al. (1995) and then Storm et al. (2005) introduced a model based directly on this microscopic relation. For an isotropic network with uniform mesh size l_c, given filaments in any orientation on the unit sphere $\hat{\mathbf{r}} = (\cos\theta, \sin\theta\cos\psi, \sin\theta\sin\psi)$ and a displacement gradient $\boldsymbol{\eta}$, his

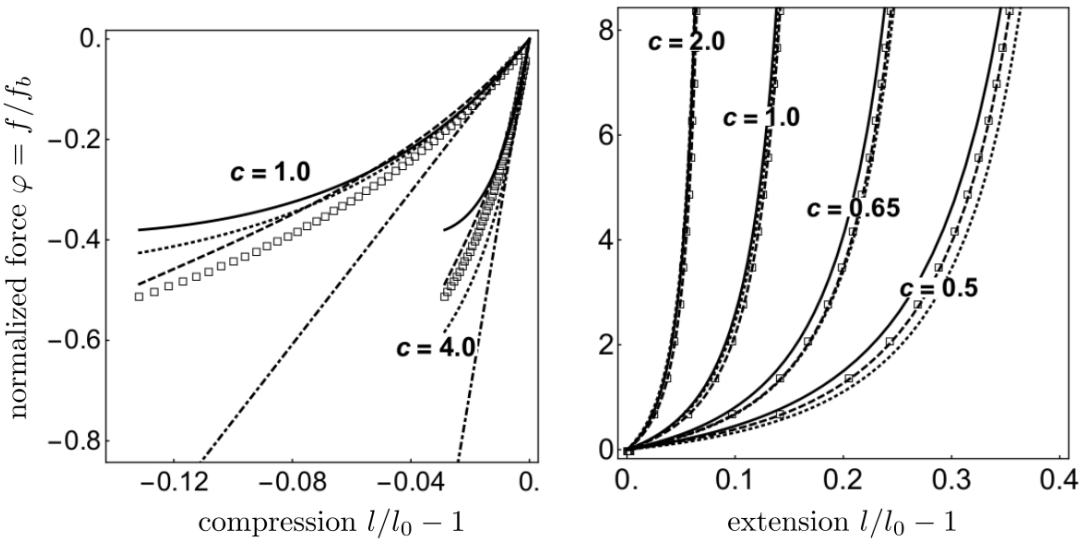

Figure 5.3: **The stretch-stiffening and compressive-softening behaviors of semiflexible polymers.** It all depends on the stiffness parameter: $c = l_p/l_c$. The complicated analytical data points from Eq. (5.17) are compared with some interpolations (thick, dashed, dotted lines) that are easier to handle. On the compression plot, the linear behavior is given by the dot-dashed curves. Adapted from (Wang and Xu, 2020).

formulation for the Cauchy stress tensor is

$$\sigma_{ij} \propto \iint \mathrm{d}\theta \mathrm{d}\psi \frac{\varphi\big(l_0/l_c \|(\mathbf{1}+\boldsymbol{\eta})\hat{\mathbf{r}}\|\big)}{\|(\mathbf{1}+\boldsymbol{\eta})\hat{\mathbf{r}}\|} \frac{[(\mathbf{1}+\boldsymbol{\eta})\hat{\mathbf{r}}]_i [(\mathbf{1}+\boldsymbol{\eta})\hat{\mathbf{r}}]_j}{\det(\mathbf{1}+\boldsymbol{\eta})}, \tag{5.18}$$

where the function φ is obtained by inverting Eq. (5.17). A closed form expression for any deformation $\boldsymbol{\eta}$ is hard to obtain, but as we will see, this model can qualitatively reproduce certain properties of fiber networks, and especially the difference between networks of flexible filaments and networks of semiflexible (or stiff) fibers.

But polymer networks in living systems can be quite far from this simplified view of a homogeneous and isotropically elastic medium. First off, actin fiber networks in the cell cytoskeleton coexist with multiple species of passive and active crosslinkers. The transient dynamics of these crosslinkers can lead irreversibly polymerized networks to flow at long times (Aufderhorst-Roberts and Koenderink, 2019; Schwarz and Safran, 2013). These passive crosslinkers can also act as stochastic ratchets to produce contraction from Brownian fluctuations, or enhance the stresses from molecular motors such as myosin in actin (Komianos and Papoian, 2018; Vale and Milligan, 2000). Moreover, contrary to actin and intermediate filament networks, collagen networks which form the bulk of the extracellular matrix have a connectivity (or mean contact number) Z that is very low (Jansen et al., 2018; Licup et al., 2015). This implies that mechanical rigidity involves the bending of individual fibers, which leads to two different stiffening regimes in networks that are bending-dominated versus stretching-dominated (Broedersz and MacKintosh, 2011; Feng et al., 2016; Lindström et al., 2010; Sheinman et al., 2012). In this case, deformations can be non-affine, *i.e.* affect each fiber differently, contrary to the formulation of Eq. (5.18) in which the displacement gradient is homogeneous.

Regarding the characteristic properties of biopolymer networks, multiple experiments from Gardel

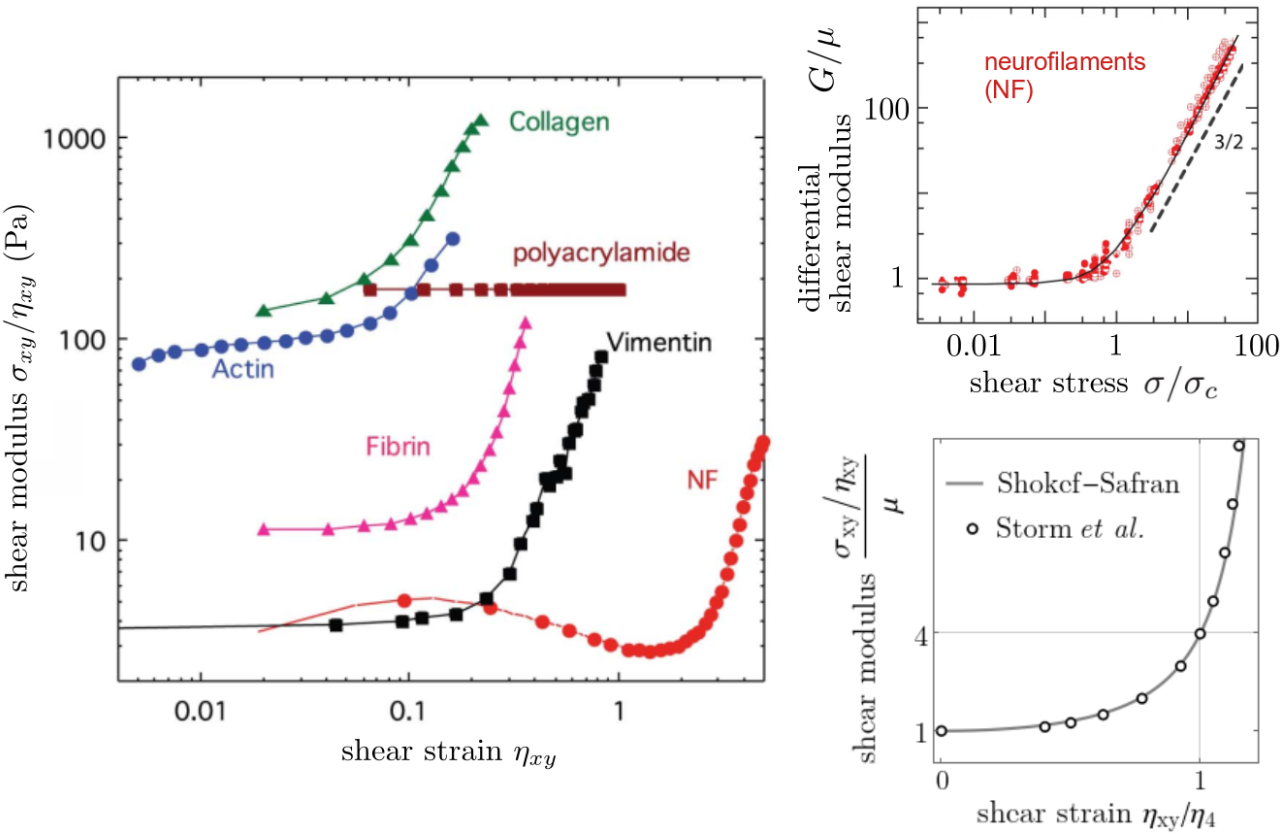

Figure 5.4: **Shear-stiffening behavior of biological fiber networks.** *Left*, experimental curves showing the stiffening of different gels at different strain thresholds. *Top*, 3/2 law of the differential shear modulus with the shear stress. Both adapted from (Broedersz and MacKintosh, 2014). *Bottom*, the shear-stiffening behavior is equivalent in the models of Storm et al. (2005) and Shokef and Safran (2012), see Eqs. (5.18) and (5.21).

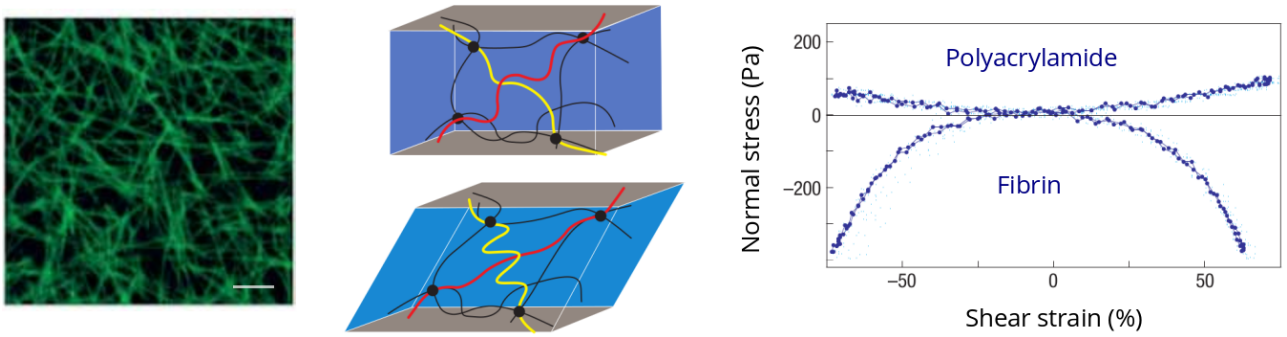

Figure 5.5: **Poynting effect in polymer networks.** *Left*, a confocal image of a fibrin network, adapted from Gersh et al. (2009). The scale bar is 10μm. *Middle*, Under shear, the normal stress response to shear stems from the competition between the compression of the yellow filament and the extension of the red one. *Right*, flexible polymer networks (rubber, polyacrylamide, etc.) display a positive normal stress. Whereas pre-stretched semiflexible polymer networks (actin, fibrin, vimentin, collagen, etc.) display a negative normal stress. Adapted from (Janmey et al., 2007).

et al. (2004), Storm et al. (2005), and Lin et al. (2010) have robustly shown that these networks display a shear-stiffening behavior, where the differential shear modulus

$$G = \frac{\partial \sigma_{xy}}{\partial \eta_{xy}} \sim \sigma_{xy}^{3/2} \tag{5.19}$$

under large strains, see Fig. 5.4. It is particularly interesting that polyacrylamide, in which the filament segments between two crosslinks are flexible, does not stiffen under shear. This is in agreement with the worm-like chain model of Fig. 5.3, in which flexible polymers with $c \ll 1$ display very few nonlinearity. Other nonlinear effects include the alignment of fibers along the principal deformation axis, which helps extend the range of force transmission in biopolymer networks (Vader et al., 2009; Wang et al., 2014; Xu and Safran, 2015). Moreover, contractile normal stresses tend to build up under shear, as the extended fibers pull the gel boundaries (Jansen et al., 2018; Licup et al., 2015; Meng and Terentjev, 2016). This is contrary to the usual Poynting effect observed in flexible polymer networks, where the entropic elasticity of the compressed filament tends to dilate the gel under shear, see Fig. 5.5. Overall, the nonlinear stress response of these networks plays a crucial role in force transmission, allowing for the enhancement of contractile stresses (Han et al., 2018; Murrell and Gardel, 2012; Ronceray et al., 2016; 2019). This also promotes long-range mechano-sensitivity (Notbohm et al., 2015; Rosakis et al., 2015; Sopher et al., 2018) and allows for better communication between *e.g.* fibroblasts in collagen networks (Grinnell, 2003).

5.2.2 Transmission of contractile stresses in bucklable fiber networks

Beyond stress amplification, the fundamental asymmetry in the response of fibrous networks to tension versus compression, be it due to buckling or fiber-alignment, can also qualitatively alter stresses upon propagation. Apart from the regular sarcomeric organization of muscle actomyosin (Dasbiswas et al., 2018), disordered actomyosin in non-muscle cells has been observed to be overwhelmingly contractile (Linsmeier et al., 2016; Murrell et al., 2015; Oakes et al., 2014; Scholey et al., 2003). In this case, the buckling of individual fibers has been shown to correlate with contractile regions (Murrell and Gardel, 2012). This contractility happens despite the fact that myosin motors can produce local force dipoles either contractile or extensile, depending on the polarity of the two filaments at both ends of the motor. Lenz et al. (2012b) successfully linked filament buckling to the rectification of local stresses to far-field contraction in a one-dimensional model. Belmonte et al. (2017) performed dynamical analyses on three-dimensional bucklable fiber assemblies in the presence of both passive and active crosslinkers, and found both analytically and numerically that these systems were biased towards large-scale contraction. Additional numerical simulations by Ronceray et al. (2016) showed a similar effect. In these simulations, a localized active unit exerts anisotropic forces in the center of a large

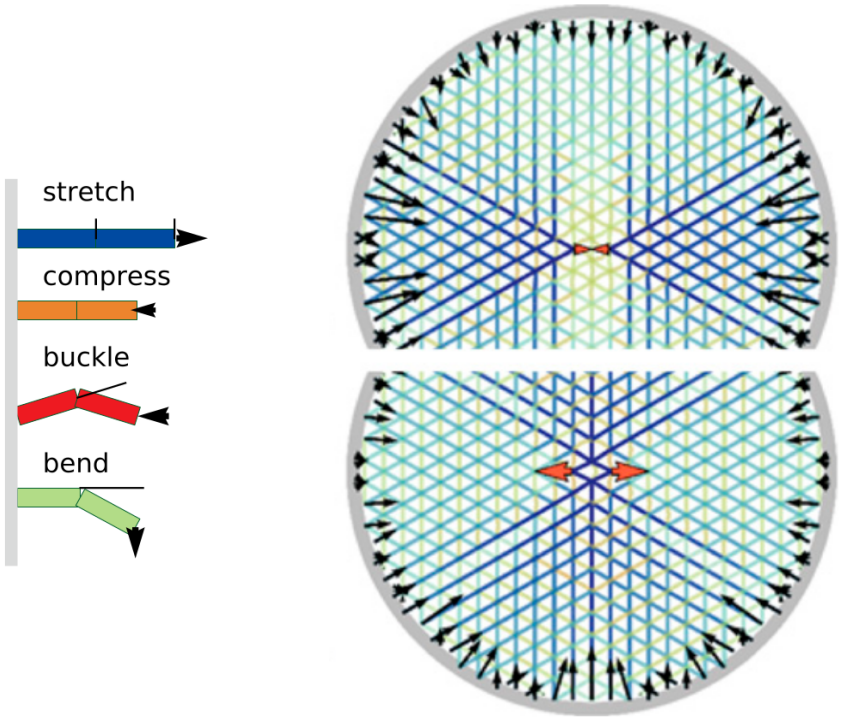

Figure 5.6: **Discrete fiber network rectify internal stresses towards contraction.** Each fiber is made of two segments, such that it can respond realistically to stress as would a semiflexible polymer chain. In particular, under a sufficient compressive force the fiber buckles which dramatically reduces the propagation of compressive stresses with respect to tensile ones. In the large internal force regime, the stresses from force dipoles of either signs are rectified to a homogeneous contraction at the fixed boundary. Adapted from (Ronceray et al., 2016).

network of discrete fibers, each of which can buckle under a sufficiently large compressive force, see Fig. 5.6. For localized forces much larger than this buckling threshold, the far-field stresses transmitted by the network become contractile. This is valid even in cases where the local forces are predominantly expansile, because the network resists and therefore propagates tension more than compression. This stress "rectification" could help explain why the actomyosin cytoskeleton is overwhelmingly observed to contract irrespective of its detailed internal architecture. Interestingly, the introduction of bond disorder in the network by *e.g.* random pruning does not induce qualitative changes in the network bias towards contraction, provided that it is averaged over the disorder (Ronceray and Lenz, 2015; Ronceray et al., 2016).

5.2.3 Continuum models with coarse-grained stresses

In the previously discussed simulations, the actomyosin gel is modeled with discrete fibers and crosslinks. But the cell cytoskeleton can also be viewed as a continuum elastic or visco-elastic medium subjected to microscopic force dipoles, in the spirit of the active gel model introduced by Prost et al. (2015). In this framework, the system is subject to a macroscopic, coarse-grained "active stress" obtained by averaging the force dipole density, at least for a linear elastic law (Ronceray and Lenz, 2015). In nonlinear elasticity, Ronceray et al. (2016) showed that the coarse-grained active stress from local force dipoles can be amplified, isotropized and rectified depending on the medium properties.

Besides, based on previous work from Knowles (1977), Shokef and Safran (2012) have developed an interesting continuum model for fibrous networks. It is a variant of the neo-Hookean model of Eq. (5.13), which has the shear-stiffening behavior $G \propto \sigma_{xy}^{3/2}$ characteristic of fiber networks under large strains [Fig. 5.4]. In 2D, its elastic energy density reads

$$E = \frac{\kappa}{2}\,(J-1)^2 + \frac{\mu}{2g}\Big[1 - g\big(I/J - 2\big)\Big]^{-1}, \tag{5.20}$$

where $I = \mathrm{Tr}(\mathbf{1} + 2\boldsymbol{\varepsilon})$, $J = \det(\mathbf{1} + \boldsymbol{\eta})$ and $g > 0$ is a parameter related to the shear-stiffening behavior. The Saint Venant-Kirchhoff model is again recovered in the small-strain regime, but under finite shear strain, the shear component of the Cauchy stress tensor reads

$$\sigma_{xy} = \mu \frac{\eta_{xy}}{(1 - g\,\eta_{xy}^2)^2}. \tag{5.21}$$

As $\eta_{xy} \to 1/\sqrt{g}$, it thus diverges as $(\eta_{xy} - 1/\sqrt{g})^{-2}$. Therefore, the differential shear modulus G scales as $(\eta_{xy} - 1/\sqrt{g})^{-3}$, and we recover Eq. (5.19). The shear strain threshold for the stiffening behavior is roughly $0.4/\sqrt{g}$, such that the neo-Hookean model is recovered for $g = 0$, see Eq. (5.16). Typical values for g lie in $[2, 50]$, corresponding to the strain thresholds displayed in Fig. 5.4, *left*. As displayed in Fig. 5.4, *bottom*, the shear-stiffening behavior of Eq. (5.21) strikingly matches the one of the model of Storm et al. (2005), given by the complicated expression in Eq. (5.18). This encourages us to use the simple model related to Eq. (5.20) in the finite element simulations of Sec. 7.1.

5.3 Plastic events in nearly-jammed grain packings

Granular matter refers to assemblies of many small solid or liquid spheroid objects in a medium filled with another immiscible liquid or gas. This terminology thus encompasses just as well sand dunes, toothpaste (colloids in a fluid), mayonnaise (emulsion of oil droplets in water), and shaving foam (gas bubbles in a fluid) (van Hecke, 2009). In particular, packings of spherical beads share a number of mechanical properties which can be characterized with a small number of observables (O'Hern et al., 2003). When sheared, granular media experience localized plastic events known as shear transformations which generate anisotropic internal stresses (Lin et al., 2014; Merabia and Detcheverry, 2016; Picard et al., 2004). Under strong confining pressure, the response of granular media to a localized force multipole is essentially linear, and elasto-plastic models predict that the far-field stresses conserve the quadrupolar symmetry resulting from the local rearrangement (Desmond and Weeks, 2015; Kabla and Debrégeas, 2003; Nicolas et al., 2018). Closer to the jamming transition however, as the confining pressure and the shear modulus vanish, nonlinear effects become relevant. We then suspect the medium not to conserve the symmetries of the local stress field and we investigate the possible rectification that may arise as stresses propagate. This could significantly modify the yielding transition of amorphous media, which has been conceptualized as an avalanche of these plastic events (Amon et al., 2012; Arévalo and Ciamarra, 2014; Budrikis et al., 2017; Nicolas et al., 2018). In the following, we discuss the characteristic features of the jamming transition in Sec. 5.3.1, and characterize the mechanical response of granular media to internal stresses in Sec. 5.3.2.

5.3.1 The jamming transition

Consider a large number of elastic beads in a d-dimensional box with periodic boundary conditions at a certain volume fraction ϕ. The interaction between two beads depends on their overlap δ via a potential of the form $\mathcal{V} \sim \delta^a$, see Fig. 5.7. Here, harmonic interactions with $a = 2$ correspond to linear springs, where the bead strength $\partial^2\mathcal{V}/\partial\delta^2$ is independent of δ. But for usual objects such as bowling balls or sand, this may be oversimplifying. Indeed, as δ increases, the contact area (assuming reasonably good contact between smooth surfaces) increases, which causes the bead strength to increase as well as $\sqrt{\delta}$. Therefore, a more accurate model relies on Hertz's potential given by $\mathcal{V} \sim \delta^{5/2}$ (Makse et al., 2004).

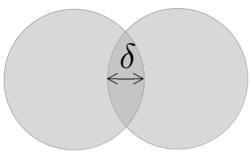

Figure 5.7: Overlap between two interacting beads in a granular simulation.

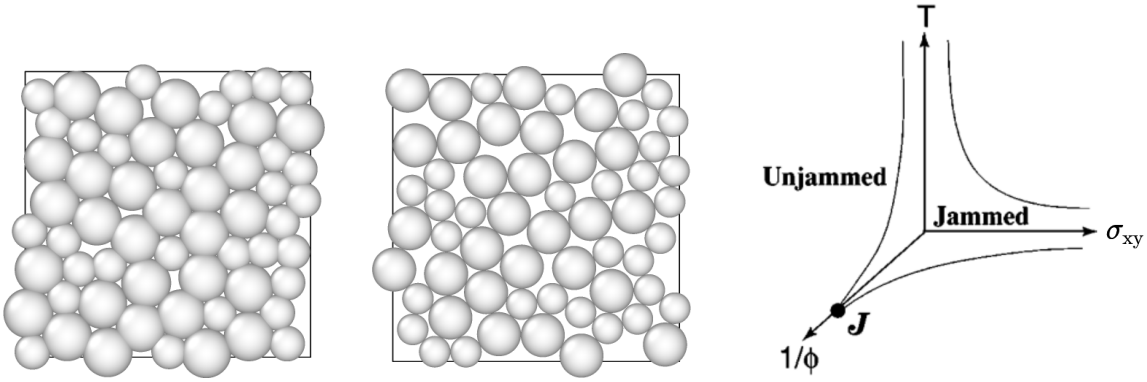

Figure 5.8: **The jamming transition in granular media.** *Left*, a strongly-jammed bidisperse configuration in 2D at area fraction $\phi = 1.09$ and contact number $Z = 5.57$. *Middle*, a bidisperse configuration near jamming ($\phi = 0.835$, $Z = 4.2$), where particles hardly overlap. *Right*, jamming phase diagram adapted from (O'Hern et al., 2003). Jammed configurations are found at low temperature T, low shear stress σ_{xy} and high ϕ. For athermal configurations under vanishing applied shear, point J indicates the critical volume fraction ϕ_c at which jamming happens. Likewise for $\phi < \phi_c$, a system can unjam under a sufficiently large shear stress at the yielding transition.

At low density $\phi \ll 1$, the beads are free to move when the box is shaken, and a slight change in the volume of the box does not solicit a response from the beads. Contrarily, at high density $\phi \gtrsim 1$, the beads are closely packed in a jammed configuration and overlap substantially, see Fig. 5.8. This creates mechanical force chains which extend from one side of the box to another. Consequently, the beads respond to an isotropic pushing on the box with a finite pressure P. Slightly changing the volume of the box varies the pressure but does not act significantly on the conformation of the beads. However, as the confining pressure is decreased from a jammed state, the beads overlap less and less until their overlap is zero and the pressure vanishes at the so-called (un)jamming point J. Just above point J, a small perturbation can produce large conformational changes. For frictionless contacts, at the isostatic point J, the contact number $Z = 2d$, while jammed systems require $Z > 2d$. Hence, in $d = 2$ dimensions, monodisperse configurations near jamming can be conceptualized as square-like arrangements of beads with $Z \gtrsim 4$. However, for monodisperse beads, the dense triangular packing is locally preferred which can create some unwanted regularity in the spatial configuration, especially at high density. A simple solution consists in introducing polydispersity in the system. Traditionally, people consider 50:50 bidisperse configurations with a ratio of diameters 1.4. This leads to the mix of square and triangular arrangements displayed in Fig. 5.8, *middle*.

This jamming transition can be characterized as a phase transition in the sense that the pressure goes from zero below the transition to a finite value for jammed system; and that relevant physical observables display universal scalings close to the jamming point. But some features of this transition are quite peculiar. Indeed, as one decreases the usual control parameter ϕ from 1, the critical value ϕ_c at which the order parameter P vanishes depends on the history of the packing. In two dimensions, $0.835 \lesssim \phi_c \lesssim 0.91$, where the upper bound corresponds to the triangular packing, while the lower bound refers to an infinite random close packing (van Hecke, 2009). This leads us to introduce $\Delta\phi = \phi - \phi_c$ as the "distance to jamming". For nearly-jammed systems $0 < \Delta\phi \ll 1$, depending on the potential exponent a, the pressure and contact number scale as

$$P \sim (\Delta\phi)^{a-1} \quad \text{and} \quad Z - 2d \sim \sqrt{\Delta\phi} \tag{5.22}$$

whatever the dimension and polydispersity. Then, the bulk and shear moduli typically scale as $K \sim (\Delta\phi)^{a-2}$ and $G \sim (\Delta\phi)^{a-3/2}$, which can lead to discontinuities at the transition (Ellenbroek et al., 2009a; O'Hern et al., 2003). One way to understand the nonlinear behavior close to jamming is that even small forces can open or close contacts. This is such that the mechanical stiffness, which results from the collective response of the packing, is highly dependent on the imposed deformation. As the shear modulus G vanishes, the system can undergo large displacements as delocalized soft modes are

easier to excite (Silbert et al., 2009; van Hecke, 2009), which can lead to non-local and irreversible effects, as well as geometric nonlinearities.

5.3.2 Shear transformations near jamming

Under shear, localized plastic events called shear transformations generate internal stresses. In principle, it creates both shear and compression, although the compression is usually neglected under the assumption that grain packings are incompressible. It is widely accepted that the relative shear stress with respect to the imposed one typically displays a quadrupolar symmetry (Desmond and Weeks, 2015; Kabla and Debrégeas, 2003; Nicolas et al., 2018), as shown in Fig. 5.9 for a foam. As explained by Nicolas et al. (2018), in two dimensions, a shear deformation in $r = 0$ consists of a stretch along a certain direction, and a contraction along the perpendicular direction, which corresponds to a dipolar dependence for the displacement $\mathbf{u}$. Within linear elasticity in an incompressible medium, Picard et al. (2004) showed that the strain and stress fields are characterized by a shear component $\propto \cos(4\theta)/r^2$. This derivation can moreover be straightforwardly extended to a tensorial form (Budrikis et al., 2017; Nicolas and Barrat, 2013). This assumption of linear elasticity seems however difficult to maintain for nearly-jammed systems. Boschan et al. (2016; 2017) argue that the shear response of soft media can be considered linearly elastic, provided the forcing is slow and weak. Yet, these approximations both break down at the point where the material loses rigidity. Actually, several crossover scales between the linear and nonlinear behaviors scale with the distance to jamming. This is such that at vanishing pressure, the material response is exclusively nonlinear, due to the many contact changes that can occur (Dagois-Bohy et al., 2017; Schreck et al., 2011a). van Deen et al. (2014) state that numerical studies of linear response have either imposed very small strains $\sim 10^{-10}$, or have focused on the strict linear response extracted from the Hessian matrix.

In experiments on sheared dense emulsions, Desmond and Weeks (2015) have measured stress propagators around individual plastic events. They show that the propagators isotropize as jamming is approached from above, see Fig. 5.10. In a more quantitative manner, the propagator for each data set is fitted to

$$\Pi(r,\theta) = \frac{\Pi_0 + \Pi_1 \cos 4\theta}{(r/\langle d\rangle)^2}, \tag{5.23}$$

and the fitting parameters are shown as functions of area fraction. We see that the isotropic part Π_0 decreases with ϕ, while the quadrupolar part increases. For the authors, this isotropization close to jamming is due to increased spatial heterogeneity and data averaging. Indeed, Ellenbroek et al. (2006) point out that the response to local forcing fluctuates over a length scale that diverges at the jamming transition. We believe however that as nonlinearities build up close to the unjamming point, more isotropic propagators can be expected due to the rectification of the locally contractile regions towards far-field expansion. Indeed, tension near jamming results in contact losses which prevents propagation, such that from a local mixture of tension and compression, it is compression that tends to take over and

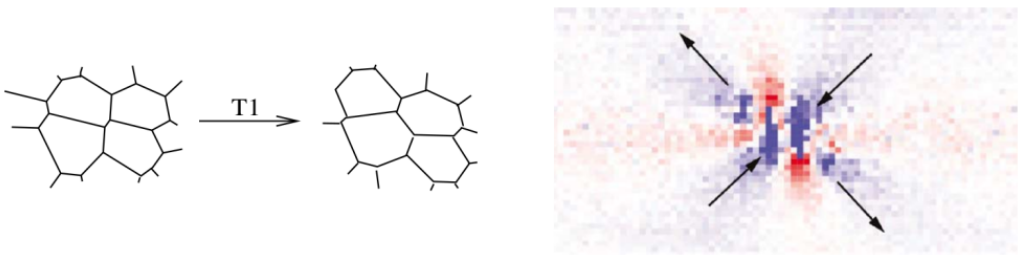

Figure 5.9: **Conformational changes in granular media generate quadrupolar stress.** *Left*, under shear, foams undergo shear transformations. Well-characterized examples include T1 events which consist in a local change of neighbors that generate internal stresses with a quadrupolar symmetry. *Right*, the plastic event is visible through the arrows denoting the motions of the rearranging bubbles. Red (blue) zones correspond to a relative increase (decrease) of the local shear stress. From (Kabla and Debrégeas, 2003).

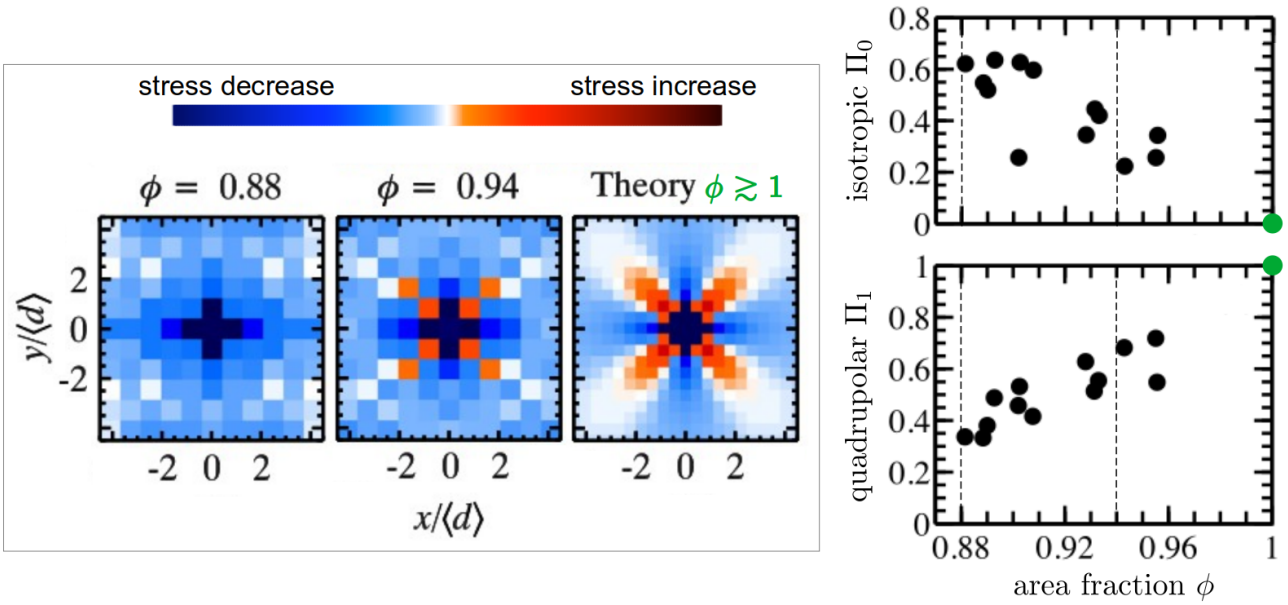

Figure 5.10: **The propagator seems to switch from quadrupolar to isotropic near jamming.** *Left*, measured stress propagator in a concentrated emulsion close to jamming ($\phi_c \approx 0.86$) shows departures from the linear elastic theory for large area fractions $\phi \gtrsim 1$. Red (blue), relative increase (decrease) of the shear stress compared to the imposed one. The spatial coordinates x, y are rescaled by the mean droplet diameter $\langle d \rangle$. *Right*, coefficients for the isotropic and quadrupolar parts of the fitted propagator of Eq. (5.23). The green points correspond to the theoretical fully quadrupolar propagator. Adapted from (Desmond and Weeks, 2015).

produce an expansion of the medium at larger scale. We further develop this statement analytically and numerically in Ch. 6 and 7. In order to study the mechanical response of bead packings to internal stresses, it can be useful to use a continuum elastic description. Yet, it is not self-evident that it can yield realistic results. For instance, the compressive force chains which build up under stress tend to induce heterogeneity and anisotropy in the medium (Geng et al., 2001; Otto et al., 2003). We hope that these effects can be neglected in our small-strain study.

Chapter 6

Analytical continuum model for fibrous and granular media

Here, we generalize the results of Ronceray et al. (2016) [Fig. 5.6] beyond bucklable fiber networks, and demonstrate that stress rectification is a generic corollary of stress propagation in a nonlinear elastic medium. Our approach is based on a continuum formalism that allows a general discussion of arbitrary nonlinearities. We consider an elastic material with a set of embedded active units. The resulting stresses are then propagated towards the fixed boundary of the material. We then investigate the conditions of emergence of rectification phenomena such as when a locally expansile active units leads to far-field contraction, as described in Ch. 5. We show here that this stress rectification may arise from geometrical and/or constitutive nonlinearities in the material elastic response, in relation to the material tendency to buckling or anti-buckling.

Our study proceeds as follows. In Sec. 6.1, to characterize the possible alteration of stress propagation during its propagation, we define coarse-grained stresses, both close to and far away from the active units. And we show that geometrical nonlinearities always bias the system towards contraction. We then present in Sec. 6.2 a small-strain model including both geometrical nonlinearities and generic material-dependent nonlinearities describing the response of the material to compression or tension. Nonlinearities whereby the material stiffens under tension and soften under compression are characteristic of bucklable fiber networks (Storm et al., 2005). Conversely, materials that soften under tension and stiffen under compression, or "anti-buckle", may offer a description of granular media, where contacts between grains are disrupted as the confining pressure is decreased (Ellenbroek et al., 2009b). In Sec. 6.3, we proceed to quantify the rectification of stresses from a circular active unit in a weakly nonlinear material. We show in Sec. 6.4 that rectification is a generic phenomenon, and that the elastic constants describing the weakly nonlinear response of a material are a reliable predictor of the sign and magnitude of rectification.

6.1 Geometrical nonlinearities favor contraction

We consider a piece of homogeneous, isotropic elastic medium of dimension d comprised in a domain Ω. A set of anisotropic active units (*e.g.*, molecular motors or shear transformation zones) exerts forces and/or imposes local displacements on the medium. This induces a force density $\mathbf{f}$, resulting in a Cauchy stress tensor $\boldsymbol{\sigma}$ given by the force balance equation $f_i = -\partial\sigma_{ij}/\partial X_j$. Here $\mathbf{X} = \mathbf{x} + \mathbf{u}$ is the final location (in the target space) of a material point initially located in $\mathbf{x}$ (in the initial space), $\mathbf{u}$ denotes the displacement vector and the summation over repeated indices is implied. The boundary $\partial\Omega$ of the medium is held fixed, such that the forces exerted by the active units are transmitted through the medium and cause it to exert a coarse-grained stress

$$\bar{\sigma}^a_{ij} = \frac{1}{V}\oint_{\partial\Omega} \sigma_{ik} X_j \,\mathrm{d}A_k \tag{6.1}$$

onto the boundary (Ronceray and Lenz, 2015), where V is the volume of the medium and $\mathrm{d}\mathbf{A}$ the outward-directed area element in the target space. In the context of active matter, $\bar{\boldsymbol{\sigma}}^a$ is known as the

active stress generated by the overall system comprised by the medium and the active units (Prost et al., 2015). We define as contraction (expansion) a situation where the active pressure $P_a = -\bar{\sigma}^a_{ii}/d$ is negative (positive). To investigate the relationship between the local forces $\mathbf{f}$ and the active stress $\bar{\boldsymbol{\sigma}}^a$, we define the coarse-grained local stress

$$\bar{\sigma}^l_{ij} = -\frac{1}{V}\int_\Omega f_i X_j \,\mathrm{d}V, \tag{6.2}$$

where $\mathrm{d}V$ is the volume element in the target space.

In the special case where the force transmission is entirely linear, this relation simply reads $\bar{\boldsymbol{\sigma}}^a = \bar{\boldsymbol{\sigma}}^l$, implying in particular an equality of the active and local pressures $P_a = P_l = -\bar{\sigma}^l_{ii}/d$. In that case, contractile (expansile) local forces always imply a contractile (expansile) active stress. These equalities are however violated in nonlinear media (Carlsson, 2006; Ronceray and Lenz, 2015), and the local and active pressures P_l and P_a can have opposite signs. Indeed, given the force balance equation $f_i = -\partial\sigma_{ij}/\partial X_j$, the difference between the local and active coarse-grained stresses can be integrated by parts to read

$$\bar{\boldsymbol{\sigma}}^a - \bar{\boldsymbol{\sigma}}^l = \frac{1}{V}\int_\Omega \boldsymbol{\sigma}\,\mathrm{d}V = \frac{1}{V}\int_\Omega \boldsymbol{\sigma}\det(\mathbf{1}+\boldsymbol{\eta})\,\mathrm{d}v, \tag{6.3}$$

where $\mathrm{d}v$ is the volume element in the initial space. Equation (6.3) is known as the mean stress theorem (Carlsson, 2006; Gurtin, 1973; Ronceray and Lenz, 2015). We can write $\mathbf{S} = \boldsymbol{\sigma}\det(\mathbf{1}+\boldsymbol{\eta})$ and decompose $\mathbf{S} = \mathbf{S}^L + \mathbf{S}^{\mathrm{NL}}$ as we did $\boldsymbol{\sigma}$ in Eq. (5.11). We thus obtain that due to our fixed boundary condition, the integral of the trace of the linear term $\mathbf{S}^L = \boldsymbol{\sigma}^L$ vanishes. Therefore, as expected, linear elastic materials propagate stresses without alteration.

We now consider a constitutively linear material with the energy density given by Eq. (5.8) and set out to prove that geometrical nonlinearities always favor contraction. Due to the relation in Eq. (6.3), writing $\mathbf{S}^{\mathrm{NL}} = \mathbf{S}^G$, the pressure difference reads

$$P_a - P_l = -\frac{1}{Vd}\int_\Omega \mathrm{d}v\, S^G_{ii}, \tag{6.4}$$

where the trace of the nonlinear term of $\mathbf{S}$ is expressed in a closed form as

$$S^G_{ii} = \frac{\kappa}{2}\left(d\eta_{ij}^2 + 4\varepsilon_{ii}^2\right) + 4\mu\left(\varepsilon_{ij}^2 - \varepsilon_{ii}^2/d\right). \tag{6.5}$$

Here, κ and μ are both positive for mechanical stability. Thus, for $d \geq 2$, the geometrical term S^G_{ii} always gives a positive (contractile) contribution to the active stress. Indeed, using the eigenvalues $\lambda_i \in \mathbb{R}$ of the symmetric matrix $\boldsymbol{\varepsilon}$, we can rewrite $\varepsilon_{ij}^2 - \varepsilon_{ii}^2/d = \sum_{i<j}(\lambda_i - \lambda_j)^2/d$, which is always non-negative. As a result S^G_{ii} is a sum of squares that is also non-negative, implying

$$P_a \leq P_l. \tag{6.6}$$

This inequality means that the system as a whole is always more contractile than the local forces, implying that geometrical nonlinearities always induce a rectification towards contraction.

Finally, we present an alternative derivation of this relation that highlights its frame indifference (Steigmann, 2007). The integrand of Eq. (6.4) can be rewritten using the deformation gradient $\boldsymbol{\Lambda} = \mathbf{1} + \boldsymbol{\eta}$ and the right Cauchy-Green deformation tensor $\mathbf{C} = \boldsymbol{\Lambda}^\mathsf{T}\boldsymbol{\Lambda} = \mathbf{1} + 2\boldsymbol{\varepsilon}$. Indeed, since

$$\mathbf{S} = \boldsymbol{\Lambda}\frac{\partial E}{\partial \boldsymbol{\varepsilon}}\boldsymbol{\Lambda}^\mathsf{T}, \quad \text{where} \quad \frac{\partial E}{\partial \boldsymbol{\varepsilon}} = \frac{\kappa}{2}(C_{ii} - d)\mathbf{1} + \mu\big(\mathbf{C} - C_{ii}\mathbf{1}/d\big), \tag{6.7}$$

we can write

$$S_{ii} = \frac{\kappa}{2}\left[(C_{ii} - d)^2 + dC_{ii}\right] + \mu\left[C_{ij}^2 - C_{ii}^2/d\right]. \tag{6.8}$$

We see that the right-hand side Eq. (6.8) is a sum of squares plus a term $\propto C_{ii} = d + 4\eta_{ii} + 4\eta_{ij}^2$. Since η_{ii} is integrated to zero due to the fixed boundary condition, the term in Eq. (6.8) also gives a contractile contribution to $P_a - P_l$.

6.2 Asymmetry in stiffness linked to buckling behaviors

To analytically compute the coarse-grained stresses in the case of geometrical and constitutive nonlinearities, we consider the small strain regime and we generically develop Hooke's law to the lowest nonlinear order. As shown in Sec. 6.2.1, this yields two new parameters corresponding to nonlinear corrections to the bulk and shear moduli. In Sec. 6.2.2, we then quantitatively relate these parameters to the buckling behavior of fiber networks. Likewise in Sec. 6.2.3, we obtain significant values of these nonlinear corrections in granular media which tend to anti-buckle. Finally, Sec. 6.2.4 focuses on other types of materials which appear to have an intermediate behavior.

6.2.1 Weakly nonlinear regime

As in Sec. 5.1.2, we quantify the elastic deformation of our medium using the displacement gradient $\eta_{ij} = \partial u_i/\partial x_j$ and the Green-Lagrange strain tensor $\boldsymbol{\varepsilon} = (\boldsymbol{\eta} + \boldsymbol{\eta}^\mathsf{T} + \boldsymbol{\eta}^\mathsf{T}\boldsymbol{\eta})/2$. To describe nonlinearities resulting from the medium constitutive properties, we consider a two-dimensional isotropic, achiral elastic medium with a non-harmonic energy density:

$$E = \frac{\kappa + \kappa'\varepsilon_{ii}/3}{2}\varepsilon_{ii}^2 + \frac{\mu + \mu'\varepsilon_{ii}}{d}\big(d\varepsilon_{ij}^2 - \varepsilon_{ii}^2\big) + \mathcal{O}\big(\eta^4\big), \tag{6.9}$$

where the coefficients κ', μ' can be of either sign and characterize the most general, lowest-order nonlinearity. According to Eq. (6.9), when the material is isotropically dilated by a relative amount $\varepsilon_{ii} \sim \delta V/V_0$ its bulk (shear) modulus exceeds that of a purely harmonic material by $\kappa'\delta V/V_0$ ($\mu'\delta V/V_0$). Under isotropic contraction however, the corrections to the moduli are of opposite sign than under dilation, which makes the material response asymmetric. The Cauchy stress which ensues from Eq. (6.9) via its definition in Eq. (5.10) can be expressed with the displacement gradient $\boldsymbol{\eta}$ and the linear strain $\mathbf{U}$ as

$$\boldsymbol{\sigma}^L = \big(\kappa - 2\mu/d\big)U_{ii}\,\mathbf{1} + 2\mu\,\mathbf{U}, \tag{6.10a}$$

$$\boldsymbol{\sigma}^G = \big(\kappa - 2\mu/d\big)\big(\eta_{ij}^2/2 - U_{ii}^2\big)\mathbf{1} + \mu\big(4\mathbf{U}^2 + \boldsymbol{\eta}\boldsymbol{\eta}^\mathsf{T}\big) + 2\big(\kappa - 2\mu/d - \mu\big)U_{ii}\mathbf{U} + \mathcal{O}\big(\eta^3\big), \tag{6.10b}$$

$$\boldsymbol{\sigma}^C = 3\big(\kappa' - 2\mu'/d\big)U_{ii}^2\,\mathbf{1}/2 + \mu' U_{ij}^2\,\mathbf{1} + 2\mu' U_{ii}\,\mathbf{U} + \mathcal{O}\big(\eta^3\big). \tag{6.10c}$$

where we have separated the linear strain term $\boldsymbol{\sigma}^L$ from the geometrical and constitutive nonlinearities $\boldsymbol{\sigma}^G$ and $\boldsymbol{\sigma}^C$. Under a combination of bulk deformation and simple shear $\boldsymbol{\eta} = \begin{pmatrix} \eta_{ii}/2 & \eta_{xy} \\ 0 & \eta_{ii}/2 \end{pmatrix}$, the stress response of a material can be characterized by its differential bulk and shear moduli as

$$K = \frac{\partial \sigma_{xx}}{\partial \eta_{ii}} = \kappa\,(1 + \kappa_1\eta_{ii}) + \mathcal{O}\big(\eta^2\big), \tag{6.11a}$$

$$G = \frac{\partial \sigma_{xy}}{\partial \eta_{xy}} = \mu\,(1 + \mu_1\eta_{ii}) + \mathcal{O}\big(\eta^2\big), \tag{6.11b}$$

The right-hand sides of these equations contains all terms up to order 2 which respect the deformation symmetries. In particular, terms linear in η_{xy} are not allowed since they would induce a chirality in the medium whose stiffness would depend on the direction of the applied shear. Higher order terms respecting the symmetries of an isotropic, achiral system include for instance η_{ii}^2 and η_{xy}^2. Here, the first order nonlinear corrections to the differential moduli

$$\kappa_1 = 1/2 + \kappa'/\kappa \quad \text{and} \quad \mu_1 = \kappa/\mu + 1/2 + \mu'/\mu. \tag{6.12}$$

include contributions from geometrical as well as constitutive nonlinearities. Given Eq. (6.11), $\kappa_1, \mu_1 > 0$ describe a material which stiffens under tension and softens under compression, similarly to the buckling of biological fiber networks described in Sec. 5.2. On the contrary, $\kappa_1, \mu_1 < 0$ refers to tension-softening and compression-stiffening, akin to the behavior of a granular material near jamming detailed in Sec. 5.3. For the expansion of Eq. (6.11) to be valid, the corrections have to be small, *i.e.* $\kappa_1\eta_{ii}, \mu_1\eta_{ii} \ll 1$.

We now detail the form of the stress tensor associated to different elementary deformation states.

- Under **simple shear strain** $\boldsymbol{\eta} = \begin{pmatrix} 0 & \eta_{xy} \\ 0 & 0 \end{pmatrix}$, all components of the symmetric stress tensor are non-zero. And while the shear stress is all linear $\sigma_{xy} = \mu\,\eta_{xy} + \mathcal{O}(\eta^3)$ (*i.e.* no shear-softening/stiffening), the axial stresses are exclusively quadratic and read

$$\sigma_{xx} = \mu\frac{5+2\mu_1}{4}\eta_{xy}^2 + \mathcal{O}(\eta^3) \quad \text{and} \quad \sigma_{yy} = \mu\frac{1+2\mu_1}{4}\eta_{xy}^2 + \mathcal{O}(\eta^3). \tag{6.13}$$

  These terms correspond to the Poynting effect in solids and gels (Janmey et al., 2007), or to Reynolds dilatancy in grain packings (Coulais et al., 2014; Ren et al., 2013). Under shear, normal stresses appear which are positive for bucklable materials, *i.e.* the material pulls inwards [Fig. 5.5]. The reverse effect of a dilating (negative) normal stress in anti-bucklable media has also been observed in rubber-like materials and in grains.

- Under **bulk deformation** $\boldsymbol{\eta} = \begin{pmatrix} \eta_{ii}/2 & 0 \\ 0 & \eta_{ii}/2 \end{pmatrix}$, the stress tensor is also diagonal. And the stress components read

$$\sigma_{xx} = \sigma_{yy} = \kappa\big(1 + \kappa_1\eta_{ii}/2\big)\eta_{ii} + \mathcal{O}(\eta^3), \tag{6.14}$$

  in agreement with Eq. (6.11a).

- Finally, under **bulk deformation plus simple shear**, the axial stresses are the sum of the terms in Eqs. (6.13) and (6.14) and the shear stress reads

$$\sigma_{xy} = \mu\big(1 + \mu_1\eta_{ii}\big)\eta_{xy} + \mathcal{O}(\eta^3). \tag{6.15}$$

  Thus, the material response to shear deformation can be decreased or increased upon isotropic compression or tension depending on the sign of μ_1, as laid out in Eq. (6.11b).

It is worth noticing that contrary to what Eq. (6.11) may indicate, a medium with $\kappa_1 = \mu_1 = 0$ is not entirely linear. Indeed, nonlinear terms are still present in this case, as in Eq. (6.13).

6.2.2 Elastic moduli in bucklable fiber networks

van Oosten et al. (2016) have performed rheology measurements on two gels of the extracellular matrix and compared their nonlinear stress response to the rather linear one of polyacrylamide. Their setup consists in a parallel-plate rheometer which allows them to induce both axial and shear deformations η_{zz} and $\eta_{r\theta}$ and to measure the resulting stresses. A buffer is placed at the boundary of the sample, which allows water to flow and thus the sample volume to change freely. The authors thus assume that that the stress resulting from η_{rr} and $\eta_{\theta\theta}$ can relax freely. We hereby extract the

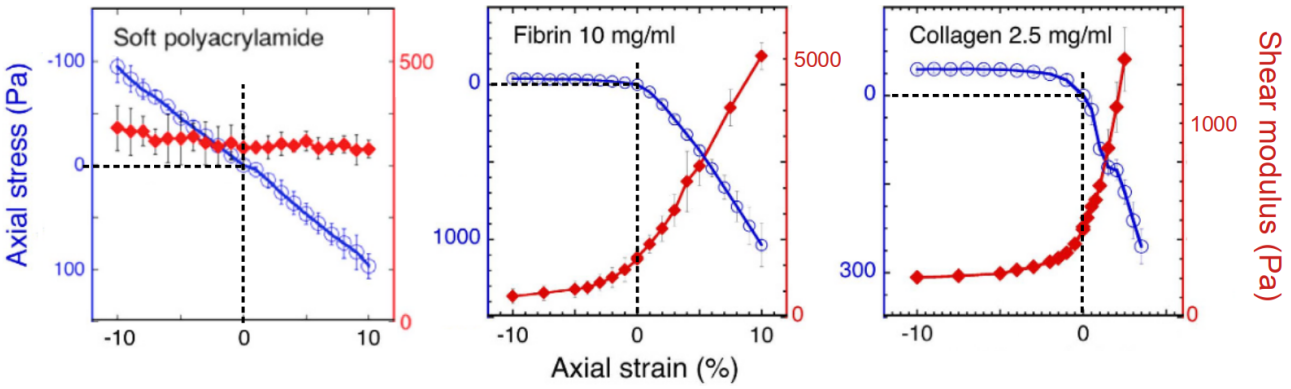

Figure 6.1: **Biological fiber networks display positive corrections.** The apparent convexity of the blue curve near the origin gives us $-\kappa_1$. The slope of the red one at zero axial strain gives us μ_1. Such that for the left figure, $\kappa_1 \approx \mu_1 \approx 0$, while for the middle and right ones, $-\kappa_1 < 0$ and $\mu_1 > 0$. Adapted from (van Oosten et al., 2016).

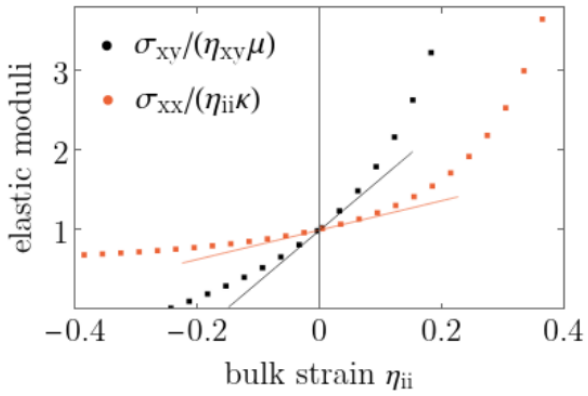

Figure 6.2: **Elastic moduli for a typical bucklable fibrous material with $c = 1$ in the model of** Storm et al. (2005)**.** Bulk modulus σ_{xx}/η_{ii} and shear modulus σ_{xy}/η_{xy} when η_{xy} vanishes against η_{ii} (markers), both fitted linearly at small strain.

coefficients κ_1 and μ_1 for these materials from the shape of their stress-strain law. On the left side of Fig. 6.1, polyacrylamide, a network of flexible polymers displays no significant nonlinearity ($\kappa_1, \mu_1 \approx 0$), since the axial stress σ_{zz} is proportional to the axial strain η_{zz}. In contrast, two networks of semiflexible polymers: collagen type I and fibrin display similarly significant nonlinear responses. We find $\kappa_1 \approx 150$, $\mu_1 \approx 22$ for fibrin, and $\kappa_1 \approx 69$, $\mu_1 \approx 36$ for collagen. These positive values are consistent with the notion that biological fiber networks buckle, and therefore soften, under compression ($\eta_{zz} < 0$).

Additionally, the model of Storm et al. (2005) described in Sec. 5.2.1, allows us to describe the behavior of the corrections to the elastic moduli with the flexibility of the crosslinked filaments. From the formulae in Eqs. (5.17) and (5.18), we compute the dependence of the bulk and shear moduli with the bulk strain η_{ii} for different values of the ratio of the persistence length to the distance between two crosslinks $c = l_p/l_c$. And we extract the values of κ_1 and μ_1 from the slope at the origin, see Fig. 6.2. In the domain of validity of the model where $c \in [0.5, 4]$, we find that they increase approximately linearly with c:

$$\kappa_1 \approx -2.2 + 6.4c \quad \text{and} \quad \mu_1 \approx 0.8 + 6.4c, \quad \text{such that} \quad \kappa_1 \approx \mu_1 - 3. \tag{6.16}$$

Thus, while Poisson's ratio remains small ($\nu \in [0, 0.2]$), κ_1, μ_1 are both positive and of the order of 1 to 30. This is in qualitative agreement with the more pronounced buckling tendency of semiflexible filaments ($c \gtrsim 1$) compared to flexible ones ($c \ll 1$). However, the values of κ_1 for $c \gtrsim 1$ are only about half as large as the ones for collagen and fibrin from measurements by van Oosten et al. (2016). For this strain-stiffening model and the curves of Fig. 6.1, we observe that the weakly nonlinear regime corresponding to the approximations of Eq. (6.11) seems valid until $\eta_{ii} \approx 0.1$.

6.2.3 Elastic moduli in granular media near jamming

Conversely, granular materials tend to increase their cohesion under compression, which yields a similar but opposite kind of nonlinearity. Here, we derive typical values of κ_1 and μ_1 for granular media near the jamming transition. Let us consider a large equilibrium packing of bidisperse frictionless spherical grains in a 2D box with area fraction ϕ. The grains interact through a harmonic or Hertzian potential $\mathcal{V} \sim k\,\delta^a$, where k is a spring constant, δ the overlap divided by the sum of the two disc diameters [Fig. 5.7], and $a = 2$ or $5/2$. For area fractions slightly above the jamming transition $\phi_c \approx 0.84$, granular media display a strongly nonlinear elastic behavior, which depends on the interaction exponent a, see Fig. 6.3.

Harmonic interactions Multiple simulations and experiments (O'Hern et al., 2003; van Hecke, 2009) have shown that while the bulk modulus goes to a finite limit in ϕ_c^+ and can thus be approximated by a constant, the shear modulus scales with $\phi - \phi_c$ and vanishes at the transition. This can be

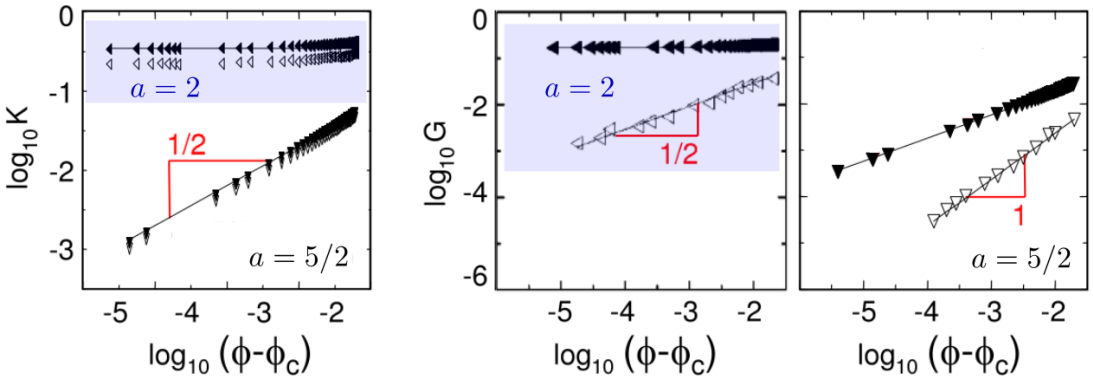

Figure 6.3: **The bulk and shear moduli scale with the distance to jamming.** The systems are two-dimensional and bidisperse with an interaction potential $\mathcal{V} \propto \delta^a$. The closed and open symbols denote moduli calculated before and after relaxation respectively. Accurate equilibrium measurements thus correspond to the open symbols. Adapted from (O'Hern et al., 2003; van Hecke, 2009).

expressed as

$$K/k \sim K_0 \quad \text{and} \quad G/k \sim G_0(\phi - \phi_c)^p, \quad \text{for} \quad 0 < \phi - \phi_c \ll 1, \tag{6.17}$$

where $K_0, G_0 \approx 0.2$ and $p \approx 0.5$. Based on this model, we impose an isotropic compression characterized by a displacement gradient tensor $\eta_{ij} = -\eta_0 \delta_{ij}/2$ on our granular material initially at ϕ_c, where $0 < \eta_0 \ll 1$. This results in a new area fraction $\phi_0 \sim \phi_c(1 + \eta_0)$. We then compute the elastic moduli κ and μ, and their nonlinear corrections κ_1 and μ_1 around this value of ϕ_0. Let the bulk strain $\eta_{ii} = -\eta_0 + \delta\eta$, where $|\delta\eta| \ll \eta_0$, corresponding to a volume fraction $\phi \sim \phi_0 - \phi_c \delta\eta$. Then similarly to Eq. (6), the moduli are expressed as $K \sim \kappa(1 + \kappa_1 \delta\eta)$ and $G \sim \mu(1 + \mu_1 \delta\eta)$, where the parameters are derived from Eq. (6.17):

$$\begin{aligned} \kappa/k &\sim K_0, & \kappa_1 &= 0, \\ \mu/k &\sim G_0(\phi_0 - \phi_c)^p, & \mu_1 &\sim -\frac{p\,\phi_c}{\phi_0 - \phi_c}. \end{aligned} \tag{6.18}$$

Therefore, while κ_1 vanishes, μ_1 diverges at the transition and scales as $(\phi_0 - \phi_c)^{-1}$. And close to the transition, around *e.g.* $\phi_0 - \phi_c = 0.001$, 0.01 or 0.1, we find respectively $\mu_1 \approx -400$, -40 or -4. With this writing, we see that Poisson's ratio $\nu = (\kappa - \mu)/(\kappa + \mu)$ also varies with the bulk strain

$$\nu \sim 1 - 2\frac{G_0}{K_0}(\phi_0 - \phi_c)^p. \tag{6.19}$$

$1 - \nu$ thus scales as $\sqrt{\phi_0 - \phi_c}$, such that media away from jamming are more compressible.

Hertzian interactions Given the interaction potential $\mathcal{V} \sim k\,\delta^{5/2}$, both moduli vanish at the jamming transition but with different scalings. This can be expressed as

$$K/k \sim K_1(\phi - \phi_c)^s \quad \text{and} \quad G/k \sim G_1(\phi - \phi_c)^t, \quad \text{for} \quad 0 < \phi - \phi_c \ll 1 \tag{6.20}$$

where $K_1 \approx 0.3$, $s \approx 0.5$, $G_1 \approx 0.2$ and $t \approx 1$. Around the area fraction ϕ_0. the elastic moduli κ and μ, and their nonlinear corrections κ_1 and μ_1 read

$$\begin{aligned} \kappa/k &\sim K_1(\phi_0 - \phi_c)^s, & \kappa_1 &\sim -\frac{s\,\phi_c}{\phi_0 - \phi_c}, \\ \mu/k &\sim G_1(\phi_0 - \phi_c)^t, & \mu_1 &\sim -\frac{t\,\phi_c}{\phi_0 - \phi_c}. \end{aligned} \tag{6.21}$$

Therefore, both κ_1 and μ_1 scale as $(\phi_0 - \phi_c)^{-1}$, and around *e.g.* $\phi_0 - \phi_c = 0.001$, 0.01 or 0.1, we find respectively $\kappa_1 \approx -400$, -40 or -4, and $\mu_1 \approx -800$, -80 or -8. Finally, Poisson's ratio reads

$$\nu \sim 1 - 2\frac{G_1}{K_1}(\phi_c \eta_0)^{t-s}, \tag{6.22}$$

such that $1-\nu$ scales again as $\sqrt{\phi_0-\phi_c}$.

To conclude, in both cases, κ_1 and μ_1 are both negative and increase in absolute value as the distance to jamming decreases. This corresponds to the picture painted in Sec. 5.3.1, in which the elastic response of systems closer to the rigidity threshold displays larger nonlinearities.

6.2.4 Corrections in other materials

Until here, we focused on fibrous materials whose stiffness increases in tension and decreases in compression due to buckling. And on granular media which act in a reverse manner which we call anti-buckling, insofar as they soften under tension and stiffen under compression. Beyond these somewhat intuitive behaviors, we hereby describe other materials which show an intermediate behavior. This is the case for instance in fiber networks with stiff grain-like inclusions mimicking connective tissues, see Fig. 6.4, *top left*. This gives rise to a more complicated sign combination which depends on the inclusion density (Shivers et al., 2020; van Oosten et al., 2019) [Fig. 6.4, *top right*]. For instance, whole blood clots made primarily of red blood cells (RCB) in a fibrin network (Collet et al., 2000; Gersh et al., 2009) tend to display low values for the corrections: $\kappa_1 \approx 0$ and $\mu_1 \approx 4$. As for adipose tissues, which consists of clusters of adipocytes (also known as fat cells) surrounded by a collagen network (Alkhouli et al., 2013; Peurichard et al., 2017), and liver tissues, we find granular-like behaviors with $\kappa_1 \approx -3$, $\mu_1 \approx -4$ and $\kappa_1 \approx -7$, $\mu_1 \approx -5$ respectively [Fig. 6.4, *bottom*].

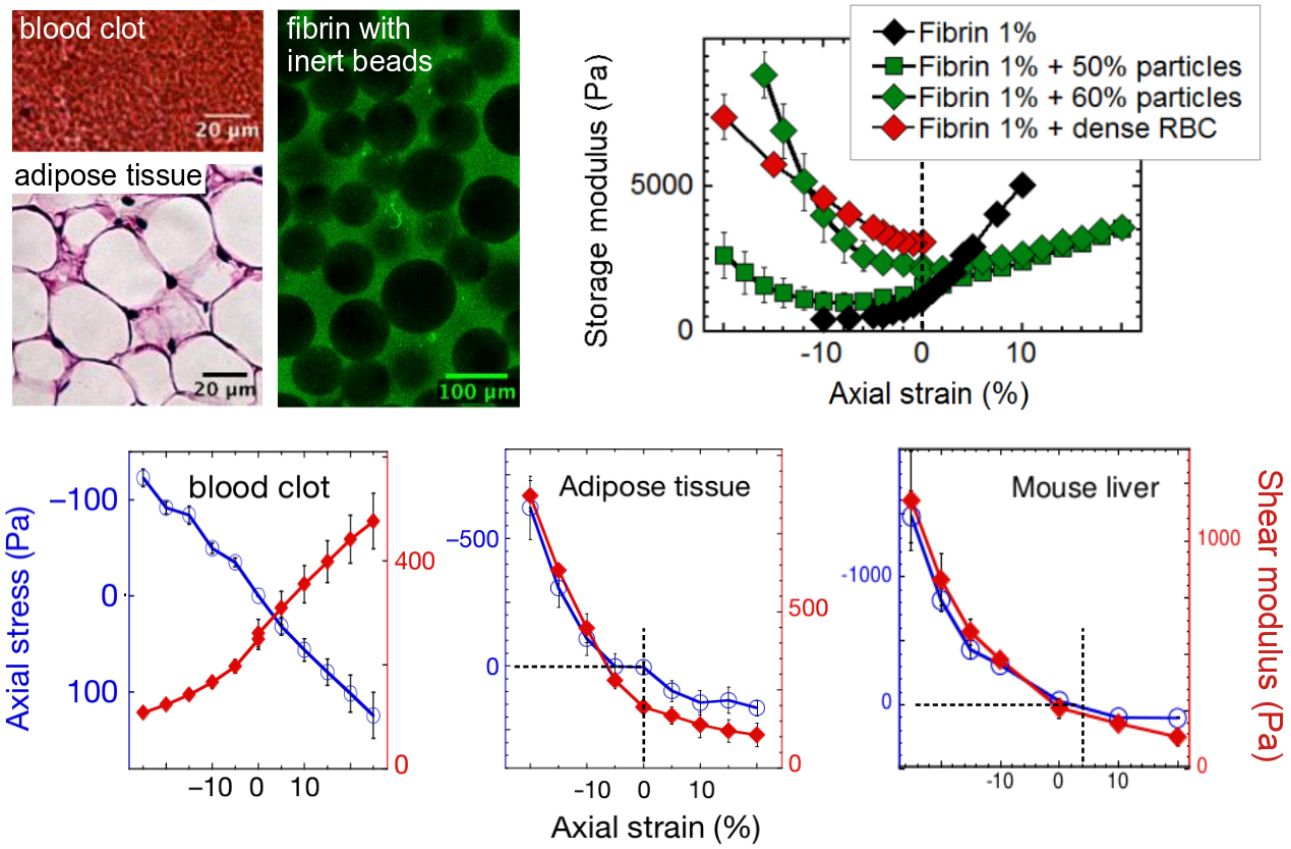

Figure 6.4: **Corrections become negative as stiff grains are added to fiber networks.** *Top left*, images of tightly packed red blood cells in a contracted blood clot, adipose tissue, and a fibrin network with incorporated inert beads. *Top right*, the slope of the shear modulus at zero axial strain shifts from a positive value to a nearly negative one as the bead concentration increases. *Bottom*, the apparent convexity of the blue curve near the origin gives us $-\kappa_1$. The slope of the red one at zero axial strain gives us μ_1. For the blood clot, $\kappa_1 \approx 0$ and $\mu_1 > 0$, but for the adipose tissue and mouse liver, it seems that $-\kappa_1 > 0$ and $\mu_1 < 0$. Adapted from (van Oosten et al., 2019) and its supplementary.

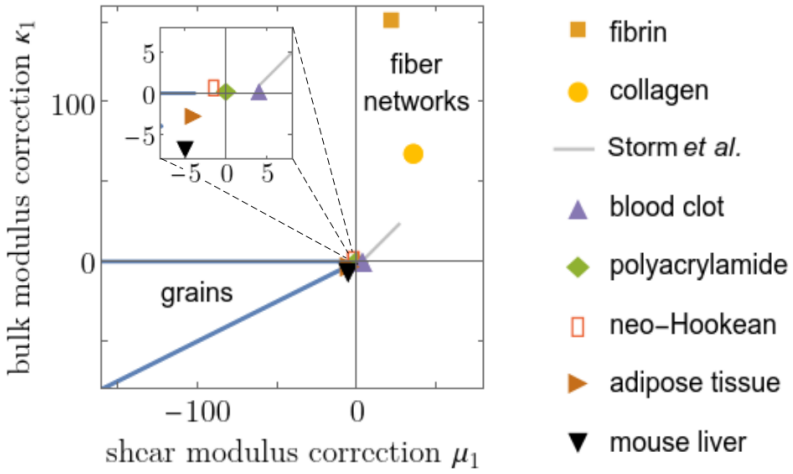

Figure 6.5: **Summary of the corrections to the elastic moduli.** Most values from experiments, simulations and usual models correspond to values of κ_1 and μ_1 either large and of the same sign, or close to 1 in absolute value. The inset shows a blow-up at small values of κ_1, μ_1.

Concerning rubber, supposed to behave like polyacrylamide for which $\kappa_1, \mu_1 \approx 0$ [Fig. 6.1], the standard neo-Hookean model discussed in Sec. 5.1.3 displays $\kappa_1 > 0$ and $\mu_1 < 0$ with small values (Treloar, 1973). Indeed, a small strain development of the energy density in Eq. (5.13) yields

$$\begin{aligned} E &= \frac{\kappa}{2}\Big[\varepsilon_{ii}^2 + \varepsilon_{ii}\big(\varepsilon_{ii}^2 - 2\varepsilon_{ij}^2\big)\Big] + \frac{\mu}{2}\Big[2\varepsilon_{ij}^2 - \varepsilon_{ii}^2 + 2\varepsilon_{ii}\big(\varepsilon_{ii}^2 - 2\varepsilon_{ij}^2\big)\Big] + \mathcal{O}\big(\varepsilon^4\big) \\ &= \frac{\kappa}{2}\varepsilon_{ii}^2 + \frac{\mu - (\kappa + 2\mu)\varepsilon_{ii}}{2}\big(2\varepsilon_{ij}^2 - \varepsilon_{ii}^2\big) + \mathcal{O}\big(\varepsilon^4\big). \end{aligned} \tag{6.23}$$

Thus the lowest-order nonlinearities are characterized by $\kappa' = 0$ and $\mu' = -(\kappa + 2\mu)$, *i.e.* $\kappa_1 = 1/2$, $\mu_1 = -3/2$. The shear-stiffening model of Eq. (5.20) also has $\kappa_1 = 1/2$, $\mu_1 = -3/2$, which corresponds to the same tendency to rectify towards contraction as in the neo-Hookean case. Indeed, the parameter g related to the stiffening threshold only affects higher order nonlinearities. In the end, all collected values of the corrections are shown in Fig. 6.5. As displayed, the data points with large absolute values are in the top-right and bottom-left quadrants.

6.3 Simple model with a circular active unit

To explicitly predict the active pressure resulting from rectification, we consider a simple circular piece of elastic medium with radius r_{out} and a single active unit at its center. The active unit is a circle with radius r_{in} at rest, and undergoes a radial displacement [Fig. 6.6(a)]

$$\mathbf{u}(r_{\text{in}}) = r_{\text{in}}\,(e_0 + e_2 \cos 2\theta)\,\hat{\mathbf{r}}. \tag{6.24}$$

In this continuum framework, the force dipole as simulated in the discrete fiber simulations of Ronceray et al. (2016) can be conceptualized as a situation where $e_0 = e_2$, such that the imposed displacement is maximal along the x direction and zero along the y direction. Here, the isotropic and dipolar parameters e_0 and e_2 are allowed to vary independently, which allows to consider weakly or strongly anisotropic settings. One can for instance imagine that it is a coarse-grained view of the deformation produced by a collection of active units. This typically induces a mixture of compression, tension and shear on the medium. Symmetry imposes that the local and active stress tensors take the form

$$\bar{\boldsymbol{\sigma}}^x = -\begin{pmatrix} P_x + S_x & 0 \\ 0 & P_x - S_x \end{pmatrix}, \tag{6.25}$$

in Cartesian coordinates, for $x \in \{l, a\}$ [Fig. 6.6(b)]. As shown in Eq. (6.2), the local coarse-grained stress $\bar{\boldsymbol{\sigma}}^l$ is the ratio of a force dipole by the volume V. Assuming a constant local dipole, $\bar{\boldsymbol{\sigma}}^l$ thus

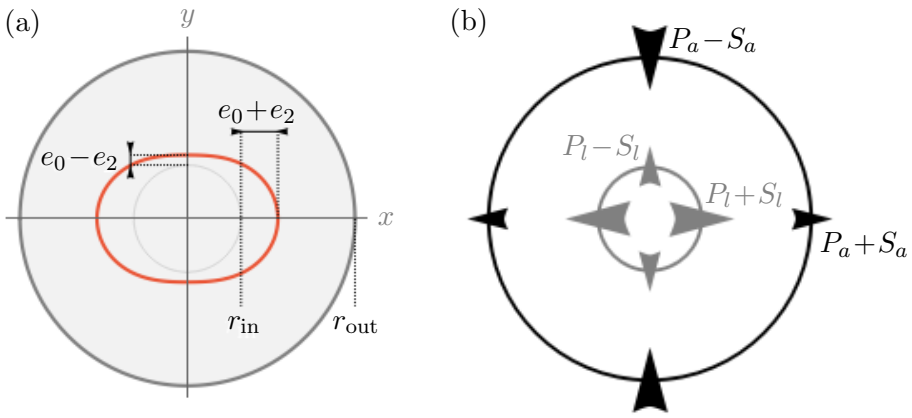

Figure 6.6: **Sketches of the imposed anisotropic displacement and the resulting coarse-grained stresses.** (a) In the target configuration, the inner light-gray circle with radius r_{in} is moved to the orange ring. (b) Stress components in a particular situation where the local pressure P_l is positive and the active pressure P_a at the boundary is negative.

decreases with increasing system size V due to dilution. A similar statement holds for $\bar{\boldsymbol{\sigma}}^a$. It is thus useful for our discussion to define the quantities

$$\mathcal{P}_x = P_x(r_{\text{out}}/r_{\text{in}})^2 \quad \text{and} \quad \mathcal{S}_x = S_x(r_{\text{out}}/r_{\text{in}})^2 \tag{6.26}$$

which are not subject to this dilution. In this sense, they behave as force dipole components. In the following, we consider the lowest order in the weakly nonlinear regime $e_0, e_2 \ll 1$. We perturbatively solve the force balance equation using Eq. (6.24) as well as the fixed boundary condition in r_{out} to compute the pressure and shear components $\mathcal{P}_x$, $\mathcal{S}_x$. In Sec. 6.3.1, we present the Ansatz for the displacement field that allows us to solve the force balance condition. The detailed expressions of the coarse-grained stresses $\bar{\boldsymbol{\sigma}}$ in the circular geometry are displayed in Sec. 6.3.2. We then discuss the obtained results in Sec. 6.4. Finally, Appendix 6.5 contains the cumbersome calculations leading to the results of Sec. 6.3.2.

6.3.1 Ansatz for the displacement field

To calculate the coarse-grained stresses, it may be easier to express them in the initial configuration, where the force density $\boldsymbol{\phi} = \mathbf{f}/\det(\mathbf{1}+\boldsymbol{\eta})$ is related to the first Piola-Kirchhoff stress tensor $\boldsymbol{\tau} = (\mathbf{1}+\boldsymbol{\eta})\frac{\partial E}{\partial \boldsymbol{\varepsilon}}$. The force balance equation thus reads $\phi_i = -\partial_j \tau_{ij}$ and the coarse-grained stresses can be rewritten as

$$\bar{\sigma}^a_{ij} = \frac{1}{V}\oint_{\partial\Omega} \tau_{ik} X_j \, \mathrm{d}a_k \quad \text{and} \quad \bar{\sigma}^l_{ij} = -\frac{1}{V}\int_{\Omega} \phi_i X_j \, \mathrm{d}v, \tag{6.27}$$

where $\mathrm{d}\mathbf{a}$ is the outward-directed area element in the initial space. There, the material is subjected to zero body force except at r_{in}, where the stress is discontinuous. The fixed boundary at r_{out} and the imposed displacement at r_{in} additionally impose boundary conditions on the stress and displacement fields, resulting in the following system of equations:

$$\begin{cases} \boldsymbol{\nabla}\cdot\boldsymbol{\tau}^{\mathsf{T}} = \mathbf{0}, & \text{for } r \in [0, r_{\text{in}}) \cup (r_{\text{in}}, r_{\text{out}}) \\ \mathbf{u} = \mathbf{0}, & \text{at } r = 0 \text{ and } r = r_{\text{out}} \\ \mathbf{u} = r_{\text{in}}\,(e_0 + e_2\cos 2\theta)\,\hat{\mathbf{r}}, & \text{at } r = r_{\text{in}} \end{cases}. \tag{6.28}$$

We solve this system perturbatively by expanding $\mathbf{u}, \boldsymbol{\eta}, \boldsymbol{\tau}$ in the small scalar quantity

$$\eta \sim |e_0| + |e_2|. \tag{6.29}$$

The elastic medium is described by the weakly nonlinear model with the non-harmonic energy density of Eq. (6.9). Up to second order in η, the first Piola-Kirchhoff stress can be decomposed as $\boldsymbol{\tau} = \boldsymbol{\tau}^L + \boldsymbol{\tau}^{\text{NL}}$,

where $\boldsymbol{\tau}^{\mathrm{NL}} = \boldsymbol{\tau}^{G} + \boldsymbol{\tau}^{C}$. This last equality distinguishes the geometrical and constitutive nonlinearities. The terms read

$$\boldsymbol{\tau}^{L} = \big(\kappa - 2\mu/d\big)U_{ii}\,\mathbf{1} + 2\mu\,\mathbf{U}, \tag{6.30a}$$

$$\boldsymbol{\tau}^{G} = \big(\kappa - 2\mu/d\big)\eta_{ij}^{2}\,\mathbf{1}/2 + \mu\,\boldsymbol{\eta}^{\mathsf{T}}\boldsymbol{\eta} + \big(\kappa - 2\mu/d\big)U_{ii}\,\boldsymbol{\eta} + 2\mu\,\boldsymbol{\eta}\mathbf{U} + \mathcal{O}\big(\eta^{3}\big). \tag{6.30b}$$

$$\boldsymbol{\tau}^{C} = 3\big(\kappa' - 2\mu'/d\big)U_{ii}^{2}\,\mathbf{1}/2 + \mu' U_{ij}^{2}\,\mathbf{1} + 2\mu' U_{ii}\,\mathbf{U} + \mathcal{O}\big(\eta^{3}\big). \tag{6.30c}$$

But the distinction between the linear and nonlinear terms in the stress is not that simple. Indeed, the displacement gradient reads $\boldsymbol{\eta} = \boldsymbol{\eta}^{L} + \boldsymbol{\eta}^{\mathrm{NL}} + \mathcal{O}\big(\eta^{3}\big)$ where the L and NL superscript refer to linear and quadratic (nonlinear) terms in η. This allows us to write the stress tensor as

$$\boldsymbol{\tau} = \boldsymbol{\tau}^{L}\big(\boldsymbol{\eta}^{L}\big) + \boldsymbol{\tau}^{L}\big(\boldsymbol{\eta}^{\mathrm{NL}}\big) + \boldsymbol{\tau}^{\mathrm{NL}}\big(\boldsymbol{\eta}^{L}\big) + \mathcal{O}\big(\eta^{3}\big), \tag{6.31}$$

where $\boldsymbol{\tau}^{L}\big(\boldsymbol{\eta}^{L}\big)$ is strictly of order 1, while the next two are strictly of order 2. The linear displacement field $\mathbf{u}^{L}$ is the solution of $\partial_i \tau_{ji}^{L}(\boldsymbol{\eta}^{L}) = 0$. This is solved by decomposing $\mathbf{u}^{L}$ in the following Fourier modes due to the chosen form of the imposed displacement:

$$u_r^{L}/r_{\mathrm{in}} = e_0\zeta_0(r) + e_2\zeta_2(r)\cos 2\theta, \tag{6.32a}$$

$$u_\theta^{L}/r_{\mathrm{in}} = e_2\omega_2(r)\sin 2\theta. \tag{6.32b}$$

Here $\zeta_0(r)$, $\zeta_2(r)$, $\omega_2(r)$ are sums of r^k, with $k \in \{-3,-1,1,3\}$ and coefficients depending on the boundary conditions. Their generic forms compatible with Eq. (6.24) are shown in Appendix 6.5.1. Then, at the first nonlinear order, $\mathbf{u}^{\mathrm{NL}}$ is the solution of the linear equation $\partial_i \tau_{ji}^{L}(\boldsymbol{\eta}^{\mathrm{NL}}) = -\partial_i \tau_{ji}^{\mathrm{NL}}(\boldsymbol{\eta}^{L})$ which is solved by expanding $\mathbf{u}^{\mathrm{NL}}$ as

$$u_r^{\mathrm{NL}}/r_{\mathrm{in}} = e_2^2\xi_0(r) + e_0e_2\xi_2(r)\cos 2\theta + e_2^2\xi_4(r)\cos 4\theta, \tag{6.33a}$$

$$u_\theta^{\mathrm{NL}}/r_{\mathrm{in}} = e_0e_2\pi_2(r)\sin 2\theta + e_2^2\pi_4(r)\sin 4\theta, \tag{6.33b}$$

where the $\xi_i(r)$, $\pi_i(r)$ are again sums of r^k with k odd between -7 and $+5$. Details can be found in Appendix 6.5.1. As a consequence, we obtain in Sec. 6.3.2 the strain and stress fields up to second order in η.

6.3.2 Coarse-grained stresses

We compute the coarse-grained active stress $\bar{\boldsymbol{\sigma}}^{a}$ and local stress $\bar{\boldsymbol{\sigma}}^{l}$ in the circular geometry by integrating the stresses in the material as in Eq. (6.27). As detailed in Appendix 6.5.2, the coarse-grained stress components are expressed in Cartesian coordinates as in Fig. 6.6(b). At the lowest order in the weakly nonlinear regime $e_0, e_2 \ll 1$, the pressure components read

$$\mathcal{P}_a = Ae_0 + B_a e_2^2 + \mathcal{O}\big(e_0^2, e_0e_2^2, e_2^4\big), \tag{6.34a}$$

$$\mathcal{P}_l = Ae_0 + B_l e_2^2 + \mathcal{O}\big(e_0^2, e_0e_2^2, e_2^4\big), \tag{6.34b}$$

and the shear components read

$$\mathcal{S}_a = Ce_2 + \mathcal{O}\big(e_2e_0, e_2^3\big), \tag{6.35a}$$

$$\mathcal{S}_l = Ce_2 + \mathcal{O}\big(e_2e_0, e_2^3\big), \tag{6.35b}$$

where the cumbersome dependence of A, B_a, B_l and C on the properties of the medium are detailed in Appendix 6.5.3. As expected from the linear elasticity analysis of Sec. 6.1, the coefficients in front of the linear e_0 and e_2 terms are identical for the local and boundary stresses, but discrepancies appear in the e_2^2 terms. In principle, at second order in η, terms in e_0^2 are allowed in P_a, P_l by the symmetries. But in the weakly nonlinear regime, they are always negligible in front of Ae_0. Likewise, the terms in

$e_0 e_2$ are insignificant in front of Ce_2 in S_a, S_l. The active stresses can then be computed from the local ones through

$$\mathcal{P}_a \sim \mathcal{P}_l + \alpha \mathcal{S}_l^2, \quad \mathcal{S}_a \sim \mathcal{S}_l. \tag{6.36}$$

Here $\alpha\mu$ is a dimensionless function of the ratio of radii $\rho = (r_{\text{out}}/r_{\text{in}})^2$, Poisson's ratio ν, and the corrections to the moduli κ_1 and μ_1 that is defined by $\alpha = (B_a - B_l)/C_l^2$. Introducing three functions of ρ and ν only:

$$\begin{aligned}
X &= 4\rho(3-\nu)^2\left[2(3+\nu)+(3-\nu)(\rho+\rho^2)\right]^2/(\rho-1),\\
\frac{Xx_1}{1-\nu^2} &= 405 - 108\nu - 54\nu^2 + 12\nu^3 + \nu^4 + (324 - 180\nu - 24\nu^2 - 36\nu^3 - 4\nu^4)\rho\\
&\quad + (378 - 288\nu + 120\nu^2 + 24\nu^3 + 6\nu^4)\rho^2 + (108 - 180\nu + 48\nu^2 + 12\nu^3 - 4\nu^4)\rho^3\\
&\quad + (81 - 108\nu + 54\nu^2 - 12\nu^3 + \nu^4)\rho^4,\\
Xx_2 &= 81 - 54\nu + 351\nu^2 - 84\nu^3 - 49\nu^4 + 10\nu^5 + \nu^6\\
&\quad - (684\nu - 204\nu^2 + 120\nu^3 + 8\nu^4 + 28\nu^5 + 4\nu^6)\rho\\
&\quad + (594 - 900\nu + 1122\nu^2 - 360\nu^3 + 102\nu^4 + 12\nu^5 + 6\nu^6)\rho^2\\
&\quad + (216 - 1116\nu + 924\nu^2 - 312\nu^3 + 16\nu^4 + 20\nu^5 - 4\nu^6)\rho^3\\
&\quad + (405 - 702\nu + 567\nu^2 - 276\nu^3 + 83\nu^4 - 14\nu^5 + \nu^6)\rho^4,
\end{aligned}$$

the rectification coefficient can be expressed as a linear function of κ_1 and μ_1 as

$$\alpha\mu = -\left(\kappa_1 + \tfrac{3}{2}\right)x_1 - \left(\mu_1 + \tfrac{3}{2}\right)x_2, \tag{6.37}$$

where x_1 and x_2 are positive for $\rho > 1$ and $\nu \in [-1, 1]$. From this point on, we no longer consider the displacement parameters e_0 and e_2, as the nonlinear stress-strain relation of Eq. (6.30) makes their translation into stress components difficult. We rather consider the coarse-grained stress response of the medium at the boundary characterized by $\mathcal{P}_a, \mathcal{S}_a$, as a function of the locally imposed coarse-grained stress components $\mathcal{P}_l, \mathcal{S}_l$.

At this order in nonlinearity, stress propagation in a medium with $\alpha = 0$ resembles that in a linear medium (namely $\mathcal{P}_a = \mathcal{P}_l$, $\mathcal{S}_a = \mathcal{S}_l$). Conversely, a medium with a negative (positive) α harnesses the anisotropy of the active unit to produce an additional medium-wide contraction (expansion). Equation (6.36) is formally valid for local stresses much smaller than the elastic moduli of the medium ($\mathcal{P}_l, \mathcal{S}_l \ll \kappa$, where "$\kappa$" stands for the typical magnitude of the linear moduli). It implies that when $\sqrt{\kappa \mathcal{P}_l} \ll \mathcal{S}_l$, the sign of the active pressure induced by a highly anisotropic active unit is determined not by the values $(\mathcal{P}_l, \mathcal{S}_l)$ characterizing the active unit, but by the properties of the medium through the sign of α. In Eqs. (6.34), (6.35) and (6.36), we consider small displacements with two independent parameters $e_0, e_2 \ll 1$. In the weakly nonlinear formalism, the simplest possible rectification requires that the term in e_0 be similar (and of opposite sign) to the term in e_2^2. In this regime, given $\epsilon \ll 1$, the displacement parameters read $e_0 = \epsilon\, \tilde{e}_0$ and $e_2 = \sqrt{\epsilon}\, \tilde{e}_2$. As a result $\mathcal{P}_x = \epsilon \tilde{\mathcal{P}}_x$ and $\mathcal{S}_x = \sqrt{\epsilon}\tilde{\mathcal{S}}_x$ for $x \in \{l, a\}$, where the tildes denote quantities of order one. Then to lowest order in ϵ, Eqs. (6.34) and (6.35) can be rewritten as

$$\tilde{\mathcal{P}}_x = A\tilde{e}_0 + B_x \tilde{e}_2^2 + \mathcal{O}(\epsilon), \tag{6.38a}$$

$$\tilde{\mathcal{S}}_x = C\tilde{e}_2 + \mathcal{O}(\epsilon), \tag{6.38b}$$

implying that the "$\sim$" symbols of Eq. (6.36) denote equalities to lowest order in ϵ. The rectification behavior thus depends on the ratio $\tilde{\mathcal{P}}_l/(\alpha\tilde{\mathcal{S}}_l^2)$, *i.e.* on $\tilde{e}_0/\tilde{e}_2^2$. In the next section, we discuss the consequences of Eqs. (6.36) and (6.37) in terms of rectification.

6.4 Rectification as a generic phenomenon

We illustrate the influence of the material properties on the sign of α in Fig. 6.7, which indicates a clear tendency of fiber-like (granular-like) materials towards contractile (expansile) rectification.

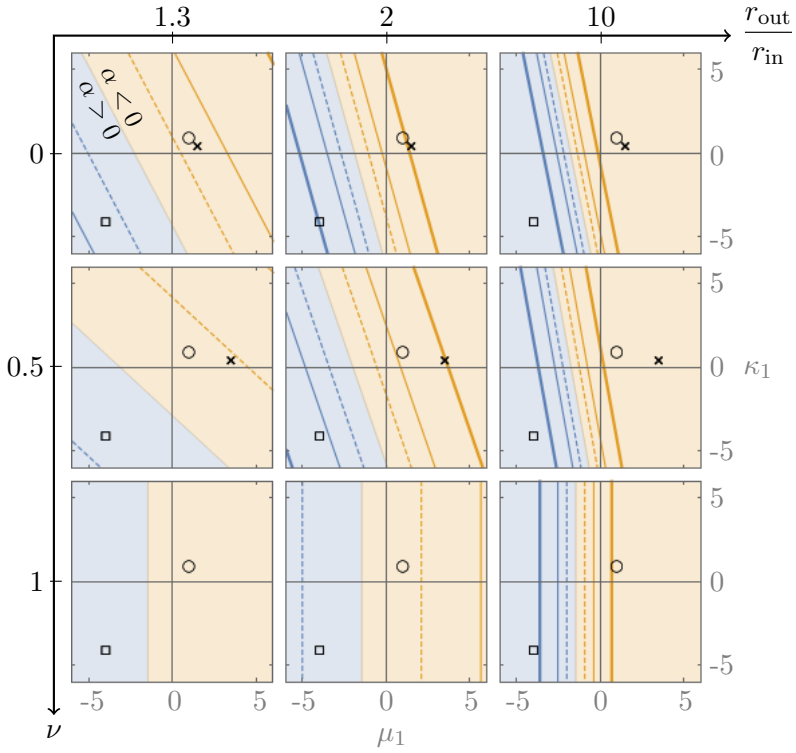

Figure 6.7: **Bucklable materials ($\kappa_1, \mu_1 > 0$) rectify towards contraction (yellow), while very anti-bucklable materials ($\kappa_1, \mu_1 < -3/2$) rectify towards expansion (blue).** Contour plot of α, indicating the overall sign of rectification as a function of the relative system size $r_{\text{out}}/r_{\text{in}}$, the Poisson ratio ν ($\nu = 1$ denotes incompressibility in 2D) and the nonlinear corrections to the moduli κ_1, μ_1. The contour lines denote $|\alpha|\mu = 2$ (thick), 1 (thin), 0.5 (dashed). Crosses indicate constitutively linear materials where only geometrical nonlinearities are present (for $\nu = 1$ they are far to the right). Circles and squares point out specific media discussed in Fig. 7.2.

Indeed, when κ_1 and μ_1 are both larger (smaller) than a critical value of $-3/2$, the system always rectifies towards contraction (expansion). As a result, a material with $\kappa_1 = \mu_1 = 0$ is contractile because of the contractile character of geometrical nonlinearities described by Eq. (6.6). Media with $\kappa_1 > -3/2$ but $\mu_1 < -3/2$ or the reverse can be either contractile or expansile depending on the system size $r_{\text{out}}/r_{\text{in}}$ and Poisson's ratio $\nu = (\kappa - \mu)/(\kappa + \mu)$. In the end, rectification is a generic phenomenon since almost all values of the corrections to the moduli κ_1 and μ_1 lead to some rectification. Additionally, $|\alpha|$ increases with increasing r_{out} such that $|\alpha(\infty) - \alpha(r_{\text{out}})| \propto (r_{\text{in}}/r_{\text{out}})^2$ for large r_{out}, implying that larger systems rectify more. For example, larger fiber networks allow for more extensive buckling, resulting in stronger rectification and the coming together of the contour lines of Fig. 6.7 as r_{out} increases. In Sec. 6.4.1, we further discuss the dependence of α in the system size, and specifically its saturation for large systems. Then Sec. 6.4.2 presents a diagram which displays the different stages of rectification, as different active stress components switch sign.

6.4.1 Behavior of α and rectification saturation radius r^*

To help better understand the lengthy expression of the rectification coefficient $\alpha = (B_a - B_l)/C_l^2$ in subsection III.D, we hereby discuss its dependence on the system size r_{out}. As is apparent from Fig. 6.7, α increases with increasing r_{out} for relatively small systems, then saturates as the size of the system goes to infinity. Indeed, away from the high-stress region close to the active unit, the stress decrease causes the nonlinearities to become negligible in front of the linear terms. Therefore, we examine the radius r^* at which stress propagation switches from nonlinear to linear. To this end we define the system size parameter $\rho = (r_{\text{out}}/r_{\text{in}})^2$. In the limit $\rho \to \infty$, Eq. (6.37) leads to

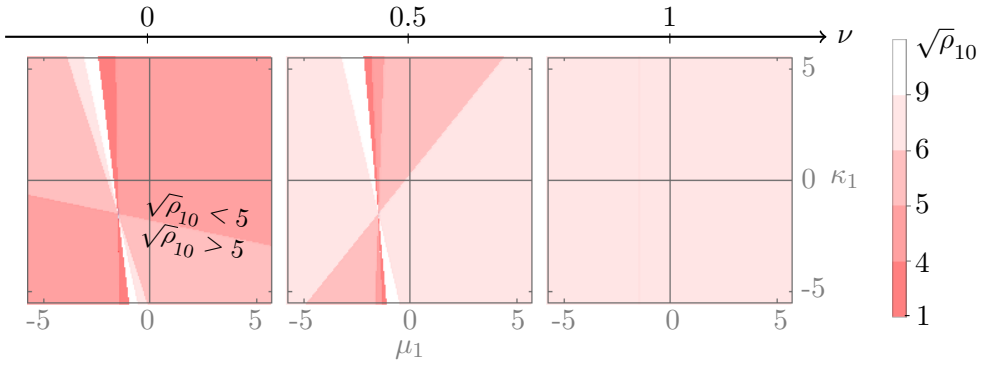

Figure 6.8: **The rectification saturation radius r^* is generally of the order of r_{in}.** Contour plot of $\sqrt{\rho}_{10} = r^*/r_{\text{in}}$ when κ_1 and μ_1 are varied for several values of Poisson's ratio ν. Except in the small white regions, $\sqrt{\rho}_{10} < 9$. In these white regions, $|\alpha|$ tends to take negligible values.

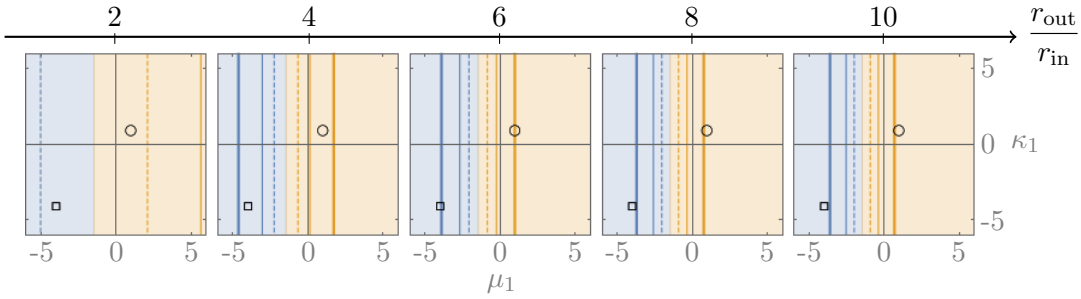

Figure 6.9: **Rectification happens mostly near the active unit.** Additional plots to Fig. 6.7 showing the stabilization of the graphs as the system size increases for a Poisson's ratio $\nu = 1$. The blue and yellow lines at constant $|\alpha|\mu$ stay quite still between $r_{\text{out}}/r_{\text{in}} = 8$ and 10. The behavior is similar for $\nu = 0$.

$\alpha(\rho) = \alpha_\infty + \alpha_1/\rho + \mathcal{O}(\rho^{-2})$, where

$$\begin{aligned} \mu\alpha_\infty &= -\frac{\left(\kappa_1 + \frac{3}{2}\right)(1-\nu^2) + \left(\mu_1 + \frac{3}{2}\right)(5 - 2\nu + \nu^2)}{4}, \\ \mu\alpha_1 &= \frac{\left(\kappa_1 + \frac{3}{2}\right)(15 - 6\nu - 8\nu^2 + 6\nu^3 - 7\nu^4) + \left(\mu_1 + \frac{3}{2}\right)(111 - 36\nu + 50\nu^2 - 20\nu^3 + 7\nu^4)}{4(3-\nu)^2}. \end{aligned} \tag{6.39}$$

We introduce the value of the parameter ρ such that α is within 10% of its large-size limit through $\left|\frac{\alpha(\rho_{10}) - \alpha_\infty}{\alpha_\infty}\right| = 0.1$. The square-root of ρ_{10}, corresponding to the ratio of the radii, lies between 4 and 9, except for insignificant values of α, see Fig. 6.8. Fig. 6.9 also illustrates this behavior by showing the stabilization of the lines at constant α as the system size increase. Therefore, defining the rectification saturation radius r^* such that $\rho_{10} = (r^*/r_{\text{in}})^2$, increasing r_{out} past $r^* \sim 10 r_{\text{in}}$ has little influence on the value of $\mathcal{P}_a - \mathcal{P}_l$, *i.e.* on the rectification effect. This indicates that the propagation is nonlinear only up to r^*. In the study of stress propagation from multiple active units, one thus needs to compare this r^* to the typical spacing between two active units.

6.4.2 The rectification diagram

The study of Eq. (6.36) leads to different rectification regimes, as different components of the active stress tensor $\bar{\boldsymbol{\sigma}}^a$ switch sign, while the corresponding local stress components remain of the same sign. These regimes are displayed with shadings in the rectification diagram of Fig. 6.10. This figure shows that for large enough local stresses, rectification can cause a sign-switching not only in the active pressure but in all components of $\bar{\boldsymbol{\sigma}}^a$.

In the circular geometry of Fig. 6.6, provided that α and $\mathcal{P}_l$ have different signs, a change of sign of P_a due to rectification can appear for all values of the local pressure $\mathcal{P}_l$ as long as the local shear stress

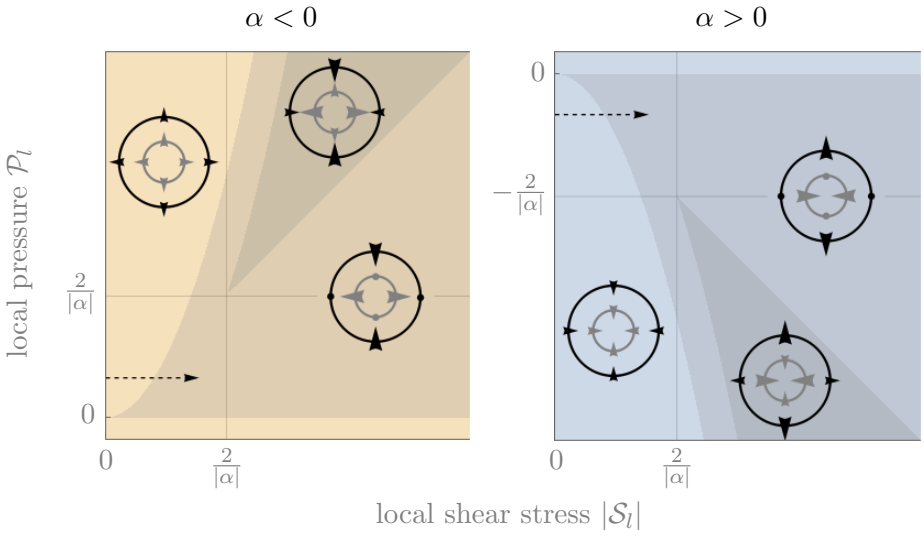

Figure 6.10: **Rectification diagram.** Dependence of the signs of the components of the active stress (dark arrows in the insets) as functions of the local stress components. Regions without shading correspond to situations where the signs are the same as in the absence of rectification. In regions with intermediate shading ($|\mathcal{P}_l| \lesssim |\alpha|\mathcal{S}_l^2$), the sign of $\mathcal{P}_a$ is reversed. In the dark regions, $|\mathcal{P}_l|$ and $|\mathcal{S}_l|$ are so large that all components of $\bar{\sigma}_a$ (dark regions) are reversed. These changes of signs are illustrated by arrows in the small pictures. Some arrows are replaced by circles in the intermediate shading regime to indicate that they are smaller than the other arrows and can point either way.

$|\mathcal{S}_l|$ is large enough. Indeed, in Eq. (6.36) the sign switching of the active pressure $\mathcal{P}_a$ (*e.g.* $\mathcal{P}_a < 0$ while $\mathcal{P}_l > 0$) requires

$$|\alpha|\mathcal{S}_l^2 \gtrsim |\mathcal{P}_l|. \tag{6.40}$$

This sets the boundary between the regions with light shading and the regions with intermediate shading. Then, the extreme case where all active stress components switch sign (*e.g.* $\mathcal{P}_a \pm \mathcal{S}_a < 0$ while $\mathcal{P}_l \pm \mathcal{S}_l > 0$) happens for

$$|\mathcal{S}_l| \lesssim |\mathcal{P}_l| \lesssim |\alpha|\mathcal{S}_l^2 - |\mathcal{S}_l|, \tag{6.41}$$

i.e. for $|\mathcal{P}_l|$ and $|\mathcal{S}_l|$ both larger than $2/|\alpha|$. This extreme case corresponds to the dark regions of Fig. 6.10.

6.5 Appendix: detailed calculations in the circular geometry

In this section, we present the analytical calculations leading to the expressions of the coarse-grained stress components P_a, P_l, S_a and S_l in Eq. (6.34) and (6.35), and of the rectification coefficient α of Eq. (6.36). Many of the following calculations were originally derived by G. Saggiorato, a former Postdoc of the group. We begin by detailing the form chosen for the displacement field in Sec. 6.5.1. Then, in Sec 6.5.2, we show the particular expressions for the coarse-grained stresses in terms of the stress and displacement fields in the geometry of Fig. 6.6. We finally display the detailed expressions of the coefficients in Eq. (6.34) and (6.35), yielding the expression of α in Sec. 6.5.3.

6.5.1 Form for the displacement field

Except at $r = r_{\text{in}}$, mechanical equilibrium is given by $\boldsymbol{\nabla} \cdot \boldsymbol{\tau}^{\mathsf{T}} = \mathbf{0}$ that in polar coordinates reads:

$$\begin{aligned} \partial_r \tau_{rr} + \partial_\theta \tau_{r\theta}/r + (\tau_{rr} - \tau_{\theta\theta})/r = 0 \\ \partial_r \tau_{r\theta} + \partial_\theta \tau_{\theta\theta}/r + 2\tau_{r\theta}/r = 0 \end{aligned}. \tag{6.42}$$

Then the stress is linked to the deformation gradient

$$\boldsymbol{\eta} = \begin{pmatrix} \partial_r u_r & (\partial_\theta u_r - u_\theta)/r \\ \partial_r u_\theta & (\partial_\theta u_\theta + u_r)/r \end{pmatrix} \tag{6.43}$$

via the weakly nonlinear relation of Eq. (6.30). Given an imposed displacement at $r = r_{\text{in}}$ as in Eq. (6.24), we can expand the displacement field into a Fourier series as

$$u_r(r,\theta) = \sum_n \chi_n(r)\cos n\theta \quad \text{and} \quad u_\theta(r,\theta) = \sum_n \psi_n(r)\sin n\theta. \tag{6.44}$$

For $\mathbf{u}^L$, the relevant Fourier coefficients in Eq. (6.32) are $\chi_0 = e_0\zeta_0$, $\chi_2 = e_2\zeta_2$ and $\psi_2 = e_2\omega_2$. While for $\mathbf{u}^{\text{NL}}$ in Eq. (6.33), we have $\chi_0 = e_2^2\xi_0$, $\chi_2 = e_0e_2\xi_2$, $\chi_4 = e_2^2\xi_4$, $\psi_2 = e_0e_2\pi_2$ and $\psi_4 = e_2^2\pi_4$. Hopefully, the perturbative method makes the equation for $\mathbf{u}^L$ and $\mathbf{u}^{\text{NL}}$ both linear. Indeed, for a displacement of order $\eta \ll 1$, then at first order $\partial_i\tau^L_{ji}(\boldsymbol{\eta}^L) = 0$, and at second order $\partial_i\tau^L_{ji}(\boldsymbol{\eta}^{\text{NL}}) = -\partial_i\tau^{\text{NL}}_{ji}(\boldsymbol{\eta}^L)$. Therefore, given the linear stress-strain relation

$$\tau^L_{ij} = \lambda(\eta_{rr} + \eta_{\theta\theta})\delta_{ij} + \mu(\eta_{ij} + \eta_{ji}), \quad \text{where} \quad \lambda = \kappa - \mu, \tag{6.45}$$

the symmetric stress tensor can be expressed as

$$\boldsymbol{\tau}^L = \sum_n \begin{pmatrix} [(\lambda+2\mu)\chi_n' + \lambda(n\psi_n + \chi_n)/r]\cos n\theta & \mu[\psi_n' - (\psi_n + n\chi_n)/r]\sin n\theta \\ . & [\lambda\chi_n' + (\lambda+2\mu)(n\psi_n + \chi_n)/r]\cos n\theta \end{pmatrix}, \tag{6.46}$$

where the $'$ denote a derivative in r.

Concerning $\mathbf{u}^L$, due to the linearity between the stress $\boldsymbol{\tau}$ and the displacement $\mathbf{u}$, each mode of deformation behaves independently and mechanical equilibrium has to be satisfied mode by mode yielding

$$\begin{aligned} \left\{\left[\chi'' r^2 + \chi' r\right](\lambda+2\mu) - \chi[\lambda + (2+n^2)\mu] + \psi' rn(\lambda+\mu) - \psi n(\lambda+3\mu)\right\}\cos n\theta = 0 \\ \left\{\left[\psi'' r^2 + \psi' r\right]\mu - \psi[n^2\lambda + (2n^2+1)\mu] - \chi' rn(\lambda+\mu) - \chi n(\lambda+3\mu)\right\}\sin n\theta = 0 \end{aligned}, \tag{6.47}$$

where, to simplify the notation, we dropped the n subscript. As the equation does not define an intrinsic scale, the coefficients take the form

$$\chi_n = \mathrm{X}_n r^{c_n} \quad \text{and} \quad \psi_n = \Psi_n r^{c_n} \tag{6.48}$$

which leads to a vectorial equation:

$$\begin{pmatrix} c^2(\lambda+2\mu) - [\lambda + (2+n^2)\mu] & cn(\lambda+\mu) - n(\lambda+3\mu) \\ -cn(\lambda+\mu) - n(\lambda+3\mu) & c^2\mu - [n^2\lambda + (2n^2+1)\mu] \end{pmatrix} \begin{pmatrix} \mathrm{X} \\ \Psi \end{pmatrix} = 0. \tag{6.49}$$

The non-trivial solution where the determinant of the matrix is zero implies that the exponents $c_n \in \{\pm(n+1), \pm(n-1)\}$. Finally, introducing

$$p_n = \frac{\lambda(n+2) + \mu(n+4)}{\lambda n + \mu(n-2)} \quad \text{and} \quad q_n = \frac{\lambda(n-2) + \mu(n-4)}{\lambda n + \mu(n+2)} \tag{6.50}$$

the solutions can be expressed as

$$\begin{aligned} n = 0, \quad & \begin{pmatrix} \chi_0 \\ \psi_0 \end{pmatrix} = r\begin{pmatrix} \mathrm{X}_{0,1} \\ \Psi_{0,1} \end{pmatrix} + \frac{1}{r}\begin{pmatrix} \mathrm{X}_{0,2} \\ \Psi_{0,2} \end{pmatrix} \\ n = 1, \quad & \begin{pmatrix} \chi_1 \\ \psi_1 \end{pmatrix} = \mathrm{X}_{1,0}\begin{pmatrix} 1 \\ -1 \end{pmatrix} + \mathrm{X}_{1,1} r^2 \begin{pmatrix} 1 \\ -p_1 \end{pmatrix} + \frac{\mathrm{X}_{1,2}}{r^2}\begin{pmatrix} 1 \\ 1 \end{pmatrix} \\ n \geq 2, \quad & \begin{pmatrix} \chi_n \\ \psi_n \end{pmatrix} = \mathrm{X}_{2,1} r^{n+1}\begin{pmatrix} 1 \\ -p_n \end{pmatrix} + \frac{\mathrm{X}_{2,2}}{r^{n+1}}\begin{pmatrix} 1 \\ 1 \end{pmatrix} + \mathrm{X}_{2,3} r^{n-1}\begin{pmatrix} 1 \\ -1 \end{pmatrix} + \frac{\mathrm{X}_{2,4}}{r^{n-1}}\begin{pmatrix} 1 \\ q_n \end{pmatrix}, \end{aligned} \tag{6.51}$$

where the remaining parameters $\mathrm{X}_{i,j}, \Psi_{i,j}$ are fixed by the boundary conditions: zero displacement at $r = 0$ and $r = r_{\text{out}}$ and the imposed displacement at $r = r_{\text{in}}$, see Eq. (6.28).

Concerning $\mathbf{u}^{\mathbf{NL}}$, the right-hand side of its equation $\partial_i \tau^L_{ji}(\boldsymbol{\eta}^{\mathrm{NL}}) = -\partial_i \tau^{\mathrm{NL}}_{ji}(\boldsymbol{\eta}^L)$ can be expressed as

$$-\begin{pmatrix} f_0(r) + f_2(r)\cos 2\theta + f_4(r)\cos 4\theta \\ g_2(r)\sin 2\theta + g_4(r)\sin 4\theta \end{pmatrix}. \tag{6.52}$$

This leads to the following equation for each mode of deformation indexed by n:

$$\begin{aligned} \left\{\left[\chi'' r^2 + \chi' r\right](\lambda+2\mu) - \chi[\lambda + (2+n^2)\mu] + \psi' r n(\lambda+\mu) - \psi n(\lambda+3\mu) + f\, r^2\right\}\cos n\theta = 0 \\ \left\{\left[\psi'' r^2 + \psi' r\right]\mu - \psi[n^2\lambda + (2n^2+1)\mu] - \chi' r n(\lambda+\mu) - \chi n(\lambda+3\mu) + g\, r^2\right\}\sin n\theta = 0 \end{aligned}$$

Since the f_i, g_i are sums of r^k with k odd between -9 and $+3$, we find that the χ_i, ψ_i are sums of r^k with k odd between -7 and $+5$.

6.5.2 Form for the coarse-grained stresses

The coarse-grained stresses of Eqs. (6.27) are expressed in Cartesian coordinates, while the stress field is more easily expressed in polar coordinates. In the following (and in this subsection only), we specifically denote Cartesian indices x, y with Greek letters (μ, ν) and polar indices r, θ with Latin letters (i, j, k). The change-of-basis matrix between these two systems reads $\mathbf{R} = \left(\begin{smallmatrix} \cos\theta & -\sin\theta \\ \sin\theta & \cos\theta \end{smallmatrix}\right)$. In the circular geometry of Fig. 6.6 where the active unit produces a discontinuity in the stress at r_{in} in the initial configuration, the coarse-grained stresses are expressed as follows:

$$\bar{\sigma}^a_{\mu\nu} = \frac{1}{\pi r^2_{\mathrm{out}}} \oint_{\partial\Omega} R_{\mu i}\, \tau_{ik}\, R_{\nu j}\, X_j \,\mathrm{d}a_k = \frac{1}{\pi}\int_0^{2\pi} \mathrm{d}\theta\, R_{\mu i}\, \tau_{ir}(r_{\mathrm{out}},\theta) R_{\nu r}, \tag{6.53a}$$

$$\begin{aligned} \bar{\sigma}^l_{\mu\nu} &= \frac{1}{\pi r^2_{\mathrm{out}}} \int_\Omega R_{\mu i}\, \partial_k \tau_{ik}\, R_{\nu j}\, X_j \,\mathrm{d}V \\ &= \frac{1}{\pi}\frac{r^2_{\mathrm{in}}}{r^2_{\mathrm{out}}} \int_0^{2\pi} \mathrm{d}\theta\, R_{\mu i}\Big[\tau_{ir}(r^+_{\mathrm{in}},\theta) - \tau_{ir}(r^-_{\mathrm{in}},\theta)\Big] R_{\nu r}\left[1 + \frac{u_r(r_{\mathrm{in}},\theta)}{r_{\mathrm{in}}}\right], \end{aligned} \tag{6.53b}$$

where $\partial_k \tau_{ik}$ denotes the stress divergence expressed in polar coordinates given by the left-hand side of Eq. (6.42). Then, introducing $\rho = (r_{\mathrm{out}}/r_{\mathrm{in}})^2$, the active pressure and shear stress rescaled so as to compensate for dilution read

$$\rho(\bar{\sigma}^a_{xx} + \bar{\sigma}^a_{yy}) = -2\mathcal{P}_a = \frac{\rho}{\pi}\int \tau_{rr}(r_{\mathrm{out}},\theta), \tag{6.54a}$$

$$\rho(\bar{\sigma}^a_{xx} - \bar{\sigma}^a_{yy}) = -2\mathcal{S}_a = \frac{\rho}{\pi}\int \Big[\tau_{rr}(r_{\mathrm{out}},\theta)\cos 2\theta - \tau_{\theta r}(r_{\mathrm{out}},\theta)\sin 2\theta\Big], \tag{6.54b}$$

with similar expressions for the local pressure and shear stress:

$$-2\mathcal{P}_l = \frac{1}{\pi}\int \Big[\tau_{rr}(r^+_{\mathrm{in}},\theta) - \tau_{rr}(r^-_{\mathrm{in}},\theta)\Big]\left[1 + \frac{u_r(r_{\mathrm{in}},\theta)}{r_{\mathrm{in}}}\right], \tag{6.55a}$$

$$\begin{aligned} -2\mathcal{S}_l = \frac{1}{\pi}\int \Big\{ &\Big[\tau_{rr}(r^+_{\mathrm{in}},\theta) - \tau_{rr}(r^-_{\mathrm{in}},\theta)\Big]\cos 2\theta \\ &- \Big[\tau_{\theta r}(r^+_{\mathrm{in}},\theta) - \tau_{\theta r}(r^-_{\mathrm{in}},\theta)\Big]\sin 2\theta\Big\}\left[1 + \frac{u_r(r_{\mathrm{in}},\theta)}{r_{\mathrm{in}}}\right]. \end{aligned} \tag{6.55b}$$

This finally leads to the expressions in Eqs. (6.34) and (6.35).

6.5.3 Expressions of the coefficients in the coarse-grained stresses

We further display the complete expressions of the coefficients in Eqs. (6.34) and (6.35) obtained after finding the strain field through force balance (see Sec. 6.5.1) and integrating the resulting stress

via Eq. (6.30), as in (6.54) and (6.55). In order to make sense of the cumbersome expressions of A, B_a, B_l and C, we introduce several quantities: $Y = (3-\nu)^2(1+\rho^2) + 2(3-6\nu-\nu^2)\rho$,

$$\begin{aligned}
y_0 &= 1215 - 1863\nu + 756\nu^2 - 126\nu^3 + 87\nu^4 - 43\nu^5 + 6\nu^6 \\
&\quad + (81 - 2457\nu + 2412\nu^2 - 594\nu^3 + 265\nu^4 + 155\nu^5 - 22\nu^6)\rho \\
&\quad + (1782 - 3798\nu + 6216\nu^2 - 3948\nu^3 + 326\nu^4 - 286\nu^5 + 28\nu^6)\rho^2 \\
&\quad - (918 + 1170\nu - 2616\nu^2 + 1044\nu^3 + 54\nu^4 - 262\nu^5 + 12\nu^6)\rho^3 \\
&\quad + (459 + 45\nu + 132\nu^2 - 918\nu^3 + 515\nu^4 - 71\nu^5 - 2\nu^6)\rho^4 \\
&\quad - (891 - 1755\nu + 1188\nu^2 - 294\nu^3 - 13\nu^4 + 17\nu^5 - 2\nu^6)\rho^5,
\end{aligned}$$

$$\begin{aligned}
y_1 &= 1863 - 756\nu - 54\nu^2 + 12\nu^3 + 7\nu^4 + (1377 - 1260\nu + 102\nu^2 - 108\nu^3 - 31\nu^4)\rho \\
&\quad + (1782 - 1368\nu + 804\nu^2 + 168\nu^3 + 54\nu^4)\rho^2 + (162 - 504\nu - 132\nu^2 - 24\nu^3 - 46\nu^4)\rho^3 \\
&\quad + (243 + 108\nu + 18\nu^2 - 84\nu^3 + 19\nu^4)\rho^4 - (243 - 324\nu + 162\nu^2 - 36\nu^3 + 3\nu^4)\rho^5,
\end{aligned}$$

$$\begin{aligned}
y_2 &= 2511 - 4104\nu + 4023\nu^2 - 1416\nu^3 + 173\nu^4 - 48\nu^5 + 13\nu^6 \\
&\quad + (1377 - 8352\nu + 6369\nu^2 - 2568\nu^3 - 77\nu^4 + 104\nu^5 - 53\nu^6)\rho \\
&\quad + (6966 - 16128\nu + 17430\nu^2 - 6480\nu^3 + 1890\nu^4 - 176\nu^5 + 82\nu^6)\rho^2 \\
&\quad + (2754 - 9216\nu + 6162\nu^2 - 1392\nu^3 - 794\nu^4 + 240\nu^5 - 58\nu^6)\rho^3 \\
&\quad + (2187 - 3672\nu + 3843\nu^2 - 1896\nu^3 + 545\nu^4 - 128\nu^5 + 17\nu^6)\rho^4 \\
&\quad - (243 - 189\nu^2 + 72\nu^3 + 9\nu^4 - 8\nu^5 + \nu^6)\rho^5,
\end{aligned}$$

and

$$\begin{aligned}
z_0 &= 81 - 270\nu + 234\nu^2 - 36\nu^3 + 13\nu^4 - 6\nu^5 \\
&\quad + (135 - 378\nu + 366\nu^2 - 196\nu^3 - 29\nu^4 + 22\nu^5)\rho \\
&\quad + (162 - 708\nu + 1116\nu^2 - 464\nu^3 + 82\nu^4 - 28\nu^5)\rho^2 \\
&\quad + (126 - 564\nu + 540\nu^2 - 168\nu^3 - 106\nu^4 + 12\nu^5)\rho^3 \\
&\quad + (45 - 222\nu + 426\nu^2 - 188\nu^3 + 17\nu^4 + 2\nu^5)\rho^4 \\
&\quad + (27 - 162\nu + 198\nu^2 - 100\nu^3 + 23\nu^4 - 2\nu^5)\rho^5,
\end{aligned}$$

$$\begin{aligned}
z_1 &= 27 - 18\nu + 3\nu^2 + (189 + 18\nu - 11\nu^2)\rho + (174 + 12\nu + 14\nu^2)\rho^2 \\
&\quad + (138 - 12\nu - 6\nu^2)\rho^3 + (39 + 6\nu - \nu^2)\rho^4 + (9 - 6\nu + \nu^2)\rho^5,
\end{aligned}$$

$$\begin{aligned}
z_2 &= 243 - 270\nu + 84\nu^2 - 34\nu^3 + 9\nu^4 + (189 - 522\nu + 404\nu^2 + 58\nu^3 - 33\nu^4)\rho \\
&\quad + (510 - 1356\nu + 568\nu^2 - 84\nu^3 + 42\nu^4)\rho^2 + (474 - 612\nu + 312\nu^2 + 100\nu^3 - 18\nu^4)\rho^3 \\
&\quad + (159 - 486\nu + 244\nu^2 - 10\nu^3 - 3\nu^4)\rho^4 + (153 - 210\nu + 116\nu^2 - 30\nu^3 + 3\nu^4)\rho^5.
\end{aligned}$$

In the end, we find

$$A = \frac{4\kappa\rho}{(1+\nu)(\rho-1)}, \tag{6.56a}$$

$$B_l = -\kappa\rho\frac{(3-\nu)y_0 + (1-\nu)^2(1+\nu)y_1\,\kappa_1 + (1-\nu)y_2\,\mu_1}{(3-\nu)^2(1+\nu)(\rho-1)^2Y^2}, \tag{6.56b}$$

$$B_a = -\kappa\rho\frac{z_0 + (1-\nu)^2(1+\nu)z_1\,\kappa_1 + (1-\nu)z_2\,\mu_1}{(1+\nu)(\rho-1)^2Y^2}, \tag{6.56c}$$

$$C = 4\mu\rho\frac{2(3+\nu) + (3-\nu)(\rho+\rho^2)}{(\rho-1)Y}. \tag{6.56d}$$

This finally yields the expression of $\alpha = (B_a - B_l)/C^2$ given in Eq. (6.37).

Chapter 7

Simulations and experiments agree with the predictions

In Ch. 6, we examined the effect of generic, lowest-order constitutive nonlinearities, and discovered that the rectification behavior depended primordially on the corrections to the elastic moduli κ_1, μ_1. In this chapter, we put this analytical finding to the test with two sets of simulations, and one set of experiment. In Sec. 7.1, we first use finite-element simulations of fully nonlinear models to show that our conclusions remain qualitatively valid at higher orders. Second, we recover the predicted expansion bias of granular media with simulations of granular dynamics in Sec. 7.2. Last, Sec. 7.3 presents preliminary experiments by F. Box showing the contraction bias of thin elastic sheets, which can freely buckle out of plane.

7.1 Finite element simulations

While the calculations in Sec. 6.3 are strictly valid only for small local stresses, one may hope that Eq. (6.36) remains qualitatively correct for strong active units with $\mathcal{P}_l \approx \mathcal{S}_l \gtrsim \kappa$. We test this expectation through finite element simulations of four fully (*i.e.*, not weakly) nonlinear models. To this end, we introduce two models with clear buckling and anti-buckling behaviors, which lead to a readily observable reversal of the active pressure sign, due to rectification. We also analyze two previously discussed models where these behaviors are less pronounced: the neo-Hookean model of rubber (Sec. 5.1.3), and another one which can mimic the shear-stiffening behavior of fiber networks (Sec. 5.1.3). Consistent with analytical predictions, these systems display a smaller propensity for rectification, and we show that the predictions of Eq. (6.36) remain valid up to intermediate stress values.

Bucklable and anti-bucklable models The simple neo-Hookean model of Eq. (5.13) has $\kappa_1 = 1/2$, $\mu_1 = -3/2$, which does not correspond to a lot of buckling or anti-buckling. From the analysis in Fig. 6.7, we expect the rectification behavior to be very small. We thus introduce another similar model with two parameters that can tune its behavior from buckling to anti-buckling. It has an elastic energy density

$$E = \frac{\kappa}{2}\frac{(J-1)^2}{1+m(J-1)} + \frac{\mu}{2}\frac{I/J-2}{1+n(J-1)}, \tag{7.1}$$

where $I = \mathrm{Tr}(\mathbf{1}+2\boldsymbol{\varepsilon})$ and $J = \det(\mathbf{1}+\boldsymbol{\eta})$. The constants m, n are defined through $\kappa_1 = 1/2 - 3m$, $\mu_1 = -3/2 - n$, such that the case $m = n = 0$ corresponds to the neo-Hookean model. We illustrate a bucklable and an anti-bucklable material by choosing two media with $\kappa_1 = \mu_1 = -4$ and $\kappa_1 = \mu_1 = 1$. These values are equidistant from $-3/2$, as denoted by symbols in Fig. 6.7.

Methods We solve the set of equations (6.28) via simulations with the finite element software Fenics (Alnæs et al., 2015) version 2019.2.0.dev0. We use a mesh with maximal size $l = 0.01$ for $r_{\mathrm{in}} = 1$ and $r_{\mathrm{out}} = 2$, and another one with $l = 0.1$ for $r_{\mathrm{out}} = 10$. They were both created with Gmsh version

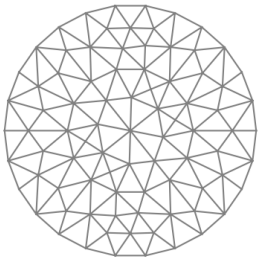

Figure 7.1: **Example of a mesh compatible with the geometry of** Fig. 6.6**.** A mesh with maximal size 0.5 for $r_{\text{in}} = 1$ and $r_{\text{out}} = 2$, and without rotational symmetry. The circular junction is visible at intermediate radius.

4.4.1. In all figures, the error bars correspond to the differences between two meshes at l and $l/10$, which gives roughly 5% of $\mathcal{S}_l$ or $\mathcal{P}_l$ for all points. The meshes are created without enforcing rotational symmetry, which results in small non-zero values for the non-diagonal coefficients that should be zero in a continuum system (*e.g.*, $\bar{\sigma}^l_{xy}$), as shown in Eq. (6.25). However, we find that these values are smaller than 5% of the diagonal coefficients in all simulations. In the geometry of Fig. 6.6, if we apply too large a deformation at r_{in}, we come into contact with the fixed boundary at r_{out}, which poses some numerical issues. Therefore, we can only perform accurate simulations up to about $\eta = |e_0| + |e_2| \sim 0.6$. In order to ensure that there are vertices at $r = r_{\text{in}}$, we join two distinct meshes: a disk of radius r_{in} and a circle between radii r_{in} and r_{out}, as displayed in Fig. 7.1.

We now discuss the results of simulations performed on the aforementioned fully nonlinear models. As expected, the bucklable model of Eq. (7.1) with $\kappa_1 = \mu_1 = 1$ induces contraction, while the anti-bucklable one with $\kappa_1 = \mu_1 = -4$ causes expansion, see Fig. 7.2. The quantitative predictions of Eq. (6.36) moreover remain largely valid up to local stress values comparable with the bulk modulus of

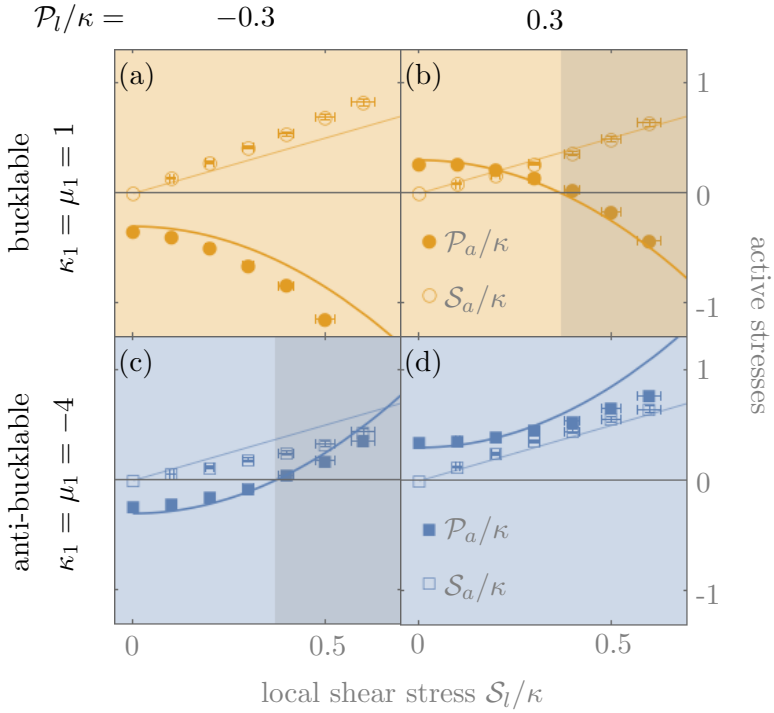

Figure 7.2: **The small-stress asymptotic prediction of** Eq. (6.36) **(lines) accurately capture the finite-element simulation results (symbols) even for intermediate stress values.** Here $\nu = 0.1$ and $r_{\text{out}}/r_{\text{in}} = 2$ in the geometry of Fig. 6.6. (a,b) A fiber-like bucklable model, (c,d) a very anti-bucklable model mimicking a granular medium. The values of $\mathcal{P}_l$, $\mathcal{S}_l$ pictured in (b,c) are marked by dashed arrows in Fig. 6.10, and background shading follows the same convention. The error bars denote the estimated magnitude of the error induced by the finiteness of the simulation mesh size.

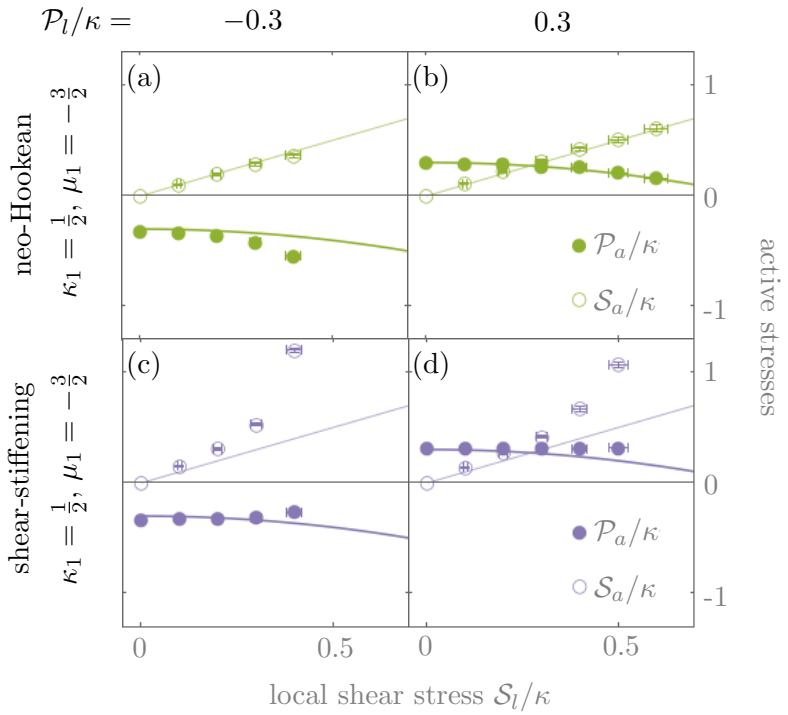

Figure 7.3: **Additional plots of the coarse-grained stresses are in agreement** with Eq. (6.36) **up to intermediate stresses and in a large scale of parameters.** (a-b) Rubber-like neo-Hookean model [$a = b = 0$ in Eq. (5.13). (c-d) Fiber-like shear-stiffening model of Eq. (5.20) with $g = 10$, following the predictions up to the point where stresses diverge (when $\eta \sim 1/\sqrt{g}$). For all plots, $\nu = 0.1$ and $r_{\text{out}}/r_{\text{in}} = 2$.

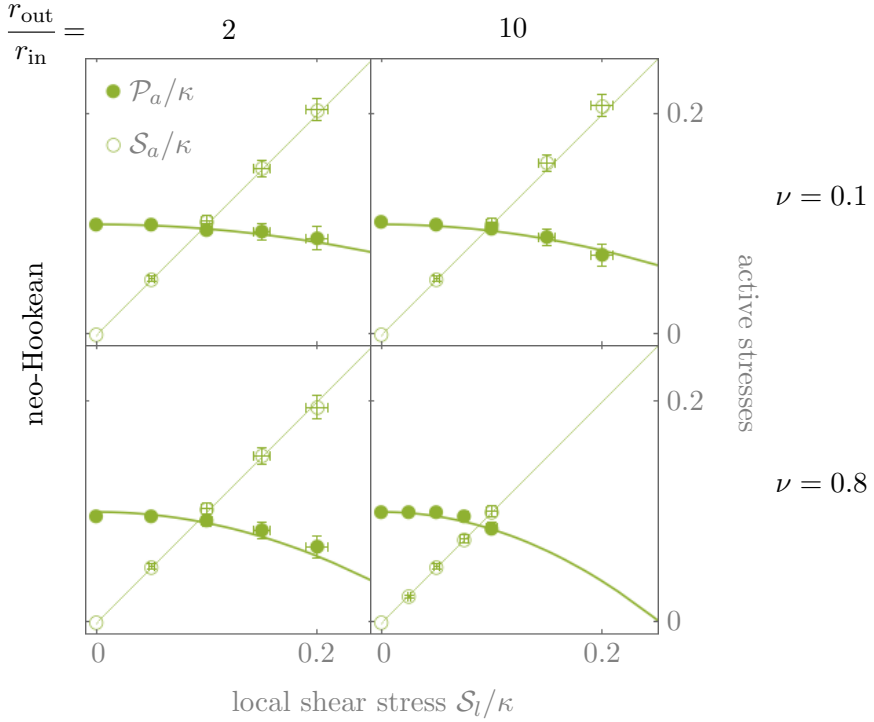

Figure 7.4: **Additional plots of the coarse-grained stresses are in agreement with** Eq. (6.36) **up to intermediate stresses and in a large scale of parameters.** For $\mathcal{P}_l = 0.1\kappa$, the predictions at $\nu = 0.8$ and $r_{\text{out}}/r_{\text{in}} = 10$ remain quantitatively accurate.

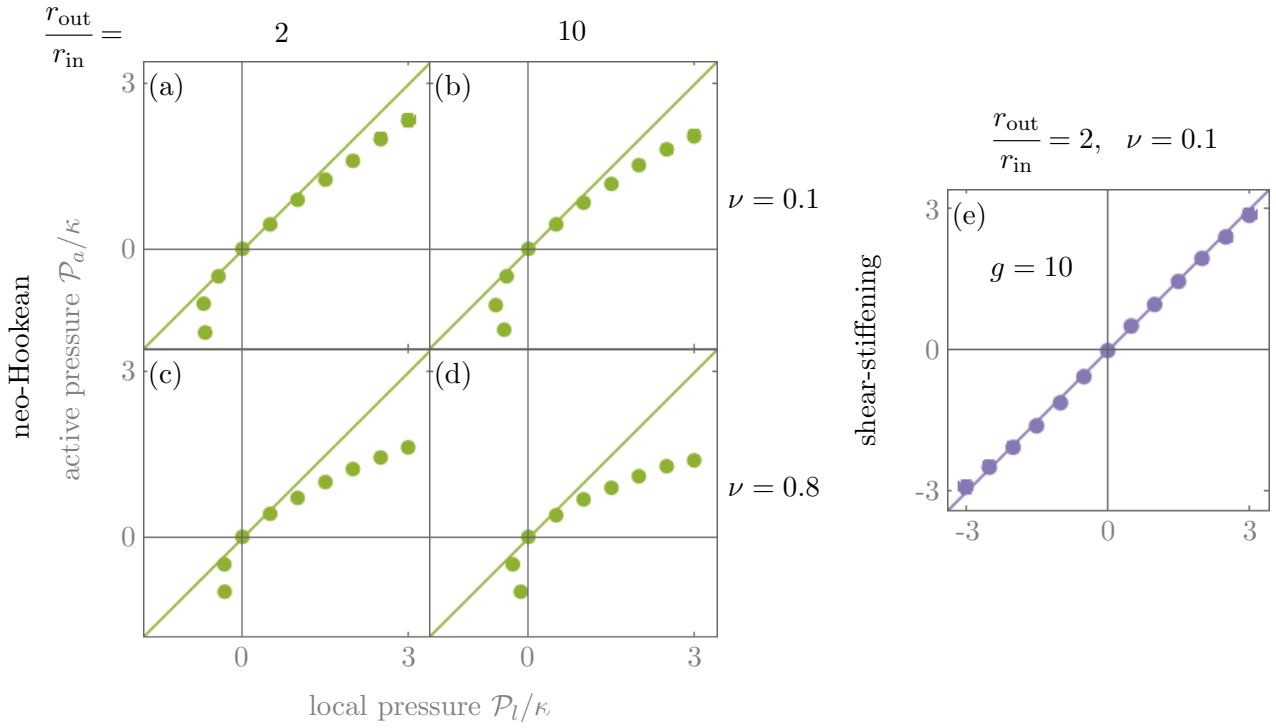

Figure 7.5: **Investigation of the $\mathcal{P}_a \sim \mathcal{P}_l$ relationship of** Eq. (6.36) **for $\mathcal{S}_l = 0$.** The predictions at zero shear stress (*i.e.* $|\mathcal{S}_l|, |\mathcal{S}_a| < 0.01\kappa$) remain reasonably accurate up to a few $\mathcal{P}_l/\kappa$. (a-d) In the neo-Hookean case, the nonlinear terms are such that $\mathcal{P}_a < \mathcal{P}_l$ and become increasingly significant as ν and $r_{\text{out}}/r_{\text{in}}$ increase. Specifically, the agreement deteriorates from panel (a) to panels (b) and (c), to panel (d). (e) In the shear-stiffening case these nonlinear terms are first decreased up to $g \sim$ 2-5 [see Eq. (5.20)] and then increased in the opposite direction (such that $\mathcal{P}_a > \mathcal{P}_l$).

the network, which implies deformations of the medium of order one. Likewise for the neo-Hookean model of Eq. (5.13), we recover the predicted small tendency to rectify towards contraction, see Fig. 7.4(a,b). Concerning the shear-stiffening model of Eq. (5.20), as shown in Fig. 7.3(c,d) where $g = 10$, we recover Eq. (6.36) at small stress. But due to the shear stress divergence at finite shear strain in Eq. (5.20), our predictions fail when $\mathcal{S}_l/\kappa \gtrsim 1/\sqrt{c}$. Furthermore, the agreement between the simulations with the neo-Hookean model and Eq. (6.36) remains quantitative in the small stress regime for all considered values of the Poisson's ratio ν and the ratio of the boundary radius to the active unit radius $r_{\text{out}}/r_{\text{in}}$, see Fig. 7.4.

We finally compare the dependence of $\mathcal{P}_a$ with $\mathcal{P}_l$ at zero shear stress with the weakly nonlinear prediction $\mathcal{P}_a \sim \mathcal{P}_l$. As displayed in Fig. 7.5, we recover the prediction for small stresses, but higher order nonlinearities induce significant deviations for $\mathcal{P}_l/\kappa$ outside of $[-0.3, 1]$. This suggests that rectification effects also manifest in the case of isotropic active units with large local stress values (Ronceray et al., 2016). In the end, we see that the predictions of Eq. (6.36) relating the active and local stress components fail when either the local pressure or the local shear stress become comparable to the bulk modulus κ. Our weakly nonlinear predictions additionally fail close to stress divergences, *i.e.* when the nonlinearities become too significant compared to the linear terms.

7.2 Granular dynamics simulations

After having investigated the mechanics of granular media modeled as a continuum, we hereby perform mechanical analyses of randomly-jammed disc packings in two dimensions. We obtain equilibrium configurations at different area fractions through relaxation, and study their elastic response to a circular active unit in the spirit of the analytics in Sec. 6.3. In the following, we describe the relaxation process to obtain relatively equilibrated circular packings in Sec. 7.2.1. In Sec. 7.2.2,

we then gently perturb the system with a circular active unit which produces isotropic or dipolar radial forces. The results discussed in Sec. 7.2.3 show an expansion bias in both cases of isotropic and dipolar forcing. The measured dipolar rectification coefficient α moreover increases near jamming, in agreement with the analytical predictions.

7.2.1 Generation of equilibrium jammed configurations

As seen in Fig. 5.8, *right* and following the discussion of Sec. 5.3, the jammed phase corresponds to high area fraction ϕ, low temperature T, and low applied shear strain σ_{xy}. In practice, there exist several methods to obtain jammed configurations (van Hecke, 2009). From an initial unjammed configuration at low density, one typically increases the disc diameters until a jammed configuration at a given target density ϕ is obtained. But this configuration is obviously out of equilibrium, such that any posterior change on the system will dramatically change its properties. In order to reach a more stable configuration, one can use conjugate-gradient techniques to find the nearest potential-energy minimum (O'Hern et al., 2003). The system can also relax by thermal agitation using algorithms akin to molecular dynamics, but with solid-like interactions, therefore referred to as "granular dynamics". In this procedure, the temperature T is slowly decreased to reach a more stable local equilibrium (Makse et al., 1999; 2004; Zhang and Makse, 2005). This is practically attained when the pressure remains unchanged over a long period of time (usually 5.10^5 simulation steps). If the initial compression is not large enough, such that the target $\phi < \phi_c$, then a jammed packing with nonzero pressure cannot be obtained [Fig. 7.6, *left*] which helps determining the particular value of ϕ_c for a given packing history. Finally, some numerical studies use combinations of the two aforementioned methods to obtain jammed packings with particular heterogeneous structures (Schreck et al., 2011b). As previously discussed, using polydisperse discs prevents triangular arrangement, such that the configurations are random.

Protocol We initialize a gas of 50:50 bidisperse discs with a diameter ratio $D_b/D_s = 1.4$ and equal mass in a square box with periodic boundary conditions, or within a circular arena. The positions are taken uniformly at random and the speeds follow a Maxwellian distribution with temperature T. A

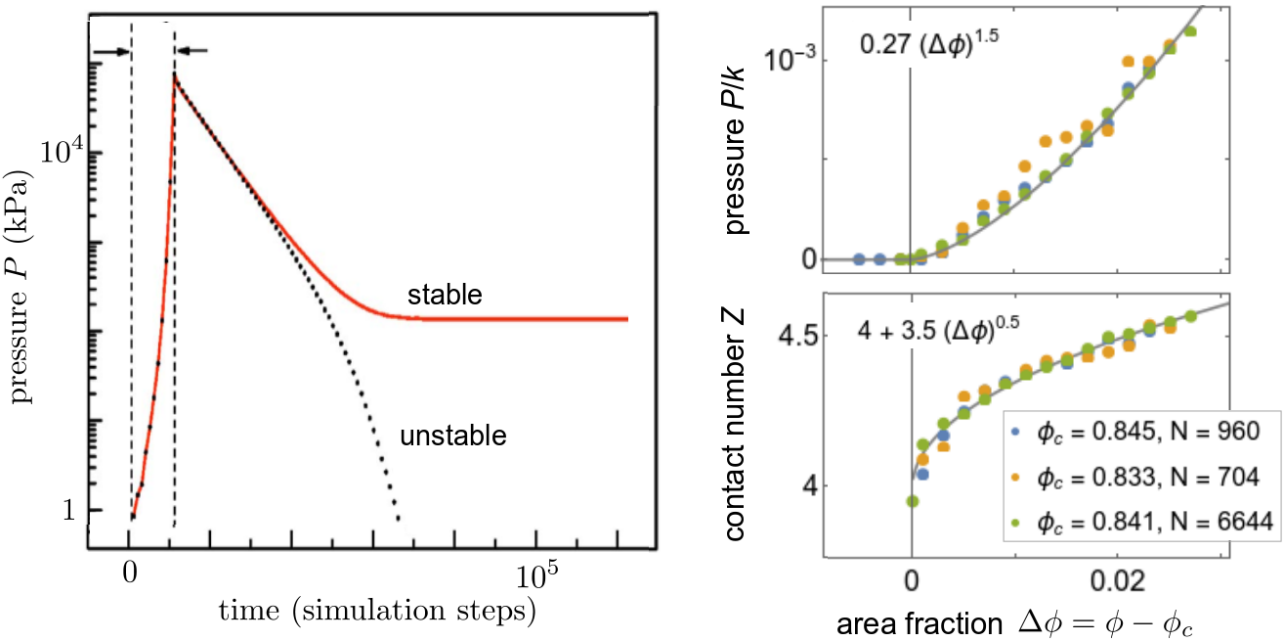

Figure 7.6: **Conclusive tests of two scaling laws near jamming.** *Left*, relaxation from an initial compression of a stable versus unstable packing, adapted from (Zhang and Makse, 2005). *Right*, numerical results from equilibrium disc packings with Hertzian interactions at different area fractions. Despite the varying of ϕ_c with the packing history, the simulated pressure and contact number follow the predicted scaling laws with the area fraction, see Eq. (5.22). By dividing the pressure by the elastic stiffness k, we even recover the prefactors given by O'Hern et al. (2003).

seed is used for the positions and the velocities, so that we can study the packings with similar histories and thus similar critical area fractions ϕ_c. We increase the radii of the big and small discs with the same rate until the desired ϕ is reached. We then let the grains equilibrate in three consecutive stages at decreasing temperatures: $T/k = 10^{-7}$, 10^{-9} and 10^{-11}, and measure the pressure P/k and the contact number Z along the way, where k is the elastic stiffness. The sudden jumps in T help ensuring that a quasi-stable equilibrium is reached, and resolve technical issues with the calculations of physical observables. As in (Schreck et al., 2011b), below ϕ_c the pressure goes to very low values ($\approx 10^{-8}$) and decreases with the temperature jumps. But above ϕ_c, once a local potential energy minimum is reached, the pressure goes to a value independent of T. We declare that a configuration is equilibrated when 5×10^5 simulation steps give similar values.

Interaction details Both inter-disc and disc-arena interactions are modeled as Hertzian, with normal elastic and viscous stiffnesses $k = 1000$ in pressure units and $\gamma = 73$ in inverse units of time. We set the friction coefficient to zero, which suppresses any tangential forces. The choice of γ corresponds to a particle mass $\frac{\pi}{6}$ and a coefficient of restitution $e_r = 0.1$. We finally take the time interval dt to be a fraction of the contact time $\tau_c = -\frac{2}{\gamma} \ln e_r \approx 0.027$ such that the dynamics is realistic (Bouzid, 2014; Silbert et al., 2001). In practice, we choose $dt = \tau_c/50 \approx 5.5 \times 10^{-4}$. The precise values of k, γ and e_r do not matter for the final values of P/k and Z.

We perform the granular dynamics simulations using the software LAMMPS (Thompson et al., 2022). By repeating the aforementioned protocol, we obtain random jammed configurations for different target densities ϕ, and for different packing histories, for which we plot the data points in Fig. 7.6, *right*. We see that by plotting the pressure and the contact number versus the area fraction difference $\Delta\phi = \phi - \phi_c$, the data with different histories and different number of discs N fall nicely onto the same master curves in agreement with the previous work of O'Hern et al. (2003). As expected, the noise in the data decreases with the number of discs, such that data with more than 6000 discs can be considered optimal.

7.2.2 Force field ring

The discs are set within a circular elastic arena, such that the displacement is not strictly zero at the boundary, but we find it always negligible compared to the displacements in the bulk. In order to limit the possible flows that arise due to forcing, we introduce an active ring-like region in which the discs feel a constant radial force, in addition to the forces due to the imposed initial pressure P_{init}. This setup is a bit far from an actual T1-like shear transformation [Fig. 5.9], but it allows us to produce mesoscopic deformations. Similar mesoscopic setups have been considered for instance in the simulations of Puosi et al. (2014) to study the time-dependent elastic response of slightly different systems. Furthermore, the active ring can be thought of as a collection of these shear transformations. We find that this minimal and versatile new setup captures some essential features of the rectification towards expansion predicted in granular media.

In the nearly-jammed systems we consider, *i.e.* $\phi \approx 0.9$-1, the largest interpenetration $P_{\text{init}}/k \approx 2\%$. The average distance between two discs in contact is thus roughly the mean disc diameter $D \approx (D_s + D_b)/2$. Inside the arena with inner radius r_{arena}, we define two rings which serve as supports for the computation of the coarse-grained stresses. In Fig. 7.7, the orange discs initially lie in the local ring with radius $r \in I_l = [r_{\text{in}} - \frac{D}{2}, r_{\text{in}} + \frac{D}{2}]$, which contains roughly one layer of discs. Likewise, the blue discs initially lie in the boundary ring $r \in I_b = [r_{\text{out}} - \frac{D}{2}, r_{\text{out}} + \frac{D}{2}]$. We set the outer part of the boundary ring at the arena radius, such that $r_{\text{arena}} = r_{\text{out}} + D/2$. Then, on each disc in the local ring, we add a small constant active component to its radial force:

$$\mathbf{f}^{\text{act}}/k = \big(f_0 + 2f_2 \cos 2\theta\big)\hat{\mathbf{r}}. \tag{7.2}$$

Here, $f_0, f_2 \ll 1$ refer to the isotropic and dipolar parts, in the spirit of the imposed displacement of Eq. (6.24).

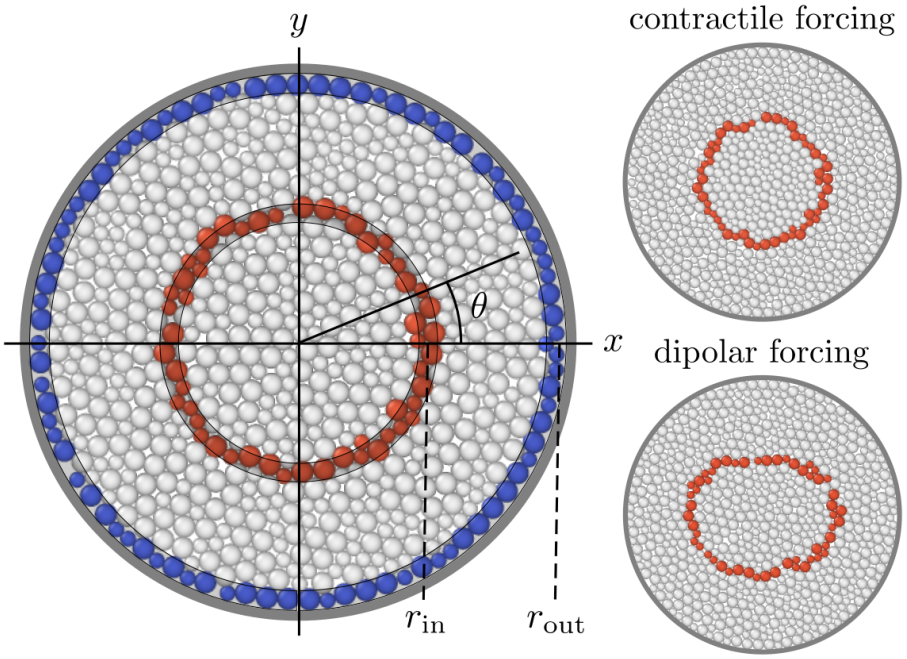

Figure 7.7: **A circular jammed packing subject to internal active forces as in** Fig. 6.6**.** *Left*, initial configuration of ≈ 700 discs. Active radial forces as in Eq. (7.2) are imposed on the orange beads, and further transmitted to the blue discs at the boundary. *Top*, the same packing under isotropic contractile forcing $f_0 < 0$. In the final configuration, some gray discs are now subject to the forcing. *Bottom*, dipolar forcing $f_2 < 0$.

Protocol We set f_0 and f_2 to a constant value and let the system relax for 30 000 simulation steps, *i.e.* roughly 16 in time units. We wait for any flow to stop before our measurement and we measure the elastic stress on each disc μ in the boundary ring, which reads

$$\sigma_{ij}^{(\mu)} = -\frac{1}{2} \sum_{\nu \,\text{neigh.}} (r_i^{(\nu)} - r_i^{(\mu)}) f_j^{\mu\to\nu}, \tag{7.3}$$

where the $\{\mathbf{r}^{(\nu)}\}$ are the positions of the neighbors of disc μ, which exert forces $\mathbf{f}^{\mu\to\nu}$. We do not take into account the data points for which there has been rearrangements all over the sample, as it clearly disrupts the packing history.

Coarse-grained stresses In the setup of Fig. 7.7, the boundary and local coarse-grained stresses $\bar{\boldsymbol{\sigma}}^b$ (previously written $\bar{\boldsymbol{\sigma}}^a$) and $\bar{\boldsymbol{\sigma}}^l$ of Eqs. (6.1), (6.2) can be defined as summations over disc quantities in the spirit of Eq. (6.53). The boundary stress is obtained by averaging a stress measure over the discs in the boundary ring:

$$\bar{\sigma}_{ij}^b = \frac{2}{N_b} \sum_{I_b} \frac{\sigma_{ik}}{k} (\hat{\mathbf{e}}_j \cdot \hat{\mathbf{r}})(\hat{\mathbf{e}}_k \cdot \hat{\mathbf{r}}), \tag{7.4}$$

where the number of discs in the boundary ring $N_b \approx 2\pi r_{\text{out}}/D$ since it contains approximately one layer. Here, the disc stress σ_{ij} is expressed in Cartesian coordinates, $\hat{\mathbf{e}}_i$ denotes the unit vector in direction i and $\cdot$ denotes the scalar product. Likewise, neglecting the correction involving the radial displacement, the local stress can be defined as an average of a diluted stress difference over the discs in the local ring. For simplicity purposes, we replace this stress difference by a term involving the active forces of Eq. (7.2), such that the local stress reads

$$\bar{\sigma}_{ij}^l = \frac{2}{N_l} \sum_{I_l} \frac{r_{\text{in}}^2}{r_{\text{out}}^2} \left(-\frac{D}{2} \frac{f_i^{\text{act}}}{k} \right) (\hat{\mathbf{e}}_j \cdot \hat{\mathbf{r}}), \tag{7.5}$$

where the number of discs in the local ring $N_l \approx 2\pi r_{\text{in}}/D$. Then, the boundary and local coarse-grained pressures corrected for dilution $\mathcal{P}_b$ (previously written $\mathcal{P}_a$) and $\mathcal{P}_l$, and shear stresses $\mathcal{S}_b$ (previously

written $\mathcal{S}_a$) and $\mathcal{S}_l$ are defined through Eqs. (6.25) and (6.26). In the following, we compare $\mathcal{P}_b, \mathcal{S}_b$ to their zero active force counterparts $\mathcal{P}_b^{f=0}, \mathcal{S}_b^{f=0}$ and we introduce

$$\Delta\mathcal{P}_b = \mathcal{P}_b - \mathcal{P}_b^{f=0} \quad \text{and} \quad \Delta\mathcal{S}_b = \mathcal{S}_b - \mathcal{S}_b^{f=0}. \tag{7.6}$$

We find that the noise level set by the values of the non-diagonal coefficients (or the diagonal ones when they should vanish) is less than 10% for $N \geq 6000$ discs. The sum of the added forces and torques ($\propto f_x^{\text{act}} \sin\theta - f_y^{\text{act}} \cos\theta$) are inside the noise.

We further consider two types of forcing: isotropic when $f_2 = 0$, and dipolar when $f_0 = 0$. In the isotropic case, since the forces are applied on all discs in the local ring at each time step, two distinct regions appear. For a contractile active unit $f_0 < 0$, the inner region has a higher contact number, while the outer region has a lower one. Whereas in the dipolar case, the elastic response of the packing can be measured up to the point where disc flows start to appear, corresponding roughly to $\mathcal{S}_l \sim P_{\text{init}}/k$.

7.2.3 Rectification towards expansion in both dipolar and isotropic cases

In the dipolar forcing case, up to the intermediate force regime where $f_2 \lesssim P_{\text{init}}/k$, the local shear stress increases linearly with the force: $\mathcal{S}_l \approx D f_2/2$ in agreement with the definitions of Eqs. (7.5) and (6.25). Then, we can express the boundary stresses in terms of the local stresses as follows:

$$\Delta\mathcal{P}_b \approx \mathcal{P}_l + \alpha_{\text{sim}} \mathcal{S}_l^2, \quad \Delta\mathcal{S}_b \approx A\,\mathcal{S}_l, \tag{7.7}$$

where α_{sim} is a dimensionless coefficient quantifying the bias of granular media in stress transmission under dipolar forcing, and the linear coefficient $A \approx 1.2$ is roughly constant. As shown in Fig. 7.8, the data for ≈ 6700 are strongly reproducible and show a bias coefficient α_{sim} that is positive. This means that as the internal dipolar stresses are transmitted to the boundary, they are rectified towards expansion. Similarly in the isotropic forcing case, the local pressure is also linear in the force $\mathcal{P}_l \approx D f_0/2$, the local and boundary shear stresses are negligible in front of f_0 and the boundary pressure reads

$$\Delta\mathcal{P}_b \approx \mathcal{P}_l + \beta_{\text{sim}} \mathcal{P}_l^2, \tag{7.8}$$

where β_{sim} is an additional bias coefficient corresponding to isotropic forcing. The data shown in Fig. 7.9 show again an expansile bias.

We then compute the bias coefficients for different area fractions $\Delta\phi$, see Fig. 7.10. We find that they are both positive for all considered values of $\Delta\phi$, which shows an expansion bias in agreement with our predictions. For reasons still unclear, the dipolar coefficient α_{sim} is larger than the isotropic coefficient β_{sim}. Furthermore, they both increase as the distance to jamming decreases with scalings close to $(\Delta\phi)^{-2}$. We now compare the simulation results for α_{sim} to the continuum medium calculations $k\alpha$. As we input the expressions of κ, μ, κ_1, and μ_1 from Eq. (6.21) into the theoretical expression of α in Eq. (6.37), we find a quantitative agreement with the simulated values in a wide range of area fractions $\Delta\phi$. This is particularly surprising as the agreement is obtained without adjustable parameter. We can also understand the scaling in $(\Delta\phi)^{-2}$ as basically the one of μ_1 times the one of $1/\mu$.

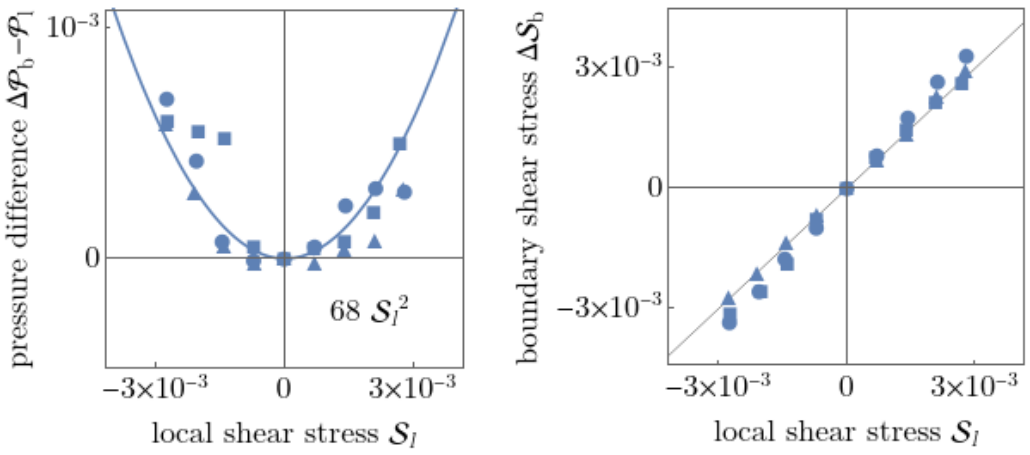

Figure 7.8: **Reproducible expansion bias under dipolar forcing.** Results for roughly 6700 discs at $\Delta\phi = 0.1$ with three initial seeds corresponding to $Z_{\text{init}} \approx 5.1$ and $P_{\text{init}}/k \approx 9 \times 10^{-3}$. The maximal values of the coarse-grained stresses are of the order of the initial pressure P_{init}/k. The data points fall nicely onto the quadratic and linear laws given by Eq. (7.7). The quadratic fit on the left gives $\alpha_{\text{sim}} \approx 68$. Geometric values are $r_{\text{in}}/D \approx 20$ and $r_{\text{out}}/r_{\text{in}} = 2$.

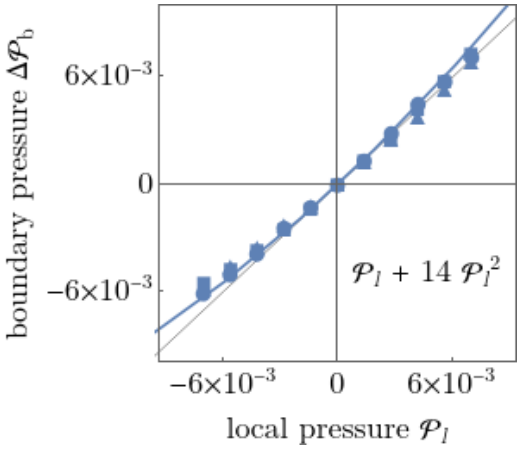

Figure 7.9: **Reproducible expansion bias under isotropic forcing.** Same settings as in Fig. 7.8. The quadratic fit to Eq. (7.8) gives $\beta_{\text{sim}} \approx 14$.

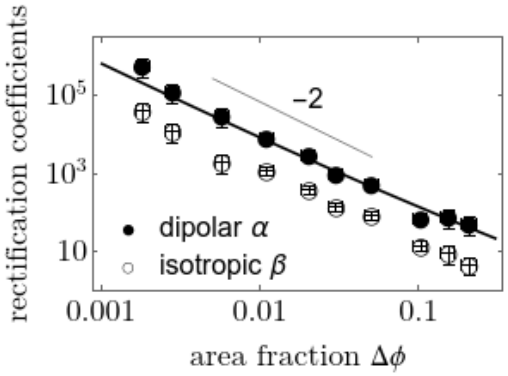

Figure 7.10: **Both α and β decrease as a power law with the distance to jamming.** Log-log plot of the rectification coefficients obtained by fitting data with the same geometrical values as in Fig. 7.8. Vertical error bars are estimated to be roughly 25%. For $r_{\text{out}}/r_{\text{in}} = 2$, α_{sim} and β_{sim} scale with the area fraction $\Delta\phi$ with an exponent close to -2. The agreement of the data points of α_{sim} with the theoretical expression $k\alpha$ of Eq. (6.37) (black line) is roughly quantitative.

7.3 Experiments on thin elastic sheets

Besides fiber networks, more common elastic materials also have a tendency to buckling. For instance, thin elastic sheets (made of *e.g.* polystyrene) submitted to large stress tend to buckle out of plane, which can lead to small wrinkles or large folds (Box et al., 2019). We have been collaborating with F. Box, which has come up with an experimental setup designed to investigate the relationship between the buckling of a thin rubber sheet and a possible contraction bias of the material. As displayed in Fig. 7.11, *left*, the thin sheet is positioned upon a flat substrate and attached at the boundary which allows out of plane deformation in the up direction.

Once stabilized, it is subjected to internal dipolar stresses locally contractile or expansile via a glued actuator. An angle-averaged radius $\langle R \rangle$ is measured between the actuator and the boundary radius. Extensive buckling is observed near the actuators, in agreement with the simulations of Ronceray et al. (2016) [Fig. 5.6]. As plotted in Fig. 7.11, *right*, preliminary results show a decrease in $\langle R \rangle$ in both cases where the actuator spacing δ is decreased and increased. This means that buckling causes a retraction of the sheet, in agreement with the predicted bias towards contraction. This qualitative behavior seems quite reproducible when sheets with slightly different thicknesses are used.

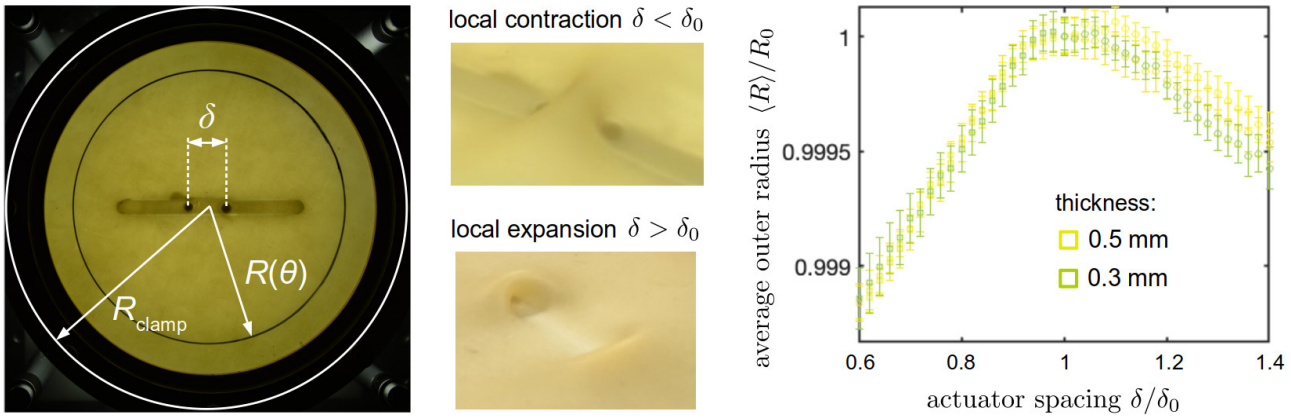

Figure 7.11: **Reproducible contraction bias of a thin elastic sheet.** *Left*, rubber sheet of 0.3-0.5 mm thickness with clamped boundary subjected to a motorized glued actuator, which can be pulled inward or outward. At high force, buckles are visible near the actuator. *Right*, for each value of the spacing δ, the outer radius R is averaged over the angle variable θ. They are compared to their initial values $R_0 \approx 5.4\,\mathrm{cm}$ and $\delta_0 \approx 1.5\,\mathrm{cm}$. The boundary is clamped at $R_{\mathrm{clamp}} \approx 8\,\mathrm{cm}$. Images and plot courtesy of F. Box.

Chapter 8

Discussion

Stress transmission in elastic materials has traditionally been studied in inanimate objects, which do not expend energy to power their own deformation. In such systems, the forces driving the elastic deformation of the material are usually applied at its boundary. The mechanical response of such systems feels rather familiar; for instance, we expect that subjecting a piece of elastic material to compressive stresses will result in its contraction. Throughout this study, we have shown that these assumptions are challenged in living systems and in systems subject to internal rearrangements. In the most extreme cases, an embedded active unit that expands (contracts) in all directions can elicit contractile (expansile) stresses in all directions. The system thus "forgets" the shape of the active units, and its large-scale behavior is controlled by the characteristics of the elastic material instead. Expansion- and shear-stiffening (softening) materials thus always rectify towards contraction (expansion), see Fig. 8.1. This rectification tends to be stronger in more compressible materials and in larger systems. These behaviors arise in a continuum model with or without constitutive nonlinearities, and are thus generic in elastic media beyond previously studied discrete fiber networks.

While most of our calculations are conducted in a circular 2D system with a single active unit, they are likely to remain valid in more complex settings provided the elastic medium is homogeneous.

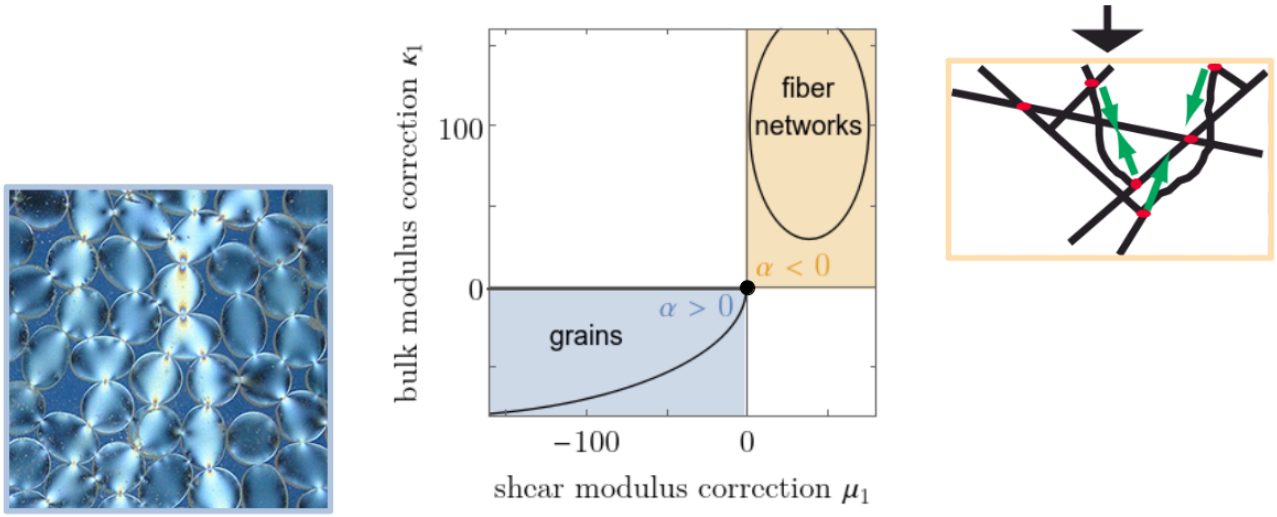

Figure 8.1: **Sketched rectification diagram in terms of κ_1 and μ_1 recapitulating** Figs. 6.5 **and** 6.7**.** On one hand, granular media (in the bottom-left quadrant) propagate compression better than tension, which yields an expansion bias $\alpha > 0$. This corresponds to the image on the left in which photoelastic disks illustrate the compressive force chains. Taken from (Daniels, 2014). On the other hand, fiber networks (in the top-right quadrant) tend to buckle and thus propagate tension more than compression, as shown in the right figure from (Chaudhuri et al., 2007). This induces a contraction bias $\alpha < 0$. Other materials with less prominent bucklable or anti-bucklable properties typically lie inside the black disc at the center. For hypothetical materials in the other white quadrants, the rectification coefficient α is in general smaller and its sign depends on Poisson's ratio ν and the system size $r_{\text{out}}/r_{\text{in}}$.

Indeed, Refs. (Ronceray and Lenz, 2015; Ronceray et al., 2016) show that if an active unit is far enough away from the boundary of the medium and from other active units, its contribution to the total active stress is independent of the characteristics of either. This remains true as long as the distance between active units is larger than the distance over which each of them induces significant nonlinear deformations. In our small-strain formalism (which also describes intermediate strains well), this distance is of the order of $r^* \sim 10\, r_{\mathrm{in}}$.

In the strongly nonlinear regime, finite element simulations show that rectification in fiber networks is strikingly similar to the results of our weakly nonlinear formalism (Ronceray et al., 2016), which may explain why actomyosin networks are always contractile despite the presence of mixed force dipoles (Hatano, 1994; Lenz et al., 2012a). Regarding the elastic response of granular media to a shear transformation, granular dynamics simulations agree with previous experimental observations from Desmond and Weeks (2015) that it becomes more isotropic in the vicinity of the jamming transition, where nonlinear effects play a large role. In a situation where internal forces locally induce mostly shear stress $\mathcal{S}_l$ and negligible pressure $\mathcal{P}_l$, the boundary pressure $\Delta\mathcal{P}_b \sim \alpha\mathcal{S}_l^2$ can become large in front of the boundary shear stress $\Delta\mathcal{S}_b \sim \mathcal{S}_l$. Especially, as the distance to jamming $\Delta\phi$ decreases and α increases, the boundary stress components can become isotropically expansile when $\alpha \gg 1/|\mathcal{S}_l|$, as shown in Fig. 8.2. Such effects due to rectification could then significantly affect the characteristics of the yielding transition in nearly-jammed systems (Merabia and Detcheverry, 2016; Nicolas et al., 2018).

In the continuum description, the principle geometric parameter is set by the ratio of the boundary radius to the active unit radius $r_{\mathrm{out}}/r_{\mathrm{in}}$. But in discrete fiber networks and disc packings, several additional lengthscales complicate the problem. Notably, the elastic response of nearly-jammed granular media to local T1 events [Fig. 5.9] could depend critically on the deformation of the second layer of grains. In the setup of Fig. 7.7, we can imagine that in a regime where the active ring radius is comparable to the radii of the discs ($r_{\mathrm{in}} \sim D$), the microscopic variability would have a large impact on the propagating stresses from T1-like events. Whereas, for pretty mesoscopic deformations $r_{\mathrm{in}} \gg D$, the elastic nonlinearities in the continuum description would be the main cause of far-field stress isotropization. Similarly, lengthscales associated to out-of-plane buckling could impact the contraction

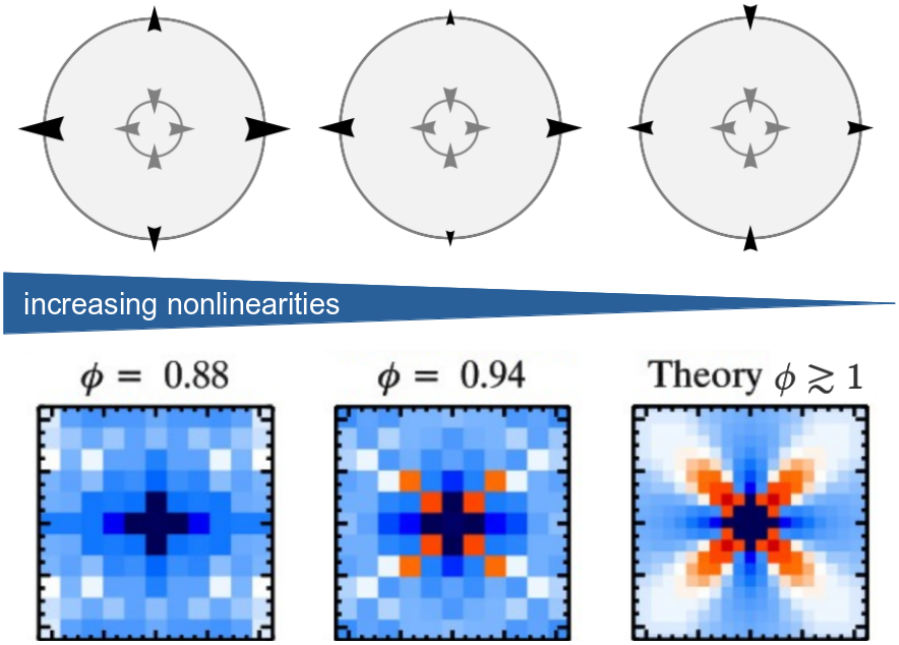

Figure 8.2: **Far-field stresses gradually isotropize as jamming is approached from above.** Sketched comparison of the rectification between the local and boundary coarse-grained stresses, with the shear stress measurements from Desmond and Weeks (2015). In both cases, anisotropic local stresses either dipolar or quadrupolar isotropize upon propagation in a nearly-jammed configuration. We claim that this is due to the anti-buckling nonlinearities which favor the propagation of expansile stresses.

bias of thin elastic sheets.

The generic tensorial development of Hooke's linear elastic law to the lowest nonlinear order brings about a simple model which allows analytical calculations in good agreement with finite element simulations. A similar weakly nonlinear formalism has been successfully used in fracture dynamics to analyze the deformations at the tip of the fracture profile (Bouchbinder et al., 2008; 2010; Livne et al., 2010). This success seems to be due to the fact that the strongly nonlinear region where strains $\gtrsim 0.2$ is small anyway. Evans and Roth (2014) also uses a scalar version of the weakly nonlinear description to model keratin intermediate filaments. In the models of Notbohm et al. (2015), Rosakis et al. (2015) and Sopher et al. (2018), the buckling tendency of the extra-cellular matrix is accounted for by different moduli in contraction and expansion.

Last, this weakly nonlinear description with the corrections to the elastic moduli κ_1, μ_1 draws an interesting parallel between fiber networks and granular matter. This is such that their similar but opposite biases towards contraction and expansion can be understood as part of the same generic rectification phenomenon. Similarities between these classes of materials were already pointed out by *e.g.* Broedersz et al. (2011) and Wyart et al. (2008) close to the rigidity transition. A deeper resemblance is found by considering granular packings as random spring networks. But near jamming, although the behavior of the shear modulus in granular packings is similar to the one of random spring networks, the behavior of the bulk modulus differs significantly in the case of harmonic interactions (Ellenbroek et al., 2009a; van Hecke, 2009). Then, just as the buckling of individual fibers is fundamental for the contraction bias of fibrous networks (Ronceray et al., 2016), the anti-buckling elastic behavior of granular materials seem to be the main factor in the observed expansion bias. Indeed, previous simulations from Ronceray (2016) on the response of networks with discrete anti-bucklable filament units to a large locally contractile force dipole yields far-field expansion, see Fig. 8.3. To a certain extent, we can thus symmetrically model biopolymer gels as networks of bucklable elements, and disc packings as networks of anti-bucklable elements. Moreover, in the values of κ_1, μ_1 that we collected from experimental or realistic models, we have so far only seen large values of $|\kappa_1|, |\mu_1|$ with the same sign. This suggests that the bucklable ($\kappa_1, \mu_1 > 0$) and anti-bucklable ($\kappa_1, \mu_1 < 0$) behaviors are mutually exclusive at the medium scale. By gradually adding grains to a fiber network, the medium behavior will likely continuously switch from a bucklable-like behavior with a contractile bias, to an anti-bucklable-like behavior with an expansile bias.

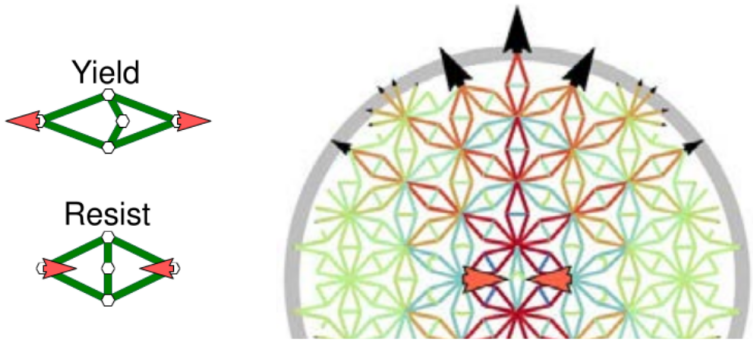

Figure 8.3: **Discrete anti-bucklable network rectify internal stresses towards expansion.** Each link between two nodes where forces (in red) can be applied is made of an anti-bucklable unit, which tends to resist in compression but yield in extension. This induces stress propagating from a locally contractile force dipole to be rectified towards expansion. Adapted from (Ronceray, 2016).

General conclusion

Throughout the two parts of this thesis, we considered very simplified models of complex biological, soft-matter or granular systems. We characterized some macroscopic behaviors in terms of only a few well-defined (combinations of) micro-parameters. In the first part, we studied the self-assembly of polygonal particles with anisotropic interactions into large-scale structures such as fibers. We showed that self-limitation effects could be parameterized by the largest eigenvalue t_1 of the pair-interaction matrix. In the second part, we studied the propagation of stresses in complex nonlinear elastic materials. We found that bucklable fiber networks tend to rectify internal stresses towards contraction, whereas granular matter shows rectification towards expansion. We analytically and numerically showed that this rectification is well captured by the corrections to the elastic moduli κ_1 and μ_1, which are of opposite values in fiber networks and granular media. Beyond the scope of this thesis, it would be interesting to see whether refined microscopic models could account for the aforementioned macroscopic behaviors more realistically.

Bibliography

M. Aizenman, J. Bricmont, and J. L. Lebowitz. Percolation of the minority spins in high-dimensional ising models. *Journal of Statistical Physics*, 49(3):859–865, Nov 1987. ISSN 1572-9613. doi: 10.1007/BF01009363. URL https://doi.org/10.1007/BF01009363.

S. Akimenko, V. Gorbunov, A. Myshlyavtsev, and V. Fefelov. Self-organization of monodentate organic molecules on a solid surface — a monte carlo and transfer-matrix study. *Surface Science*, 639:89–95, 2015. ISSN 0039-6028. doi: 10.1016/j.susc.2015.05.001. URL https://www.sciencedirect.com/science/article/pii/S0039602815001193.

S. S. Akimenko, V. A. Gorbunov, A. V. Myshlyavtsev, and P. V. Stishenko. Generalized lattice-gas model for adsorption of functional organic molecules in terms of pair directional interactions. *Phys. Rev. E*, 93:062804, Jun 2016. doi: 10.1103/PhysRevE.93.062804. URL https://link.aps.org/doi/10.1103/PhysRevE.93.062804.

P. Alam, L. Bousset, R. Melki, and D. Otzen. Alpha-synuclein oligomers and fibrils: a spectrum of species, a spectrum of toxicities. *Journal of Neurochemistry*, 150, 06 2019. doi: 10.1111/jnc.14808. URL https://doi.org/10.1111/jnc.14808.

S. Alberti, A. Gladfelter, and T. Mittag. Considerations and challenges in studying liquid-liquid phase separation and biomolecular condensates. *Cell*, 176(3):419–434, 2019. ISSN 0092-8674. doi: 10.1016/j.cell.2018.12.035. URL https://www.sciencedirect.com/science/article/pii/S0092867418316490.

B. Alberts, A. Johnson, J. Lewis, D. Morgan, M. Raff, K. Roberts, and P. Walter. *Proteins. In: Molecular Biology of the Cell*, pages 109–172. Garland Science, New York, 6th edition, 2015. ISBN 978-0-8153-4432-2.

N. Alkhouli, J. Mansfield, E. Green, J. Bell, B. Knight, N. Liversedge, J. C. Tham, R. Welbourn, A. C. Shore, K. Kos, and C. P. Winlove. The mechanical properties of human adipose tissues and their relationships to the structure and composition of the extracellular matrix. *American Journal of Physiology-Endocrinology and Metabolism*, 305(12):E1427–E1435, 2013. doi: 10.1152/ajpendo.00111.2013. URL https://doi.org/10.1152/ajpendo.00111.2013. PMID: 24105412.

M. S. Alnæs, J. Blechta, J. Hake, A. Johansson, B. Kehlet, A. Logg, C. Richardson, J. Ring, M. E. Rognes, and G. N. Wells. The fenics project version 1.5. *Archive of Numerical Software*, 3(100), 2015. URL https://dx.doi.org/10.11588/ans.2015.100.20553.

A. Amon, V. B. Nguyen, A. Bruand, J. Crassous, and E. Clément. Hot spots in an athermal system. *Phys. Rev. Lett.*, 108:135502, Mar 2012. doi: 10.1103/PhysRevLett.108.135502. URL https://link.aps.org/doi/10.1103/PhysRevLett.108.135502.

R. Arévalo and M. P. Ciamarra. Size and density avalanche scaling near jamming. *Soft Matter*, 10: 2728–2732, 2014. doi: 10.1039/C3SM53134A. URL http://dx.doi.org/10.1039/C3SM53134A.

E. M. Arruda and M. C. Boyce. A three-dimensional constitutive model for the large stretch behavior of rubber elastic materials. *Journal of the Mechanics and Physics of Solids*, 41(2):389–412, 1993. ISSN 0022-5096. doi: 10.1016/0022-5096(93)90013-6. URL https://www.sciencedirect.com/science/article/pii/0022509693900136.

N. Asherie, A. Lomakin, and G. B. Benedek. Phase diagram of colloidal solutions. *Phys. Rev. Lett.*, 77:4832–4835, Dec 1996. doi: 10.1103/PhysRevLett.77.4832. URL https://link.aps.org/doi/10.1103/PhysRevLett.77.4832.

L. D. Aubrey, B. J. F. Blakeman, L. Lutter, C. J. Serpell, M. F. Tuite, L. C. Serpell, and W.-F. Xue. Quantification of amyloid fibril polymorphism by nano-morphometry reveals the individuality of filament assembly. *Communications Chemistry*, 3(1):125, Sept. 2020. URL https://doi.org/10.1038/s42004-020-00372-3.

A. Aufderhorst-Roberts and G. H. Koenderink. Stiffening and inelastic fluidization in vimentin intermediate filament networks. *Soft Matter*, 15:7127–7136, 2019. doi: 10.1039/C9SM00590K. URL http://dx.doi.org/10.1039/C9SM00590K.

J. M. Belmonte, M. Leptin, and F. Nédélec. A theory that predicts behaviors of disordered cytoskeletal networks. *Molecular Systems Biology*, 13(9):941, Sept. 2017. ISSN 1744-4292, 1744-4292, 1744-4292. doi: 10.15252/msb.20177796. URL https://doi.org/10.15252/msb.20177796.

L. Blanchoin, R. Boujemaa-Paterski, C. Sykes, and J. Plastino. Actin Dynamics, Architecture, and Mechanics in Cell Motility. *Physiological Reviews*, 94(1):235–263, Jan. 2014. ISSN 0031-9333. doi: 10.1152/physrev.00018.2013. URL https://doi.org/10.1152/physrev.00018.2013.

J. Boschan, D. Vågberg, E. Somfai, and B. P. Tighe. Beyond linear elasticity: jammed solids at finite shear strain and rate. *Soft Matter*, 12:5450–5460, 2016. doi: 10.1039/C6SM00536E. URL http://dx.doi.org/10.1039/C6SM00536E.

J. Boschan, S. A. Vasudevan, P. E. Boukany, E. Somfai, and B. P. Tighe. Stress relaxation in viscous soft spheres. *Soft Matter*, 13:6870–6876, 2017. doi: 10.1039/C7SM01700F. URL http://dx.doi.org/10.1039/C7SM01700F.

E. Bouchbinder, A. Livne, and J. Fineberg. Weakly nonlinear theory of dynamic fracture. *Phys. Rev. Lett.*, 101:264302, Dec 2008. doi: 10.1103/PhysRevLett.101.264302. URL https://link.aps.org/doi/10.1103/PhysRevLett.101.264302.

E. Bouchbinder, A. Livne, and J. Fineberg. Weakly nonlinear fracture mechanics: experiments and theory. *International Journal of Fracture*, 162(1):3–20, Mar 2010. ISSN 1573-2673. doi: 10.1007/s10704-009-9427-3. URL https://doi.org/10.1007/s10704-009-9427-3.

L. Bousset, N. H. Thomson, S. E. Radford, and R. Melki. The yeast prion ure2p retains its native alpha-helical conformation upon assembly into protein fibrils in vitro. *The EMBO journal*, 21(12):2903–2911, Jun 2002. ISSN 0261-4189. doi: 10.1093/emboj/cdf303. URL https://pubmed.ncbi.nlm.nih.gov/12065404. 12065404[pmid].

M. Bouzid. *Comportement rhéologique et effets non-locaux dans les écoulements granulaires denses*. Thesis, Université Paris Diderot, 2014.

F. Box, D. O'Kiely, O. Kodio, M. Inizan, R. Castrejon-Pita, and D. Vella. Dynamics of wrinkling in ultrathin elastic sheets. *Proceedings of the National Academy of Sciences*, 116:201905755, 09 2019. doi: 10.1073/pnas.1905755116. URL https://doi.org/10.1073/pnas.1905755116.

D. R. Boyer, B. Li, C. Sun, W. Fan, K. Zhou, M. P. Hughes, M. R. Sawaya, L. Jiang, and D. S. Eisenberg. The alpha-synuclein hereditary mutation e46k unlocks a more stable, pathogenic fibril structure. *Proceedings of the National Academy of Sciences*, 117(7):3592–3602, 2020. doi: 10.1073/pnas.1917914117. URL https://www.pnas.org/doi/abs/10.1073/pnas.1917914117.

C. P. Broedersz and F. C. MacKintosh. Molecular motors stiffen non-affine semiflexible polymer networks. *Soft Matter*, 7(7):3186–3191, Mar. 2011. ISSN 1744-6848. doi: 10.1039/C0SM01004A. URL https://doi.org/10.1039/C0SM01004A.

C. P. Broedersz and F. C. MacKintosh. Modeling semiflexible polymer networks. *Reviews of Modern Physics*, 86(3):995–1036, July 2014. ISSN 0034-6861, 1539-0756. doi: 10.1103/RevModPhys.86.995. URL https://doi.org/10.1103/RevModPhys.86.995.

C. P. Broedersz, X. Mao, T. C. Lubensky, and F. C. MacKintosh. Criticality and isostaticity in fibre networks. *Nature Physics*, 7(12):983–988, Oct. 2011. ISSN 1745-2473, 1745-2481. doi: 10.1038/nphys2127. URL https://doi.org/10.1038/nphys2127.

P. Brundin, R. Melki, and R. Kopito. Prion-like transmission of protein aggregates in neurodegenerative diseases. *Nature Reviews Molecular Cell Biology*, 11(4):301–307, Apr 2010. ISSN 1471-0080. doi: 10.1038/nrm2873. URL https://doi.org/10.1038/nrm2873.

Z. Budrikis, D. F. Castellanos, S. Sandfeld, M. Zaiser, and S. Zapperi. Universal features of amorphous plasticity. *Nature Communications*, 8(1):15928, Jul 2017. ISSN 2041-1723. doi: 10.1038/ncomms15928. URL https://doi.org/10.1038/ncomms15928.

A. E. Carlsson. Contractile stress generation by actomyosin gels. *Physical Review E*, 74(5):051912, Nov. 2006. doi: 10.1103/PhysRevE.74.051912. URL https://doi.org/10.1103/PhysRevE.74.051912.

O. Chaudhuri, S. H. Parekh, and D. A. Fletcher. Reversible stress softening of actin networks. *Nature*, 445(7125):295–298, Jan. 2007. ISSN 0028-0836. doi: 10.1038/nature05459. URL https://doi.org/10.1038/nature05459.

J. Chen, H.-J. Liao, H. Xie, X.-J. Han, R.-Z. Huang, S. Cheng, Z.-C. Wei, Z. Y. Xie, and T. Xiang. Phase transition of the q -state clock model: Duality and tensor renormalization. *Chinese Physics Letters*, 34:050503, 05 2017. doi: 10.1088/0256-307X/34/5/050503. URL https://doi.org/10.1088/0256-307X/34/5/050503.

X. Chen, M. Chen, N. P. Schafer, and P. G. Wolynes. Exploring the interplay between fibrillization and amorphous aggregation channels on the energy landscapes of tau repeat isoforms. *Proceedings of the National Academy of Sciences*, 117(8):4125–4130, 2020. doi: 10.1073/pnas.1921702117. URL https://www.pnas.org/doi/abs/10.1073/pnas.1921702117.

J. P. Collet, D. Park, C. Lesty, J. Soria, C. Soria, G. Montalescot, and J. W. Weisel. Influence of fibrin network conformation and fibrin fiber diameter on fibrinolysis speed: dynamic and structural approaches by confocal microscopy. *Arterioscler Thromb Vasc Biol*, 20(5):1354–1361, May 2000. URL https://www.ahajournals.org/doi/10.1161/01.ATV.20.5.1354.

C. Coulais, A. Seguin, and O. Dauchot. Shear Modulus and Dilatancy Softening in Granular Packings above Jamming. *Physical Review Letters*, 113(19), Nov. 2014. ISSN 0031-9007, 1079-7114. doi: 10.1103/PhysRevLett.113.198001. URL https://doi.org/10.1103/PhysRevLett.113.198001.

S. Dagois-Bohy, E. Somfai, B. P. Tighe, and M. van Hecke. Softening and yielding of soft glassy materials. *Soft Matter*, 13:9036–9045, 2017. doi: 10.1039/C7SM01846K. URL http://dx.doi.org/10.1039/C7SM01846K.

K. Daniels. Viewpoint: Pushing on a nonlinear material. *Physics*, 7(113), 2014. URL https://physics.aps.org/articles/v7/113.

K. Dasbiswas, S. Hu, F. Schnorrer, S. A. Safran, and A. D. Bershadsky. Ordering of myosin ii filaments driven by mechanical forces: experiments and theory. *Philosophical Transactions of the Royal Society B: Biological Sciences*, 373(1747):20170114, 2018. doi: 10.1098/rstb.2017.0114. URL https://royalsocietypublishing.org/doi/abs/10.1098/rstb.2017.0114.

K. W. Desmond and E. R. Weeks. Measurement of stress redistribution in flowing emulsions. *Phys. Rev. Lett.*, 115:098302, Aug 2015. doi: 10.1103/PhysRevLett.115.098302. URL https://link.aps.org/doi/10.1103/PhysRevLett.115.098302.

W. A. Eaton and J. Hofrichter. Sickle cell hemoglobin polymerization. *Adv Protein Chem*, 40:63–279, 1990. doi: 10.1016/S0065-3233(08)60287-9. URL https://doi.org/10.1016/S0065-3233(08)60287-9.

E. Efrati, Z. Wang, A. Kolan, and L. P. Kadanoff. Real-space renormalization in statistical mechanics. *Rev. Mod. Phys.*, 86:647–667, May 2014. doi: 10.1103/RevModPhys.86.647. URL https://link.aps.org/doi/10.1103/RevModPhys.86.647.

W. Ellenbroek, Z. Zeravcic, W. Saarloos, and M. van Hecke. Non-affine response: Jammed packings vs. spring networks. *EPL (Europhysics Letters)*, 87:34004, 08 2009a. doi: 10.1209/0295-5075/87/34004. URL https://doi.org/10.1209/0295-5075/87/34004.

W. G. Ellenbroek, E. Somfai, M. van Hecke, and W. van Saarloos. Critical scaling in linear response of frictionless granular packings near jamming. *Phys. Rev. Lett.*, 97:258001, Dec 2006. doi: 10.1103/PhysRevLett.97.258001. URL https://link.aps.org/doi/10.1103/PhysRevLett.97.258001.

W. G. Ellenbroek, M. van Hecke, and W. van Saarloos. Jammed frictionless disks: Connecting local and global response. *Phys. Rev. E*, 80:061307, Dec 2009b. doi: 10.1103/PhysRevE.80.061307. URL https://link.aps.org/doi/10.1103/PhysRevE.80.061307.

S. Eltinge. Numerical ising model simulations on exactly solvable and randomized lattices. 2015. URL http://web.mit.edu/8.334/www/grades/projects/projects15/EltingeStephen.pdf.

M. E. Evans and R. Roth. Shaping the skin: The interplay of mesoscale geometry and corneocyte swelling. *Phys. Rev. Lett.*, 112:038102, Jan 2014. doi: 10.1103/PhysRevLett.112.038102. URL https://link.aps.org/doi/10.1103/PhysRevLett.112.038102.

J. Feng, H. Levine, X. Mao, and L. M. Sander. Nonlinear elasticity of disordered fiber networks. *Soft Matter*, 12:1419–1424, 2016. doi: 10.1039/C5SM01856K. URL http://dx.doi.org/10.1039/C5SM01856K.

M. E. Fisher. The theory of equilibrium critical phenomena. *Reports on Progress in Physics*, 30(2): 615–730, jul 1967. doi: 10.1088/0034-4885/30/2/306. URL https://doi.org/10.1088/0034-4885/30/2/306.

D. Fusco and P. Charbonneau. Crystallization of asymmetric patchy models for globular proteins in solution. *Phys. Rev. E*, 88:012721, Jul 2013. doi: 10.1103/PhysRevE.88.012721. URL https://link.aps.org/doi/10.1103/PhysRevE.88.012721.

M. L. Gardel, J. H. Shin, F. C. MacKintosh, L. Mahadevan, P. Matsudaira, and D. A. Weitz. Elastic Behavior of Cross-Linked and Bundled Actin Networks. *Science*, 304(5675):1301–1305, May 2004. ISSN 0036-8075, 1095-9203. doi: 10.1126/science.1095087. URL https://doi.org/10.1126/science.1095087.

F. Gelain, D. Bottai, A. Vescovi, and S. Zhang. Designer self-assembling peptide nanofiber scaffolds for adult mouse neural stem cell 3-dimensional cultures. *PLOS ONE*, 1(1):1–11, 12 2006. doi: 10.1371/journal.pone.0000119. URL https://doi.org/10.1371/journal.pone.0000119.

J. Geng, D. Howell, E. Longhi, R. P. Behringer, G. Reydellet, L. Vanel, E. Clément, and S. Luding. Footprints in sand: The response of a granular material to local perturbations. *Phys. Rev. Lett.*, 87:035506, Jul 2001. doi: 10.1103/PhysRevLett.87.035506. URL https://link.aps.org/doi/10.1103/PhysRevLett.87.035506.

K. C. Gersh, C. Nagaswami, and J. W. Weisel. Fibrin network structure and clot mechanical properties are altered by incorporation of erythrocytes. *Thrombosis and haemostasis*, 102(6):1169–1175, Dec 2009. ISSN 2567-689X. doi: 10.1160/TH09-03-0199. URL https://pubmed.ncbi.nlm.nih.gov/19967148. 19967148[pmid].

S. Ghosh, T. B. Sil, S. Dolai, and K. Garai. High-affinity multivalent interactions between apolipoprotein E and the oligomers of amyloid-β. *FEBS J*, 286(23):4737–4753, July 2019. doi: 10.1111/febs.14988. URL https://doi.org/10.1111/febs.14988.

V. A. Gorbunov, S. S. Akimenko, A. V. Myshlyavtsev, V. F. Fefelov, and M. D. Myshlyavtseva. Adsorption of triangular-shaped molecules with directional nearest-neighbor interactions on a triangular lattice. *Adsorption*, 19(2):571–580, Apr 2013. ISSN 1572-8757. doi: 10.1007/s10450-013-9480-0. URL https://doi.org/10.1007/s10450-013-9480-0.

F. Grinnell. Fibroblast biology in three-dimensional collagen matrices. *Trends in Cell Biology*, 13 (5):264–269, 2003. ISSN 0962-8924. doi: 10.1016/S0962-8924(03)00057-6. URL https://www.sciencedirect.com/science/article/pii/S0962892403000576.

M. E. Gurtin. *The Linear Theory of Elasticity*, pages 1–295. Springer Berlin Heidelberg, Berlin, Heidelberg, 1973. ISBN 978-3-662-39776-3. doi: 10.1007/978-3-662-39776-3_1. URL https://doi.org/10.1007/978-3-662-39776-3_1.

M. F. Hagan and G. M. Grason. Equilibrium mechanisms of self-limiting assembly. *Rev. Mod. Phys.*, 93:025008, Jun 2021. doi: 10.1103/RevModPhys.93.025008. URL https://link.aps.org/doi/10.1103/RevModPhys.93.025008.

Y. L. Han, P. Ronceray, G. Xu, A. Malandrino, R. D. Kamm, M. Lenz, C. P. Broedersz, and M. Guo. Cell contraction induces long-ranged stress stiffening in the extracellular matrix. *Proc. Natl. Acad. Sci. U.S.A.*, April 2018. doi: 10.1073/pnas.1722619115. URL https://doi.org/10.1073/pnas.1722619115.

S. Hatano. Actin-binding proteins in cell motility. *Int. Rev. Cytology*, 156:199–273, 1994. doi: 10.1016/S0074-7696(08)62255-X. URL https://doi.org/10.1016/S0074-7696(08)62255-X.

R. A. Horn and C. R. Johnson. *Matrix Analysis*. Cambridge University Press, Cambridge, 2012.

J. Howard. *Mechanics of Motor Proteins and the Cytoskeleton*. Sinauer Associates, Feb. 2001. ISBN 0-87893-333-6.

Y. Hu and P. Charbonneau. Resolving the two-dimensional axial next-nearest-neighbor ising model using transfer matrices. *Phys. Rev. B*, 103:094441, Mar 2021. doi: 10.1103/PhysRevB.103.094441. URL https://link.aps.org/doi/10.1103/PhysRevB.103.094441.

E. Ising. Beitrag zur theorie des ferromagnetismus. *Zeitschrift für Physik*, 31(1):253–258, Feb 1925. ISSN 0044-3328. doi: 10.1007/BF02980577. URL https://doi.org/10.1007/BF02980577.

P. A. Janmey, M. E. McCormick, S. Rammensee, J. L. Leight, P. C. Georges, and F. C. MacKintosh. Negative normal stress in semiflexible biopolymer gels. *Nature Materials*, 6(1), 2007. doi: 10.1038/nmat1810. URL https://doi.org/10.1038/nmat1810.

K. A. Jansen, A. J. Licup, A. Sharma, R. Rens, F. C. MacKintosh, and G. H. Koenderink. The role of network architecture in collagen mechanics. *Biophysical journal*, 114(11):2665–2678, Jun 2018. ISSN 1542-0086. doi: 10.1016/j.bpj.2018.04.043. URL https://pubmed.ncbi.nlm.nih.gov/29874616.

Z. Jia, J. D. Schmit, and J. Chen. Amyloid assembly is dominated by misregistered kinetic traps on an unbiased energy landscape. *Proceedings of the National Academy of Sciences*, 117(19):10322–10328, 2020. doi: 10.1073/pnas.1911153117. URL https://www.pnas.org/doi/abs/10.1073/pnas.1911153117.

A. Kabla and G. Debrégeas. Local stress relaxation and shear banding in a dry foam under shear. *Phys. Rev. Lett.*, 90:258303, Jun 2003. doi: 10.1103/PhysRevLett.90.258303. URL https://link.aps.org/doi/10.1103/PhysRevLett.90.258303.

L. P. Kadanoff. Notes on migdal's recursion formulas. *Annals of Physics*, 100(1):359–394, 1976. ISSN 0003-4916. doi: 10.1016/0003-4916(76)90066-X. URL https://www.sciencedirect.com/science/article/pii/000349167690066X.

C. Karner, C. Dellago, and E. Bianchi. How patchiness controls the properties of chain-like assemblies of colloidal platelets. *Journal of Physics: Condensed Matter*, 32(20):204001, feb 2020. doi: 10.1088/1361-648x/ab6e44. URL https://doi.org/10.1088/1361-648x/ab6e44.

A. R. Khan, S. James, M. K. Quinn, I. Altan, P. Charbonneau, and J. J. McManus. Temperature-dependent interactions explain normal and inverted solubility in a γd-crystallin mutant. *Biophysical Journal*, 117(5):930–937, 2019. ISSN 0006-3495. doi: 10.1016/j.bpj.2019.07.019. URL https://www.sciencedirect.com/science/article/pii/S0006349519305879.

J. K. Knowles. The finite anti-plane shear field near the tip of a crack for a class of incompressible elastic solids. *International Journal of Fracture*, 13:611–639, 1977. doi: 10.1007/BF00017296. URL https://doi.org/10.1007/BF00017296.

T. Knowles, M. Vendruscolo, and C. Dobson. The amyloid state and its association with protein misfolding diseases. *Nature Reviews Molecular Cell Biology*, 15:384, 2014. doi: 10.1038/nrm3810. URL https://www.nature.com/articles/nrm3810.

T. P. Knowles, A. W. Fitzpatrick, S. Meehan, H. R. Mott, M. Vendruscolo, C. M. Dobson, and M. E. Welland. Role of intermolecular forces in defining material properties of protein nanofibrils. *Science*, 318(5858):1900–1903, 2007. doi: 10.1126/science.1150057. URL https://www.science.org/doi/abs/10.1126/science.1150057.

J. Komianos and G. Papoian. Stochastic ratcheting on a funneled energy landscape is necessary for highly efficient contractility of actomyosin force dipoles. *Physical Review X*, 8, 05 2018. doi: 10.1103/PhysRevX.8.021006. URL https://doi.org/10.1103/PhysRevX.8.021006.

H. A. Kramers and G. H. Wannier. Statistics of the two-dimensional ferromagnet. part i. *Phys. Rev.*, 60:252–262, Aug 1941. doi: 10.1103/PhysRev.60.252. URL https://link.aps.org/doi/10.1103/PhysRev.60.252.

R. Kurita and H. Tanaka. Drastic enhancement of crystal nucleation in a molecular liquid by its liquid-liquid transition. *Proceedings of the National Academy of Sciences*, 116(50):24949–24955, 2019. doi: 10.1073/pnas.1909660116. URL https://www.pnas.org/doi/abs/10.1073/pnas.1909660116.

R. Lakes. Advances in negative poisson's ratio materials. *Advanced Materials*, 5(4):293–296, 1993. doi: 10.1002/adma.19930050416. URL https://onlinelibrary.wiley.com/doi/abs/10.1002/adma.19930050416.

L. D. Landau, E. M. Lifshitz, and L. P. Pitaevskii. Chapter i - fundamental equations. In *Theory of Elasticity (Third Edition)*, pages 1–37. Butterworth-Heinemann, Oxford, third edition edition, 1986. ISBN 978-0-08-057069-3. doi: 10.1016/B978-0-08-057069-3.50008-5. URL https://www.sciencedirect.com/science/article/pii/B9780080570693500085.

R. Langer. New methods of drug delivery. *Science*, 249(4976):1527–1533, 1990. doi: 10.1126/science.2218494. URL https://www.science.org/doi/abs/10.1126/science.2218494.

T. D. Lee and C. N. Yang. Statistical theory of equations of state and phase transitions. ii. lattice gas and ising model. *Phys. Rev.*, 87:410–419, Aug 1952. doi: 10.1103/PhysRev.87.410. URL https://link.aps.org/doi/10.1103/PhysRev.87.410.

M. Lenz and T. Witten. Geometrical frustration yields fibre formation in self-assembly. *Nature Physics*, 13:1100–1104, 2017. doi: 10.1038/nphys4184. URL https://www.nature.com/articles/nphys4184.

M. Lenz, M. L. Gardel, and A. R. Dinner. Requirements for contractility in disordered cytoskeletal bundles. *New Journal of Physics*, 14(3):033037, mar 2012a. doi: 10.1088/1367-2630/14/3/033037. URL https://doi.org/10.1088/1367-2630/14/3/033037.

M. Lenz, T. Thoresen, M. L. Gardel, and A. R. Dinner. Contractile units in disordered actomyosin bundles arise from F-actin buckling. *Phys. Rev. Lett.*, 108(23):238107, June 2012b. doi: 10.1103/PhysRevLett.108.238107. URL https://doi.org/10.1103/PhysRevLett.108.238107.

A. J. Licup, S. Münster, A. Sharma, M. Sheinman, L. M. Jawerth, B. Fabry, D. A. Weitz, and F. C. MacKintosh. Stress controls the mechanics of collagen networks. *Proceedings of the National Academy of Sciences*, 112(31):9573–9578, 2015. doi: 10.1073/pnas.1504258112. URL https://www.pnas.org/doi/abs/10.1073/pnas.1504258112.

J. Lin, E. Lerner, A. Rosso, and M. Wyart. Scaling description of the yielding transition in soft amorphous solids at zero temperature. *Proceedings of the National Academy of Sciences*, 111(40): 14382–14387, 2014. doi: 10.1073/pnas.1406391111. URL https://www.pnas.org/doi/abs/10.1073/pnas.1406391111.

Y.-C. Lin, N. Y. Yao, C. P. Broedersz, H. Herrmann, F. C. MacKintosh, and D. A. Weitz. Origins of elasticity in intermediate filament networks. *Phys. Rev. Lett.*, 104:058101, Feb 2010. doi: 10.1103/PhysRevLett.104.058101. URL https://link.aps.org/doi/10.1103/PhysRevLett.104.058101.

S. B. Lindström, D. A. Vader, A. Kulachenko, and D. A. Weitz. Biopolymer network geometries: Characterization, regeneration, and elastic properties. *Phys. Rev. E*, 82:051905, Nov 2010. doi: 10.1103/PhysRevE.82.051905. URL https://link.aps.org/doi/10.1103/PhysRevE.82.051905.

I. Linsmeier, S. Banerjee, P. W. Oakes, W. Jung, T. Kim, and M. P. Murrell. Disordered actomyosin networks are sufficient to produce cooperative and telescopic contractility. *Nature Communications*, 7(1):12615, Aug 2016. ISSN 2041-1723. doi: 10.1038/ncomms12615. URL https://doi.org/10.1038/ncomms12615.

A. Livne, E. Bouchbinder, I. Svetlizky, and J. Fineberg. The near-tip fields of fast cracks. *Science*, 327 (5971):1359–1363, 2010. doi: 10.1126/science.1180476. URL https://www.science.org/doi/abs/10.1126/science.1180476.

H. Lodish, A. Berk, C. Kaiser, M. Krieger, A. Bretscher, H. Ploegh, K. Martin, M. Yaffe, and A. Amon. *Molecular Cell Biology*. W. H. Freeman, 2021. ISBN 9781319365516. URL https://www.macmillanlearning.com/college/us/product/Molecular-Cell-Biology/p/1319208525.

A. Lomakin, N. Asherie, and G. B. Benedek. Aeolotopic interactions of globular proteins. *Proceedings of the National Academy of Sciences*, 96(17):9465–9468, 1999. ISSN 0027-8424. doi: 10.1073/pnas.96.17.9465. URL https://www.pnas.org/content/96/17/9465.

M. A. Lovette and M. F. Doherty. Needle-shaped crystals: Causality and solvent selection guidance based on periodic bond chains. *Crystal Growth & Design*, 13(8):3341–3352, Aug 2013. ISSN 1528-7483. doi: 10.1021/cg301830u. URL https://doi.org/10.1021/cg301830u.

F. C. MacKintosh, J. Käs, and P. A. Janmey. Elasticity of semiflexible biopolymer networks. *Phys. Rev. Lett.*, 75:4425–4428, Dec 1995. doi: 10.1103/PhysRevLett.75.4425. URL https://link.aps.org/doi/10.1103/PhysRevLett.75.4425.

S. K. Maji, D. Schubert, C. Rivier, S. Lee, J. E. Rivier, and R. Riek. Amyloid as a depot for the formulation of long-acting drugs. *PLOS Biology*, 6(2):1–13, 02 2008. doi: 10.1371/journal.pbio.0060017. URL https://doi.org/10.1371/journal.pbio.0060017.

H. A. Makse, N. Gland, D. L. Johnson, and L. M. Schwartz. Why effective medium theory fails in granular materials. *Phys. Rev. Lett.*, 83:5070–5073, Dec 1999. doi: 10.1103/PhysRevLett.83.5070. URL https://link.aps.org/doi/10.1103/PhysRevLett.83.5070.

H. A. Makse, N. Gland, D. L. Johnson, and L. Schwartz. Granular packings: Nonlinear elasticity, sound propagation, and collective relaxation dynamics. *Phys. Rev. E*, 70:061302, Dec 2004. doi: 10.1103/PhysRevE.70.061302. URL https://link.aps.org/doi/10.1103/PhysRevE.70.061302.

I. Malhotra and S. B. Babu. Phase diagram of two-patch colloids with competing anisotropic and isotropic interactions. *Journal of Physics: Condensed Matter*, 32(35):355101, jun 2020. doi: 10.1088/1361-648x/ab8c8e. URL https://doi.org/10.1088/1361-648x/ab8c8e.

S. Mankar, A. Arunagiri, S. Sen, and S. Maji. Nanomaterials: Amyloids reflect their brighter side. *Nano reviews*, 2, 05 2011. doi: 10.3402/nano.v2i0.6032. URL https://doi.org/10.3402/nano.v2i0.6032.

H. J. Maris and L. P. Kadanoff. Teaching the renormalization group. *American Journal of Physics*, 46 (6):652–657, 1978. doi: 10.1119/1.11224. URL https://doi.org/10.1119/1.11224.

S. A. Maskarinec, C. Franck, D. A. Tirrell, and G. Ravichandran. Quantifying cellular traction forces in three dimensions. *Proceedings of the National Academy of Sciences*, 106(52):22108–22113, Dec. 2009. ISSN 0027-8424, 1091-6490. doi: 10.1073/pnas.0904565106. URL https://doi.org/10.1073/pnas.0904565106.

J. J. McManus, P. Charbonneau, E. Zaccarelli, and N. Asherie. The physics of protein self-assembly. *Current Opinion in Colloid & Interface Science*, 22:73–79, 2016. ISSN 1359-0294. doi: 10.1016/j.cocis.2016.02.011. URL https://www.sciencedirect.com/science/article/pii/S1359029416300292.

J. Meinhardt, C. Sachse, P. Hortschansky, N. Grigorieff, and M. Fändrich. Abeta(1-40) fibril polymorphism implies diverse interaction patterns in amyloid fibrils. *Journal of molecular biology*, 386(3):869–877, Feb 2009. ISSN 1089-8638. doi: 10.1016/j.jmb.2008.11.005. URL https://pubmed.ncbi.nlm.nih.gov/19038266. 19038266[pmid].

S. Meiri and E. Efrati. Cumulative geometric frustration in physical assemblies. *Physical Review E*, 104(5), nov 2021. doi: 10.1103/physreve.104.054601. URL https://doi.org/10.1103%2Fphysreve.104.054601.

S. Meiri and E. Efrati. Non-trivial attenuation of geometric frustration by discretization of the degrees of freedom: A study of a potts-like frustrated spin system, 2022. URL https://arxiv.org/abs/2203.05247.

F. Meng and E. M. Terentjev. Nonlinear elasticity of semiflexible filament networks. *Soft Matter*, 12: 6749–6756, 2016. doi: 10.1039/C6SM01029F. URL http://dx.doi.org/10.1039/C6SM01029F.

G. Meng, J. Paulose, D. R. Nelson, and V. N. Manoharan. Elastic instability of a crystal growing on a curved surface. *Science*, 343(6171):634–637, 2014. doi: 10.1126/science.1244827. URL https://www.science.org/doi/abs/10.1126/science.1244827.

S. Merabia and F. Detcheverry. Thermally activated creep and fluidization in flowing disordered materials. *EPL (Europhysics Letters)*, 116(4):46003, nov 2016. doi: 10.1209/0295-5075/116/46003. URL https://doi.org/10.1209/0295-5075/116/46003.

N. Metropolis and S. Ulam. The monte carlo method. *Journal of the American Statistical Association*, 44(247):335–341, 1949. doi: 10.1080/01621459.1949.10483310. URL https://www.tandfonline.com/doi/abs/10.1080/01621459.1949.10483310. PMID: 18139350.

C. D. Meyer. *Matrix Analysis and Applied Linear Algebra*. Society for Industrial and Applied Mathematics, USA, 2000. ISBN 0898714540.

T. C. T. Michaels, A. Šarić, G. Meisl, G. T. Heller, S. Curk, P. Arosio, S. Linse, C. M. Dobson, M. Vendruscolo, and T. P. J. Knowles. Thermodynamic and kinetic design principles for amyloid-aggregation inhibitors. *Proceedings of the National Academy of Sciences*, 117(39):24251–24257, 2020. doi: 10.1073/pnas.2006684117. URL https://www.pnas.org/doi/abs/10.1073/pnas.2006684117.

S. Mossa, F. Sciortino, P. Tartaglia, and E. Zaccarelli. Ground-state clusters for short-range attractive and long-range repulsive potentials. *Langmuir*, 20(24):10756–10763, Nov 2004. ISSN 0743-7463. doi: 10.1021/la048554t. URL https://doi.org/10.1021/la048554t.

M. Murrell, P. W. Oakes, M. Lenz, and M. L. Gardel. Forcing cells into shape: the mechanics of actomyosin contractility. *Nature reviews. Molecular cell biology*, 16(8):486–498, Aug 2015. ISSN 1471-0080. doi: 10.1038/nrm4012. URL https://pubmed.ncbi.nlm.nih.gov/26130009. 26130009[pmid].

M. P. Murrell and M. L. Gardel. F-actin buckling coordinates contractility and severing in a biomimetic actomyosin cortex. *Proceedings of the National Academy of Sciences*, 109(51):20820–20825, 2012. doi: 10.1073/pnas.1214753109. URL https://www.pnas.org/doi/abs/10.1073/pnas.1214753109.

National Heart, Lung and Blood Institute. Sickle cell disease, 2022. URL https://www.nhlbi.nih.gov/health/sickle-cell-disease.

A. Nicolas and J.-L. Barrat. A mesoscopic model for the rheology of soft amorphous solids, with application to microchannel flows. *Faraday Discuss.*, 167:567–600, 2013. doi: 10.1039/C3FD00067B. URL http://dx.doi.org/10.1039/C3FD00067B.

A. Nicolas, E. E. Ferrero, K. Martens, and J.-L. Barrat. Deformation and flow of amorphous solids: Insights from elastoplastic models. *Rev. Mod. Phys.*, 90:045006, Dec 2018. doi: 10.1103/RevModPhys.90.045006. URL https://link.aps.org/doi/10.1103/RevModPhys.90.045006.

T. Niemeijer and J. van Leeuwen. *Renormalization Theory for Ising-Like Spin Systems. In: Domb, C. and Green, M.S., Eds., Phase Transitions and Critical Phenomena*, volume 6, pages 425–505. 1976.

T. Niemeijer and J. M. J. van Leeuwen. Wilson theory for spin systems on a triangular lattice. *Phys. Rev. Lett.*, 31:1411–1414, Dec 1973. doi: 10.1103/PhysRevLett.31.1411. URL https://link.aps.org/doi/10.1103/PhysRevLett.31.1411.

J. Notbohm, A. Lesman, P. Rosakis, D. A. Tirrell, and G. Ravichandran. Microbuckling of fibrin provides a mechanism for cell mechanosensing. *Journal of The Royal Society Interface*, 12(108): 20150320, July 2015. ISSN 1742-5689, 1742-5662. doi: 10.1098/rsif.2015.0320. URL https://doi.org/10.1098/rsif.2015.0320.

P. W. Oakes, S. Banerjee, M. C. Marchetti, and M. L. Gardel. Geometry regulates traction stresses in adherent cells. *Biophysical journal*, 107(4):825–833, Aug 2014. ISSN 1542-0086. doi: 10.1016/j.bpj.2014.06.045. URL https://pubmed.ncbi.nlm.nih.gov/25140417. 25140417[pmid].

C. S. O'Hern, L. E. Silbert, A. J. Liu, and S. R. Nagel. Jamming at zero temperature and zero applied stress: The epitome of disorder. *Phys. Rev. E*, 68:011306, Jul 2003. doi: 10.1103/PhysRevE.68.011306. URL https://link.aps.org/doi/10.1103/PhysRevE.68.011306.

J. Oitmaa, M. T. Batchelor, and M. N. Barber. A finite lattice study of the critical behaviour of the two-dimensional biaxial next-nearest-neighbour ising model. *Journal of Physics A: Mathematical and General*, 20(6):1507–1519, apr 1987. doi: 10.1088/0305-4470/20/6/033. URL https://doi.org/10.1088/0305-4470/20/6/033.

L. Onsager. Crystal statistics. i. a two-dimensional model with an order-disorder transition. *Phys. Rev.*, 65:117–149, Feb 1944. doi: 10.1103/PhysRev.65.117. URL https://link.aps.org/doi/10.1103/PhysRev.65.117.

F. Oosawa and M. Kasai. A theory of linear and helical aggregations of macromolecules. *Journal of Molecular Biology*, 4(1):10–21, 1962. ISSN 0022-2836. doi: 10.1016/S0022-2836(62)80112-0. URL https://www.sciencedirect.com/science/article/pii/S0022283662801120.

M. Otto, J.-P. Bouchaud, P. Claudin, and J. Socolar. Anisotropy in granular media: Classical elasticity and directed-force chain network. *Phys. Rev. E*, 67:031302, 04 2003. doi: 10.1103/PhysRevE.67.031302. URL https://doi.org/10.1103/PhysRevE.67.031302.

T. R. Peskett, F. Rau, J. O'Driscoll, R. Patani, A. R. Lowe, and H. R. Saibil. A liquid to solid phase transition underlying pathological huntingtin exon1 aggregation. *Molecular Cell*, 70(4):588–601.e6, May 2018. ISSN 1097-2765. doi: 10.1016/j.molcel.2018.04.007. URL https://doi.org/10.1016/j.molcel.2018.04.007.

D. Peurichard, F. Delebecque, A. Lorsignol, C. Barreau, J. Rouquette, X. Descombes, L. Casteilla, and P. Degond. Simple mechanical cues could explain adipose tissue morphology. *Journal of Theoretical Biology*, 429:61–81, 2017. ISSN 0022-5193. doi: 10.1016/j.jtbi.2017.06.030. URL https://www.sciencedirect.com/science/article/pii/S0022519317303065.

G. Picard, A. Ajdari, F. Lequeux, and L. Bocquet. Elastic consequences of a single plastic event : a step towards the microscopic modeling of the flow of yield stress fluids. *Eur. Phys. J. E*, 15:371–381, 2004. doi: 10.1140/epje/i2004-10054-8. URL https://hal.archives-ouvertes.fr/hal-00008762.

S. V. Plotnikov, A. M. Pasapera, B. Sabass, and C. M. Waterman. Force fluctuations within focal adhesions mediate ecm-rigidity sensing to guide directed cell migration. *Cell*, 151(7):1513–1527, 2012. ISSN 0092-8674. doi: 10.1016/j.cell.2012.11.034. URL https://www.sciencedirect.com/science/article/pii/S0092867412014195.

C. Pohl, G. Effantin, E. Kandiah, S. Meier, G. Zeng, W. Streicher, G. H. Peters, G. Schoehn, C. Mueller-Dieckmann, A. Noergaard, and P. Harris. Reversible supramolecular assembly of the anti-microbial peptide plectasin into helical non-amyloid fibrils. *bioRxiv*, 2021. doi: 10.1101/2021.09.06.458672. URL https://www.biorxiv.org/content/early/2021/09/06/2021.09.06.458672.

J. Prost, F. Jülicher, and J.-F. Joanny. Active gel physics. *Nat. Phys.*, 11(2):111–117, February 2015. doi: 10.1038/NPHYS3224. URL https://doi.org/10.1038/NPHYS3224.

F. Puosi, J. Rottler, and J.-L. Barrat. Time-dependent elastic response to a local shear transformation in amorphous solids. *Phys. Rev. E*, 89:042302, Apr 2014. doi: 10.1103/PhysRevE.89.042302. URL https://link.aps.org/doi/10.1103/PhysRevE.89.042302.

L. Pytowski, C. F. Lee, A. C. Foley, D. J. Vaux, and L. Jean. Liquid-liquid phase separation of type ii diabetes-associated iapp initiates hydrogelation and aggregation. *Proceedings of the National Academy of Sciences*, 117(22):12050–12061, 2020. doi: 10.1073/pnas.1916716117. URL https://www.pnas.org/doi/abs/10.1073/pnas.1916716117.

D. R. Reid, N. Pashine, J. M. Wozniak, H. M. Jaeger, A. J. Liu, S. R. Nagel, and J. J. de Pablo. Auxetic metamaterials from disordered networks. *Proceedings of the National Academy of Sciences*, 115(7):E1384–E1390, 2018. doi: 10.1073/pnas.1717442115. URL https://www.pnas.org/doi/abs/10.1073/pnas.1717442115.

J. Ren, J. A. Dijksman, and R. P. Behringer. Reynolds pressure and relaxation in a sheared granular system. *Phys. Rev. Lett.*, 110:018302, Jan 2013. doi: 10.1103/PhysRevLett.110.018302. URL https://link.aps.org/doi/10.1103/PhysRevLett.110.018302.

P. Ronceray. *Active contraction in biological fiber networks*. Thesis, Université Paris-Saclay, May 2016. URL https://tel.archives-ouvertes.fr/tel-01359592.

P. Ronceray and B. Le Floch. Range of geometrical frustration in lattice spin models. *Phys. Rev. E*, 100:052150, Nov 2019. doi: 10.1103/PhysRevE.100.052150. URL https://link.aps.org/doi/10.1103/PhysRevE.100.052150.

P. Ronceray and M. Lenz. Connecting local active forces to macroscopic stress in elastic media. *Soft Matter*, 11(8):1597–1605, Feb. 2015. ISSN 1744-6848. doi: 10.1039/C4SM02526A. URL https://doi.org/10.1039/C4SM02526A.

P. Ronceray, C. P. Broedersz, and M. Lenz. Fiber networks amplify active stress. *Proceedings of the National Academy of Sciences*, 113(11):2827–2832, Mar. 2016. ISSN 0027-8424, 1091-6490. doi: 10.1073/pnas.1514208113. URL https://doi.org/10.1073/pnas.1514208113.

P. Ronceray, C. P. Broedersz, and M. Lenz. Stress-dependent amplification of active forces in nonlinear elastic media. *Soft Matter*, 15:331–338, 2019. doi: 10.1039/C8SM00949J. URL http://dx.doi.org/10.1039/C8SM00949J.

P. Rosakis, J. Notbohm, and G. Ravichandran. A model for compression-weakening materials and the elastic fields due to contractile cells. *Journal of the Mechanics and Physics of Solids*, 85:16–32, Dec. 2015. ISSN 0022-5096. doi: 10.1016/j.jmps.2015.08.013. URL https://doi.org/10.1016/j.jmps.2015.08.013.

C. A. Ross and M. A. Poirier. Protein aggregation and neurodegenerative disease. *Nat Med*, 10 Suppl: S10–7, July 2004. doi: 10.1038/nm1066. URL https://doi.org/10.1038/nm1066.

S. Salinas. *The Ising Model. In: Introduction to Statistical Physics*, pages 257–276. 01 2001. ISBN 978-1-4419-2884-9. doi: 10.1007/978-1-4757-3508-6. URL https://doi.org/10.1007/978-1-4757-3508-6.

A. Šarić, Y. C. Chebaro, T. P. J. Knowles, and D. Frenkel. Crucial role of nonspecific interactions in amyloid nucleation. *Proceedings of the National Academy of Sciences*, 111(50):17869–17874, 2014. doi: 10.1073/pnas.1410159111. URL https://www.pnas.org/doi/abs/10.1073/pnas.1410159111.

T. Scheibel, R. Parthasarathy, G. Sawicki, X.-M. Lin, H. Jaeger, and S. L. Lindquist. Conducting nanowires built by controlled self-assembly of amyloid fibers and selective metal deposition. *Proceedings of the National Academy of Sciences*, 100(8):4527–4532, 2003. doi: 10.1073/pnas.0431081100. URL https://www.pnas.org/doi/abs/10.1073/pnas.0431081100.

J. D. Schmit, K. Ghosh, and K. Dill. What drives amyloid molecules to assemble into oligomers and fibrils? *Biophysical journal*, 100(2):450–458, Jan 2011. ISSN 1542-0086. doi: 10.1016/j.bpj.2010.11.041. URL https://pubmed.ncbi.nlm.nih.gov/21244841.

J. M. Scholey, I. Brust-Mascher, and A. Mogilner. Cell division. *Nature*, 422(6933):746–752, Apr. 2003. ISSN 0028-0836. URL https://doi.org/10.1038/nature01599.

C. F. Schreck, T. Bertrand, C. S. O'Hern, and M. D. Shattuck. Repulsive contact interactions make jammed particulate systems inherently nonharmonic. *Phys. Rev. Lett.*, 107:078301, Aug 2011a. doi: 10.1103/PhysRevLett.107.078301. URL https://link.aps.org/doi/10.1103/PhysRevLett.107.078301.

C. F. Schreck, C. S. O'Hern, and L. E. Silbert. Tuning jammed frictionless disk packings from isostatic to hyperstatic. *Phys. Rev. E*, 84:011305, Jul 2011b. doi: 10.1103/PhysRevE.84.011305. URL https://link.aps.org/doi/10.1103/PhysRevE.84.011305.

U. S. Schwarz and S. A. Safran. Physics of adherent cells. *Rev. Mod. Phys.*, 85(3):1327, August 2013. doi: 10.1103/RevModPhys.85.1327. URL https://doi.org/10.1103/RevModPhys.85.1327.

F. Sciortino, S. Mossa, E. Zaccarelli, and P. Tartaglia. Equilibrium cluster phases and low-density arrested disordered states: The role of short-range attraction and long-range repulsion. *Phys. Rev. Lett.*, 93:055701, Jul 2004. doi: 10.1103/PhysRevLett.93.055701. URL https://link.aps.org/doi/10.1103/PhysRevLett.93.055701.

F. Sciortino, P. Tartaglia, and E. Zaccarelli. One-dimensional cluster growth and branching gels in colloidal systems with short-range depletion attraction and screened electrostatic repulsion. *The Journal of Physical Chemistry B*, 109(46):21942–21953, Nov 2005. ISSN 1520-6106. doi: 10.1021/jp052683g. URL https://doi.org/10.1021/jp052683g.

M. Sheinman, C. P. Broedersz, and F. C. MacKintosh. Nonlinear effective-medium theory of disordered spring networks. *Physical Review E*, 85(2):021801, Feb. 2012. doi: 10.1103/PhysRevE.85.021801. URL https://doi.org/10.1103/PhysRevE.85.021801.

H. Shen, J. A. Fallas, E. Lynch, W. Sheffler, B. Parry, N. Jannetty, J. Decarreau, M. Wagenbach, J. J. Vicente, J. Chen, L. Wang, Q. Dowling, G. Oberdorfer, L. Stewart, L. Wordeman, J. De Yoreo, C. Jacobs-Wagner, J. Kollman, and D. Baker. De novo design of self-assembling helical protein filaments. *Science (New York, N.Y.)*, 362(6415):705–709, Nov. 2018. doi: 10.1126/science.aau3775. URL https://doi.org/10.1126/science.aau3775.

H. Shintani and H. Tanaka. Frustration on the way to crystallization in glass. *Nature Physics*, 2(3): 200–206, Mar 2006. ISSN 1745-2481. doi: 10.1038/nphys235. URL https://doi.org/10.1038/nphys235.

J. L. Shivers, J. Feng, A. S. G. van Oosten, H. Levine, P. A. Janmey, and F. C. MacKintosh. Compression stiffening of fibrous networks with stiff inclusions. *Proceedings of the National Academy of Sciences*, 117(35):21037–21044, 2020. ISSN 0027-8424. doi: 10.1073/pnas.2003037117. URL https://www.pnas.org/content/117/35/21037.

Y. Shokef and S. A. Safran. Scaling Laws for the Response of Nonlinear Elastic Media with Implications for Cell Mechanics. *Physical Review Letters*, 108(17):178103, Apr. 2012. doi: 10.1103/PhysRevLett.108.178103. URL https://doi.org/10.1103/PhysRevLett.108.178103.

L. E. Silbert, D. Ertaş, G. S. Grest, T. C. Halsey, D. Levine, and S. J. Plimpton. Granular flow down an inclined plane: Bagnold scaling and rheology. *Phys. Rev. E*, 64:051302, Oct 2001. doi: 10.1103/PhysRevE.64.051302. URL https://link.aps.org/doi/10.1103/PhysRevE.64.051302.

L. E. Silbert, A. J. Liu, and S. R. Nagel. Normal modes in model jammed systems in three dimensions. *Phys. Rev. E*, 79:021308, Feb 2009. doi: 10.1103/PhysRevE.79.021308. URL https://link.aps.org/doi/10.1103/PhysRevE.79.021308.

L. Sneddon and M. N. Barber. Decimation transformations for two-dimensional ising spin systems. *Journal of Physics C: Solid State Physics*, 10(14):2653–2664, jul 1977. doi: 10.1088/0022-3719/10/14/017. URL https://doi.org/10.1088%2F0022-3719%2F10%2F14%2F017.

R. S. Sopher, H. Tokash, S. Natan, M. Sharabi, O. Shelah, O. Tchaicheeyan, and A. Lesman. Nonlinear elasticity of the extracellular matrix fibers facilitates efficient inter-cellular mechanical communication. *Biophysical journal*, page 1802.05075, 2018. doi: 10.1016/j.bpj.2018.07.036. URL https://doi.org/10.1016/j.bpj.2018.07.036.

D. J. Steigmann. On the frame invariance of linear elasticity theory. *Zeitschrift für angewandte Mathematik und Physik*, 58(1):121–136, Jan 2007. ISSN 1420-9039. doi: 10.1007/s00033-006-6047-x. URL https://doi.org/10.1007/s00033-006-6047-x.

J. Stephenson. Ising-model spin correlations on the triangular lattice. iii. isotropic antiferromagnetic lattice. *Journal of Mathematical Physics*, 11(2):413–419, 1970. doi: 10.1063/1.1665154. URL https://doi.org/10.1063/1.1665154.

C. Storm, J. J. Pastore, F. C. MacKintosh, T. C. Lubensky, and P. A. Janmey. Nonlinear elasticity in biological gels. *Nature*, 435(7039):191–194, May 2005. ISSN 0028-0836, 1476-4679. doi: 10.1038/nature03521. URL https://doi.org/10.1038/nature03521.

R. H. Swendsen. Monte carlo renormalization group. *Phys. Rev. Lett.*, 42:859–861, Apr 1979. doi: 10.1103/PhysRevLett.42.859. URL https://link.aps.org/doi/10.1103/PhysRevLett.42.859.

A. P. Thompson, H. M. Aktulga, R. Berger, D. S. Bolintineanu, W. M. Brown, P. S. Crozier, P. J. in 't Veld, A. Kohlmeyer, S. G. Moore, T. D. Nguyen, R. Shan, M. J. Stevens, J. Tranchida, C. Trott, and S. J. Plimpton. LAMMPS - a flexible simulation tool for particle-based materials modeling at the atomic, meso, and continuum scales. *Comp. Phys. Comm.*, 271:108171, 2022. doi: 10.1016/j.cpc.2021.108171. URL https://doi.org/10.1016/j.cpc.2021.108171.

L. R. G. Treloar. The elasticity and related properties of rubbers. *Reports on Progress in Physics*, 36(7):755, 1973. ISSN 0034-4885. doi: 10.1088/0034-4885/36/7/001. URL https://doi.org/10.1088/0034-4885/36/7/001.

M. S. Turner, R. W. Briehl, F. A. Ferrone, and R. Josephs. Twisted protein aggregates and disease: The stability of sickle hemoglobin fibers. *Phys. Rev. Lett.*, 90:128103, Mar 2003. doi: 10.1103/PhysRevLett.90.128103. URL https://link.aps.org/doi/10.1103/PhysRevLett.90.128103.

D. Vader, A. Kabla, D. Weitz, and L. Mahadevan. Strain-induced alignment in collagen gels. *PLOS ONE*, 4(6):1–12, 06 2009. doi: 10.1371/journal.pone.0005902. URL https://doi.org/10.1371/journal.pone.0005902.

R. D. Vale and R. A. Milligan. The way things move: Looking under the hood of molecular motor proteins. *Science*, 288(5463):88–95, 2000. doi: 10.1126/science.288.5463.88. URL https://www.science.org/doi/abs/10.1126/science.288.5463.88.

M. S. van Deen, J. Simon, Z. Zeravcic, S. Dagois-Bohy, B. P. Tighe, and M. van Hecke. Contact changes near jamming. *Phys. Rev. E*, 90:020202, Aug 2014. doi: 10.1103/PhysRevE.90.020202. URL https://link.aps.org/doi/10.1103/PhysRevE.90.020202.

M. van Hecke. Jamming of soft particles: geometry, mechanics, scaling and isostaticity. *Journal of Physics: Condensed Matter*, 22(3):033101, dec 2009. doi: 10.1088/0953-8984/22/3/033101. URL https://doi.org/10.1088/0953-8984/22/3/033101.

A. S. G. van Oosten, M. Vahabi, A. J. Licup, A. Sharma, P. A. Galie, F. C. MacKintosh, and P. A. Janmey. Uncoupling shear and uniaxial elastic moduli of semiflexible biopolymer networks: compression-softening and stretch-stiffening. *Scientific Reports*, 6:19270, 2016. doi: 10.1038/srep19270. URL https://doi.org/10.1038/srep19270.

A. S. G. van Oosten, X. Chen, L. Chin, K. Cruz, A. E. Patteson, K. Pogoda, V. B. Shenoy, and P. A. Janmey. Emergence of tissue-like mechanics from fibrous networks confined by close-packed cells. *Nature*, 573(7772):96–101, 2019. doi: 10.1038/s41586-019-1516-5. URL https://doi.org/10.1038/s41586-019-1516-5.

H. Wang and X. Xu. Continuum elastic models for force transmission in biopolymer gels. *Soft Matter*, 16:10781–10808, 2020. doi: 10.1039/D0SM01451F. URL http://dx.doi.org/10.1039/D0SM01451F.

H. Wang, A. Abhilash, C. S. Chen, R. G. Wells, and V. B. Shenoy. Long-Range Force Transmission in Fibrous Matrices Enabled by Tension-Driven Alignment of Fibers. *Biophysical Journal*, 107(11):2592–2603, Dec. 2014. ISSN 00063495. doi: 10.1016/j.bpj.2014.09.044. URL https://doi.org/10.1016/j.bpj.2014.09.044.

G. H. Wannier. Antiferromagnetism. the triangular ising net. *Phys. Rev.*, 79:357–364, Jul 1950. doi: 10.1103/PhysRev.79.357. URL https://link.aps.org/doi/10.1103/PhysRev.79.357.

S. Whitelam and R. L. Jack. The statistical mechanics of dynamic pathways to self-assembly. *Annual Review of Physical Chemistry*, 66(1):143–163, 2015. doi: 10.1146/annurev-physchem-040214-121215. URL https://doi.org/10.1146/annurev-physchem-040214-121215. PMID: 25493714.

S. Whitelam, C. Rogers, A. Pasqua, C. Paavola, J. Trent, and P. L. Geissler. The impact of conformational fluctuations on self-assembly: Cooperative aggregation of archaeal chaperonin proteins. *Nano Letters*, 9(1):292–297, Jan 2009. ISSN 1530-6984. doi: 10.1021/nl8029306. URL https://doi.org/10.1021/nl8029306.

K. G. Wilson. Problems in physics with many scales of length. *Scientific American*, 241(2):158–179, Aug. 1979. doi: 10.1038/scientificamerican0879-158. URL https://doi.org/10.1038/scientificamerican0879-158.

P. Wriggers. *Nonlinear Finite Element Methods*. Springer, Berlin, Heidelberg, 1 edition, 2008. ISBN 978-3-642-09002-8. URL https://doi-org.inp.bib.cnrs.fr/10.1007/978-3-540-71001-1.

F. Y. Wu. The potts model. *Rev. Mod. Phys.*, 54:235–268, Jan 1982. doi: 10.1103/RevModPhys.54.235. URL https://link.aps.org/doi/10.1103/RevModPhys.54.235.

M. Wyart, H. Liang, A. Kabla, and L. Mahadevan. Elasticity of floppy and stiff random networks. *Phys. Rev. Lett.*, 101:215501, Nov 2008. doi: 10.1103/PhysRevLett.101.215501. URL https://link.aps.org/doi/10.1103/PhysRevLett.101.215501.

X. Xu and S. A. Safran. Nonlinearities of biopolymer gels increase the range of force transmission. *Physical Review E*, 92(3):032728, Sept. 2015. doi: 10.1103/PhysRevE.92.032728. URL https://doi.org/10.1103/PhysRevE.92.032728.

XVIVO and Harvard University. The inner life of the cell, 2006. URL https://xvivo.com/examples/the-inner-life-of-the-cell.

C. N. Yang and T. D. Lee. Statistical theory of equations of state and phase transitions. i. theory of condensation. *Phys. Rev.*, 87:404–409, Aug 1952. doi: 10.1103/PhysRev.87.404. URL https://link.aps.org/doi/10.1103/PhysRev.87.404.

Y. Ye, W. Sun, Y. Wang, X. Shao, X. Xu, F. Cheng, J. Li, and K. Wu. A unified model: self-assembly of trimesic acid on gold. *The Journal of Physical Chemistry C*, 111(28):10138–10141, Jul 2007. ISSN 1932-7447. doi: 10.1021/jp072726o. URL https://doi.org/10.1021/jp072726o.

T. Yokoyama, S. Yokoyama, T. Kamikado, Y. Okuno, and S. Mashiko. Selective assembly on a surface of supramolecular aggregates with controlled size and shape. *Nature*, 413(6856):619–621, Oct 2001. ISSN 1476-4687. doi: 10.1038/35098059. URL https://doi.org/10.1038/35098059.

T. Yokoyama, T. Kamikado, S. Yokoyama, and S. Mashiko. Conformation selective assembly of carboxyphenyl substituted porphyrins on au (111). *The Journal of Chemical Physics*, 121(23):11993–11997, 2004. doi: 10.1063/1.1819877. URL https://doi.org/10.1063/1.1819877.

A. Zbinden, M. Pérez-Berlanga, P. De Rossi, and M. Polymenidou. Phase separation and neurodegenerative diseases: A disturbance in the force. *Dev Cell*, 55(1):45–68, Oct. 2020. doi: 10.1016/j.devcel.2020.09.014. URL https://doi.org/10.1016/j.devcel.2020.09.014.

H. P. Zhang and H. A. Makse. Jamming transition in emulsions and granular materials. *Phys. Rev. E*, 72:011301, Jul 2005. doi: 10.1103/PhysRevE.72.011301. URL https://link.aps.org/doi/10.1103/PhysRevE.72.011301.

Z. Zhang and S. C. Glotzer. Self-assembly of patchy particles. *Nano Letters*, 4(8):1407–1413, Aug 2004. ISSN 1530-6984. doi: 10.1021/nl0493500. URL https://doi.org/10.1021/nl0493500.

université PARIS-SACLAY

ÉCOLE DOCTORALE
Physique en Île-de-France (PIF)

Titre : Matériaux complexes : auto-assemblages frustrés et élasticité non-linéaire.....
Mots clés : auto-assemblage, frustration géométrique, groupe de renormalisation, milieux granulaires, cytosquelette, élasticité non-linéaire

Résumé : Cette thèse est divisée en deux parties avec peu de recoupement. La première partie traite de l'auto-assemblage pathologique de protéines normalement solubles. Dans un certain nombre de cas, elles ont tendance à former des agrégats "frustrés" qui ne grandissent que dans une seule direction. Nous étudions ici la forme et la taille des agrégats à l'équilibre formés par des particules avec des interactions directionnelles. Cette étude devrait permettre de mieux comprendre le mécanisme sous-jacent à la formation de fibres. La deuxième partie se concentre sur la transmission des contraintes internes dans les matériaux complexes tels que les réseaux de fibres biologiques et la matière granulaire. Nous développons un modèle continu de ces matériaux, qui tient compte de l'asymétrie mesurée dans leur réponse à la tension par rapport à la compression. Nous montrons analytiquement et numériquement que cela peut conduire les réseaux fibreux à rectifier les contraintes internes vers la contraction, et les milieux granulaires vers l'expansion.

Title : Complex Materials : Frustrated Self-Assembly and Nonlinear Elasticity.....
Keywords : self-assembly, geometrical frustration, renormalization group, granular media, cytoskeleton, nonlinear elasticity

Abstract : This thesis is divided into two parts with little overlap. The first part deals with the pathological self-assembly of normally soluble proteins. In a number of cases, they tend to form "frustrated" aggregates which grow only in one direction. We hereby study the shape and size of the equilibrium clusters formed by particles with directional interactions. This investigation hopefully leads to a better understanding of the underlying mechanism of fiber-formation. The second part focuses on the transmission of internal stresses in complex materials such as biological fiber networks and granular matter. We develop a continuum model of such materials, which accounts for the measured asymmetry in their response to tension versus compression. We show analytically and numerically that this may lead fibrous networks to rectify internal stresses towards contraction, and granular media to rectify towards expansion.